
Nanoparticle-Functionalized Polymers for Laser Powder Bed Fusion

Dissertation

by

Tim Hupfeld

for the degree of
Doctor of Natural Science
– Dr. rer. nat. –

presented to
The Faculty of Chemistry
University of Duisburg-Essen
Germany

2020

DuEPublico

Duisburg-Essen Publications online

UNIVERSITÄT
DUISBURG
ESSEN

Offen im Denken

ub | universitäts
bibliothek

Diese Dissertation wird via DuEPublico, dem Dokumenten- und Publikationsserver der Universität Duisburg-Essen, zur Verfügung gestellt und liegt auch als Print-Version vor.

DOI: 10.17185/duepublico/74518

URN: urn:nbn:de:hbz:464-20210714-082639-3

Alle Rechte vorbehalten.

This thesis was prepared from *November 2016* to *July 2020* in the group of Priv.-Doz. Dr. Bilal Gökce, Institute of Technical Chemistry I (headed by Prof. Dr.-Ing. Stephan Barcikowski), University of Duisburg-Essen.

Date of the oral examination:

07.12.2020

Referees:

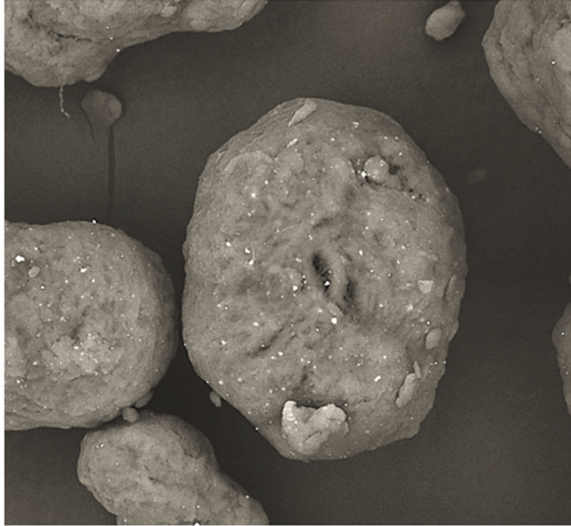
Prof. Dr. Stephan Barcikowski
University of Duisburg-Essen

Prof. Dr. Michael Giese
University of Duisburg-Essen

Prof. Dr. Michael Schmidt
Friedrich-Alexander-Universität Erlangen-Nürnberg

Chairman:

Prof. Dr. Rainer Meckenstock
University of Duisburg-Essen



Variety's the very spice of life,
That gives it all its flavour.

William Cowper, The Task (1785)

Acknowledgement

Putting together bits and pieces to form this dissertation was a great experience. Numerous people have contributed to this success and have provided me with inspiration and support. I would like to express my deepest appreciation to all of them.

Special thanks to Stephan Barcikowski for giving me the opportunity to be a part of his group and to work on a variety of interesting topics. Thanks should also go to Bilal Gökce, who recruited me in the first place and convinced me to stay after my master's thesis instead of going straight into industry. Stephan and Bilal, I cannot begin to express my gratitude for consistently providing me with new challenges and for giving me the freedom to find my own path, but also for steering me in the right direction whenever necessary.

Many thanks to the whole department of Technical Chemistry and its current and former members. Thank you for a delightful time with group events, team building and coffee breaks, but also for practical suggestions and technical or administrative support. Special thanks to Simon Siebeneicher, Anna Ziefuß, Dieter Jacobi, Elisabeth Mühlhausen, Claudine Florian and Nina Stockem.

My research work was not possible without cooperation. I very much appreciate Carlos Doñate-Buendía for his help during experiments and for his valuable ideas and comments on the manuscripts. I thank Michael Schmidt, Jochen Schmidt, Evgeny Zhuravlev, Alexander Sommereyns, Johannes Heberle and Stan Gann for a successful collaboration within the DFG priority program SPP 2122 “Materials for Additive Manufacturing” (MATframe). I would also like to thank Michael Giese for a fruitful collaboration and for taking on the second review of my dissertation. Further thanks to the collaboration partners Ulf Wiedwald, Andreas Wegner, Soma Salamon, Joachim Landers, Matthias Krause, Milen Nachev, Meik Blanke and Alexandra Ingendoh-Tsakmakidis. I also had great pleasure of working with the team of the luminescence group at the Université Claude Bernard Lyon 1.

Special thanks to David Amans and Gaétan Laurens for their warm welcome und constant support. My stay in Lyon was certainly one of the highlights of my doctoral studies.

I would like to extend my sincere thanks to my students (in alphabetical order): Leyla Cakir, Christian Gollner, Karsten Knop, Moritz Krebs, Philipp May, Simon Nieskens, Elisavet Papadopoulou, Farbod Riahi, Alexander Schmitz, Alexander Schug, Vladyslav Sharov and Frederic Stein. Your hard work played a decisive role in my research.

I am also grateful to the Faculty of Chemistry, the European Cooperation in Science and Technology, and Evonik Industries for their financial support of my research and I gratefully acknowledge the DFG for setting up the priority program SPP 2122.

Finally, the completion of my dissertation would not have been possible without the continuous support of my family and friends, and the unparalleled patience and encouragement of my wife Anna.

Abstract

As one of the major additive manufacturing (AM) techniques, laser powder bed fusion (PBF-LB) of polymers is of great interest for prototyping and flexible small-scale production of geometrically complex parts. Since polymer powders have material-related limitations regarding their processability, the modification and control of their optical and thermal properties have become decisive factors in PBF-LB. In order to expand the material variety, nano-functionalization captures high interest and even small nanoparticle loadings (≤ 0.1 wt%) affect the processing behavior. One challenge of nanoparticle-functionalization is nanoparticle dispersion and therefore also avoiding aggregates with sizes of hundreds of nm up to the μm -range, which may influence laser absorption, heat conduction, melting, or resolidification behavior, and could negatively affect the properties of the final part. However, a deep understanding of the interplay between the PBF-LB process and small mass fractions of nanoparticulate additives in the ppm range is required in order to exploit the potential of nanoparticle additivation. In this thesis, colloidal additivation is introduced as an approach to create nanoparticle-functionalized polymer powder materials for PBF-LB. Since colloids used in this approach are synthesized by laser ablation and laser post-processing in liquids, this thesis also aims to develop a deeper understanding of these laser-based synthesis methods. Research was conducted on the process kinetics and determinants of colloidal additivation based on adjustment of electrostatic interactions between nanoparticles and polymer microparticles. The effects of the nanoparticle material, its optical properties, and degree of dispersion on PBF-LB were investigated for different polymer-nanoparticle systems based on polyamide 12 and thermoplastic polyurethane. This thesis emphasizes the extraordinary importance of nanoparticle dispersion rather than just considering their mass loading (wt%), and sets out for a new way to functionalize parts generated by PBF-LB.

Table of Contents

Abbreviations	XIII
1 Introduction	1
2 State of the Art.....	5
2.1 The advent and rise of additive manufacturing.....	5
2.2 Laser powder bed fusion	9
2.3 Polymers for laser powder bed fusion	10
2.4 Nano-Functionalized polymer powders	14
2.5 Nano-functionalization by colloidal additivation	17
2.6 Laser-generated nanoparticles.....	19
3 Experimental methods	26
4 Laser synthesis of nanoadditives	28
4.1 Laser ablation in highly viscous media	30
4.2 Laser post-processing of magnetic nanoparticles.....	39
5 A colloidal additivation process for polymer powders.....	54
5.1 Proof of concept	56
5.2 Identification of process determinants	62
5.3 Upscaling of nano-functionalization towards kg/h.....	73
6 3D printing of nanoparticle-functionalized powders.....	80
6.1 Tuning the laser absorption of polymer powders.....	81
6.2 Calorimetric properties and microstructure	94
7 Application potential of 3D printed functionalized parts.....	113
7.1 Magnetic functionalization	115
7.2 Plasmonic and antibacterial properties.....	130

8	Summary and Outlook.....	137
	References	140
	Appendix.....	153
A1	Supporting Information: Dynamics of laser-induced cavitation bubbles at a solid-liquid interface in high viscosity and high capillary number regimes.....	153
A2	Supporting Information: Manipulation of the size and magnetic properties of colloidal $Y_3Fe_5O_{12}$ nanoparticles by laser post-processing	159
A3	Tools and procedure for oxide target preparation from mixed powders.....	164
A4	LFL of ball milled YIG powder, ready to use as nanoadditive in AM	166
A5	Flexibel passage reactor design	167
A6	Supporting Information: How colloidal surface additivation of polyamide 12 powders with well-dispersed silver nanoparticles influences the crystallization already at low 0.01 vol%.....	168
A7	Drying procedure of powders after colloidal additivation	170
A8	Supporting Information	171
A9	Spray drying of TPU powder suspensions for nanoparticle-functionalization	181
A10	Adsorption efficiency as a function of polymer concentration.....	183
A11	Comparison of ns- and ps-LPP of iron oxide	184
	Curriculum Vitae	185
	Publications and conference contributions.....	187
	List of publications included in this thesis	190
	List of student works.....	193
	Eigenständigkeitserklärung (Declaration)	196

Abbreviations

ADC	Analytical disc centrifugation
AM	Additive manufacturing
BJT	Binder jetting
CAD	Computer-aided design
CB-NP	Carbon black nanoparticles
DED	Direct energy depositions
DLP	Digital light processing
DLS	Dynamic light scattering
DSC	Differential scanning calorimetry
FDM	Fused deposition modelling
FFF	Fused filament fabrication
FSC	Fast scanning calorimetry
GMF	Gold molar fraction
IEP	Isoelectric point
LAL	Laser ablation in liquids
LCD	Liquid-crystal display
LED	Light emitting diode
LFL	Laser fragmentation in liquid
LML	Laser melting in liquid
LPP	Laser post-processing (of colloids)
LSPC	Laser synthesis and processing of colloids
MEX	Material extrusion
MJ	Material jetting
MJF	Multi Jet Fusion
OB	Optical breakdown

ODS	Oxide dispersion-strengthened (alloy)
PA	Polyamide
PAEK	Polyaryletherketones
PAO	poly-alpha-olefin
PBF	Powder bed fusion
PBF-LB	Powder bed fusion - Laser beam (according to ISO/ASTM 52900); synonyms: L-PBF, LPBF, SLS
PBF-LB/C	Powder bed fusion-Laser beam / ceramics
PBF-LB/Co	Powder bed fusion-Laser beam / composites
PBF-LB/M	Powder bed fusion-Laser beam / metals
PBF-LB/P	Powder bed fusion-Laser beam / polymers
PBS	Phosphate buffered saline solution
PEEK	Polyetheretherketone
PEK	Polyetherketone
PEKK	Polyetherketoneketone
PLA	Poly lactide
PP	Polypropylene
SEM	Scanning electron microscope
SLA	Stereolithography
SLM	Selective laser melting
SLS	Selective laser sintering
SPR	Surface plasmon resonance
TEM	Transmission electron microscope
TPE	Thermoplastic elastomers
TPE	Thermoplastic polyelastomere
TPU	Thermoplastic polyurethane
UT	Untreated
VPP	Vat photopolymerization
XRD	X-Ray diffraction
YIG	Yttrium iron garnet ($Y_3Fe_5O_{12}$)
YIP	Yttrium iron perovskite ($YFeO_3$)
YIG	Yttrium iron garnet

1 Introduction

Additive manufacturing (AM), which is typically referred to as 3D printing, has fundamentally changed the way we create objects, which has resulted in profound socio-economic changes [1,2]. Starting right from a digital design, AM combines a printer and a tailored material to generate customized 3D parts. Due to its versatility and wide range of applications, including aerospace and automotive, from aerospace and automotive [3], catalysis [4], medicine [2], construction [5] and the food industry [6], the use of AM has shown dynamic growth and has transformed traditional markets and supply chains [3,7]. Initially, components made by AM were used in rapid prototyping; however, the technology has evolved towards rapid manufacturing and industrial mass customization of technically sophisticated components [8,9]. One of the main methods for AM of polymers is laser powder bed fusion (PBF-LB, according to ISO/ASTM 52900). However, PBF-LB is limited to only a few polymer powder materials that are available for complex processing tasks, and the market is dominated by the standard material polyamide 12 (PA12) [10]. Expanding the material portfolio beyond the PBF-LB standard material toward other engineering and high performance polymers is challenging [11]. It is necessary to design the material specifically for the PBF-LB process, which requires a profound understanding of the relationship between the powder and the process parameters, as well as between the resulting microstructure and the final part properties.

Apart from preparation of new powders by dry and wet grinding [12,13], precipitation [14] or melt emulsification [15], the modification of powders by additivation with organic and inorganic micro- and nanoadditives allows adaption of the powder properties to the PBF-LB process, which improves processing and final part properties [16,17]. Nanomaterial loadings are commonly expressed as wt% without further information of their dispersion, which strongly depends on the additivation method [16,18]. Most of the conventional additivation methods, like dry coating or melt compounding, substantially result in nanoparticle aggregation and weak dispersion [16,19,20] since they typically use aggregated

nanomaterials from gas phase synthesis. Even small nanoparticle loadings (≤ 0.1 wt%) can affect the PBF-LB processing [21–23] and it can be assumed that the dispersion of nanoparticles, especially on the polymer particle surface, plays a decisive role during PBF-LB; e.g., influencing laser absorption, heat conduction, and melting or resolidification behavior. Therefore, addressing these low filler loadings with highly dispersed nanoparticle coatings is of significant interest.

The need for high dispersion is also known from other fields. For example in heterogeneous catalyst [24–29], where colloidal additivation can be utilized in order to achieve homogeneous surface decoration of inorganic particles by pH-controlled adsorption of colloidal nanoparticles [30–32]. Laser synthesis and processing of colloids (LSPC) is an ideal method for generating the colloids needed for colloidal additivation [33]. Not only are laser-generated nanoparticles free of surfactants that results in a higher adsorption (supporting) efficiency [32], but they also contain a high degree of surface defects caused by partial oxidation, which increases their electrostatic stability and therefore their dispersion on the support [34,35]. As a flexible one-step synthesis without chemical precursors, laser ablation in liquids is also applicable to liquid monomers [36,37], polymer solutions [38], and inks [39]. This is of significant interest for nano-additivation of materials for AM; e.g., base material for resins, filaments and powders, but for such an application, high productivity of LSPC is crucial. Additionally, it is known that laser-induced cavitation bubbles play an important role in nanoparticle formation and productivity [40]. However, there are still knowledge gaps when it comes to understanding nanoparticle formation and bubble dynamics during laser synthesis, especially in viscous liquids like monomers, polymer solutions, and inks.

This thesis is built on the approach of transferring the colloidal additivation from heterogeneous catalysis to the production of functionalized polymer powders using laser-generated colloids. By focusing on the following four aims, this thesis will make substantial contributions to finding new nanoparticle-functionalized polymer materials, tailored for AM:

1. Synthesis of nanoadditives for AM via LSPC and investigation of the cavitation bubble dynamics during laser ablation in viscous liquid
2. Achieve high dispersion of nanoparticulate decoration on polymer microparticles for PBF-LB
3. Utilize highly dispersed nanoparticle-functionalization to manipulate the processability of the feedstock powder via CO₂ and diode laser PBF, especially at small nanoparticle loadings ≤ 0.1 wt%
4. Introduction of new functionalities in printed parts through additivation of the feedstock materials with highly dispersed nanoparticles

After discussing the theoretical background in *Chapter 2* (Figure 1), the experimental methods are presented in *Chapter 3*. Based on the four aims, this thesis addresses the topics of LSPC, colloidal additivation of polymer powders, PBF-LB of functionalized powders, and applications for 3D printed parts.

Using high speed imaging, laser-induced cavitation bubbles are investigated in liquids with high viscosities, similar to monomer and polymer solutions used in AM (*Chapter 4*), which is expected to enable a better understanding and control of nanoparticle formation and productivity. Laser post-processing (LPP) is investigated as a method for manipulating the size of magnetic nanoparticles, which could facilitate new magnetic-functionalized materials for AM [41–43]; e.g., design of 3D printed magnetic structures [39,44,45].

Following discussion of nanoparticle synthesis, a new approach is introduced in *Chapter 5* for the production of nanoparticle-functionalized feedstock materials for PBF-LB by colloidal additivation, which proves the applicability of the colloidal additivation route known for inorganic supports. With the model system PA12-silver, this chapter introduces nanoparticle-functionalized powder material for PBF-LB and outlines the difference between mass specific and surface specific nanoparticle dose. Analytical methods, including 2D and

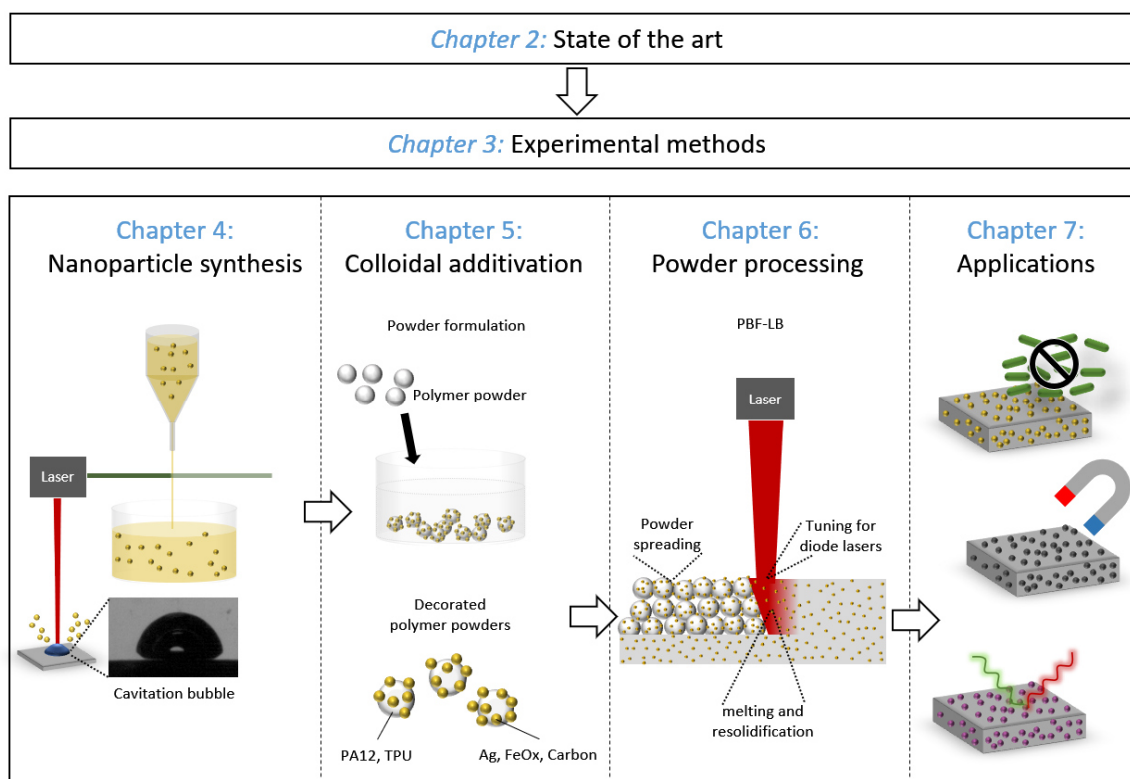


Figure 1: Process route toward nanoparticle-functionalized powders: investigation of laser synthesis of nanoparticles in high viscosity liquids and LPP of oxide nanoparticles. Application-specific nanoparticles are adsorbed on polymer microparticles after laser synthesis and processing of colloids to produce nanoparticle-functionalized powders that are qualified for powder bed fusion.

3D imaging techniques, are used to investigate the relevant parameters for successful colloidal additivation, focusing on the correlation of surface properties (e.g., Zeta potential) and deposition time constant, yield, and quality. This chapter also presents the upscaling potentials of colloidal additivation toward the kg-scale of polymer powder, with a focus on developing a continuous process system to generate enough powder for PBF-LB.

For development of nanoparticle-functionalized powders, it is essential to understand how nanoparticle size, dispersion, and nanoparticle load affect processability during PBF-LB. Therefore, *Chapter 6* analyzes the nanoparticle-material-related effects during PBF-LB. Laser absorption can be tuned, e.g., by plasmonic nanoparticles that act as photothermal sensitizers that enhance absorption at 445 nm, which allows PBF with a diode laser. Furthermore, the influence of nanoparticles on the melting and resolidification behavior of the polymer is investigated.

Finally, *Chapter 7* provides examples of new additive manufactured plasmonic, magnetic, and antibacterial functionalized feedstock materials based on LSPC and colloidal additivation of polymer micropowders, which highlights the potential of high dispersion for enabling new functionalities of the final part.

2 State of the Art

After a general overview of the field of AM, the following chapter gives an introduction into the PBF-LB process and its possibilities and limits when it comes to printing complex parts. The importance of the polymer powder materials for PBF-LB and the complex relation of process and powder is underlined. This chapter will further continue with the potentials of nanoparticle-composites for PBF-LB as an established method to introduce new functionalities into the powder and the final part. In addition, different methods to achieve nano-additivation are specified and the typical problem of aggregation of nanoadditives is pointed out. Laser synthesis and processing of colloids (LSPC) is introduced as a green synthesis route for generation of highly dispersed nanoparticle colloids in a variety of liquids. The state-of-the-art section also covers the knowledge of the involved mechanism during laser ablation in liquids (LAL). Finally, the fundamentals of colloidal additivation are introduced, a method to homogeneously adsorb nanoparticles on a support structure to create nanoparticle-composites.

2.1 The advent and rise of additive manufacturing

In the world of manufacturing, additive technologies represent a relatively small and young discipline. Instead of creating an object by removing material, AM (often referred to as “3D printing”) creates an object layer by layer from a material feedstock. After the first attempts to create 3D objects by AM in the 1960s, it took until 1987 for a first commercial AM machine, using stereolithography (SLA) [46], where the object was built by localized light induced polymerization of a resin. Today, many industries are accelerating implementation of 3D printing technologies, while 4D printing of smart structures is already entering the market [39,47–51] and trends like nanoscale 3D printing come within reach [52]. A multitude of AM methods exists to create complex objects right from a 3D computer-aided design (3D CAD) file in a rapid process (Figure 2)[7,53,54]. Fused deposition modelling (FDM) for example dominates the market for home use and finds applications in building large scale

parts (several meters) within a relatively short time span by well-established and cheap material extrusion. Similar to FDM, printing of concrete can be used to print complete houses [55,56] and even printing of food via material extrusion finds relevant applications [57]. In addition, binder jetting, light polymerization techniques (e.g. SLA), powder bed fusion (PBF), and direct energy depositions (DED) play an important role for industrial applications [7]. In 2018, approx. 28 % of the industries in Germany used AM for prototyping or small-scale production [58]. While SLA is limited to polymers, binder jetting is an approach to fabricate 3D parts from sand and ceramic (e.g. casting forms), metal, glass or polymer powders in combination with polymeric binders [59]. Compared to binder jetting, PBF has proven to have greater potential for manufacturing final parts for end-use applications, since it comes with higher resolution and better mechanical strength than binder jetting parts. Furthermore, PBF and DED not only work for polymers, but are well established for the fabrication of advanced metal parts [60]. They use lasers, electron beams or IR sources to fuse powder particles to a 3D object.

(a)

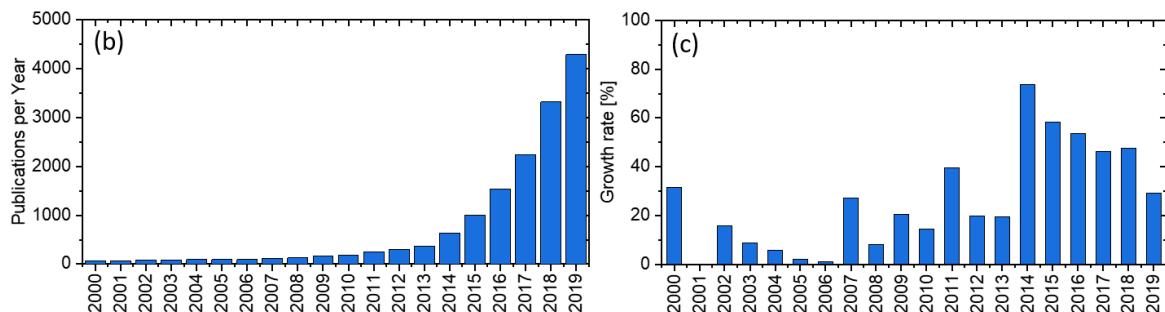
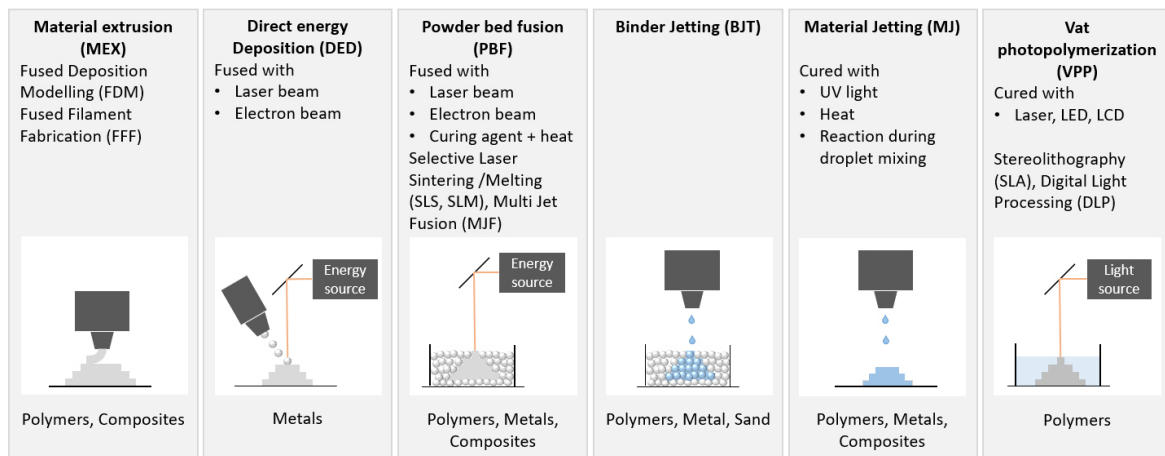


Figure 2: (a) Important classes of AM technology according to DIN EN ISO/ASTM 52900:2018. (b) Publications per year and (c) growth rate of publications in the field of AM based on publication count from Web of Science™ (Thomson Reuters) between 2000 and 2018 (Searched for the TOPIC “Additive manufacturing”). The number of publications related to AM increased dramatically since 2010.

The largest industry sectors, where AM techniques are applied, are the automotive and aerospace industries [61]. In 2015, Frost and Sullivan predicted a 15 % growth per year of the AM market until 2025, driven by a trend toward cost-effective manufacturing and rapid production [62]. Together, aerospace, automotive and medical industry account for more than 50 % of the growth in AM. The exponential growth rates are also reflected in the number of scientific publications in the field of AM (Figure 2b,c). In the last 5 years the growth rate of the numbers of scientific publications was constantly above 20 %.

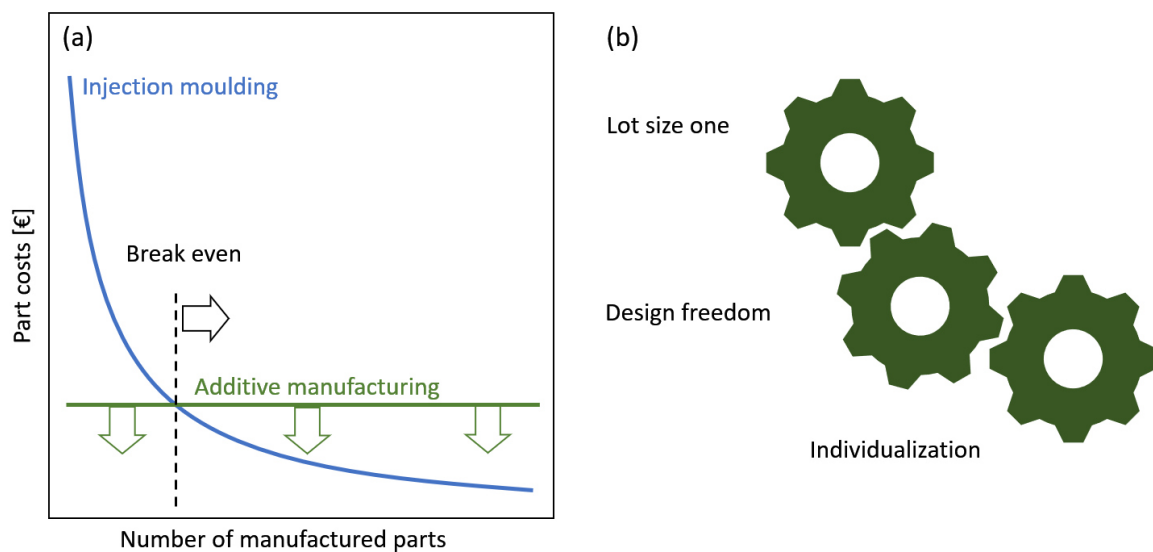


Figure 3: Limits and strength of AM from an economical perspective. (a) Qualitative comparison of polymer part costs as a function of the number of manufactured parts for injection molding and AM. The tendency of decreasing part costs in AM shifts the break-even toward a higher part number at which AM is economically more useful. (b) Central features that result in AM's disruptive potential.

While industrial application of AM advances, standardization and quality management are becoming important aspects [48,63]. In industrial AM, the print cost only account for 30-40 % of the value chain with decreasing tendency. Compared to mass production via injection molding, where part cost decrease with increasing part number, AM features almost no economy of scale. Part costs depend on the part number for a constant volume of a single build job (Figure 3). If larger machines are used and thereby the build job volume increases, part costs decrease as well [64], but not in a way known from other manufacturing methods. On the first glance this looks like a major disadvantage for AM, but it can be turned into an advantage if small series or high degree of individualization are needed (Figure 3). AM overcomes the limits of traditional manufacturing techniques and enables building novel geometries, introducing new material properties [5]. It saves material, time and gives new possibilities for designers. Thus, it is especially important for parts with high level of geometric complexity and individualization like prosthesis [65], bio-medical implants [66] or light weight and fuel saving construction, e.g. stationary turbine components and

small Titanium aerospace components [67]. In order to profit from AM, it is therefore necessary to start right from the CAD file with individualized parts that are using the design freedom and flexibility, e.g. for design changes during production. Instead of looking at AM just from the print job perspective it is crucial to take a look at the whole process chain (Figure 4), which also needs smart software to connect the individual process steps like post-processing and part testing in order to organize and automatize AM operations, as it was recently shown by a consortium of Premium AEROTEC (Airbus), Daimler und EOS in their fully automatized NextGenAM project [68]. Hereby, AM also provides opportunities to rethink supply chains and logistics, and develop new business models [69]. For example, a digitalized spare part depot could provide printable spare parts on demand wherever needed [7,70].

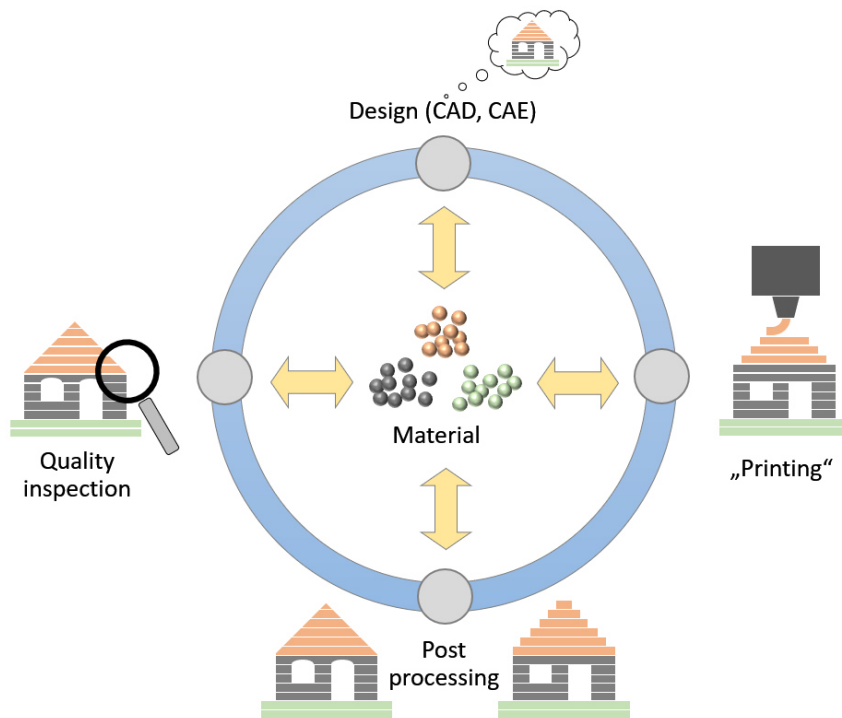


Figure 4: Schematic AM process chain featuring design, printing, post processing and quality inspection.

Besides services and equipment, material makes 15 % of sales throughout the AM value chain [67]. The German National Academy of Sciences (Leopoldina), the German Academy of Science and Engineering (acatech) and the Union of German Academies of Sciences and Humanities recently proposed 13 action fields for AM. Six of these action fields are material-related, which underlines the importance of material as a central element for further growth in AM [71]. A prominent example for the need of material development is the field PBF-LB, where polymers have become increasingly important [63]. Since the market is dominated

by only a hand full of process qualified powders, the applications for parts made by PBF-LB are limited by the properties of these materials [12].

2.2 Laser powder bed fusion

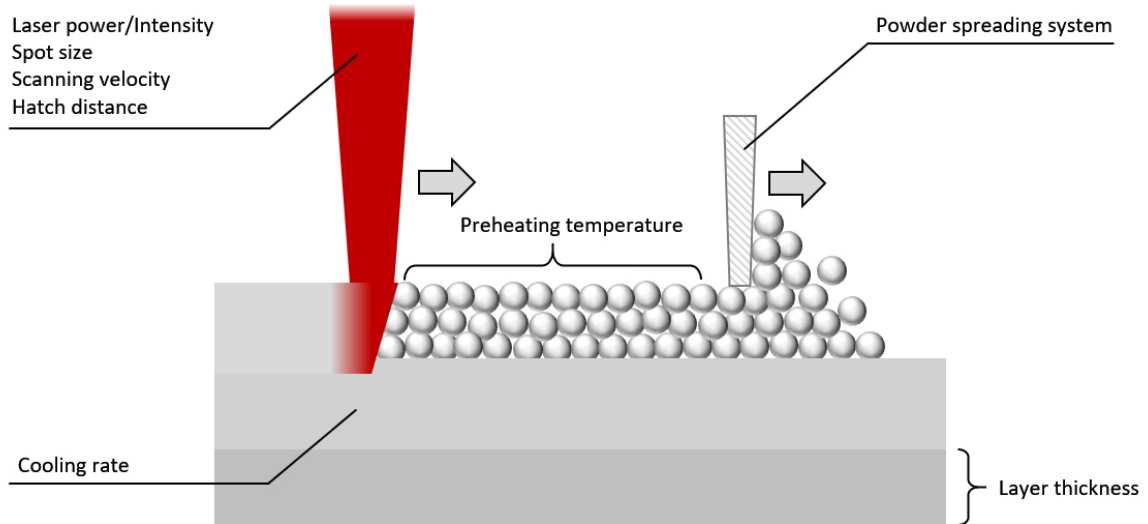


Figure 5: Schematic illustration of the PBF-LB process with relevant process parameters.

Laser powder bed fusion (PBF-LB) is known as L-PBF, LPBF or PBF-LB, selective laser sintering (SLS) as PBF's first commercial process for polymer powder bed fusion [8], or selective laser melting (SLM) for metals. However, according to the latest standardization efforts by ISO/ASTM [72], the term PBF-LB will be used throughout this thesis. PBF-LB has been extensively studied for polymers (PBF-LB/P), metals (PBF-LB/M), ceramics (PBF-LB/C) and composites (PBF-LB/Co) and can be divided into the sub-processes powder spreading/recoating, preheating, irradiation (IR, Laser or electron beam) and cooling, as illustrated in Figure 5. It involves a large set of parameters that affects build speed and final part properties. At the beginning of each build job, several layers of powder are spread on the build plate from a reservoir close to the powder bed as a homogeneous basis for the print job. There are different methods for powder recoating, including roller and blades [73]. In the next step, the whole powder bed is pre-heated. In general, this step provides most of the energy for fusion, so that the laser just needs to add a small energy dose to induce the fusion process. Furthermore, preheating allows the sintered areas to remain at an elevated temperature after laser irradiation and to cool down slowly, providing sufficient time to minimize thermal stress, which is induced by fast cooling rates [74,75]. It also improves wetting and thus the adhesion between sintered layers, which reduces porosity. For a semi-crystalline polymer, the powder bed is pre-heated close to the melting temperature and above the crystallization temperature, which gives the process window for

polymer PBF-LB. It is particularly important how well these two transition points are defined. Typically, the onset of the melting peak and the onset of the crystallization peak are chosen, instead of the peak maximum temperatures [76,77]. After irradiation, the powder bed is lowered by a defined height to recoat the next layer. Typical layer heights range from 50 – 300 μm and the unsintered powder provides support for the next layers. 3D parts are now generated layer by layer by repeating the cycle of lowering the powder bed, powder recoating, preheating and laser irradiation (Figure 5). As the irradiated layers are covered with new layers, they slowly cool down and a few layers below the surface, parts are already solidified as it was recently shown by Drummer *et al.* [78]. After finishing the print job, the build volume is cooled down and unfused powder is removed, sifted and mixed with fresh powder for the next print job. The ration of recycled and fresh powder depends on the material, the process conditions and the requirements on final part properties [79].

Besides the process window defined by melting and crystallization, each polymer powder material also has an optimum temperature region, which is referred to as stable sintering region [80]. In this temperature range the polymer can be processed without decomposition [81]. The fusion of polymer powder particles during PBF-LB requires a diffusion of organic material and thus enough thermal energy to overcome the activation energy for mass transport. In polymers the diffusion transport is significantly slower compared to metal PBF due to the highly viscous flow of polymers. Therefore, the fusion rate increases with decreasing melt viscosity and increasing temperature [82].

From the machine part of view, the powder spreading system [73] and the light absorption of the powder are highly important for processability. The latter depends on the used laser source [83] and is very different for PBF-LB of polymers with CO_2 and diode lasers. CO_2 lasers emit at 10.6 μm wavelength, where most polymers show enough absorption, but they result in expensive and large machines. Therefore, the market of small desktop machines is dominated by diode laser-based machines, resulting in the need for special absorption optimized polymer powder materials. Recent developments also point towards industrial scale use of diode laser arrays and beam shaping to achieve shorter processing times [84] which makes tailored polymer powder materials even more important.

2.3 Polymers for laser powder bed fusion

In theory, any polymer material in powder form is processable in PBF-LB. However, only few polymer powder materials available today fulfil the requirements for advanced processing tasks to comply with up-to-date process routes and lead to reproduceable final part quality. Compared to the broad variety of polymers for injection molding the currently

available range of polymer powder materials, let alone their modifications, is extremely limited and represents a significant obstacle to the further development of PBF-LB [85–87].

The restriction in the choice of material is based on the requirements of the sintering process on the material [88] (Figure 6). Optical properties like transmission, absorption, and reflection influence the energy deposition and thus the thermal gradient in the powder bed, which is also affected by laser parameters, powder layer thickness and powder packing density. Powder morphology, particle size distribution and flowability also play an important role [15,89]. Insufficient flowability [90] and high losses of the laser power due to high scattering and low absorption of the powder materials [83] results in insufficient final part properties such as porosity [91] or incomplete melting of particles. These defects in turn lead to variations in mechanical properties and geometrical accuracy [91]. A decisive factor for determining whether a polymer is suitable for the process is the thermal behavior [87,92].

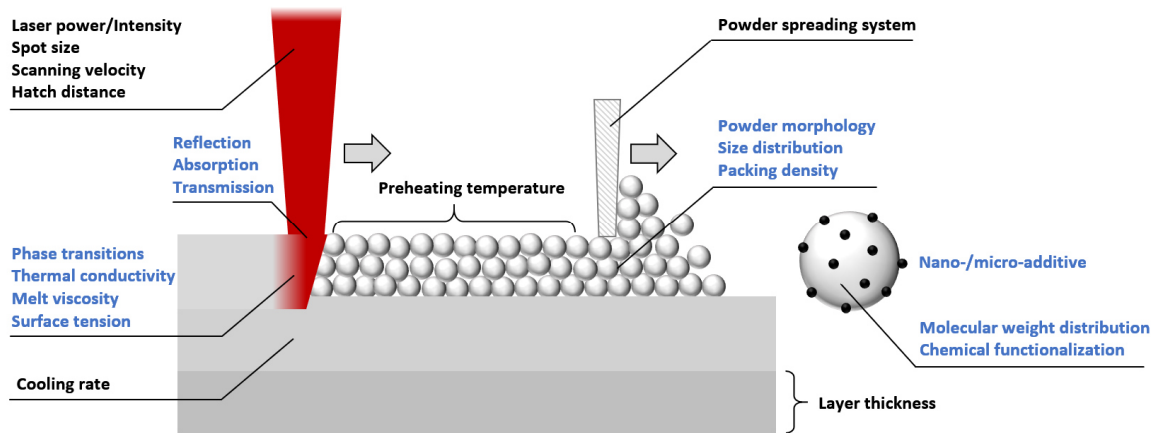


Figure 6: Schematic illustration of the PBF-LB process with relevant machine parameters (black) and material parameters (blue).

Phase transitions, especially the start of melting and resolidification as well as rheological properties of the molten state (melt viscosity) and decomposition temperature define the requirements for the PBF-LB equipment. During PBF-LB, crystallization should be inhibited for several sintered layers. Therefore, processing temperature must be precisely controlled in-between melting and crystallization of the given polymer. This temperature interval of undercooled polymer melt determines the thermal process window for PBF-LB. Polymers with a sharp softening, melting and resolidification behavior adapted to the process can be used in a narrow processing window [86]. Most alternative polymer powder materials relevant for PBF-LB, however, show broad phase transitions and a barely defined process window. This makes precise control of melting and resolidification difficult and is one of the main obstacles in the development of new materials for PBF-LB. Closely related to this issue are temperature instability and aging of the powder during several heating

cycles in the powder bed [89], e.g. post condensation of active amine carboxylic groups leads to chain growth and increase in melt viscosity in PA. In addition, the recyclability of polymeric powders is strongly dependent on molecular properties, such as molecular weight distribution and functional groups [93,94]. In order to prevent aging and improve recyclability, an excess of free amine and carboxylic groups can be used [95]. For the development of new powder materials for laser based PBF a good understanding of all these influencing factors is essential.

Depending on their structure and the resulting mechanical and thermal properties, polymers are classified into three main groups of elastomers, thermosets and thermoplastics [96]. Elastomers have long polymer chains which are tangled and slightly cross-linked, leading to low mechanical strength but high elastic deformability. Thermosets, on the other hand, have densely networked structures, which gives them a high degree of hardness. In elastomers as well as in thermosets, the polymer molecules are chemically bonded to each other, which is the reason why they cannot be brought into a plastic state after curing. In the last group of thermoplastics, the linear polymer molecules are not crosslinked and physically bonded to each other, which leads to an amorphous or semi-crystalline structure. They are mechanically solid at room temperature, but become plastically deformable at elevated temperatures caused by softening of the physical bonds between the molecules [97].

Typically, semi-crystalline thermoplastics powder fulfill the criteria for PBF-LB [87,98]. More than 80 % of commercial powder materials for PBF-LB consist of polyamide (PA) and polyamide based thermoplastics [12]. Due to its sharp melting and crystallization transitions and a large and well-defined sintering window (Figure 7a), PA12 is the predominant material in polymer PBF-LB. Its relatively long hydrocarbon chain length and therefore a large distance between the amide groups (Figure 7b) results in a lower melting temperature than other important polyamides like PA6 or PA6.6, but with similar mechanical and electrical properties. The larger the process window, the smaller the sensitivity for temperature instabilities and thermal stress induced during resolidification. But a large process window does not always guarantee for a good PBF-LB processability [99]. Besides the dominating PA12, other polyamides like PA11 [14] or PA6 are under investigation for PBF-LB and are becoming commercially available. Furthermore, efforts are made to qualify polylactide (PLA)[100], polyaryletherketones (PAEK) [101], polycarbonates [102], polypropylene (PP)[103] and thermoplastic elastomers (TPE) for PBF-LB [86,92,104–106]. PAEKs, like PEEK, PEK and PEKK are high-performance polymers with outstanding mechanical performances, chemical resistance and biocompatibility [101,107–110] but come with poor recyclability [111] and also set high

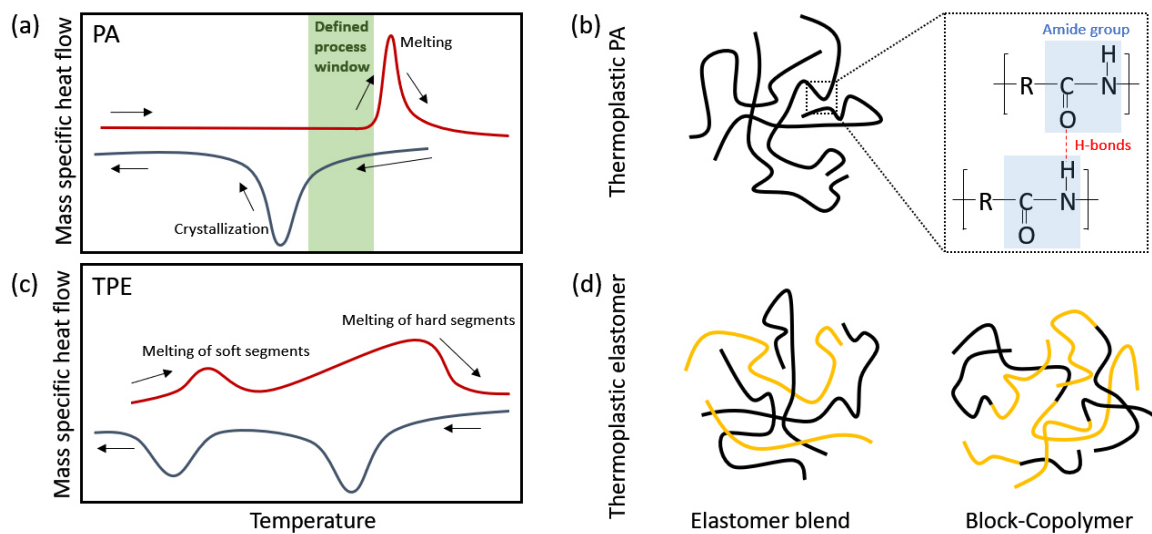


Figure 7: (a) Qualitative Comparison of the calorimetric properties of polyamide and thermoplastic poly elastomer (TPE). (b) Schematic illustration of molecular differences between PA and TPE. The latter can be either a polymer blend or a copolymer.

requirements to PBF-LB equipment in terms of high build temperature (up to 260°C) and temperature stability [112]. TPEs on the other hand are interesting because of their flexibility, but typically come with very undefined phase transitions which makes PBF-LB difficult [99] (Figure 7c,d). In general, this is a problem for completely amorphous polymers, where the processing window is hard to define. It is known for semicrystalline thermoplastics that the resulting microstructure (degree of crystallization, crystalline structure, crystallite/spherulite size, crystal modifications) depends on the processing conditions and the intrinsic temperature-time behavior of the polymer [97,113–119]. Depending on the cooling characteristics of the PBF-LB machine, cooling rates in the range of a few K/min are typically applied to the powder bed which are much lower than cooling rates in injection molding. The part properties are strongly related to the microstructure formed by the polymer and can be manipulated by adapting the crystallization behavior. Low cooling rates result in a higher degree of crystallinity, much lower elongation at break compared to injection molding [114,120–122]. High cooling rates in turn result in more nucleation and hindered crystal growth caused by the larger number of nuclei [113,120]. The finer spherulitic microstructure can increase the stiffness, strength and decrease elongation at break of the final part [97].

Different routes exist to produce processable powders from bulk polymers and the production process influences the particle morphology and PBF-LB processing behavior [94]. PA12 powders can be produced by emulsion polymerization, suspension polymerization or precipitation processes [12,14,15,54,123–125]. The shape of those polymer particles is spherical, round, or potato shaped. A very flexible method for powder production is

cryogenic wet and dry grinding of polymers [12,13,92], which typically comes with low flowability due to the unregular shaped particles and often needs further processing via rounding [12,126]. Difficulties in the powder quality are typically compensated by process engineering measures rather than by a material-development approach [127]. Overall, there is significant need to further adapt polymer powder materials to the PBF-LB process and increase the variety of powders ready for PBF-LB.

2.4 Nano-Functionalized polymer powders

Modification of polymer powders by organic and inorganic micro- and nanofillers is a versatile approach to influence the processing behavior during PBF-LB and to introduce new functionalities in the generated parts [16,17]. Table 1 summarizes the thermophysical and functional benefit of adding nanomaterials to polymer powders for PBF-LB.

Table 1: Summary of nano-fillers and additivition methods for modification and functionalization of PBF-LB powders.

Matrix	(Nano-)filler		Additivition method	Effect	Ref.
PA12	Gold-SiO ₂ hybrid particles	0.01 wt%	Mechanically mixing of powder and colloid until evaporation	NIR absorber	[128]
PA12	Carbon Black, WO ₃ , gold nanoparticles	0.03 – 1.0 wt%	Mechanically mixing of powder and colloid until evaporation	Tuning absorption at different wavelengths	[129]
PEEK	Carbon Black (Vulcan XC72R)	0.03 - 0.1 wt%	Shaking/mixing	IR absorber	[22]
PA12	Clay	0 – 5 wt%	mechanically mixed	Reduction of melting temperature and heat of fusion	[130]
PA6	Clay	5 wt%	Mechanical grinding	Reduction of crystallization temperature	[131]
PA12	Clay	3 wt%	Solution precipitation	Impact on calorimetric properties and increase of crystal content	[132]
PA12	Rectorite (OREC)	5 wt%	Mechanically mixing	Decreased necessary laser energy input	[133]
PA12	SiO ₂	3 wt%	dissolution–precipitation process	heterogeneous nucleation effect	[134]
PA12	Silica	10 wt%	emulsion polymerization	Increasing density and flowability	[135]
PA12	Carbon Black	4 wt%	Mixing in a rotary tumbler	Enhanced electrical conductivity	[136]
HDPE	Graphite	NA	melt compounding	Enhanced electrical conductivity	[137]
PA12	carbon nanofiber	3 wt%	Melt mixing and cryogenic milling	increase in the storage modulus	[138]
PA12	multi-walled carbon nanotubes	0.5 wt%	Mechanical mixing	Higher flexural modulus and ultimate strength	[139]
PA12	graphite nanoplatelets	0.1 – 0.25 wt%	solution intercalation / precipitation	No influence of PBF-LB processing but improved material properties	[18]
PA12	carbon nanotubes	0.1 wt%	Heated mixture with suspension	enhanced flexural, impact, and tensile properties	[140,141]

Matrix	(Nano-)filler		Additivation method	Effect	Ref.
PA12	Al ₂ O ₃	NA	Mixing	Green parts for subsequent furnace sintering	[142]
PA6	Yttrium stabilized zirconia / clay	5 wt%	Dissolving, mixing and spray drying	Increased mechanical strength	[143]
PMMA	SiC	91.5 wt%	Spray drying	Polymer-encapsulated silicon carbide powder	[144]

To increase the flowability, for anti-caking and electrostatic charge control, micro- and nanoscale silicon dioxide, titanium dioxide and other oxide particles are admixed to the polymer powder [13]. Studies have also shown that the introduction of inorganic nanomaterials such as carbon nanotubes [140,145,146] and ceramics [147] can significantly affect sintering characteristics and final mechanical properties of the printed parts, decreasing their shrinkage and distortion. For instance, 5 wt% nano-clay was added to PA6 to improve the properties of the matrix polymer by inhibiting polymer chain mobility, especially during the cooling cycle. The nanoparticles lead to a reduction of the crystallization temperature by 3 °C and the crystallization peak was narrowed [131]. Moreover, nanoparticles can also show significant influences on the melting temperature [148] and enthalpy, and can cause the relative crystalline content and crystallization temperature to increase via heterogeneous nucleation during cooling [113,132,133]. At weight fractions of below 0.1 wt%, the melt flow index and the crystallinity of the powder remain unchanged [18], in particular if the dispersion quality is low after mechanical mixing. Carbon nanoparticles are utilized in PBF-LB for light absorptivity adjustment due to its broad absorption spectrum [22,136,138,139] and can therefore be found in many commercial products. In order to optimize the powder absorption to the specific wavelength of diode and solid-state lasers without coloring the powder black, *Powell et al.* used plasmonic nanoparticles with an absorption maximum at 808 nm [128], resulting in significant absorption of the functionalized PA12 powder. Carbon nanomaterials such as particles, tubes and sheets are also utilized for introducing electrical conductivity of the generated part. However, it was also found that high amounts of filler can reduce the mechanical performance of parts made by PBF-LB. For example, *Athreya et al.* observed a decrease in flexural modulus for PA12 with 4 wt% of carbon nanoparticles, attributed to agglomeration of the high amount of carbon filler [136]. Moreover, PBF-LB process parameters could remain unchanged if the filling factor is low [130]. For carbon black this value is <0.1 wt% as shown by *Kim et al.* [18], but an influence of particle dispersion has not been investigated in this study. It can be expected that a high degree of agglomeration leads to the need of high filler loadings in order, e.g. to increase the surface area of the nuclei accessible by the polymer chains and to avoid disadvantages in the processability (by light scattering and inhomogeneous particle quality). Already a small aggregate fraction can have distinct effects

on the optical properties, as doubling the diameter of a particle would already increase the scattering intensity caused by this single object by a factor of 64 (Rayleigh law of scattering scales with the 6th power of particle diameter). It is therefore essential for PBF-LB that the dispersion of the nanoparticles within the polymer matrix and the interfacial bonding between nanoadditive and polymer-matrix are optimized [18,136,149], while the mass fraction of additives is minimized [140]. A systematic variation of the nano-additive material, its particle size and dispersion quality, and their influence on the melting and resolidification behavior in PBF-LB is missing. In addition, there is still a huge deficit in the knowledge about fundamental polymer-nanoparticle interaction and only little knowledge is available on metal and binary metal oxides nanoparticles as additives.

As summarized in Table 1, various methods can be utilized to generate nano-functionalized polymer powders. Dry coating is the most common approach for post-treatment of powders, e.g. to adjust the flowability [138]. On the other hand, methods like melt compounding [137,150], solution intercalation [151,152], in situ polymerization [153], spray drying [143] and ex situ dispersion into polymer solution [154–156] involve more complex process steps and the melting or dissolution of the polymer before admixing of nanoparticles. All mentioned additivation techniques have in common, that they mostly use aggregated nanomaterials in powdery form, e.g. silicon oxide from gas phase synthesis as flow aid. During additivation, these aggregated nanomaterials can only be dispersed to a certain extend [141], depending on the applied force during additivation. Common scalable additivation methods like dry-coating or melt compounding lead to significant aggregation of the filler, as it was shown in many studies [16,19,20]. Therefore, the choice of method has a decisive influence on the degree of dispersion in the polymer matrix and on the surface of the polymer particles after additivation [16,18,134]. Yang *et al.* investigated the influence of different dry coating procedures and used a hybridizer, which circulates the powder through a high-speed rotating rotor/stator setup that allows dis-aggregation of the aggregated filler and coating of the polymer within a few minutes [20]. They found that particle coating with high impact forces in a hybridizer lead to a surface coverage of 13.3 surf%, compared to 6.7 surf% for mixing the powders at low rotation speed in a blender. Although the descriptor “wt%” is unable to represent the degree of aggregation or dispersion of the nanomaterial, alternative parameters like surf% are rarely used to describe the nanoparticle dose. Typically, nanoparticle dispersion is only described qualitatively in terms of “good” or “sufficient”, rather than quantitatively.

2.5 Nano-functionalization by colloidal additivation

An alternative approach for surface-functionalization of particles is the colloidal additivation. It is used for the formation of heterogeneous catalysts [24–26,28–30] by adsorption (supporting) of colloidal nanoparticles on inorganic supports such as TiO_2 [25,32], Al_2O_3 or ZnO [31]. This route was also transferred to ODS steel powders for laser-based AM [157] and includes the pH-controlled, mixing of colloidal nanoparticles with a suspension of the nano- or microsize support, followed by precipitation or filtration and drying of the surface-functionalized powder. The colloids are typically water-based and free of surfactants, while the procedure does typically not involve organic solvents and temperatures above 50°C during drying.

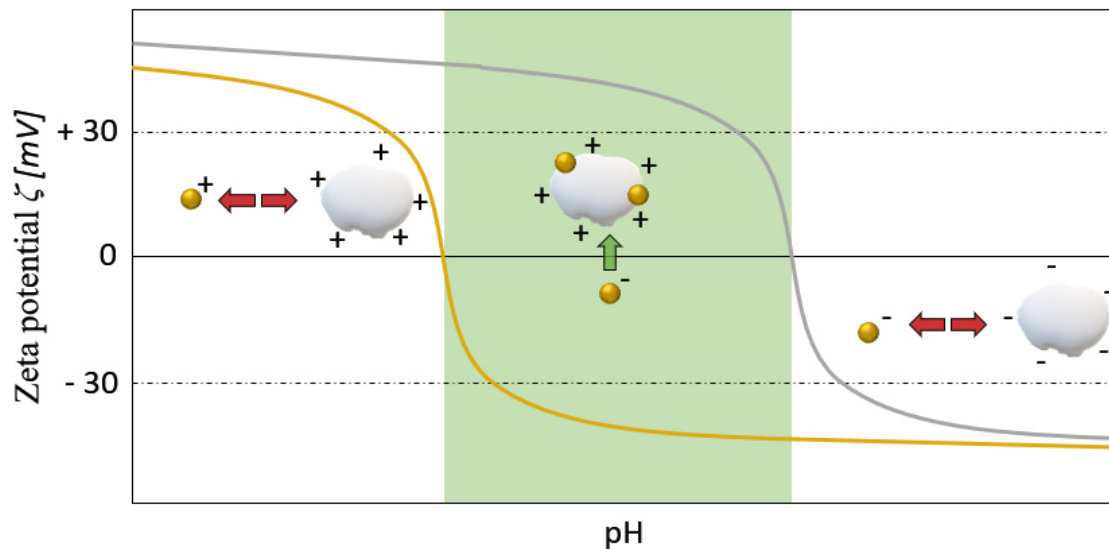


Figure 8: Schematic representation of the electrostatic repulsion and the electrostatic attraction between support material and nanoparticle dependent on zeta potential and isoelectric point (IEP). The process window for efficient support is marked in green and represents the pH area of opposite charge.

In order to achieve a good dispersion and homogeneous distribution of metal nanoparticles on the support, the surface charge of nanoparticles is used, which is caused by oxidation [34,35]. The support also carries a surface charge, which is positive in the case of TiO_2 in the neutral range due to hydroxyl groups on the surface [158]. By varying the pH, the surface charge of the particles (nanoparticles and support) can be controlled, which also effects colloidal stability by changing the electrostatic repulsion between nanoparticles. The transition point from positive to negative surface charge (zeta potential = 0 mV) is called the isoelectric point (IEP). For colloids in the region of the IEP with a zeta potential of ± 30 mV, colloidal stability is no longer given and the thermal energy $K_B T$ of the system is sufficient to overcome repulsive forces and induce agglomeration [159]. The surface charge of nanoparticles is not only exploited in order to stabilize or destabilize the colloid, but is

also utilized for electrostatic deposition of nanoparticles on the support material [25,32]. As shown in Figure 8, an electrostatic attraction between nanoparticle and support occurs when pH is set in a way, that both particle species have inverted zeta potentials. This process window lies between the two IEPs and is characterized by a high supporting efficiency, as shown by Marzun *et al.*[25]. Ligand-free nanoparticles are essential for the success of the supporting, since stabilizing agents can decrease supporting efficiency [32]. For example, sodium citrate completely prevents the adsorption of silver nanoparticles on BaSO₄ when exceeding a critical concentration, which is attributed to steric hindrance [32] and change in pH [160]. Only below the critical ligand concentration, where the nanoparticle surface is not fully covered with citrate ions, supporting takes place and can be described by a Freundlich-Isotherm with a linear increase in nanoparticle loading [wt%] until 6 %. The yield of this electrostatic supporting procedure is almost 100 % and particle size does not change during deposition (no size-selectivity). In addition to the electrostatic support, diffusion also leads to adsorption of nanoparticles without electrostatic attraction, whereby this process is usually very inefficient, time consuming or highly dependent on the surface of the support [24,28].

Irrespective of whether supporting is carried out by an electrostatic- or diffusion-driven process, mixing of the suspension always plays an important role for homogeneity of the product. One can distinguish between macroscopic and microscopic mixing. Macroscopic mixing depends on the liquid's viscosity and density and on the geometry of both, the reactor and the stirrer, whereas microscopic mixing is driven by diffusion and cannot be influenced by stirring. But a good microscopic mixing can decrease the size of the smallest fluid element and eliminate educt gradients in the fluid, which also shortens the diffusion length and necessary diffusion time. For small laboratory batch sizes, a stirred-tank reactor is the most common choice. To achieve a good macroscopic mixing with small fluid elements within a short time, the setup should work in the turbulent regime (high Reynolds numbers Re of the stirrer).

Although a batch process is useful for small scale experiments, it comes with disadvantages if upscaling is necessary. An increase of batch size automatically results in a different flux and mixing time as well as stirring parameters and reactor geometries need to be adjusted (incl. dimensions of flow breakers). The concentrations of both, educt and product change exponentially over time and are governed by concentration gradients in the reactor (Figure 9a). Alternatively, supporting can also be conducted continuously with a static mixer. In a static mixer, the suspension runs through a pipe of length L and mixing is not achieved through stirring but through flow breakers that inhibit laminar flow. To achieve a high

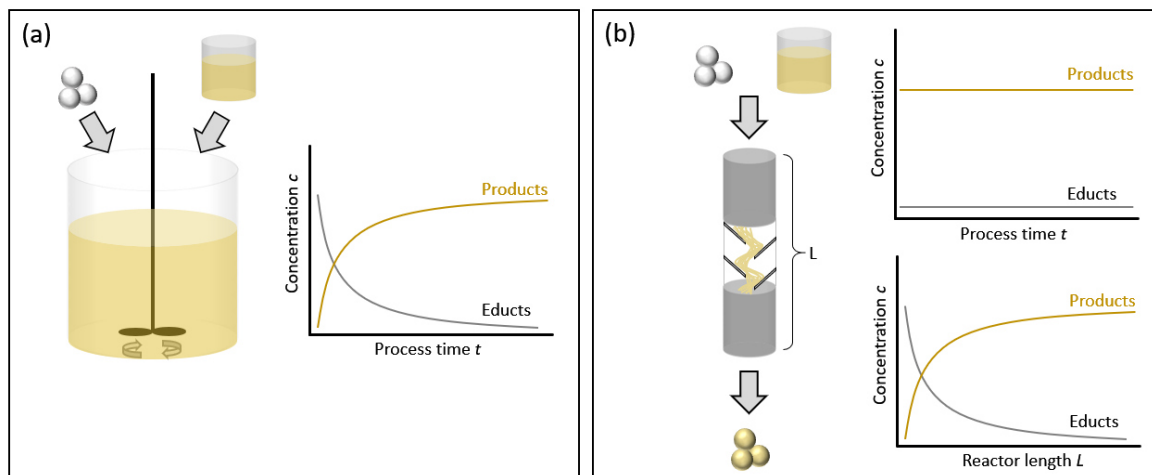


Figure 9: Mixing of colloid and support: Schematic representation of discontinuous ideal stirred-tank reactor and static mixer.

yield, the volume flow and the length of the static mixer need to fit to result in enough residence time. The product quality is constant over time (see Figure 9b) due to a constant residence time and the product amount can be easily increased by increasing the runtime.

2.6 Laser-generated nanoparticles

In order to perform colloidal additivation, the nanomaterial needs to be dispersed in a liquid and the dispersion quality of the colloid limits the accessible dispersion quality after additivation. Common routes for nanomaterial synthesis, like gas phase synthesis or ball milling offer excellent scalability and low costs. Even though primary particles sizes in the sub 100 nm range can be easily accessed by these methods, agglomeration and aggregation are inevitable and lead to large secondary particle sizes up to several μm . These aggregates cannot fully be eliminated during dispersion in a liquid. Therefore, nanoparticle synthesis and preparation of the colloid play an important role for colloidal additivation.

Laser synthesis and processing of colloids (LSPC) offers an alternative to conventional methods of nanoparticle generation and comes with excellent dispersion quality in a scalable on-step process [33]. In contrast to gas phase synthesis, LSPC produces nanoparticles directly in a liquid, where agglomeration is prevented by electrostatic or steric stabilization. Because of its applicability to a variety of materials and fluids laser-generated nanoparticles can further be easily combined with different routes to fabricate composite materials, e.g. laser-generated noble metal nanoparticles such as silver, platinum, palladium or gold have proven exceptional applicability for colloidal additivation of powders due to their characteristic negative surface charge at neutral pH, which can be manipulated by change of pH value [25,161].

The approach of laser ablation in liquid (LAL) was first reported by Fojtik and Henglein for simple and surfactant-free synthesis of nanoparticles [162]. It involves the ablation of a solid bulk target immersed in a liquid and is a green method that does not need any chemical precursors to form nanoparticles in an easy one-step process. On the first glance, LAL looks like a physical top-down method without any chemistry involved. However, since the attempts by Fojtik and Henglein the complex mechanisms involved in the process were investigated step by step and lead to a better, deeper understanding of LAL and an improved control over nanoparticle properties and productivity. Today, LAL belongs to a family of processes that are grouped under the name “laser synthesis and processing of colloids” (LSPC). LSPC further contains laser post-processing (LPP) processes such as laser fragmentation in liquid (LFL) or laser melting in liquid (LML) to modify colloidal particle properties by laser irradiation. From its early days in the nineties until now, LSPC has evolved from a barely known technique for preparing small amounts of metal colloids [163] to a versatile and flexible route to generate nanoparticles from a wide variety of materials in different liquids [164–166]. In contrast to wet chemical approaches, laser-synthesis does not need chemical precursors and organic surfactants. The evolution and current state of LSPC was recently summarized by Amans *et al.* [167]. Scalability of LSPC towards several g/h, equivalent to > 20 l of nanoparticle colloid per hour is possible via continuously operating synthesis setups, advanced scanning strategies [168,169] and continuous centrifugation setups for direct size separation [170]. At this scale, LSPC has proven to be economical, even compared to the established wet-chemical synthesis methods [171]. It enables promising applications in catalysis [26,28,172,173] or for nanoparticle-composites [37,38,174–176], where relatively high nanoparticle amounts are needed for application. In order to understand and control the formation of nanoparticles during LSPC, a close look on the microscopic scale of this ultrafast process is the key. As nanoparticles form within a fraction of a second, high speed analysis techniques [177] and simulations [178,179] are needed. However, the involved processes are yet not fully understood.

Laser induced cavitation bubbles during LAL

LAL requires a high laser energy density to overcome the ablation threshold and remove material from a bulk target, which is achieved by means of short or ultrashort laser pulses in the regime of fs to ns instead of a continuous emission. Figure 10 schematically depicts the first seconds after laser impact. Under laser illumination electrons in the material are

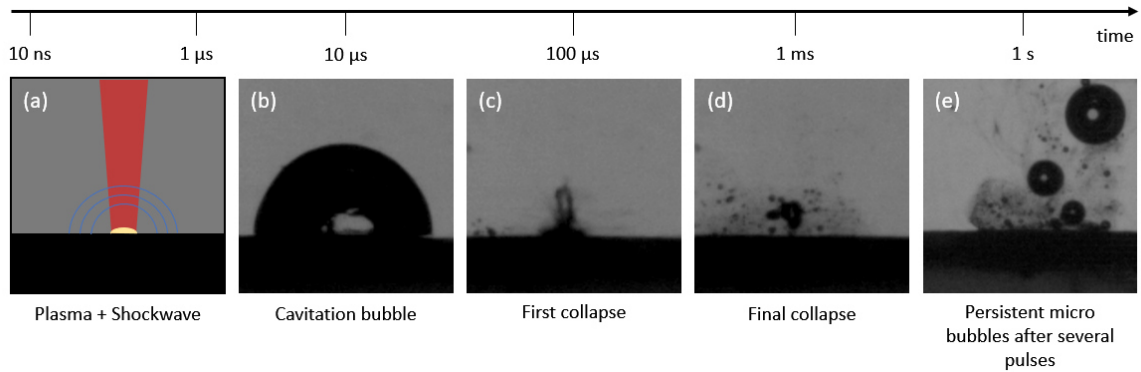


Figure 10: Shadowgraphic imaging after laser irradiation of a gold target in water. (a) Schematic illustration of the laser impact and the shockwave front, (b-d) images from a high-speed camera at 210,000 frames per second showing the cavitation bubble during expansion, first collapse and final collapse. (e) depicts the persistent microbubbles after several laser pulses.

excited by the electromagnetic field and transfer their energy to other electrons after an electron coupling time of approx. 100 fs. A few ps after the start of the irradiation, the electron-phonon coupling begins, whereby an energy transfer to the atomic lattice takes place within a few ps [180] followed by an energy transfer from the surface layer (a few nm) to the bulk after several 100 ns to a few μs [181]. Consequently, laser ablation with pulses in the fs range does not transfer energy to the bulk material, which is why it is referred to as cold ablation with an instant transition from solid to vapor [182], whereas longer pulses with ns duration lead to hot ablation and a melting and evaporation of the target surface [182]. Due to the high energy density on the target surface a plasma with a few ns to μs of lifetime [183–185] is generated with maximum temperatures above 5000 K [186,187]. As the plasma cools down rapidly, acoustic shockwaves are emitted hemispherical and transfer energy to the fluid [188]. The longer the pulse duration, the longer the lifetime of the plasma, which shields the target surface from the laser beam when pulses are in the ns regime and consequently results in pumping the plasma and increasing its lifetime [189][190]. This also enlarges the cavitation bubble volume and lifetime [191,192].

The transfer of energy from the plasma to the fluid leads to the formation of a cavitation bubble in which pressure and temperature are decreasing during expansion and which has been studied by many researchers [180,192–199]. In a first stage the laser-induced plasma coexists with the arising vapor bubble for hundreds of ns [200] but grows fast [185,187,194,200–202] before it collapses for the first time within a few hundreds of microseconds. The bubble containing nanoparticles [177,203–205] and after several oscillations it finally collapses after a few 100 μs to ms [187,192,194–196,206], leading to the release of the nanoparticles into the liquid [177,204]. Recent studies have shown that the first bubble expands quasi-adiabatically [207] and its temporal evolution can be fitted with

Rayleigh-Plesset's model for cavitation bubbles in liquids [208], whereas this is presumably no longer valid for further oscillation. Especially when compressibility cannot be neglected, Rayleigh-Plesset's model fails [209] and Gilmores equation should be used instead [210]. At its maximum expansion the first bubble measures up to several mm in diameter depending on the applied laser fluence [189,204] and the history of the target [211,212]. In addition, the temperature and pressure of the fluid [213] influence the properties of the cavitation bubble [214]. Most of the studies on laser induced cavitation bubbles, which were done in common LAL fluids (water, low viscosity organic solvents) observed a hemispherical bubble shape, which would be expected for low viscosity [215]. In a few reports on an inward jet [205], bell-shaped bubbles [196] and a rim, separating the bubble in a hemispherical upper part and an interlayer close to the target was observed [204], but no clear explanation was given for the rim and the contact angle between bubble and target in the interlayer. For laser induced cavitation bubbles close to a solid boundary (no ablation) numerical study and experiments have shown significant impact on the cavitation bubble shape when low and high viscous liquids are used [215–217]. However, the distance between bubble and solid boundary is $D=0$ for LAL, which makes LAL also a unique tool for testing the influence of $D=0$ on the bubble shape. From a deeper investigation and understanding of the bubble dynamics in combination with simulation of the bubbles inside, especially in non-standard liquids with high viscosity, conclusions can be drawn on particle formation and growth, since most of the ablated material is located inside the bubble [195]. Additionally, most of the matter inside the bubble are solvent molecules [194] which makes the cavitation bubble act as a microscopic reactor where nucleation of the target material, cluster formation and particle growth take place [177,195,201,218]. Furthermore, gases like H_2 and O_2 are generated during the early stage of LAL, resulting in remanent gases after final cavitation bubble collapse, referred to as persistent bubbles [219–222].

Nanoparticle synthesis by laser ablation in liquids

The properties of laser-generated nanoparticles are determined by a broad variety of parameters [33]. First of all, the material parameters are important, e.g. the material-dependent threshold fluence F_{th} for the given pulse duration [181,189]. Target geometries range from bulk targets, plates or wires [198,207] to pressed powder targets which are obtained by mixing, pressing and optionally sintering powders [223–228]. They can be made from metals or oxides and even organic targets are possible [229,230]. As a result, the composition is variable and nanoparticles can be made from alloys and metastable phases which are not accessible by conventional alloying [231–233]. Target porosity [223] and the surface structure (reflectivity) [234] moreover effect nanoparticle yield. Reactions between

the solvent and the ablated species can create nanoparticles with carbon shells [235], oxides [236,237] or doped particles [238]. Additives in concentration of μM can also alter the solvent properties or trigger direct interactions with the nanoparticles directly in the cavitation bubble [201] or thereafter [239]. On the other hand, impurities in the solvents can lead to uncontrolled influences and by-products [226,240,241]. The influence of viscosity and surface tension on the cavitation bubble shape, lifetime and size as well as their influence on nanoparticle growth and agglomeration inside the bubble is mostly unknown [193,214]. Due to their different dipole moments, organic solvents can influence the productivity and size distribution of the resulting nanoparticles, since different polarities of the solvent influence the repulsive forces between the nanoparticles in the growth phase [242–244].

From a laser perspective, the fluence, repetition rate (pulse frequency) and pulse duration give a data triplet which is very important for laser ablation. Computational simulations by Shih *et al.* revealed a significant difference in the size distribution between ps and ns pulses attributed to nano jet formation out of a molten layer of material during ps formation before a cavitation bubble is formed [179,203]. As a result, a fraction of matter is located outside the cavitation bubble during picosecond LAL as it was found by Ibrahimkuty *et al.* [177]. Furthermore, the scanning speed with which the laser beam is guided over the material influences the spatial interpulse distance [180]. In order to scale-up LAL it is not useful to just increase the laser fluence to achieve higher productivities since the fluence is limited by non-linear effects. Increasing the repetition rate in turn leads to another problem. The higher the repetition rate, the smaller the spatial distance of consecutive pulses during scanning and the higher the probability of shielding effects. These shielding effects decrease nanoparticle productivity but can be eliminated through optimized scanning strategies [169]. Shielding is also caused by nanoparticles in the beam path. Surrounding the target with fresh solvent removes the nanoparticles from the beam path and additionally has the positive effect of minimizing bubble shielding since bubbles can be flushed away from the target. Instead of a batch chamber, a flow chamber is used for scale-up to minimize shielding effects and nanoparticle reirradiation [168,245,246].

Laser post-processing of colloids

The typically unwanted process of re-irradiation of colloidal nanoparticles during ablation can also be utilized in a separate process to modify colloids [247]. Post-processing techniques like LFL and LML can selectively influence the size and phase composition of nanoparticles [29] or induce defects without a change of particle morphology [248]. It is not limited to metals [249,250], oxides [223,251,252] or carbon [253–255] particles, but can also be utilized

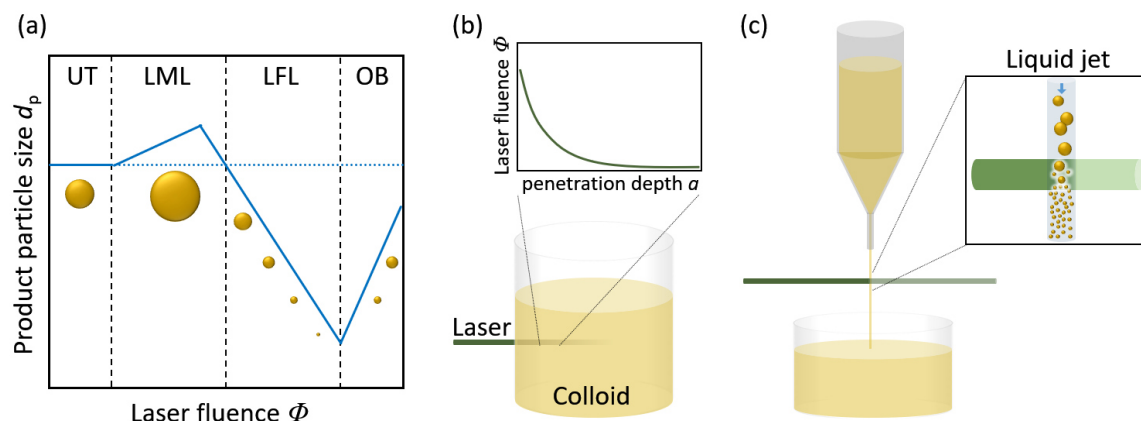


Figure 11: (a) Illustration of different fluence regimes and its influence on particle size (UT: untreated, LML: melting, LFL: fragmentation, OB: optical breakdown, according to Lau *et al.* [257]). Different reactor configurations for post irradiation: (b) batch reactor, where the laser is focused right into the colloid, leading to inhomogeneous fluence distribution along the beam path and (c) liquid flow reactor, where the laser is directed on a thin liquid jet, which enables better control over the fluence.

to process organic substances, e.g. to increase biological availability of drugs [256]. Whether a particle is fragmented or melted depends primarily on the absorbed energy dose, which is influenced by particle size, laser fluence [74] and wavelength. According to Lau *et al.* different fluence regimes can be observed, as depicted in Figure 11c [257]. The fluence can either be controlled via shifting the position of the liquid jet relative to the focal plane or by variation of pulse energy. As explained above, change of particle size or morphology occurs in the LFL and LML regime. In the untreated (UT) and optical breakdown (OB) regime neither fragmentation nor melting happens since the effective fluence is not high enough. At very high fluences optical breakdown is characterized by ionization of the solvent, which causes enhanced absorption of the laser energy, an increased evaporation and finally a decrease in fragmentation efficiency due to shielding effects by gas bubbles [27].

As the particle size increases, so does the energy density required for LFL/LML processes [65] due to the decreasing absorption cross section [75]. Necessary fluences also increase for very large particles (several 100 nm to μm), resulting in a bath tub like function [178]. Metwally *et al.* numerically calculated an optimal particle size for which the fluence necessary for fragmentation is minimal [66]. It has also been shown that the hydrodynamic diameter in fragmentation decreases linearly with specific energy input in J/g, which is typically determined by measuring the transmitted laser powder [27]. Therefore, it is important to precisely control the fluence, which is not possible with the typical batch setup, as it is shown in Figure 11a. In this setup the laser is focused in a vessel filled with colloid. The resulting fluence gradient along the beam path makes a controlled fragmentation or melting difficult. Instead, the laser beam can be focused on a colloid jet (liquid jet reactor)

which results in a much better homogeneous illumination of the particles [27] (Figure 11b). For reproduceable results a homogeneous flow rate and a thin and homogeneously illuminated liquid jet are desired. But self-focusing effects caused by the round couture of the liquid jet and absorbance due to Lamberd-Beer's law lead to inhomogeneous fluence distribution within the jet. In addition, approximately 12 % of the jet are even completely unirradiated. To irradiate > 99 % of all particles is necessary to irradiate the same colloid several times (at least 3x). An approach to overcome this issue is the shaping of the liquid jet to an ellipsis or plane where self-focusing is less pronounced or could even be avoided [258]. Although these approaches are promising, the process control for such a setup is much more complex (adjustment of laser beam and liquid jet) compared to the basic liquid jet reactor and does not allow fast parameter screening for nanomaterial development.

3 Experimental methods

Based on the state-of-the-art chapter and the scientific questions formulated in the introduction, hypotheses are presented that will be verified within the subsequent results chapters. Each results chapter focuses on one aspect of the process chain for the fabrication of nanoparticle-functionalized 3D printed parts, based on laser generated colloids. Figure 12 summarizes the result chapters and the main experimental methodology for verification of the hypothesis.

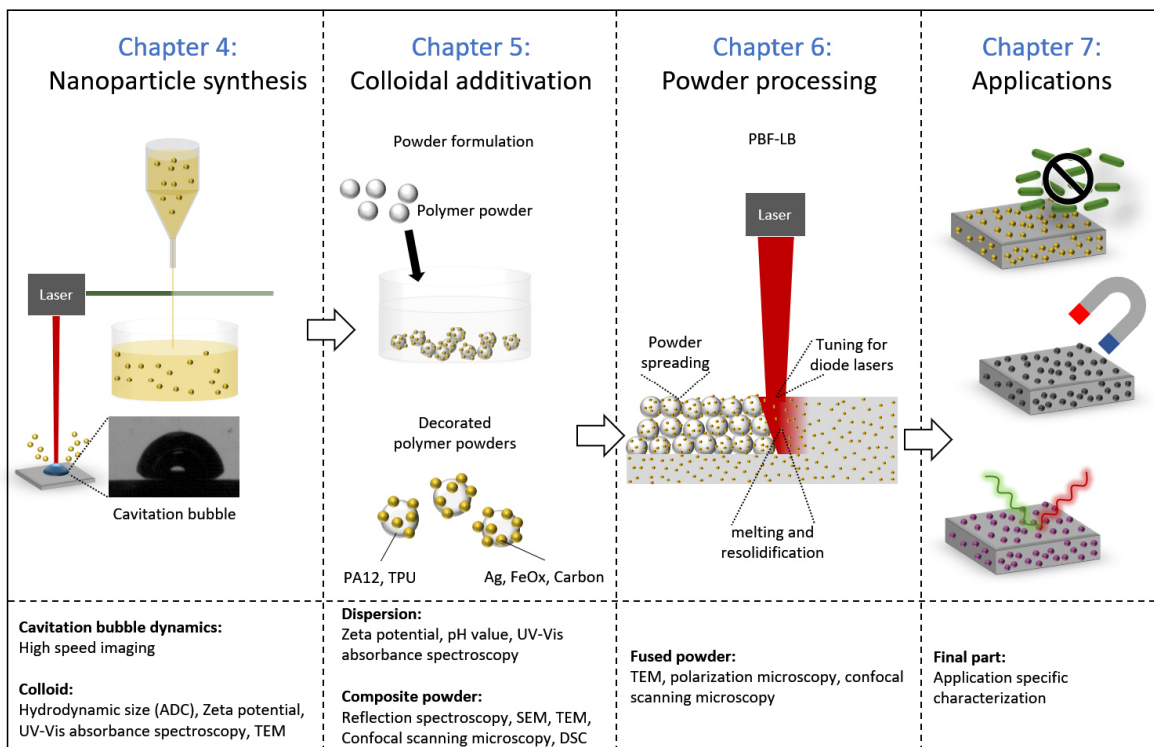


Figure 12: Illustration of the route toward nanoparticle-functionalized printed parts: investigation of laser synthesis of nanoparticles in high viscosity liquids and LPP of oxide nanoparticles. Application specific nanoparticles are adsorbed on polymer microparticles after laser synthesis and processing of colloids to produce nanoparticle-functionalized powders that are qualified for PBF-LB. In each step, products and educts are characterized, which enables process optimization and tailored final-part properties.

Colloidal nanoparticles are generated by LAL in a batch or flow reactor, depending on the necessary mass of colloidal nanoparticles. In order to investigate the cavitation bubbles during LAL in high viscosity, ultrafast imaging experiments of laser induced bubbles on metal and oxide targets were performed. For size and phase modification by LPP, colloids were irradiated in a liquid jet setup. For nanoparticle size analysis, analytical disc centrifugation (ADC), dynamic light scattering (DLS), and transmission electron microscopy (TEM) were applied. Optical properties were analyzed through UV-Vis extinction spectroscopy, whereas pH-dependent colloidal stability will be evaluated by measuring zeta potential. Depending on the nanomaterial and the specific scientific question, further nanoparticle properties were investigated using methods such as X-ray diffraction, Raman spectroscopy, Mößbauer spectroscopy, or vibrating sample magnetometry.

Qualitative and quantitative outcomes of the colloidal additivation procedure were determined by filtering the polymer particle dispersion after colloidal additivation and identifying the portion of unabsorbed nanoparticles in the permeate using UV-Vis absorbance spectroscopy or mass spectroscopy. Furthermore, scanning electron microscopy (SEM) of the nanoparticle-functionalized polymer powder provides quantitative information regarding agglomeration and dispersion of the nanoparticles on the polymer powder surface, e.g. particle size and interparticle distance histograms. SEM histograms were also be validated by transmission electron microscopy (TEM) of ultra-microtome slices of powder particles and final parts. Complementary to SEM, dark-field confocal laser scanning microscopy was used to create 2D and 3D images of polymer particles before and after PBF-LB, respectively. This method does not resolve single nanoparticles in the polymer matrix, but it allows the scattering intensity to be investigated and therefore an analysis of the distribution of light-scattering nanoparticles. Powder qualification was also be performed by diffuse reflection spectroscopy. Importantly, this method was used to analyze the surface plasmon resonance (SPR) of the nanoparticle-functionalized powders that contain plasmonic silver or gold nanoparticles. The SPR position was also compared to interparticle distance histograms. Differential scanning calorimetry (DSC) and fast scanning calorimetry (FSC) were performed to analyze calorimetric material properties (melting, crystallization temperature, enthalpy, and degree of crystallization) at different cooling rates (up to 50,000 K/s) to gain a more profound understanding of the interaction between nanoparticles and polymers during melting and resolidification. Finally, polymer powders were tested to evaluate their Hausner ratio, particle size distribution, and flowability before being printed on different PBF-LB machines, that were equipped with CO₂ or diode lasers. Details for each characterization method as well as parameters for PBF-LB are given in the respective results sections.

4 Laser synthesis of nanoadditives

Despite a significant increase in the knowledge of nanoparticle formation during LSPC over the last several years, there are still knowledge gaps regarding an understanding of the mechanisms that influence productivity and particle properties, especially concerning non-standard liquids such as liquid monomers, polymer solutions, and inks [36–38,174,259,260]. These liquids are of particular interest for AM, since they can either be used for direct printing of 3D structures [39,261–263] or could potentially serve as a base material for resins, filaments, and powders for SLA, FDM, or PBF-LB, respectively. One-step synthesis via LAL offers the potential for dispersing nanoparticles in these liquids that avoids agglomeration and thus facilitates highly efficient nanoparticle-additivation. In this context, high productivity of laser-based nanoparticle synthesis is a key factor in the production of relevant amounts for AM. It is expected that the laser-induced cavitation bubble dynamics influence the mechanism of nanoparticle formation and also its productivity, but the dynamics in highly viscous liquids have not yet been investigated. Therefore, ultrafast imaging experiments of laser induced cavitation bubbles on metal and oxide targets in synthetic polyolefin (PAO) were performed at the Institute of Light and Matter (ILM, Lyon University) in the “Luminescence” team of David Amans. The results of the study presented in chapter 4.1 [264] were expected to provide a better understanding of the influence of viscosity on bubble formation (contact angle, rim, and interface layer thickness) during LAL. This could ultimately lead to new materials for AM by ablation directly in monomer or polymer solutions for functionalization of inks and resins, for example.

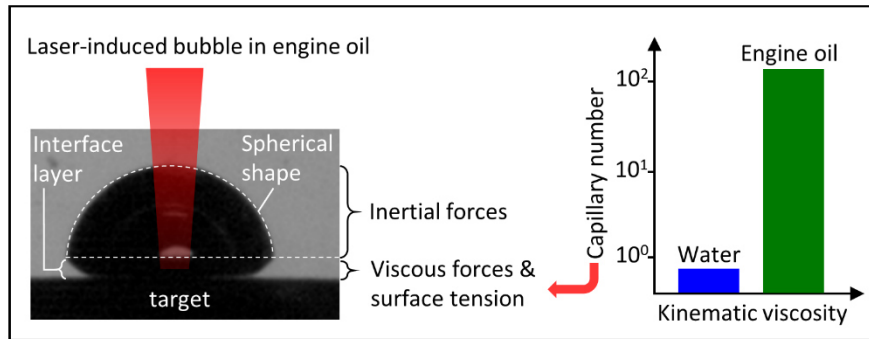
As an alternative to laser ablation, LPP techniques (LFL and LML) are presented in chapter 4.2 that can be used to synthesize magnetic ternary oxide colloids of yttrium iron garnet (YIG) [265]. The results emphasize the flexibility of LPP regarding particle size and material variety, which enables new possibilities for functionalized polymers. Since magnetic nanoparticle-functionalized materials are highly relevant to AM [41–43], especially for the design of magnetic structures in 4D printing [39,44,45], LPP represents a scalable method

for synthesis and size variation of nanoparticles in liquids. The educts for LPP of nanoparticles can either come from LAL of high-density targets [223,266] or directly from nano- or micropowders dispersed in liquid [157]. The usability of YIG nanoparticles synthesized by this approach as additives for laser-based AM of steel powder was previously demonstrated by Doñate-Buendía *et al.* [157].

4.1 Laser ablation in highly viscous media

Dynamics of laser-induced cavitation bubbles at a solid–liquid interface in high viscosity and high capillary number regimes

Reproduced from Journal of Applied Physics 127 (2020) 044306, with the permission of AIP Publishing



Highlights:

- Viscous forces and surface tension (capillary number Ca) govern the ablation-induced cavitation bubble (Contact angle, spherical part and interface layer)
- The lifetime, shape, size and the damping of cavitation bubble oscillation are rather dependent on the kinematic viscosity than on the target material
- A contact angle hysteresis is observed whereas the thickness of the interlayer is consistent with a boundary layer equation
- Increasing the viscosity also results in phenomenological differences of persistent microbubbles after the cavitation bubble oscillation compared to water

Appendix:

- Supporting information (A1)

Dynamics of laser-induced cavitation bubbles at a solid-liquid interface in high viscosity and high capillary number regimes

Cite as: J. Appl. Phys. 127, 044306 (2020); doi: 10.1063/1.5116111

Submitted: 24 June 2019 · Accepted: 9 January 2020 ·

Published Online: 28 January 2020



Tim Hupfeld,¹ Gaétan Laurens,² Samy Merabia,² Stephan Barcikowski,¹ Bilal Gökce,^{1,a)}
and David Amans^{2,a)}

AFFILIATIONS

¹Technical Chemistry I and Center for Nanointegration Duisburg-Essen (CENIDE), University of Duisburg-Essen, Universitaetsstrasse 7, 45141 Essen, Germany

²Univ Lyon, Univ Claude Bernard Lyon 1, CNRS, Institut Lumière Matière, F-69622 Villeurbanne, France

^{a)}Authors to whom correspondence should be addressed: bilal.goekce@uni-due.de and david.amans@univ-lyon1.fr

ABSTRACT

No unified model is available yet to explain the dynamics of laser-induced cavitation bubbles during laser ablation of solid targets in liquids, when an extremely high capillary number is achieved (>100), i.e., when the viscous forces strongly contribute to the friction. By investigating laser-induced bubbles on gold and yttrium-iron-garnet targets as a function of the liquid viscosity, using a nanosecond laser and an ultrafast shadowgraph imaging setup, we give a deeper insight into what determines the bubble dynamics. We find that the competition between the viscous forces and the surface tension (capillary number Ca), on the one hand, and the competition between the viscous forces and inertia (Reynolds number Re), on the other hand, are both key factors. Increasing the viscous forces, and hereby Ca up to 100 has an impact on the bubble shape and results in a very pronounced rim, which separates the bubble in a spherical cap driven by inertia and an interlayer. The temporal evolution of the footprint radius of the interlayer can be addressed in the framework of the inertio-capillary regime. For an intermediate viscosity, the thickness of the interlayer is consistent with a boundary layer equation. Interestingly, our data cannot be interpreted with simplified hydrodynamic (Cox-Voinov) or molecular-kinetic theory models, highlighting the originality of the dynamics reported when extremely high capillary numbers are achieved. Upon bubble collapse, spherical persistent microbubbles are created and partly dispersed in water, whereas the high-viscous polyalphaolefines lead to long-standing oblate persistent bubbles sticking to the target's surface, independent of the ablated target. Overall, liquid's viscosity determines laser ablation-induced cavitation.

Published under license by AIP Publishing. <https://doi.org/10.1063/1.5116111>

I. INTRODUCTION

Producing colloids through laser ablation in liquid (LAL) has become a popular technique for its variety of accessible materials.^{1–5} In contrast to chemical routes, LAL works without using surfactants or chemical precursors in a one-step process⁶ with a wide variety of liquids.^{7–14} Although LAL is scalable,¹⁵ economically feasible,¹⁶ and has high potential for applications in biomedicine,^{17,18} catalysis,^{2,19} optics,^{20–22} additive manufacturing,^{23,24} and nanoparticle-polymer composites,^{25,26} there is still a lack of understanding of the basic mechanism involved during nanoparticle synthesis. The dynamics after the impact of a short laser pulse on a target in a liquid environment can be separated into the following stages. An

early laser-induced plasma is quickly quenched a few microseconds after the impact, leading to a vapor bubble^{27–32} containing nanoparticles.^{33–36} The bubble grows and collapses at first within a few hundreds of microseconds and finally leads to the release of the nanoparticles into the liquid^{34,35} when the bubble fully collapses and disappears after a few oscillations.^{26,37–39} Persistent microbubbles are released during the collapse phase, which may shield a large portion of subsequent laser pulse, in particular, at high liquid viscosities,⁴⁰ and consist of chemical reaction products of the solvent and target, such as volatile carbohydrates,⁴⁰ hydrogen, oxygen, and hydrogen peroxide.⁴¹

The dynamics of the cavitation bubble and its influence on the nanoparticle formation has been investigated by many

researchers.^{28,37–39,42–44} Surprisingly, there is a lack of literature investigating cavitation bubbles in highly viscous liquids, although viscous liquids are becoming more and more interesting for LAL applications in oils^{45,46} or monomers⁴⁷ through offering the possibility for a one-step synthesis of colloids. For example, nanoparticles as additives in engine oil are relevant in the automotive industry, where nanoparticles are often used to enhance the tribological properties of the lubricant.^{46,48} The one-step synthesis via LAL could replace the process of dispersing chemical synthesized particles in oils which often leads to agglomeration and thus to lower functionality. However, it is still mostly unknown how viscosity and surface tension influence shape, lifetime, and size of the laser-generated bubble, and how they influence the nanoparticle growth and agglomeration inside the bubble.^{49,50} A deeper understanding could offer new ways to ultimately improve the overall LAL process, i.e., repeatability and productivity. A perfect hemispherical bubble is expected in an inviscid flow,⁵¹ and most of the above-mentioned studies on laser ablation in low-viscosity liquids (water, ethanol, etc.) assume a hemispherical shape. Only a few reports deal with the complete description of the bubble shape (rim, interlayer, and contact angle). Tomko *et al.* reported an asymmetric shrinking.³⁵ Contact angle hysteresis and bell-shaped bubbles in water have been observed.³⁹ Ibrahimkutty *et al.* reported an inward jet³⁶ which agrees with a numerical study by Lechner *et al.* using the finite-volume method applied to Navier–Stokes equations for a compressible fluid.^{51,52} From studies of cavitation bubbles close to a solid–liquid interface, it is further known that the viscosity has a significant influence on the bubble shape.⁵³ Furthermore, the very fast and thin jet observed in the cavitation-collapse-simulations by Lechner *et al.* is unlikely to be observed at liquid viscosity 40 times higher than water as the annular inflow is no longer fast enough. At such high viscosities, a jet forms which is much wider and much slower (on the order of 100 m/s) than in water (about 1000 m/s).⁵⁴ Still, there is no model available yet to fully describe the shape of the LAL-induced bubbles for any viscosity. Moreover, laser-induced bubbles close to a surface are characterized by a fast moving vapor–liquid interface. By experimentally investigating the bubble dynamics in viscous liquids, we could get access to an unusually high value for the capillary number and address the original and unprecedented condition in the literature. In this study, we investigate the relevant parameters (e.g., bubble size, velocity, lifetime, contact angle, contact area) for laser ablation of both gold and yttrium-iron-garnet (YIG) in water and in highly viscous polyalphaolefin (PAO), and we take a deeper look into the origin of the deviations from the semispherical shape.

II. EXPERIMENTAL

The experiments were carried out in commercially available Spectrasync PAO6 (density $\rho = 0.827 \text{ g/cm}^3$, kinematic viscosity $\nu = 80.8 \text{ mm}^2/\text{s}$ @ 293 K) and Spectrasync PAO40 (density $\rho = 0.850 \text{ g/cm}^3$, kinematic viscosity $\nu = 764 \text{ mm}^2/\text{s}$ @ 293 K) supplied by Exxon Mobile. The viscosity of PAO is influenced by its chain length. Pure water ($18.2 \text{ M}\Omega/\text{cm}^2$) was used as a reference fluid (density $\rho = 0.997 \text{ g/cm}^3$, kinematic viscosity $\nu = 1.00 \text{ mm}^2/\text{s}$ @ 293 K, surface tension $\gamma = 72.8 \text{ mN/m}$). The surface tension γ

also changes to 29.7 mN/m for PAO6 and 31.5 mN/m for PAO40 (@ 297 K). As ablation targets, we have chosen a commercially available gold foils (99.99%) and yttrium-iron-garnet (YIG, $\text{Y}_3\text{Fe}_5\text{O}_{12}$) wafers to experience different wettability. The uncleaned gold foil is assumed more hydrophobic than the hydrophilic oxides. Note that the hydrophilicity does not only depend on the material, but can also be altered by impurities, microstructures, and adsorbed species on the surfaces.⁵⁵ The first bubble expansion and its collapse are very fast with respect to the heat conduction characteristic time. Therefore, the bubble growth is assumed to be adiabatic as it was shown by Lam *et al.*²⁸ and we can neglect the heat transfer from the inner bubble to the liquid. As a result, we consider the kinematic viscosity and the surface tension constant during the first bubble expansion and collapse.

For the fast imaging shadowgraphy experiments, a target is placed in a cubic vessel with 6 ml of liquid. The liquid layer thickness above the target is 6.5 mm. For the sake of comparability, the liquid layer thickness above the target is fixed throughout all experiments. The third harmonic of a pulsed Nd-YAG-laser (355 nm, 5 ns, 9 Hz, 7.2 mJ/pulse) is focused on a spot with a diameter of approximately $260 \mu\text{m}$, resulting in a fluence of 13.6 J/cm^2 . In our setup geometry, the liquid's transmission at 355 nm for a 6.5 mm liquid thickness is 99% for water, 97% for PAO6, and 96% for PAO40, ensuring similar fluence for the three liquids (see Fig. S1 in the [supplementary material](#)). Ablation is observed at 210 000 frames per second, which corresponds to an integration time of $4.75 \mu\text{s}$, by an ultrafast camera (Phantom v711, Vision Research). On the camera, a Zoom 6000 from Navitar is mounted. The magnification of the optical system is 0.65. According to its performance specification, the resolution limit of the Zoom 6000 optical assembly is then $31 \mu\text{m}$, which also corresponds to the image of a single-pixel ($20 \mu\text{m}$ in size divided by the magnification). It leads to an overall resolution of $44 \mu\text{m}$ ($\sqrt{2} \times 31 \mu\text{m}$). A pattern of ultra-bright LEDs is used for illumination. To avoid distorting the results by inhomogeneities of the target surface or through changes in the liquid parameters causing changes in the target illumination, each experiment is performed on a fresh target spot in fresh liquid while the vessel is cleaned between each experiment. The camera is synchronized with a laser beam shutter to ensure that the camera starts imaging right after the first laser shot on a fresh surface.

III. RESULTS

Figure 1(a) shows the dynamics of the bubbles in three liquids for a gold target (videos for both the gold and YIG targets are available in the [supplementary material](#)). Starting with the first image $4.75 \mu\text{s}$ after the laser impact, the bubble starts to expand, reaching its maximum expansion after 100–150 μs . Interestingly, the bubbles in PAO6 and PAO40 continue expanding in the vertical direction, even after the expansion in the horizontal direction stopped, highlighting the strength of the friction. The footprint of the bubble in PAO40 stays almost constant during the collapse which could affect the reposition of the ablated material on the target surface [see Fig. 1(b)].

Figure 1(c) depicts the vertical bubble radius (height) for the different liquids as a function of time. Assuming a rotational symmetry of the bubble shape, the maximum volume is deduced from

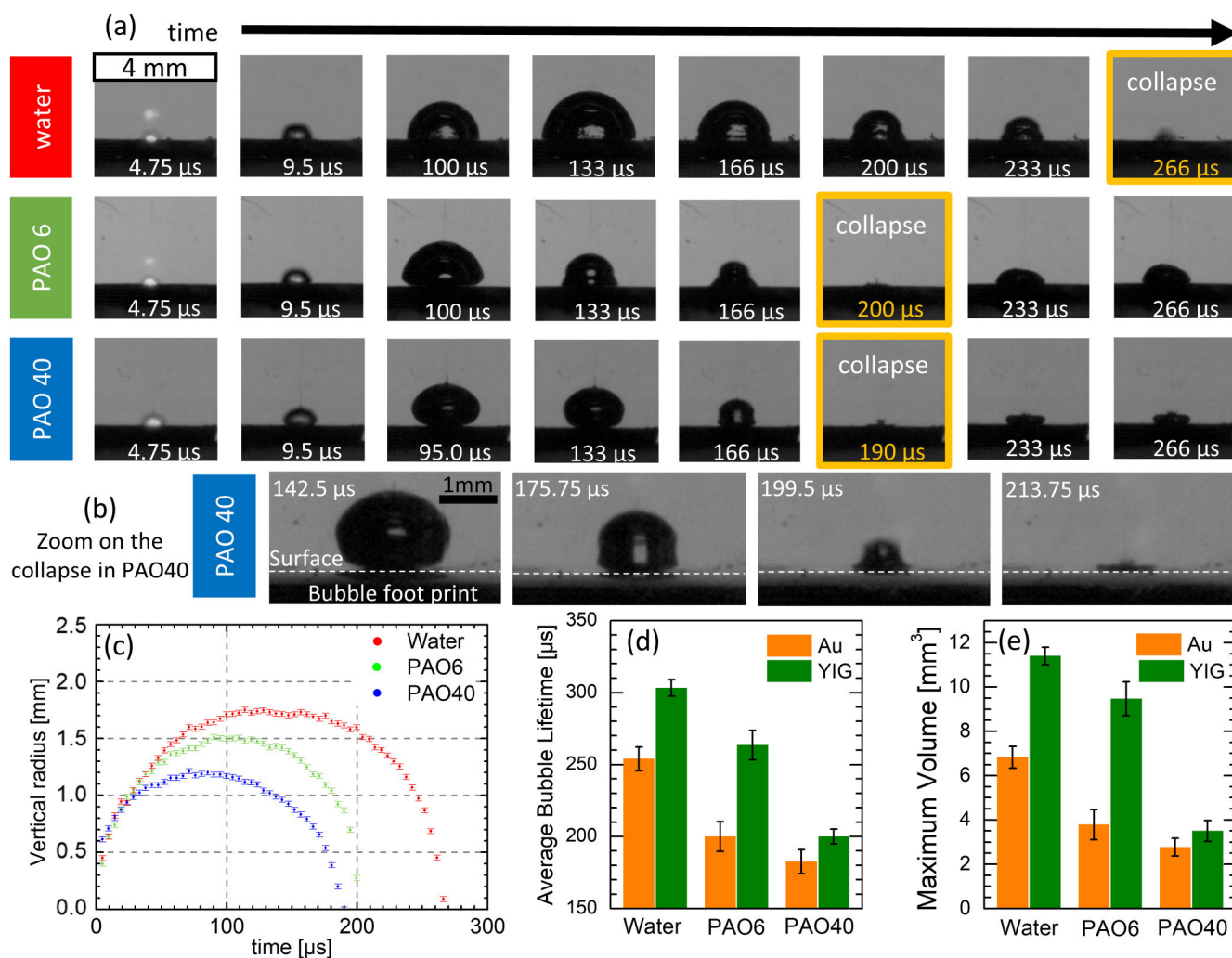


FIG. 1. (a) Shadowgrams of the cavitation bubbles after the impact of a ns-laser pulse on a gold target in water (top), PAO6 (middle), and PAO40 (bottom). Videos of both gold and YIG LAL in water and PAOs are available in the [supplementary material](#). (b) Zoom on the collapse in PAO40 with a focus on the footprint diameter, as well as the persistent oblate bubble after oscillation. (c) Vertical radius (height) for each liquid plotted as a function of time. The error bars correspond to the resolution of the imaging system ($\pm 22 \mu\text{m}$). (d) Lifetime and (e) maximum volume of the first bubble for a gold target and an YIG target. The error bars correspond to the 80% confidence interval according to Student's *t*-distribution.

the bubble shape at its maximum vertical radius. The average maximum volume for each liquid is shown in Fig. 1(e). After the maximum expansion, the shrinking starts, ending with the collapse of the cavitation bubble followed by bubble oscillations (videos of the whole process including oscillation are provided in the [supplementary material](#)). The total lifetime of the first bubble is between 190 and 280 μs , depending on the liquid [Fig. 1(d)]. For each bubble, the lifetime is consistent with the Rayleigh collapse time deduced from the maximum vertical radius (see Fig. S2 in the [supplementary material](#)). Compared to water, the number of oscillations is smaller in the PAOs. Obviously, the highly viscous PAOs provide higher damping of the bubble oscillation through viscous

energy dissipation, resulting in only one oscillation for PAO40. After oscillations, persistent bubbles⁵⁶ are formed from the cavitation bubble, and their mobility decreases dramatically for high viscosities. The collapse in water releases microbubbles into the liquid that only partly adhere to the target surface. In contrary, LAL in PAO40 results in persistent oblate-shaped bubbles sticking to the target, independent of the ablated target material [see Fig. 2(c) and the videos in the [supplementary material](#)].

There are changes when increasing the viscosity of the liquid, not only in the lifetime and the maximal size of the bubble, but also in the shape and contact angle between the target and the bubble. The physics of spherical and hemispherical

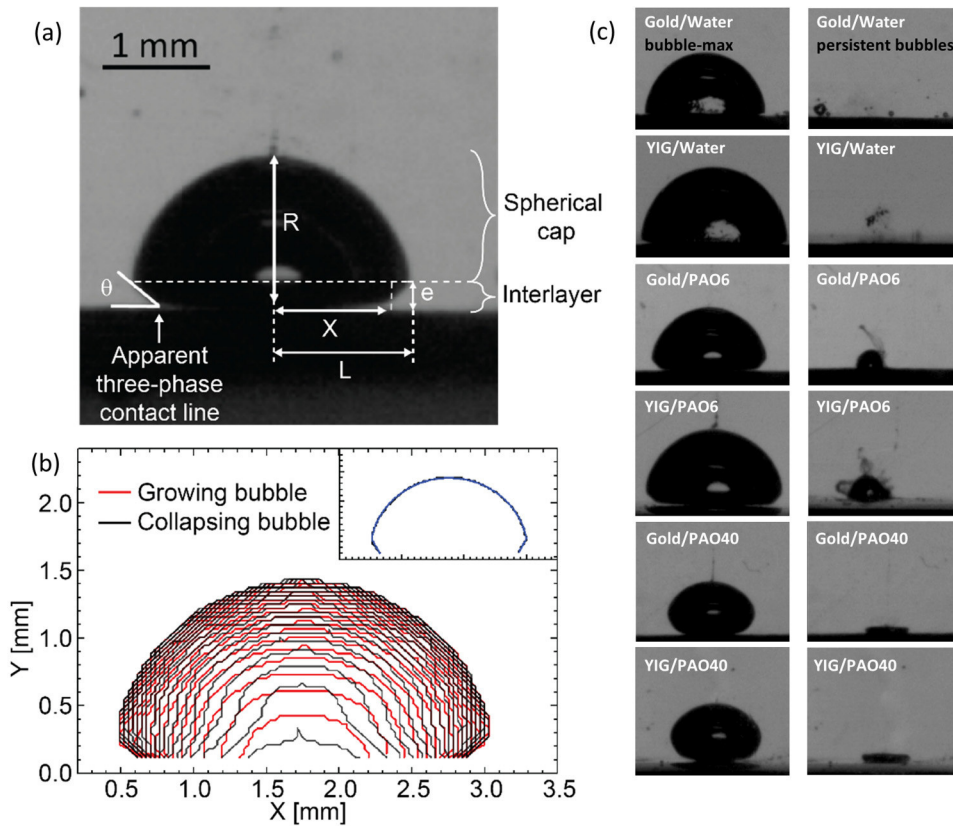


FIG. 2. (a) Image of a laser-generated bubble on gold in PAO6 showing the relevant geometrical parameters. (b) The red and black curves correspond to the bubble shape returned by the image processing (raw data) for the expanding and receding phases, respectively. Inset: the black curve is the bubble contour obtained from raw data and the blue curve corresponds to its fit. (c) Images of the cavitation bubbles at their maximal expansion (left panel) and persistent bubbles after oscillation (right panel) depending on the target (gold, YIG) and liquid (water, PAO6, and PAO40) combinations.

bubble oscillation has extensively been studied in the past⁵⁷ with focus on bubbles in water. Various studies are also available for cavitation bubbles at different distances from a solid boundary.^{52,58,59} To discuss the differences in the bubble dynamics in the present case, we have developed a Python code to deduce from the movie the time evolution of the relevant geometrical parameters characterizing the bubble shape. For each image, the bubble shape is fitted using a circular arc for the top of the bubble (spherical shape) and a continuous line for the interlayer (conical shape). The shape of the interlayer is assumed to be conical to measure the apparent contact angle θ . The geometrical quantities deduced from the fit are the height of the bubble R , which remains almost equal to the radius of curvature during the bubble expansion, the footprint radius X , the distance L between the bubble boundary (edge of the interlayer) and the center of the bubble, the thickness e of the interlayer, and the contact angle θ [see Figs. 2(a) and 2(b)].

From the measurement of R , X , and L as a function of time, we can compute velocities,

$$V_t = \frac{dR}{dt}; V_{cl} = \frac{dX}{dt}; V_e = \frac{dL}{dt}, \quad (1)$$

where V_t is the velocity of the vapor/liquid interface at the top of the bubble, V_{cl} is the velocity of the apparent three-phase contact

line, and V_e is the velocity of the vapor/liquid interface at the edge of the bubble.

Figures 3(a) and 3(b) show the Reynolds number Re and the Weber number We computed from the velocity V_t of the top of the bubble, while Fig. 3(c) shows the capillary number Ca computed from the velocity V_{cl} of the apparent contact line,

$$We = \rho V_t^2 R / \gamma, \quad (2)$$

$$Re = V_t R / \nu, \quad (3)$$

$$Ca = \rho \nu V_{cl} / \gamma, \quad (4)$$

where ρ is the fluid mass density, γ is the surface tension, and ν is the kinematic viscosity. R is the height of the bubble, which remains almost equal to the radius of curvature of the cap during bubble expansion. Re and We values do not appear to significantly depend on the target material. Re and We mainly scale with the kinematic viscosity ($\propto \nu^{-1}$) and the surface tension ($\propto \gamma^{-1}$), respectively, because the velocity V_t and the height R of the bubbles do not differ significantly from a liquid to another (for a given normalized time, less than one order of magnitude). As Re and Ca depend on the kinematic viscosity, three regimes are clearly distinguishable, on the opposite of We evolution which only deals with

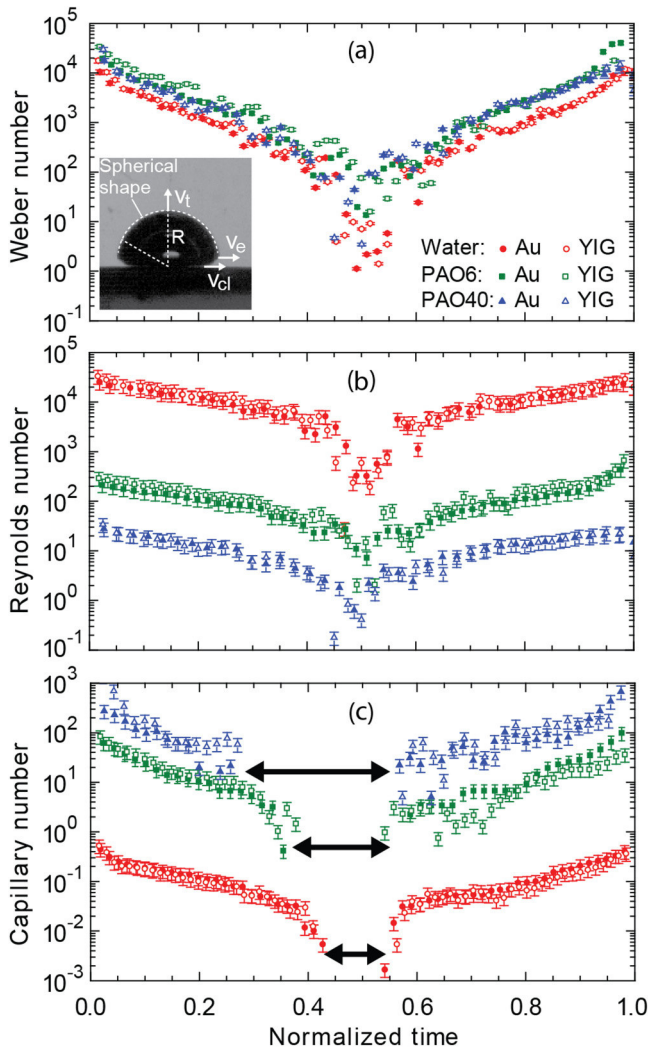


FIG. 3. (a) Weber number We and (b) Reynolds Re number calculated from the velocity V_t at the top of the bubble. (c) Capillary number Ca was calculated from the velocity V_{cl} of the apparent contact line. The normalized time corresponds to the duration of the first expansion and shrinking of the bubble. No movement is observed ($V_{cl} = 0$) for the apparent contact line during the period delimited by the arrows. Error bars are deduced from the propagation of uncertainty (see the [supplementary material](#)) and take into account an uncertainty of $\pm 30\%$ on the viscosity, an uncertainty of $\pm 3\%$ on the surface tension,^{60,61} and an uncertainty of $\pm 22 \mu\text{m}$ on the geometrical parameters (R and X).

surface tension. High values of We and Re are achieved for the three solvents, which indicate that the balance between inertia and inner pressure dominates the motion of the bubbles cap. The three regimes then mainly concern the bubble motion close to the surface. By comparing viscous force with inertia, Re shows decreasing values with viscosity. From water to PAO6 and PAO40, Re is reduced by 2 and 3 orders of magnitude, respectively, and is close to unity for the more viscous oil. This trend is confirmed by the

TABLE I. Value of the parameter n from the fit with $X(t) \propto t^n$, where $X(t)$ is the time-dependent footprint radius of the bubble during its early expansion, i.e., the first quarter of the bubble lifetime (see Figs. S3 and S4 in the [supplementary material](#)). The values in brackets correspond to the 80% confidence interval according to Student's t -distribution.

n	Gold	YIG
Water	0.389 (± 0.051)	0.393 (± 0.028)
PAO6	0.332 (± 0.073)	0.334 (± 0.05)
PAO40	0.194 (± 0.035)	0.200 (± 0.053)

evolution of Ca . In water, Ca is less than unity in the first μs before reaching 10^{-2} at the maximum bubble size. In PAO6 and PAO40, the same evolution is shifted by 2 and 3 orders of magnitude toward high capillary numbers. Contrary to the case of water, the viscous force cannot be neglected anymore with respect to inertia in polyolefin. The relatively high polyolefin viscosity leads to contact-line friction,⁶² which competes with inertia and then drives the bubble motion close to the surface.

The main differences in the bubble dynamics between different viscosities can be observed in the behavior of the interlayer defined in Fig. 2. The spreading of the bubble on the solid target can be compared to the advancing and receding sessile droplet^{63–65} or a spreading bubble.^{66,67} During the early stage of bubble expansion (first quarter of the bubble lifetime), the time-dependent footprint radius $X(t)$ of the bubble follows the power-law $X(t) \propto t^n$ (see Figs. S3 and S4 of the [supplementary material](#)). The corresponding exponent n which characterizes the spreading regimes is shown in Table I and indicates only a weak dependence of the bubble expansion on the target material. The exponent n is around 0.39 for water. Such value is consistent with regimes where the dominant resistance is liquid inertia. For a bubble characterized by a constant volume, these regimes lead to theoretical time evolution between $t^{1/2}$ and $t^{1/366}$ depending on the driving force, the gravity or the capillarity, respectively, which counterbalances the inertia. If the bubble size is larger or smaller than the capillary length, this leads to a flattened or a spherical shape, respectively. By considering our bubble shape as hemispherical, an inertio-capillary regime with $t^{1/3}$ is in good agreement with the data in Table I for water and PAO6. However, for laser-generated bubbles, the driving force during the early expansion of the bubble is clearly different and corresponds to the bubble inner pressure. Moreover, the bubble volume is not constant. In water, for large Weber and Reynolds numbers, a simplified Rayleigh–Plesset equation applies and reflects the balance between inertia and inner pressure (P_B),²⁸

$$\rho \left(R\ddot{R} + \frac{3}{2}\dot{R}^2 \right) = P_B(t) - P_l, \quad (5)$$

where P_l denotes the surrounding liquid pressure ($\ll P_B$), and the inner pressure P_B follows the isentropic relation $P_B \propto A R^{-3\alpha}$ with α being the heat capacity ratio and a constant A .²⁸ It leads to the balance $\rho \frac{R^2}{T} = A R^{-3\alpha}$ and then to the power-law coefficient $n = \frac{2}{3\alpha+2}$. For a laser-generated bubble, we can expect $n = 1/3$ for water ($\alpha_{\text{water}} = 1.33$) and $n = 2/5$ for large molecules (α tends

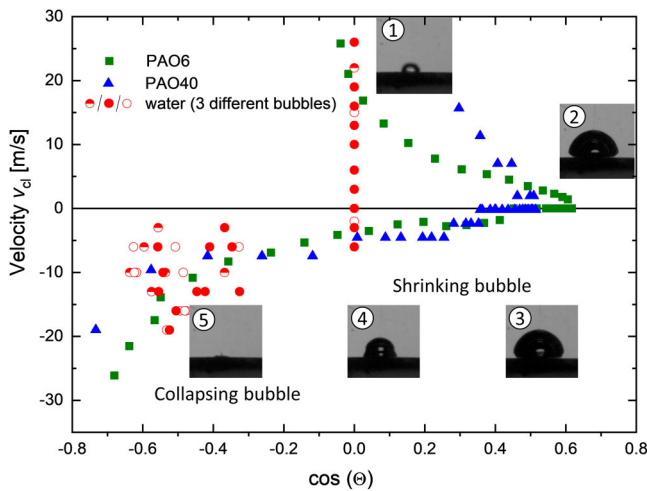


FIG. 4. Velocity of the apparent contact line as a function of the apparent contact angle plotted for a few laser-induced bubbles on a gold target in PAO6 (green squares), PAO40 (blue triangles), and in water (red circles). Pictures correspond to a laser-generated bubble in PAO6.

to 1). These values are consistent with the measured ones for water [$X(t)$ and $R(t)$ are identical for water] and PAO6. In contrast, n is significantly smaller for the most viscous PAO40 ($n \approx 0.2$) which indicates a change of regime to domination of viscous forces. By increasing the viscosity, the Reynolds number decreases, and the

Capillary number drastically increases. Close to the surface, friction has to be included in the resistance forces along with inertia. For a droplet characterized by a constant volume, when inertia is marginal, the balance between the surface tension and the viscous dissipation leading to friction at a small scale is described by Tanner's law with $t^{1/10}$. A decrease of the n value with increasing viscosity makes sense, even if Tanner's law assumes again a constant volume, as well as a low capillary number ($Ca \ll 1$), which only applies for the bubble's dynamics close to their maximum radius (see Fig. 3). To the best of our knowledge, there is no study available in the literature describing a droplet or bubble spreading in a high capillary number regime such the ones reached for high-viscous PAOs, i.e., up to 100. However, large Ca numbers are achieved in the context of high-speed coating, up to 1000 for the coating of optical fibers (see Refs. 68 and 69 and references inside).

The velocity of the apparent three-phase contact line is drawn as a function of the apparent dynamic contact angle in Fig. 4 for PAO6, PAO40, and water. In the case of water, the expanding bubble is hemispherical, and the apparent contact angle is constant around 90° during most of the bubble lifetime [also see Fig. 1(a)] due to the inertial regime with a low capillary number [see Fig. 3(c)]. There is only a deviation from 90° during the collapse phase (see Fig. 4) characterized by a sharp acceleration of the bubble. When increasing the liquid viscosity and hereby the capillary number Ca by several orders of magnitude [see Fig. 3(c)], we observe the appearance of hysteresis between expanding and shrinking bubble for the apparent contact angle between the target and bubble. The hysteresis is similar to the behavior observed for a moving liquid droplet or a dynamic sessile drop at small Ca numbers.^{64,70,71} In the limit of the small Ca number, the apparent contact angle is

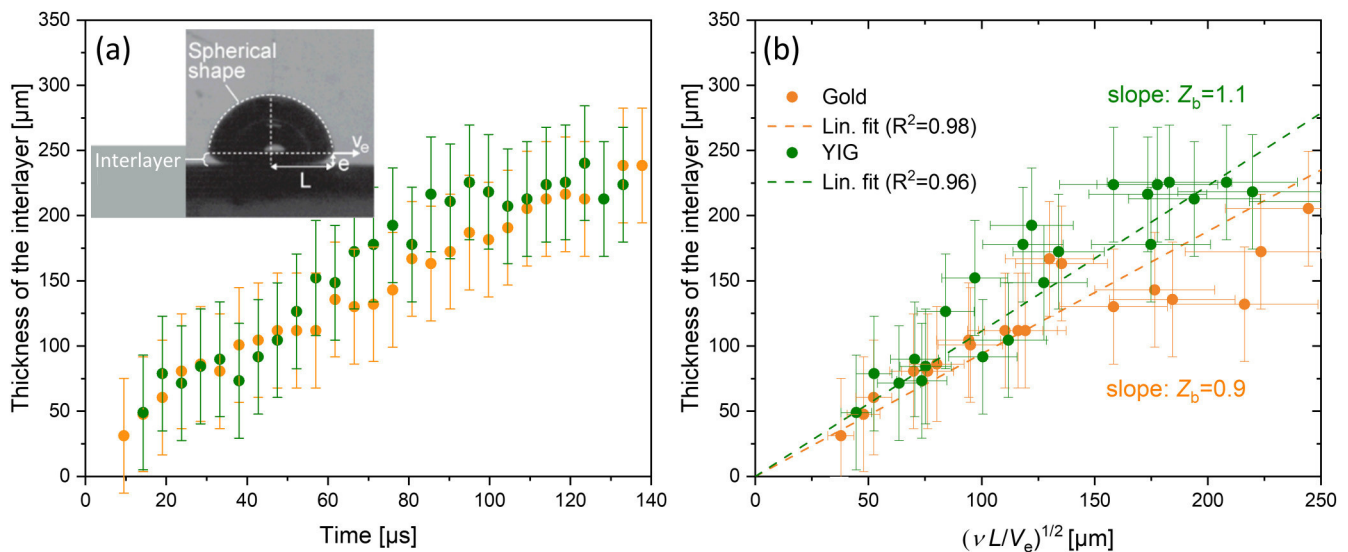


FIG. 5. Measured thickness e of the interlayer of bubbles on gold and YIG in PAO6 during the expansion phase of the bubble (a) as a function of time and (b) as a function of the ratio $\sqrt{v \cdot L / V_e}$ with the slope Z_b as a proportionality factor (the inset shows the definition of the interlayer). The coefficient of determination is $R^2 = 0.96$ for YIG and $R^2 = 0.98$ for gold. The error bars for the layer thickness are based on the optical resolution (see Sec. II) and the x axis error is estimated following the propagation of uncertainty.

described by the Cox–Voinov hydrodynamic model of dynamic wetting⁷² and has been extensively studied.^{64,70} But, this relation does not apply here. A molecular-kinetic theory has been also developed to describe the velocity-dependence of the dynamic contact.^{59,62} Blake *et al.* introduced activation energies of adsorption and desorption from the surface of the molecules of the liquid. The velocity-dependence of the dynamic contact angle is then due to the perturbation of the adsorption equilibrium due to motion of the contact line. Yet again, the model did not succeed to fit the data for the largest capillary numbers, highlighting the originality of the dynamics reported here.

The interlayer does not only come with a time-dependent angle, but also with a time-dependent height. Figure 5(a) shows the time-dependent height of the interlayer during the expansion for the two targets in PAO6. The error bars are based on the calculated temporal and special resolution of the experimental setup. The interlayer for PAO40 is not addressed because the round shape of the bubble would lead to an arbitrary definition of the parameters L and e . For PAO6, Fig. 5(a) shows no differences in the height of the boundary layer between a gold and an oxide target. The thickness of the interlayer increases with time and fits the following boundary layer equation with the dimensionless constant Z_b ,

$$e = Z_b \sqrt{\frac{\nu L}{V_e}}, \quad (6)$$

where $V_e = \frac{dt}{dt}$ is the velocity of the liquid/vapor interface at the edge of the bubble, ν is the kinematic viscosity, and L is the distance between the bubble boundary at the edge of the interlayer and the center of the bubble. The slope of the regression lines in Fig. 5(b) represent the dimensionless constant Z_b . The slope is almost independent of the target material with $Z_{b,YIG} = 1.1$ and $Z_{b,Gold} = 0.9$. A similar behavior has been observed by Van Ouwerkerk for bubbles on a hot surface during boiling of the liquid.^{73,74} Assuming no change in the shape during the bubble growth, Van Ouwerkerk deduced $Z_b = 0.9$ from a self-similar approach and reported experimental values for Z_b between 0.3 and 0.8.

IV. CONCLUSION

Laser-induced cavitation in liquids is a key method applied to understand cavitation near solid boundaries, but also highly relevant for the laser synthesis of colloids. Indeed, the cavitation bubble and also the resulting persistent microbubbles may shield subsequent laser pulses, affecting productivity and reproducibility of the laser generation of nanoparticles. While it is intuitive that viscosity plays a role, experimental investigations under variation of both the target and liquid types have been missing. In this work, we showed that an increase of the kinematic viscosity by 2 orders of magnitude compared to water does affect the lifetime, the shape, the size, and the damping of the oscillation of laser-induced cavitation bubbles. Bubbles can be divided into two geometrical sections, separated by a rim: a spherical cap with a dynamic driven by inertial forces and an interlayer close to the target where the shape differs from a sphere when the contribution of the viscous forces to the friction drastically increases. Indeed, looking at the bubble footprint dynamics close the target, an inertio-capillary regime is

observed for intermediate viscosity and the thickness of the interlayer is in accordance with a boundary layer equation. Moreover, a contact angle hysteresis appears with increasing viscosity. These findings poorly depend on the target material which suggests that the shape and the dynamics of the bubble are driven by the contribution of the viscous forces to the friction, rather than by static hydrophilicity of the target. However, by increasing the viscosity, the behavior of the contact line cannot be interpreted with simplified hydrodynamic (Cox–Voinov) or molecular-kinetic theory models, highlighting the originality of the dynamics reported when extremely high capillary numbers are achieved. In addition to viscosity effects on the first cavitation of laser-induced bubbles, persistent bubbles show noteworthy phenomenological differences caused by the liquid and appear independent of the target type. These bubbles are spherical and partly dispersed for laser ablation in water, whereas in PAO40 a larger, flat, persistent bubble adheres to the target.

SUPPLEMENTARY MATERIAL

See the [supplementary material](#) for more information on bubble height, bubble shrinking, and the automated data processing for shadowgraph imaging. The [supplementary material](#) also provides information on the time dependence of the footprint radius and on the Rayleigh collapse time.

ACKNOWLEDGMENTS

This work has been financially supported by the European Cooperation in Science and Technology through COST Action MP1302 Nanospectroscopy. Tim Hupfeld acknowledges Evonik Industries for financial support. The authors would like to thank Carsten Dubs from INNOVENT e.V. Technologieentwicklung for providing the YIG wafer. B.G. and S.B. acknowledge the Deutsche Forschungsgemeinschaft (DFG) for funding.

REFERENCES

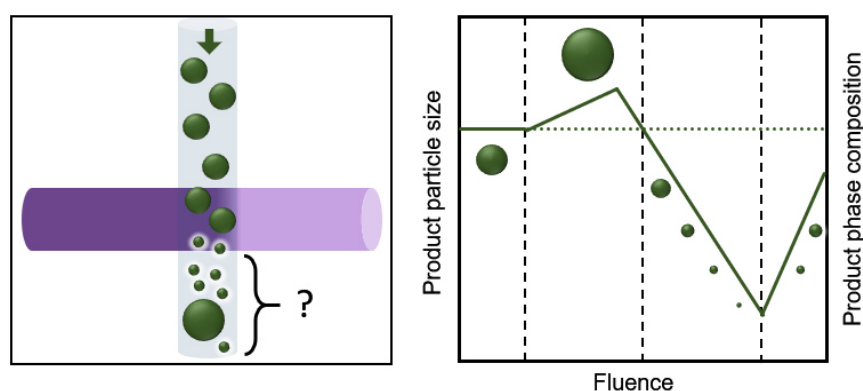
- ¹D. Zhang, B. Gökce, and S. Barcikowski, *Chem. Rev.* **117**, 3990 (2017).
- ²D. Zhang, J. Liu, P. Li, Z. Tian, and C. Liang, *Chem. Nanomater.* **3**, 512 (2017).
- ³V. Amendola and M. Meneghetti, *Phys. Chem. Chem. Phys.* **11**, 3805 (2009).
- ⁴J. Xiao, P. Liu, C. X. Wang, and G. W. Yang, *Prog. Mater. Sci.* **87**, 140 (2017).
- ⁵D. Amans, W. Cai, and S. Barcikowski, *Appl. Surf. Sci.* **488**, 445 (2019).
- ⁶J. G. Walter, S. Petersen, F. Stahl, T. Scheper, and S. Barcikowski, *J. Nanobiotechnol.* **8**, 21 (2010).
- ⁷V. Amendola, S. Polizzi, and M. Meneghetti, *Langmuir* **23**, 6766 (2007).
- ⁸H. Wender, M. L. Andreatza, R. R. B. Correia, S. R. Teixeira, and J. Dupont, *Nanoscale* **3**, 1240 (2011).
- ⁹H. P. S. Castro, V. S. Souza, J. D. Scholten, J. H. Dias, J. A. Fernandes, F. S. Rodembusch, R. Dos Reis, J. Dupont, S. R. Teixeira, and R. R. B. Correia, *Chem. Eur. J.* **22**, 138 (2016).
- ¹⁰G. Compagnini, A. A. Scalisi, and O. Puglisi, *Phys. Chem. Chem. Phys.* **4**, 2787 (2002).
- ¹¹N. Takada, T. Sasaki, and K. Sasaki, *Appl. Phys. A Mater. Sci. Process.* **93**, 833 (2008).
- ¹²N. Tabatabaie and D. Dorrnanian, *Appl. Phys. A* **122**, 558 (2016).
- ¹³T. Kato, S. Stauss, S. Kato, K. Urabe, M. Baba, T. Suemoto, and K. Terashima, *Appl. Phys. Lett.* **101**, 224103 (2012).
- ¹⁴E. B. Gordon, A. V. Karabulin, V. I. Matyushenko, V. D. Sizov, and I. I. Khodos, *J. Low Temp. Phys.* **172**, 94 (2013).

- ¹⁵R. Streubel, G. Bendt, and B. Gökce, *Nanotechnology* **27**, 205602 (2016).
- ¹⁶S. Jendrzej, B. Gökce, M. Epplé, and S. Barcikowski, *Chem. Phys. Chem.* **18**, 1012 (2017).
- ¹⁷N. Luo, X. Tian, J. Xiao, W. Hu, C. Yang, L. Li, and D. Chen, *J. Appl. Phys.* **113**, 164306 (2013).
- ¹⁸C. Streich, L. Akkari, C. Decker, J. Bormann, C. Rehbock, A. Müller-Schiffmann, F. C. Niemeyer, L. Nagel-Steger, D. Willbold, B. Sacca, C. Korth, T. Schrader, and S. Barcikowski, *ACS Nano* **10**, 7582 (2016).
- ¹⁹J. Zhang, M. Chaker, and D. Ma, *J. Colloid Interface Sci.* **489**, 138 (2017).
- ²⁰J. Liu, X. Tian, N. Luo, C. Yang, J. Xiao, Y. Shao, X. Chen, G. Yang, D. Chen, and L. Li, *Langmuir* **30**, 13005 (2014).
- ²¹C. Ma, J. Yan, Y. Huang, and G. Yang, *Adv. Opt. Mater.* **5**, 1700761 (2017).
- ²²V. Amendola, S. Scaramuzza, S. Agnoli, G. Granozzi, M. Meneghetti, G. Campo, V. Bonanni, F. Pineider, C. Sangregorio, P. Ghigna, S. Polizzi, P. Riello, S. Fiameni, and L. Nodari, *Nano Res.* **8**, 4007 (2015).
- ²³T. Hupfeld, T. Laumer, T. Stichel, T. Schuffenhauer, J. Heberle, M. Schmidt, S. Barcikowski, and B. Gökce, *Procedia CIRP* **74**, 244 (2018).
- ²⁴C. Doñate-Buendía, F. Frömel, M. B. Wilms, R. Streubel, J. Tenkamp, T. Hupfeld, M. Nachev, E. Gökce, A. Weisheit, S. Barcikowski, F. Walther, J. H. Schleifenbaum, and B. Gökce, *Mater. Des.* **154**, 360 (2018).
- ²⁵D. Longano, N. Ditaranto, N. Cioffi, F. Di Niso, T. Sibillano, A. Ancona, A. Conte, M. A. Del Nobile, L. Sabbatini, and L. Torsi, *Anal. Bioanal. Chem.* **403**, 1179 (2012).
- ²⁶N. Lasemi, U. Pacher, L. V. Zhigilei, O. Bomati-Miguel, R. Lahoz, and W. Kautek, *Appl. Surf. Sci.* **433**, 772 (2018).
- ²⁷D. Amans, M. Diouf, J. Lam, G. Ledoux, and C. Dujardin, *J. Colloid Interface Sci.* **489**, 114 (2017).
- ²⁸J. Lam, J. Lombard, C. Dujardin, G. Ledoux, S. Merabia, and D. Amans, *Appl. Phys. Lett.* **108**, 074104 (2016).
- ²⁹A. Letzel, B. Gökce, P. Wagener, S. Ibrahimkutty, A. Menzel, A. Plech, and S. Barcikowski, *J. Phys. Chem. C* **121**, 5356 (2017).
- ³⁰M. Dell'Aglio, R. Gaudiuso, O. De Pascale, and A. De Giacomo, *Appl. Surf. Sci.* **348**, 4 (2015).
- ³¹M. Tiberi, A. Simonelli, G. Cristoforetti, P. Marsili, F. Giammanco, and E. Giorgetti, *Appl. Phys. A Mater. Sci. Process.* **110**, 857 (2013).
- ³²A. Tamura, A. Matsumoto, K. Fukami, N. Nishi, and T. Sakka, *J. Appl. Phys.* **117**, 173304 (2015).
- ³³C. Y. Shih, R. Streubel, J. Heberle, A. Letzel, M. V. Shugaev, C. Wu, M. Schmidt, B. Gökce, S. Barcikowski, and L. V. Zhigilei, *Nanoscale* **10**, 6900 (2018).
- ³⁴S. Ibrahimkutty, P. Wagener, A. Menzel, A. Plech, and S. Barcikowski, *Appl. Phys. Lett.* **101**, 103104 (2012).
- ³⁵J. Tomko, J. J. Naddeo, R. Jimenez, Y. Tan, M. Steiner, J. M. Fitz-Gerald, D. M. Bubb, and S. M. O'Malley, *Phys. Chem. Chem. Phys.* **17**, 16327 (2015).
- ³⁶S. Ibrahimkutty, P. Wagener, T. D. S. Rolo, D. Karpov, A. Menzel, T. Baumbach, S. Barcikowski, and A. Plech, *Sci. Rep.* **5**, 16313 (2015).
- ³⁷S. Reich, P. Schönfeld, P. Wagener, A. Letzel, S. Ibrahimkutty, B. Gökce, S. Barcikowski, A. Menzel, T. dos Santos Rolo, and A. Plech, *J. Colloid Interface Sci.* **489**, 106 (2017).
- ³⁸R. Tanabe, T. T. P. Nguyen, T. Sugiura, and Y. Ito, *Appl. Surf. Sci.* **351**, 327 (2015).
- ³⁹N. Dabir-Moghaddam, Z. Liu, and B. Wu, *J. Appl. Phys.* **121**, 044908 (2017).
- ⁴⁰M.-R. Kalus, N. Bärsch, R. Streubel, E. Gökce, S. Barcikowski, and B. Gökce, *Phys. Chem. Chem. Phys.* **19**, 7112 (2017).
- ⁴¹M.-R. Kalus, R. Lanyumba, N. Lorenzo-Parodi, M. A. Jochmann, K. Kerpen, U. Hagemann, T. C. Schmidt, S. Barcikowski, and B. Gökce, *Phys. Chem. Chem. Phys.* **21**, 18636 (2019).
- ⁴²K. Sasaki, T. Nakano, W. Soliman, and N. Takada, *Appl. Phys. Express* **2**, 046501 (2009).
- ⁴³A. De Giacomo, M. Dell'Aglio, A. Santagata, R. Gaudiuso, O. De Pascale, P. Wagener, G. C. Messina, G. Compagnini, and S. Barcikowski, *Phys. Chem. Chem. Phys.* **15**, 3083 (2013).
- ⁴⁴N. Takada, A. Fujikawa, and K. Sasaki, *Jpn. J. Appl. Phys.* **50**, 126201 (2011).
- ⁴⁵S. Jendrzej, B. Gökce, and S. Barcikowski, *Chem. Eng. Technol.* **40**, 1569 (2017).
- ⁴⁶M. Zhang, X. Wang, X. Fu, and Y. Xia, *Tribol. Int.* **42**, 1029 (2009).
- ⁴⁷A. Menéndez-Manjón, A. Schwenke, T. Steinke, M. Meyer, U. Giese, P. Wagener, and S. Barcikowski, *Appl. Phys. A Mater. Sci. Process.* **110**, 343 (2013).
- ⁴⁸R. Chou, A. H. Battez, J. J. Cabello, J. L. Viesca, A. Osorio, and A. Sagastume, *Tribol. Int.* **43**, 2327 (2010).
- ⁴⁹J. Tomko, S. M. O. Malley, C. Trout, J. J. Naddeo, R. Jimenez, J. C. Griepenburg, W. Soliman, and D. M. Bubb, *Colloids Surf. A* **522**, 368 (2017).
- ⁵⁰T. Tsuji, D.-H. Thang, Y. Okazaki, M. Nakanishi, Y. Tsuboi, and M. Tsuji, *Appl. Surf. Sci.* **254**, 5224 (2008).
- ⁵¹C. Lechner, W. Lauterborn, M. Koch, and R. Mettin, *Phys. Rev. Fluids* **4**, 021601 (2019).
- ⁵²M. Koch, C. Lechner, F. Reuter, K. Köhler, R. Mettin, and W. Lauterborn, *Comput. Fluids* **126**, 71 (2016).
- ⁵³S. R. Gonzalez Avila, C. Song, and C. D. Ohl, *J. Fluid Mech.* **767**, 31 (2015).
- ⁵⁴C. Lechner, W. Lauterborn, M. Koch, and R. Mettin, "Jet formation from bubbles near a solid boundary in a compressible liquid: Numerical study of distance dependence," *J. Fluid Mech.* (submitted) (2019).
- ⁵⁵J. Drelich, E. Chibowski, D. D. Meng, and K. Terpilowski, *Soft Matter* **7**, 9804 (2011).
- ⁵⁶M. Kalus, N. Bärsch, R. Streubel, E. Gökce, S. Barcikowski, and B. Gökce, *Phys. Chem. Chem. Phys.* **19**, 7112 (2017).
- ⁵⁷W. Lauterborn and T. Kurz, *Rep. Prog. Phys.* **73**, 106501 (2010).
- ⁵⁸L. Van Wijngaarden, *Ultrason. Sonochem.* **29**, 524 (2016).
- ⁵⁹C. F. Naudé and A. T. Ellis, *J. Basic Eng.* **83**, 648 (1961).
- ⁶⁰W. V. Kayser, *J. Colloid Interface Sci.* **56**, 622 (1976).
- ⁶¹P. Pötschke, J. Pionteck, and H. Stutz, *Polymer* **43**, 6965 (2002).
- ⁶²E. Bertrand, T. D. Blake, and J. De Coninck, *Colloids Surf. A* **369**, 141 (2010).
- ⁶³B. Lavi and A. Marmur, *Colloids Surf. A* **250**, 409 (2004).
- ⁶⁴D. Bonn, J. Eggers, J. Indekeu, and J. Meunier, *Rev. Mod. Phys.* **81**, 739 (2009).
- ⁶⁵S. F. Toosi, S. Moradi, and S. Hatzikiriakos, *Rev. Adhes. Adhes.* **5**, 55 (2017).
- ⁶⁶H. De Maleprade, C. Clanet, and D. Quéré, *Phys. Rev. Lett.* **117**, 094501 (2016).
- ⁶⁷J. D. Paulsen, R. Carmigniani, A. Kannan, J. C. Burton, and S. R. Nagel, *Nat. Commun.* **5**, 3182 (2014).
- ⁶⁸D. Jacqmin, *J. Fluid Mech.* **455**, 347 (2002).
- ⁶⁹T. D. Blake, R. A. Dobson, and K. J. Ruschak, *J. Colloid Interface Sci.* **279**, 198 (2004).
- ⁷⁰J. H. Snoeijer and B. Andreotti, *Annu. Rev. Fluid Mech.* **45**, 269 (2013).
- ⁷¹T. D. Blake and J. M. Haynes, *J. Colloid Interface Sci.* **30**, 421 (1969).
- ⁷²R. G. Cox, *J. Fluid Mech.* **168**, 169 (1986).
- ⁷³H. J. van Ouwkerk, *Int. J. Heat Mass Transfer* **14**, 1415 (1971).
- ⁷⁴H. J. Van Ouwkerk, *Chem. Eng. Sci.* **27**, 1957 (1972).

4.2 Laser post-processing of magnetic nanoparticles

Manipulation of the Size and Phase Composition of Yttrium Iron Garnet Nanoparticles by Pulsed Laser Post-Processing in Liquid

Reprinted from *Molecules* 25 (2020) 1869 under CC BY



Highlights:

- Influence of LPP parameters on the phase composition and size of yttrium iron garnet (YIG) nanoparticles was investigated
- ps-LFL is found to be much more efficient for fragmentation as compared to ns-LFL
- ns-LML results in larger particle sizes, phase purification of the garnet structure and ultimately higher magnetization
- ps-LFL reduces particle size from 14 nm to 5 nm, significantly increases monomodality compared to ns-irradiation, and transforms YIG nanoparticles to another nanocrystalline species with far lower magnetization

Appendix:

- Supporting information (A2)
- Tools and procedure for oxide target preparation from mixed powders (A3)
- LFL of ball milled YIG powder, ready to use as nanoadditive in AM (A4)
- Flexibel passage reactor design (A5)

Article

Manipulation of the Size and Phase Composition of Yttrium Iron Garnet Nanoparticles by Pulsed Laser Post-Processing in Liquid

Tim Hupfeld ¹, Frederic Stein ¹, Stephan Barcikowski ¹, Bilal Gökce ^{1,*} and Ulf Wiedwald ^{2,*}

¹ Technical Chemistry I and Center for Nanointegration Duisburg-Essen (CENIDE), University of Duisburg-Essen, Universitaetsstrasse 7, 45141 Essen, Germany; tim.hupfeld@uni-due.de (T.H.); frederic.stein@uni-due.de (F.S.); stephan.barcikowski@uni-due.de (S.B.)

² Faculty of Physics and Center for Nanointegration Duisburg-Essen (CENIDE), University of Duisburg-Essen, Lotharstr. 1, 47057 Duisburg, Germany

* Correspondence: bilal.goekce@uni-due.de (B.G.); ulf.wiedwald@uni-due.de (U.W.)

Academic Editor: Tatiana E. Itina

Received: 4 March 2020; Accepted: 10 April 2020; Published: 17 April 2020



Abstract: Modification of the size and phase composition of magnetic oxide nanomaterials dispersed in liquids by laser synthesis and processing of colloids has high implications for applications in biomedicine, catalysis and for nanoparticle-polymer composites. Controlling these properties for ternary oxides, however, is challenging with typical additives like salts and ligands and can lead to unwanted byproducts and various phases. In our study, we demonstrate how additive-free pulsed laser post-processing (LPP) of colloidal yttrium iron oxide nanoparticles using high repetition rates and power at 355 nm laser wavelength can be used for phase transformation and phase purification of the garnet structure by variation of the laser fluence as well as the applied energy dose. Furthermore, LPP allows particle size modification between 5 nm (ps laser) and 20 nm (ns laser) and significant increase of the monodispersity. Resulting colloidal nanoparticles are investigated regarding their size, structure and temperature-dependent magnetic properties.

Keywords: yttrium iron oxide; perovskite; garnet; phase transformation; ferrimagnetic nanoparticles; laser ablation; laser fragmentation; laser melting; monodisperse

1. Introduction

Magnetic mixed metal oxide nanoparticles are an important class of materials for catalysis [1,2], biomedicine [3–5], and nanoparticle-polymer composites [6,7] and are also of high interest for applications in additive manufacturing, e.g., for 4D printing of magnetic structures [8–10]. For many of these applications, nanoparticles are required in colloidal form, dispersed in liquids such as pure water, organic solvents or polymer solutions. As a green method for synthesis and size modifications of colloidal nanoparticles, laser ablation in liquid (LAL) and laser post-processing (LPP) [11] have proven to be scalable [12,13] and versatile regarding nanoparticle composition [14–23] and choice of the liquid medium [24–28]. By LAL, metal and metal oxide nanoparticles have been successfully generated in relevant amounts, which is a key requirement for application. To increase the nanoparticle yield from oxide targets in LAL, unwanted byproducts in the form of microparticles should be minimized, which is achieved by using mechanically stable targets. In this way, challenging materials like ternary oxide nanoparticles [29,30] or doped nanoparticles [31,32] can be produced.

One of these challenging materials is $Y_3Fe_5O_{12}$ (yttrium iron garnet, YIG), which is widely used as a material for microwave devices [33]. YIG is also known for its outstanding magneto-optical

properties [34–36] and low spin-wave damping [37]. Furthermore, YIG nanoparticles synthesized by LPP were successfully used in laser-based additive manufacturing of steel powder [38]. As a competing phase to YIG, YFeO_3 (yttrium iron perovskite, YIP) also features excellent magneto-optical properties [39]. It is a canted antiferromagnet with a very low magnetization of $0.2 \text{ Am}^2\text{kg}^{-1}$ and a high domain wall velocity [39]. However, there are only a few studies available on the magnetic properties of ultra-small YIG and YIP nanoparticles $<10 \text{ nm}$. It is known that the surface-to-volume ratio affects the anisotropy constant, which makes ultra-small YIG particles particularly interesting [40]. Schmitz et al. demonstrated a LAL approach to obtain YIG nanoparticles, followed by LPP of the colloid via ns laser fragmentation in liquid (ns-LFL) for subsequent nanoparticle size reduction and ended up with unexpected high coercive and irreversibility fields at low temperatures [30]. The generated nanoparticles were much smaller than by wet chemical approaches [40], but considering their volume-weighted particle size distribution, still, a significant number of larger particles above 10 nm was present. The broad size distribution is a disadvantage which hinders the correlation of interesting magnetic properties and size and phase of the nanoparticles. Typically, size control during LAL and LPP can be achieved by variation of laser parameters and the choice of specific additives or saline solutions [41–44]. Variation of salinity works well with noble metals like gold, but in the case of less noble metals, molecular oxygen can oxidize the resulting nanoparticles. Moreover, in the case of oxides, stabilization with salts does not work and macromolecular ligands can affect the chemical composition of the nanoparticles [29,30], which makes size control of oxide nanoparticles challenging.

To overcome this, we investigate LPP of ligand-free YIG colloids with ps and ns pulses to manipulate the particle size distribution and possibly the phase composition to get deeper insights into the magnetic properties of the resulting nanoparticles.

2. Results and Discussion

2.1. Nanoparticle Size Modification

To achieve a particle size modification, the applied laser fluence is a crucial parameter. According to Lau et al. there are four different fluence regimes [45]. In the first regime, there is no effect of the laser irradiation on nanoparticle size (untreated, UT), in the melting regime, particles partially melt and/or fuse together (LML), in the fragmentation regime the fluence is large enough to fragmentize particles (LFL) and in the optical breakdown regime (OB), losses through ionization of the liquid reduce fragmentation efficiency. Figure 1a shows colloid samples right after LAL and after LPP with different fluences and pulse durations. As expected, the influence of laser fluence variation can be observed right from the clouding (flocculation) of the YIG colloids, since particle size directly influences the scattering intensity. Colloids show the most pronounced clouding after LAL and low fluence ns post-processing. After high fluence post-processing, the clouding is significantly reduced, indicating smaller particles. The lowest scattering intensity can be observed for high fluence ps-LFL. To quantify this effect, the ratio of the absorbance at 320 and 800 nm was calculated from UV-Vis absorbance spectra (Figure 1b). At 320 nm, YIG shows a concentration-dependent absorbance, whereas the scattering of larger particles dominates absorbance at 800 nm. This ratio gives a good impression on the scattering intensity and is expected to correlate with nanoparticle size, similar to the primary particle index (PPI) known for gold and ZnO colloids [45–47]. On this basis, one can calculate a process efficiency which is given by the $\text{Abs}_{320}/\text{Abs}_{800}$ -ratio after post-processing relative to the $\text{Abs}_{320}/\text{Abs}_{800}$ -ratio before post-processing (after LAL).

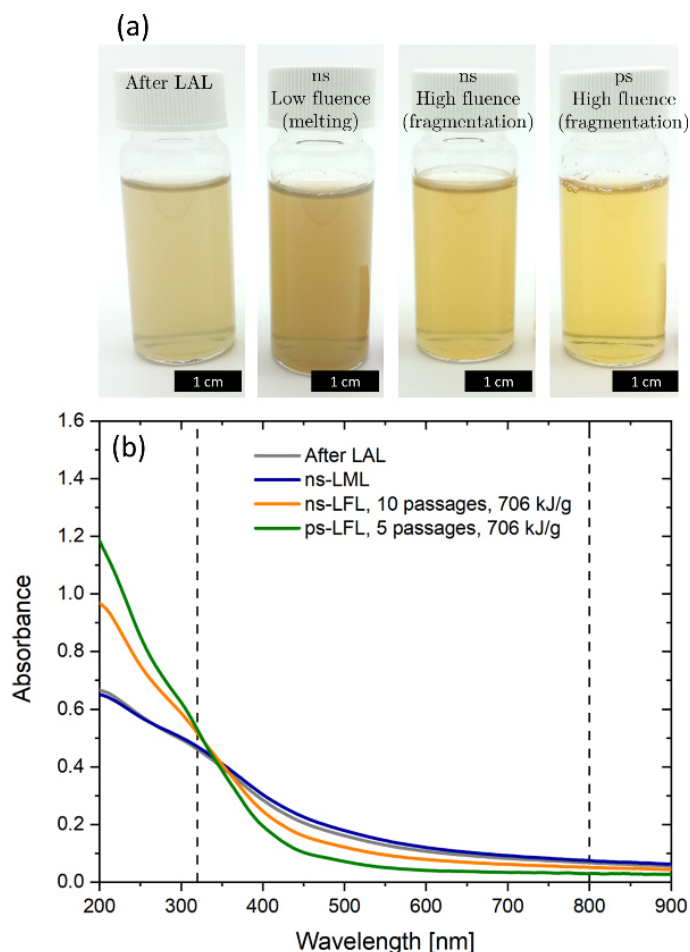


Figure 1. (a) Image of the educt colloid gained by laser ablation in water and the colloids after laser post-processing with different pulse durations and fluences at the same nanoparticle concentration. From left to right: educt, ns low fluence, ns high fluence, ps high fluence. (b) Corresponding UV-Vis-extinction spectra. Differences in the ratio of the absorbance at 320 and 800 nm (wavelength marked in the graph) already indicate differences in nanoparticle size distribution. An alternative measure for the process efficiency is the Furlong slope, presented in the Supplementary Material, Figure S3.

The process efficiency as a function of fluence is depicted in Figure 2. For ns-LPP (Figure 2a), all the regimes mentioned above are passed as a function of fluence. Below 5 mJ/cm^2 , the process efficiency is negative, which indicates more scattering and slightly larger particles. There is some uncertainty regarding the transition between UT and LML regime since the absolute values of the process efficiency are rather small. Since we aimed for working in the LML and LFL regime, no further investigation of the transition between the UT and the LML regime was performed. Above 5 mJ/cm^2 the process efficiency shows positive values (LFL regime) with a maximum at 30 to 40 mJ/cm^2 . As expected, the process efficiency does not increase further for higher fluences (OB regime). A similar trend can be observed for ps post-processing (Figure 2b), but the optical breakdown occurs at lower fluences due to the higher pulse energy of ps pulses. Note that deviations of the optical breakdown threshold from literature might be due to self-focusing effects of the cylindrical liquid jet, which results in a much higher fluence [48]. Compared to the ns-LFL, ps-LFL shows an approximately 200% higher process efficiency at the same specific energy input, which is attributed to the shorter pulse duration and less thermal energy losses through electron-phonon coupling and a higher pulse intensity due to shorter pulses.

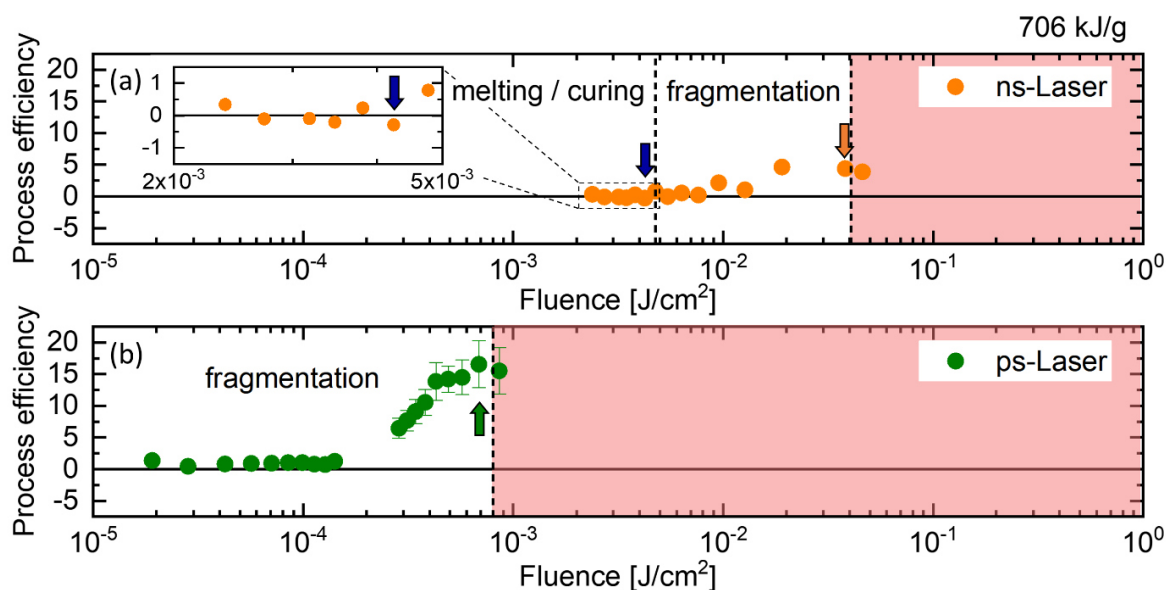


Figure 2. Process efficiency as a function of laser fluence for (a) ns and (b) ps post-processing. The process efficiency is based on the UV-Vis absorbance spectra and is calculated from the Abs_{320}/Abs_{800} -ratio after post-processing relative to the Abs_{320}/Abs_{800} -ratio before post-processing. The arrows indicate the optimum parameters for melting/curing (blue) and fragmentation (orange and green). In all cases, the specific energy input was 706 kJ/g. Note that the choice of specific energy dose represents a compromise between maximum fragmentation and minimum process duration. Further information on the variation of the specific energy dose can be found in Supplementary Materials, Figure S2.

In contrast to ns irradiation, ps irradiation does not show any negative values for YIG in the investigated fluence range above 1.8×10^{-5} J/cm² (no LML regime). In general, melting and fragmentation processes strongly depend on the pulse duration, the laser fluence, the particle absorption cross-section, and the thermal diffusion length in combination with the nanoparticle size or volume. For long pulse durations in the range of ns, more homogeneous heating can be expected and LML was observed in many studies. If the pulse duration is much shorter (e.g., ps pulses), homogeneous heating is unlikely and evaporation at the particle surface leads to nanoparticle byproducts even below the fragmentation threshold. To our best knowledge, there are just a few studies reporting ps-LML [45,49–51]. Sakaki et al. reported on burst-mode laser irradiation for homogeneous heating depending on the number of pulses and the interval between them to generate submicron spheres [50]. In other studies, high nanoparticle concentrations in the range of g/L were used for ps-LML [45,51], which is much higher than in our study and can lead to stability issues. All in all, we conclude that the chosen laser parameter, especially the laser fluence, in combination with the YIG colloid of the given concentration and particle size distribution, were not suitable for efficient ps-LML.

Results of optical characterization and determination of the process efficiency are reflected in the mass-weighted hydrodynamic size distribution shown in Figure 3. In general, LFL results in a narrowed distribution at smaller particle size, whereby ps-LFL is much more efficient than ns-LFL. In contrast, ns-LML results in a preservation of the initial particle size distribution after LAL and only minor reduction of the particle's mass fraction below 40 nm. Compared to ns-LFL, ns-LML features a slightly smaller peak maximum, but a broader distribution and a higher number of particles >60 nm.

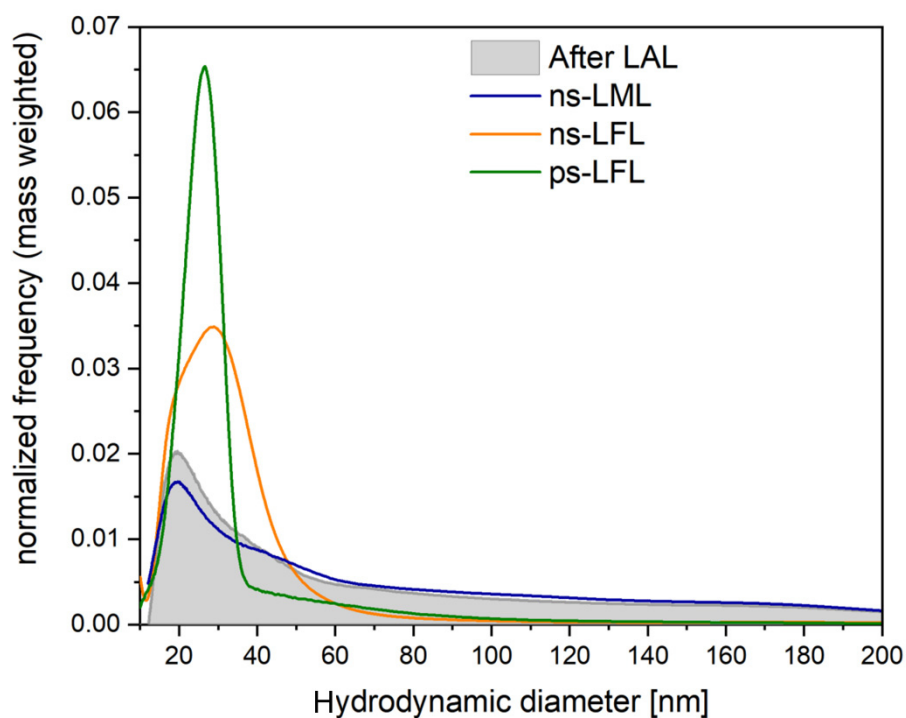


Figure 3. Mass-weighted hydrodynamic size distribution of the educt colloid after LAL and of the colloids after post-processing with lasers of different pulse durations and fluences, respectively.

TEM images in Figure 4 support these trends. Feret diameter distributions after LML show a clear difference between the educt and the LML-treated colloid. The x_c -value (expected value) of the lognormal fit increases from 14.9 nm to 20.0 nm and the polydispersity index (PDI), which is calculated from the square of the expected value x_c^2 divided by its variance σ^2 , decreases from 0.33 to 0.14. This indicates an improved degree of monodispersity and an improved degree of monodispersity. LFL, on the other hand, significantly reduces the number of large particles >20 nm and leads to an x_c -value of 7.8 nm for ns-LFL and 5.3 nm for ps-LFL, respectively. Monodispersity increases significantly from LAL generated colloids (PDI = 0.33) to ns-LFL (PDI = 0.17) and ps-LFL (PDI = 0.07). Overall, the size analysis clearly shows a trend toward ps-LFL being much more efficient than ns-LFL at the same specific energy input, leading to a narrower particle size distribution. Thus, we only compare ps-LFL, ns-LML with the educt after LAL in the following structural and magnetically characterization.

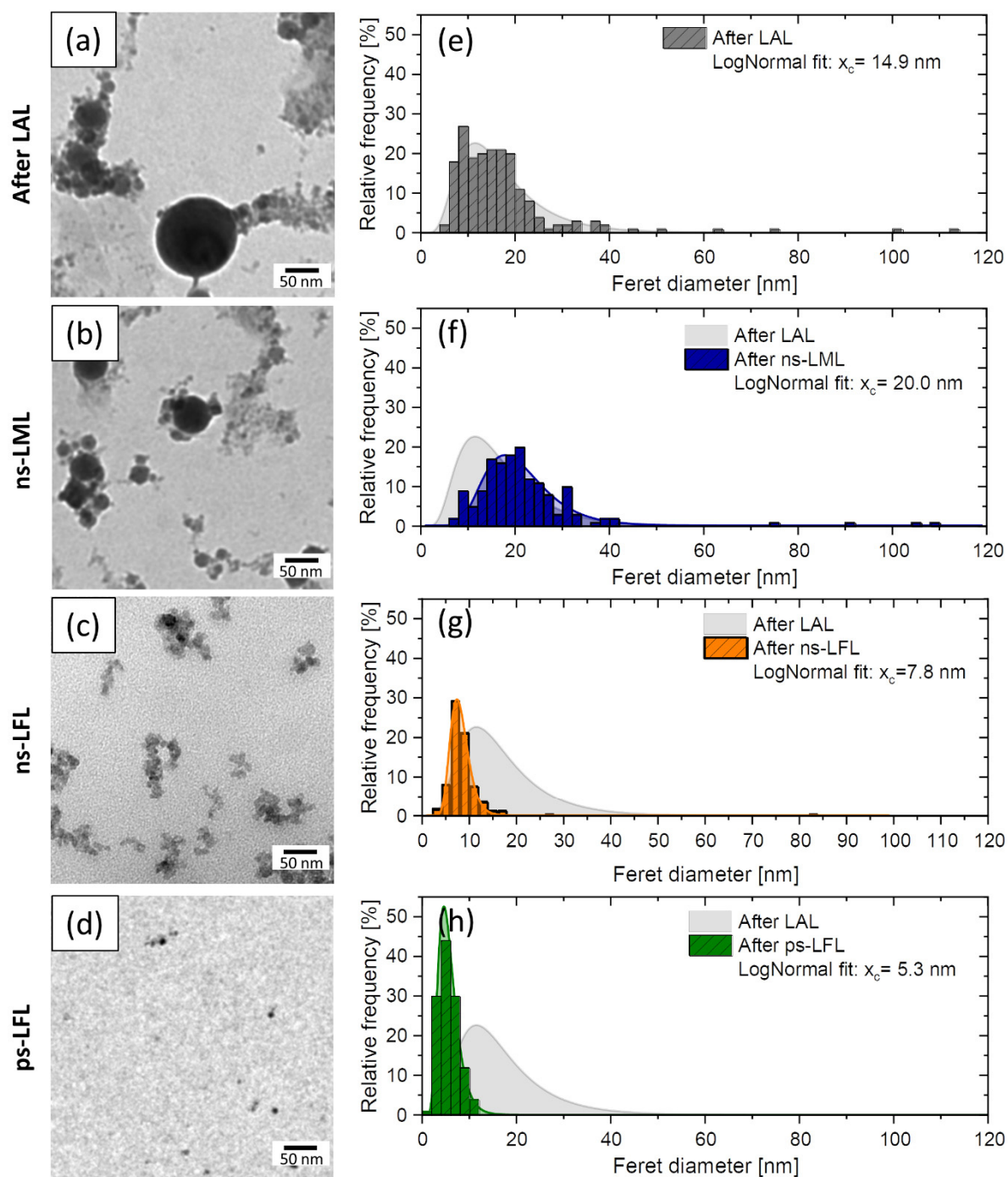


Figure 4. (a–d) TEM images and (e–h) corresponding size distributions (number-weighted) for the educt colloid after LAL and of the colloids after post-processing with lasers of different pulse durations and fluences. For each size distribution >500 particles were counted. The x_c value (expected value of the lognormal fit) is given for each size distribution.

2.2. Structural Analysis

X-ray powder diffraction is applied for the phase identification of the generated nanoparticles. Figure 5 presents the diffractograms on a linear scale after LAL, ns-LML, and ps-LFL. It is obvious that all diffractograms show the typical signature of YIG nanoparticles [52–54]. After LAL, however, an additional broad peak is found underneath the YIG(420) diffraction peak, which may indicate small grains of YIG or an additional phase. Note that the YIG(420) peak is the most prominent in powder

XRD at about 32° . After ns-LML, the broad feature under the (420) peak vanishes and the YIG peaks further sharpen. This observation points to a growing grain size after the particles' melting and is entirely in line with the observed particle growth in Figure 5. When ps-LFL is applied, the TEM size distribution gives a reduced particle size ($x_c = 5.3$ nm) and a sharper distribution. Although in the TEM investigations no larger particles have been found, it is clear from the diffractogram of the ps-LFL sample that the fragmentation is incomplete, and thus, some large YIG particles remain. Furthermore, the diffractogram exhibits again the broad feature overlapping with the YIG(420) diffraction peak and an additional broad peak at about 47° as indicated by the red stars. We carefully checked possible side phases such as several Fe oxides and Y_2O_3 , since phase transformation can occur for LPP of oxide colloids [55], but none of those fits with their largest diffraction peaks to the two broad features (red stars). Another Y-Fe oxide, namely the yttrium iron perovskite phase $YFeO_3$ (YIP), exhibits several diffraction peaks in the respective range, as reported by Nagrare et al. for $YFeO_3$ nanocrystals [56]. Considering the small crystallite size of about 5 nm, several closely located XRD peaks will overlap and merge. As a result, very broad diffraction peaks appear and only a few, well-separated diffraction 'bands' can be distinguished. We conclude that it is likely that $YFeO_3$ -like nanocrystallites, presumably highly distorted, form by ps-LFL.

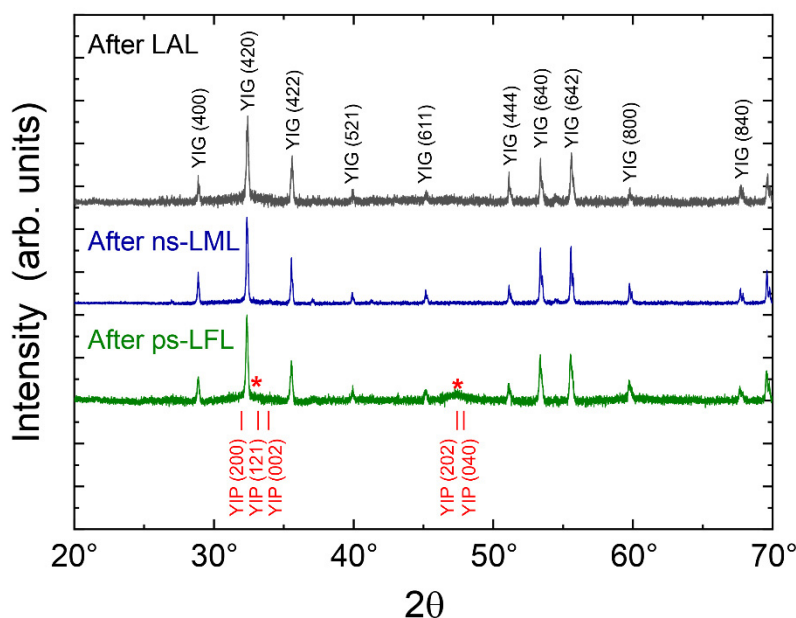


Figure 5. X-ray diffraction data after laser ablation in liquids (LAL), ns laser melting in liquids (ns-LML) and after ps laser fragmentation in liquids (ps-LFL). The pronounced YIG diffraction peaks (JCPDS PDF card 33-693) are indexed in black. Red stars indicate additional broad XRD features after ps-LFL. The positions of main diffraction peaks of YIP (JCPDS PDF card 39-1489.) are indexed in red (a plot with a logarithmic scale can be found in the Supplementary Materials, Figure S4).

Further evaluation of the XRD data yields the crystallite size by applying the Scherrer equation on the (420) peak at about 32° . We obtain crystallite sizes of 30 ± 5 nm, 48 ± 8 nm, and 35 ± 6 nm after LAL, ns-LML, and ps-LFL, respectively, and conclude that ns-LML enhances the crystallite size while the XRD crystallite size is much larger than the most probable TEM diameter. This arises from the small number of large particles comprising a dominant scattering volume in XRD. However, the tendency of an increased size by ns-LML is clear from both TEM and XRD investigations. Fragmentation, on the other side has no significant influence on the XRD grain size of the YIG phase. We ascribe this to a very small, remaining fraction of non-fragmented educt particles in the ps-LFL processed colloid. The additional peaks indicated by the red stars correspond to a crystallite size of 4.5 ± 1.5 nm. This value is in good agreement with the size distribution after ps-LFL.

In summary, the structural investigations suggest the formation of larger YIG crystallite sizes after ns-LML, while ps-LFL leads to smaller particles, crystallized probably in the YIP phase. A further magnetic inspection may allow identifying these two distinct phases.

2.3. Magnetic Properties

The magnetic properties of the educt and further sample processing can help to identify both the phase and the size of magnetic nanoparticles. Starting with the sample after LAL, it can be expected to find different magnetic properties after ns-LML and ps-LFL. Figure 6a presents the magnetization of the three samples as a function of temperature. The points below 300 K were extracted from the magnetic hysteresis loops after LAL, ns-LML, and ps-LFL, respectively (Figure 6b–d). The dotted line is a guide to the eye. Data above 300 K were continuously recorded in the vibrating sample magnetometer. All samples show the expected behavior for ferrimagnetic YIG with a Néel temperature of about 550 K. This is essentially the Néel temperature of YIG single crystals of $T_N = 553$ K [39] (and references in there) reflecting the high-quality YIG produced by LAL and the post-processing steps. The absolute values of the magnetization after LAL of $6 \text{ Am}^2\text{kg}^{-1}$ at low temperatures is, however, strongly reduced as compared to a single crystal ($26.8 \text{ Am}^2\text{kg}^{-1}$) [39] or the lower magnetization of YIG nanoparticles of similar size ($M_S = 10 \text{ Am}^2\text{kg}^{-1}$ for a diameter of 14 nm) [40]. Interestingly, the magnetization changes upon post-processing. When ns-LML is applied, we obtain $M = 10.5 \text{ Am}^2\text{kg}^{-1}$ confirming the above M_S of similar-sized particles [40]. Thus, ns-LML improves the nanocrystal quality and may transform quasi-amorphous particles and YIP phases to YIG nanocrystals.

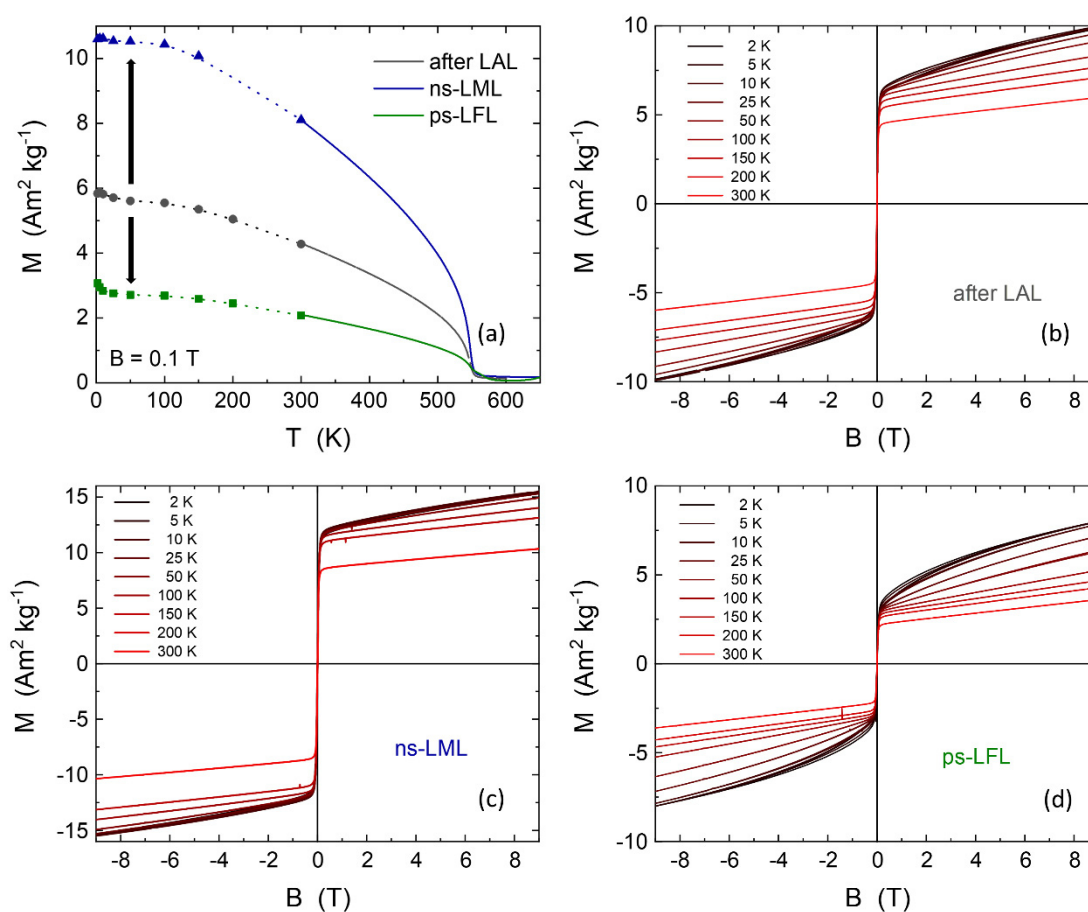


Figure 6. Magnetic properties of laser-generated yttrium iron oxide nanoparticles: (a) Magnetization as a function of temperature in $B = 0.1$ T after LAL, ns-LML, and ps-LFL. Points below 300 K are extracted from the hysteresis loops after LAL (b), ns-LML (c), and ps-LFL (d) connected by the dotted lines as guides to the eye. Data above 300 K were continuously recorded.

When ps-LFL is applied, the magnetization decreases to about $3 \text{ Am}^2\text{kg}^{-1}$ at low temperatures, where additionally a slight hyperbolic decrease appears. The latter feature can be ascribed to paramagnetic species generated by ps-LFL. Nonetheless, the major contribution to the temperature-dependent magnetization still shows the YIG volume Néel temperature. The magnification of the high-temperature region ($T > 400 \text{ K}$, zoom-in is presented in Supplementary Materials, Figure S5), however, gives a clear indication of a second magnetic species with higher ordering temperature. We suggest that $T_{N2} = 570 \text{ K}$ arising after ps-LFL is due to the formation of the YIP phase from larger YIG nanoparticles. YIP is a canted antiferromagnet. Single crystals of YIP have a Néel temperature of 643 K and a very low magnetization of $0.2 \text{ Am}^2\text{kg}^{-1}$ [39]. It is often found that for small particles the magnetic ordering temperature is reduced. Due to the low magnetization of the canted antiferromagnet, we can expect that YIP only shows up in magnetometry when the relative amount is rather large. Assuming the full magnetization of YIG nanoparticles develops in all samples ($M_{\text{YIG}} = 10.5 \text{ Am}^2\text{kg}^{-1}$), the reduction to $3 \text{ Am}^2\text{kg}^{-1}$ for ps-LFL is equivalent to a phase composition of about 30% YIG and 70% of a second, quasi-antiferromagnetic phase (presumably YIP) after ps-LFL. Note that magnetometry measures the mass averaged magnetization.

Further analysis of the magnetic hysteresis loops at various temperatures in Figure 6b–d also exhibits the features of the two phases. After LAL, a very soft magnetic hysteresis loop is observed as expected for YIG. After saturation of this component well below 1 T , a paramagnetic slope is recorded. This can arise from a (quasi-)antiferromagnetic phase, presumably the canted antiferromagnetic YIP phase, as it has been observed before for 30 nm and 60 nm YFeO_3 nanoparticles. Prokov et al. reported a high field susceptibility of $\chi_{\text{HF}} = 0.004 \text{ emu mol}^{-1}\text{Oe}^{-1}$ at $T = 4 \text{ K}$ and slightly lower at 300 K [57]. For comparison, we calculated the high field susceptibility in the identical units. The present samples show $\chi_{\text{HF}} = 0.003$ and $0.006 \text{ emu mol}^{-1}\text{Oe}^{-1}$ for 300 K and 5 K , respectively, which is comparable to earlier results for pure YFeO_3 . Such a relatively small variation of χ_{HF} by only 50% from 5–300 K is inconsistent with a Langevin paramagnet which shows a hyperbolic decrease. Thus, we have three parameters, i.e., the reduced magnetization, the second Néel temperature T_{N2} , and the high field susceptibility, suggesting the formation of the second (main) phase at about 70% phase content after ps-LFL. All these features and in the light of the structural investigations, it is likely that a highly distorted YIP-like phase forms.

3. Materials and Methods

Iron oxide (Fe_2O_3) and yttrium oxide (Y_2O_3) nanopowders for target manufacturing were both purchased from Sigma-Aldrich (St. Louis, MO, USA), homogeneously mixed and pressed at 330 MPa . Thereafter, the green compacts were sintered at $1550 \text{ }^\circ\text{C}$ for 6 h (Nabertherm LHT 01/17D, Lilienthal, Germany) to create targets with a pure YIG phase (details on Target manufacturing are shown in [30]). Since there is an influence of the target porosity on the nanoparticle yield, only dense targets with a density of more than 95% compared to the bulk density were used for laser ablation in liquids (LAL).

LAL was performed in pure water, obtained from a Milli-Q purification system (Merck, Darmstadt, Germany), with a 1064 nm Nd:YAG-laser in a batch setup introduced in [58]. At 10 kHz , the laser (Rofin PowerLine E, Hamburg, Germany) delivered 8 ns pulses with a fluence of 16.7 J/cm^2 , and LAL was performed for 5 min . Analog to earlier studies [30,45,59], a liquid jet setup was used for laser post-processing (LPP) of the laser-generated YIG colloids with a concentration of 160 mg/L (Figure 7). The colloid was directed through a glass nozzle (60 mL/min), forming a liquid jet with a diameter of 1.3 mm , which was irradiated with either ns- or ps-pulses at 80 kHz repetition rate (Coherent Avia 355-23, Santa Clara, CA, USA, or Edgewave PX400-3-GH, Würselen, Germany). Since YIG is well absorbing in the UV range below a wavelength of 370 nm , the third harmonic of the lasers was used by calculation of absorption efficiency and melting threshold (see Supplementary Materials, Figure S1. for details on wavelength selection). The liquid jet reactor allows flexible tuning of the applied fluences, just by changing the distance between the lens and the liquid jet. Further, it is possible to irradiate colloids several times (several passages) to increase the specific energy dose. According to Lau et al.

the specific energy dose is calculated by subtracting the transmitted laser powder from the nominal laser power without liquid jet and normalization of this value to the nanoparticle concentration and volume flow rate [45]. In the present case, roughly 10–20% of the laser power was transmitted through the liquid jet to the power meter and showed fluctuations of several %. Furthermore, scattering effects caused by the nanoparticles and diffraction effects at the air-water-interface of the liquid jet make the calculation of the dose rather inaccurate [48]. Therefore, we ignore transmission and calculate the nominal specific energy input right from the laser output power in front of the liquid jet and normalized to the nanoparticle concentration and volume flow rate.

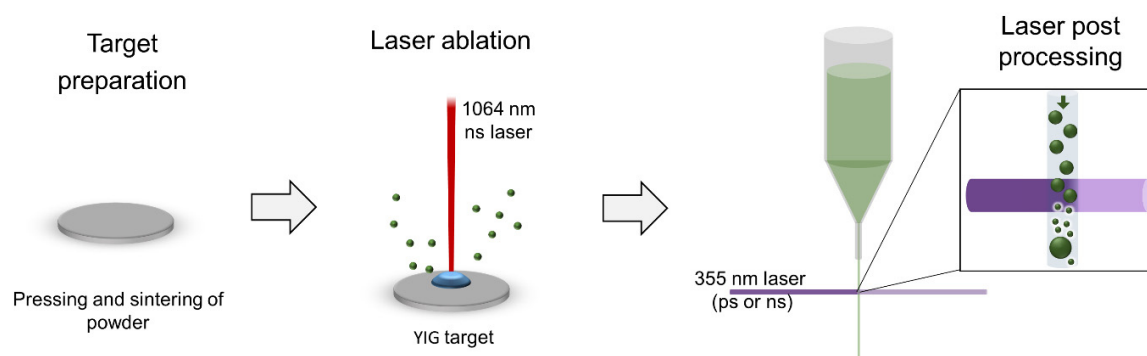


Figure 7. Schematic illustration of process steps for laser-synthesis of ligand free nanoparticles from powder materials. From left to right: target manufacturing, laser ablation in liquid (LAL) and laser post processing (LPP) of colloids.

After LAL and LPP, absorbance spectra in the UV-Vis range were collected for all colloids (Thermo Scientific Evolution 201, Waltham, MA, USA) and hydrodynamic size distribution was measured by analytical disc centrifugation (ADC, CPS Instruments, Prairieville, LA, United States). Transmission electron microscopy (TEM, Zeiss EM 910, Oberkochen, Germany) and X-ray powder diffraction (XRD, PANalytical X'Pert PRO, Almelo, Netherlands) were used for more information on the Feret particle size and the phase composition. Finally, the magnetic properties of dried powders were characterized in a vibrating sample magnetometer (VSM, Quantum Design MPMS XL, Darmstadt, Germany).

4. Conclusions

Laser post-processing (LPP) of colloids is a powerful tool for the modification of particle size and phase composition of magnetic mixed oxide nanoparticles and therefore an important aspect for their applicability. Irradiating a laser-generated YIG colloid with ps laser pulses (ps-LFL) results in particle fragmentation from 14 to 5 nm, accompanied by a significant increase of monodispersity. ps-LFL is found to be much more efficient for fragmentation as compared to ns-LFL at the same specific energy dose. At low fluences, however, ns-irradiation allows laser melting (ns-LML) and an increase of particle size to 20 nm. Furthermore, purification of the YIG phase occurs during ns-LML, which is reflected by an increase of magnetization from $6 \text{ Am}^2\text{kg}^{-1}$ to $10.5 \text{ Am}^2\text{kg}^{-1}$ in $B = 0.1 \text{ T}$, in accordance to values measured for similar-sized YIG particles in literature. In turn, ps-irradiation reduces the magnetization to $3 \text{ Am}^2\text{kg}^{-1}$ and gives a clear indication of a second magnetic species with a higher Néel temperature than YIG. Considering the two Néel temperatures after ps-LFL, the low magnetization which has been increased by ns-LML and decreased by ps-LFL, and a high field susceptibility, it is very likely that ps-LFL transforms YIG nanoparticles to another nanocrystalline species with small particle size. From the measured magnetization, we were also able to approximate a phase composition of 30% YIG and 70% of a second (quasi-)antiferromagnetic phase, presumably Yttrium Iron Perovskite (YIP). Our results underline the flexibility of LPP for modification of oxide nanomaterials, which could enable better applicability, e.g., in nanoparticle-polymer composites.

Supplementary Materials: The following are available online Figure S1: (a) Absorption efficiency Q_{abs}/λ as a function of the particle size (b) Estimation of the fluence required for melting particles (yellow line) and evaporate them (gray line); Figure S2: UV-Vis absorbance ratio between 320 and 800 nm as a function of the (a) number of passages during fragmentation and (b) specific energy input in kJ/g which considers, that the ps-laser has twice the pulse energy and total laser power compared to the ns-laser; Figure S3: (a) Double logarithmic plot of the UV-Vis absorbance spectra to calculate (b) the Furlong slope from the linear slope between 250 and 300 nm; Figure S4: Experimental data of the ps-LFL sample in logarithmic scale together with the YIP reference positions and intensities (JCPDS PDF card 39-1489); Figure S5: Magnetization as a function of temperature at $B = 0.1$ T in the high-temperature region after ps-LFL. Two ordering temperatures T_{N1} and T_{N2} are detected.

Author Contributions: Conceptualization, T.H., U.W., B.G. methodology, T.H., F.S. formal analysis, T.H., F.S., U.W., investigation, T.H., F.S. data curation, T.H., F.S. writing—original draft preparation, T.H., U.W. writing—review and editing, T.H., F.S., S.B., B.G., U.W., visualization, T.H., U.W. supervision, B.G., U.W., S.B. funding acquisition, B.G. All authors have read and agreed to the published version of the manuscript.

Funding: This study received external funding from the following projects Deutsche Forschungsgemeinschaft: Project-ID 405553726, GO 2566/3-1, INST 20876/212-1.

Acknowledgments: The authors thank Jurij Jacobi for TEM imaging of laser-generated nanoparticles. We also thank Alexander Schmitz and Alexander Schug for their support during the optimization of target manufacturing. Further, Michael Vennemann is acknowledged for the help and training in XRD. Tim Hupfeld gratefully acknowledges Evonik industries for financial support. This work is funded by the Deutsche Forschungsgemeinschaft (DFG, German Research Foundation) – Project-ID 405553726 within CRC/TRR 270 and grant number DFG GO 2566/3-1. We further thank the DFG and NRW for funding in the frame of the program “Forschungsgeräte” (INST 20876/212-1).

Conflicts of Interest: The authors declare no conflict of interest.

References

1. Pizzolato, E.; Scaramuzza, S.; Carraro, F.; Sartori, A.; Agnoli, S.; Amendola, V.; Bonchio, M.; Sartorel, A. Water oxidation electrocatalysis with iron oxide nanoparticles prepared via laser ablation. *J. Energy Chem.* **2016**, *25*, 246–250. [[CrossRef](#)]
2. Wu, W.; Jiang, C.; Roy, V.A.L. Recent progress in magnetic iron oxide-semiconductor composite nanomaterials as promising photocatalysts. *Nanoscale* **2015**, *7*, 38–58. [[CrossRef](#)] [[PubMed](#)]
3. Hola, K.; Markova, Z.; Zoppellaro, G.; Tucek, J.; Zboril, R. Tailored functionalization of iron oxide nanoparticles for MRI, drug delivery, magnetic separation and immobilization of biosubstances. *Biotechnol. Adv.* **2015**, *33*, 1162–1176. [[CrossRef](#)] [[PubMed](#)]
4. Rosenweing, R.E. Heating magnetic fluid with alternating magnetic field. *J. Magn. Magn. Mater.* **2002**, *252*, 370–374. [[CrossRef](#)]
5. Hu, Y.; Mignani, S.; Majoral, J.P.; Shen, M.; Shi, X. Construction of iron oxide nanoparticle-based hybrid platforms for tumor imaging and therapy. *Chem. Soc. Rev.* **2018**, *47*, 1874–1900. [[CrossRef](#)]
6. Prasanna, S.R.V.S.; Balaji, K.; Pandey, S.; Rana, S. Metal Oxide Based Nanomaterials and Their Polymer Nanocomposites. *Nanomater. Polym. Nanocompos.* **2019**, 123–144. [[CrossRef](#)]
7. Streubel, R.; Wilms, M.B.; Doñate-Buendía, C.; Weisheit, A.; Barcikowski, S.; Schleifenbaum, J.H.; Gökce, B. Depositing laser-generated nanoparticles on powders for additive manufacturing of oxide dispersed strengthened alloy parts via laser metal deposition. *Jpn. J. Appl. Phys.* **2018**, *57*. [[CrossRef](#)]
8. Wehner, M.; Truby, R.L.; Fitzgerald, D.J.; Mosadegh, B.; Whitesides, G.M.; Lewis, J.A.; Wood, R.J. An integrated design and fabrication strategy for entirely soft, autonomous robots. *Nature* **2016**, *536*, 451–455. [[CrossRef](#)]
9. Kim, Y.; Yuk, H.; Zhao, R.; Chester, S.A.; Zhao, X. Printing ferromagnetic domains for untethered fast-transforming soft materials. *Nature* **2018**, *558*, 274–279. [[CrossRef](#)]
10. Wei, H.; Zhang, Q.; Yao, Y.; Liu, L.; Liu, Y.; Leng, J. Direct-write fabrication of 4D active shape-changing structures based on a shape memory polymer and its nanocomposite. *ACS Appl. Mater. Interfaces* **2017**, *9*, 876–883. [[CrossRef](#)]
11. Zhang, D.; Gökce, B.; Barcikowski, S. Laser Synthesis and Processing of Colloids: Fundamentals and Applications. *Chem. Rev.* **2017**, *117*, 3990–4103. [[CrossRef](#)] [[PubMed](#)]
12. Streubel, R.; Barcikowski, S.; Gökce, B. Continuous multigram nanoparticle synthesis by high-power, high-repetition-rate ultrafast laser ablation in liquids. *Opt. Lett.* **2016**, *41*, 1486–1489. [[CrossRef](#)] [[PubMed](#)]

13. Jendrzej, S.; Gökce, B.; Epple, M.; Barcikowski, S. How Size Determines the Value of Gold: Economic Aspects of Wet Chemical and Laser-Based Metal Colloid Synthesis. *ChemPhysChem* **2017**, *18*, 1012–1019. [[CrossRef](#)]
14. Rehbock, C.; Jakobi, J.; Gamrad, L.; van der Meer, S.; Tiedemann, D.; Taylor, U.; Kues, W.; Rath, D.; Barcikowski, S. Current state of laser synthesis of metal and alloy nanoparticles as ligand-free reference materials for nano-toxicological assays. *Beilstein J. Nanotechnol.* **2014**, *5*, 1523–1541. [[CrossRef](#)] [[PubMed](#)]
15. Yang, G. Laser ablation in liquids: Applications in the synthesis of nanocrystals. *Prog. Mater. Sci.* **2007**, *52*, 648–698. [[CrossRef](#)]
16. Barcikowski, S.; Baranowski, T.; Durmus, Y.; Wiedwald, U.; Gökce, B. Solid solution magnetic FeNi nanostrand–polymer composites by connecting-coarsening assembly. *J. Mater. Chem. C* **2015**, *3*, 10699–10704. [[CrossRef](#)]
17. Kohsakowski, S.; Gökce, B.; Tanabe, R.; Wagener, P.; Plech, A.; Ito, Y.; Barcikowski, S. Target geometry and rigidity determines laser-induced cavitation bubble transport and nanoparticle productivity – a high-speed videography study. *Phys. Chem. Chem. Phys.* **2016**, *18*, 16585–16593. [[CrossRef](#)]
18. Wagener, P.; Jakobi, J.; Rehbock, C.; Chakravadhanula, V.S.K.; Thede, C.; Wiedwald, U.; Bartsch, M.; Kienle, L.; Barcikowski, S. Solvent-surface interactions control the phase structure in laser-generated iron-gold core-shell nanoparticles. *Sci. Rep.* **2016**, *6*, 23352. [[CrossRef](#)]
19. Zhang, D.; Gökce, B.; Notthoff, C.; Barcikowski, S. Layered Seed-Growth of AgGe Football-like Microspheres via Precursor-Free Picosecond Laser Synthesis in Water. *Sci. Rep.* **2015**, *5*, 13661. [[CrossRef](#)]
20. Hu, S.; Tian, M.; Ribeiro, E.L.; Duscher, G.; Mukherjee, D. Tandem laser ablation synthesis in solution-galvanic replacement reaction (LASIS-GRR) for the production of PtCo nanoalloys as oxygen reduction electrocatalysts. *J. Power Sources* **2016**, *306*, 413–423. [[CrossRef](#)]
21. Zhang, J.; Oko, D.N.; Garbarino, S.; Imbeault, R.; Chaker, M.; Tavares, A.C.; Guay, D.; Ma, D. Preparation of PtAu alloy colloids by laser ablation in solution and their characterization. *J. Phys. Chem. C* **2012**, *116*, 13413–13420. [[CrossRef](#)]
22. Marzun, G.; Levis, A.; Mackert, V.; Kallio, T.; Barcikowski, S.; Wagener, P. Laser synthesis, structure and chemical properties of colloidal nickel-molybdenum nanoparticles for the substitution of noble metals in heterogeneous catalysis. *J. Colloid Interface Sci.* **2016**. [[CrossRef](#)] [[PubMed](#)]
23. Neumeister, A.; Jakobi, J.; Rehbock, C.; Moysig, J.; Barcikowski, S. Monophasic ligand-free alloy nanoparticle synthesis determinants during pulsed laser ablation of bulk alloy and consolidated microparticles in water. *Phys. Chem. Chem. Phys.* **2014**, *16*, 23671–23678. [[CrossRef](#)] [[PubMed](#)]
24. Stelzig, S.H.; Menneking, C.; Hoffmann, M.S.; Eisele, K.; Barcikowski, S.; Klapper, M.; Müllen, K. Compatibilization of laser generated antibacterial Ag- and Cu-nanoparticles for perfluorinated implant materials. *Eur. Polym. J.* **2011**, *47*, 662–667. [[CrossRef](#)]
25. Zhang, D.; Gökce, B. Perspective of laser-prototyping nanoparticle-polymer composites. *Appl. Surf. Sci.* **2017**, *392*, 991–1003. [[CrossRef](#)]
26. Jakobi, J.; Petersen, S.; Menéndez-Manjón, A.; Wagener, P.; Barcikowski, S. Magnetic alloy nanoparticles from laser ablation in cyclopentanone and their embedding into a photoresist. *Langmuir* **2010**, *26*, 6892–6897. [[CrossRef](#)]
27. Menéndez-Manjón, A.; Schwenke, A.; Steinke, T.; Meyer, M.; Giese, U.; Wagener, P.; Barcikowski, S. Ligand-free gold-silver nanoparticle alloy polymer composites generated by picosecond laser ablation in liquid monomer. *Appl. Phys. A Mater. Sci. Process* **2013**, *110*, 343–350. [[CrossRef](#)]
28. Lau, M.; Waag, F.; Barcikowski, S. Direct Integration of Laser-Generated Nanoparticles into Transparent Nail Polish: The Plasmonic “goldfinger”. *Ind. Eng. Chem. Res.* **2017**, *56*, 3291–3296. [[CrossRef](#)]
29. Amans, D.; Malaterre, C.; Diouf, M.; Mancini, C.; Chaput, F.; Ledoux, G.; Breton, G.; Guillin, Y.; Dujardin, C.; Masenelli-Varlot, K.; et al. Synthesis of Oxide Nanoparticles by Pulsed Laser Ablation in Liquids Containing a Complexing Molecule: Impact on Size Distributions and Prepared Phases. *J. Phys. Chem. C* **2011**, *115*, 5131–5139. [[CrossRef](#)]
30. Schmitz, T.; Wiedwald, U.; Dubs, C.; Gökce, B. Ultrasmall Yttrium Iron Garnet Nanoparticles with High Coercivity at Low Temperature Synthesized by Laser Ablation and Fragmentation of Pressed Powders. *ChemPhysChem* **2017**, *18*, 1125–1132. [[CrossRef](#)]
31. Chemin, A.; Lam, J.; Laurens, G.; Trichard, F.; Motto-Ros, V.; Ledoux, G.; Jarý, V.; Laguta, V.; Nikl, M.; Dujardin, C.; et al. Doping nanoparticles using pulsed laser ablation in a liquid containing the doping agent. *Nanoscale Adv.* **2019**. [[CrossRef](#)]

32. Wang, H.; Odawara, O.; Wada, H. Facile and Chemically Pure Preparation of YVO₄: Eu³⁺ + Colloid with Novel Nanostructure via Laser Ablation in Water. *Sci. Rep.* **2016**, *6*. [[CrossRef](#)]
33. Adam, J.D.; Davis, L.E.; Dionne, G.F.; Schloemann, E.F.; Stitzer, S.N. Ferrite devices and materials. *IEEE Trans. Microw. Theory Tech.* **2002**, *50*, 721–737. [[CrossRef](#)]
34. Fu, H.P.; Hong, R.Y.; Wu, Y.J.; Di, G.Q.; Xu, B.; Zheng, Y.; Wei, D.G. Preparation and Faraday rotation of Bi-YIG/PMMA nanocomposite. *J. Magn. Magn. Mater.* **2008**, *320*, 2584–2590. [[CrossRef](#)]
35. Kim, T.Y.; Yamazaki, Y.; Hirano, T. Magneto-optical properties of Bi-YIG nanoparticle with polymethacrylate matrix materials. *Phys. Status Solidi Basic Res.* **2004**, *241*, 1601–1604. [[CrossRef](#)]
36. Kucera, M.; Bok, J.; Nitsch, K. Faraday rotation and MCD in Ce doped yig. *Solid State Commun.* **1989**, *69*, 1117–1121. [[CrossRef](#)]
37. Serga, A.A.; Chumak, A.V.; Hillebrands, B. YIG magnonics. *J. Phys. D Appl. Phys.* **2010**, *43*, 264002. [[CrossRef](#)]
38. Doñate-Buendía, C.; Frömel, F.; Wilms, M.B.; Streubel, R.; Tenkamp, J.; Hupfeld, T.; Nachev, M.; Gökce, E.; Weisheit, A.; Barcikowski, S.; et al. Oxide dispersion-strengthened alloys generated by laser metal deposition of laser-generated nanoparticle-metal powder composites. *Mater. Des.* **2018**, *154*, 360–369. [[CrossRef](#)]
39. Shen, H.; Xu, J.; Wu, A.; Zhao, J.; Shi, M. Magnetic and thermal properties of perovskite YFeO₃ single crystals. *Mater. Sci. Eng. B Solid-State Mater. Adv. Technol.* **2009**, *157*, 77–80. [[CrossRef](#)]
40. Rajendran, M.; Deka, S.; Joy, P.A.; Bhattacharya, A.K. Size-dependent magnetic properties of nanocrystalline yttrium iron garnet powders. *J. Magn. Magn. Mater.* **2006**, *301*, 212–219. [[CrossRef](#)]
41. Barcikowski, S.; Amendola, V.; Marzun, G.; Rehbock, C.; Reichenberger, S.; Zhang, D.; Gökce, B. *Handbook of Laser Synthesis of Colloids*; DueEPublico: Duisburg-Essen, Germany, 2016. [[CrossRef](#)]
42. Letzel, A.; Reich, S.; Rolo, T.D.S.; Kanitz, A.; Hoppius, J.; Rack, A.; Olbinado, M.P.; Ostendorf, A.; Gökce, B.; Plech, A.; et al. Time and Mechanism of Nanoparticle Functionalization by Macromolecular Ligands during Pulsed Laser Ablation in Liquids. *Langmuir* **2019**, *35*, 3038–3047. [[CrossRef](#)] [[PubMed](#)]
43. Letzel, A.; Gökce, B.; Wagener, P.; Ibrahimkuty, S.; Menzel, A.; Plech, A.; Barcikowski, S. Size Quenching during Laser Synthesis of Colloids Happens Already in the Vapor Phase of the Cavitation Bubble. *J. Phys. Chem. C* **2017**, *121*, 5356–5365. [[CrossRef](#)]
44. Merk, V.; Rehbock, C.; Becker, F.; Hagemann, U.; Nienhaus, H.; Barcikowski, S. In situ non-DLVO stabilization of surfactant-free, plasmonic gold nanoparticles: Effect of Hofmeister’s anions. *Langmuir* **2014**, *30*, 4213–4222. [[CrossRef](#)] [[PubMed](#)]
45. Lau, M.; Barcikowski, S. Quantification of mass-specific laser energy input converted into particle properties during picosecond pulsed laser fragmentation of zinc oxide and boron carbide in liquids. *Appl. Surf. Sci.* **2015**, *348*, 22–29. [[CrossRef](#)]
46. Jendrzzej, S.; Gökce, B.; Barcikowski, S. Colloidal Stability of Metal Nanoparticles in Engine Oil under Thermal and Mechanical Load. *Chem. Eng. Technol.* **2017**, *40*, 1569–1576. [[CrossRef](#)]
47. Gökce, B.; Zand, D.D.V.; Menéndez-Manjón, A.; Barcikowski, S. Ripening kinetics of laser-generated plasmonic nanoparticles in different solvents. *Chem. Phys. Lett.* **2015**, *626*, 96–101. [[CrossRef](#)]
48. Waag, F.; Gökce, B.; Kalapu, C.; Bendt, G.; Salamon, S.; Landers, J.; Hagemann, U.; Heidelmann, M.; Schulz, S.; Wende, H.; et al. Adjusting the catalytic properties of cobalt ferrite nanoparticles by pulsed laser fragmentation in water with defined energy dose. *Sci. Rep.* **2017**, *7*, 1–13. [[CrossRef](#)]
49. Sakaki, S.; Saitow, K.I.; Sakamoto, M.; Wada, H.; Swiatkowska-Warkocka, Z.; Ishikawa, Y.; Koshizaki, N. Comparison of picosecond and nanosecond lasers for the synthesis of TiN sub-micrometer spherical particles by pulsed laser melting in liquid. *Appl. Phys. Express* **2018**, *11*, 4–8. [[CrossRef](#)]
50. Sakaki, S.; Ishikawa, Y.; Koshizaki, N. Heating process control of pulsed-laser melting in liquid via a burst-mode laser. *Appl. Phys. Express* **2019**, *12*. [[CrossRef](#)]
51. Zhang, G.B.; Lau, D.; Lu, M.; Barcikowski, S.; Gökce, B. Germanium Sub-Microspheres Synthesized by Picosecond Pulsed Laser Melting in Liquids: Educt Size Effects. *Sci. Rep.* **2017**, *7*, 40355. [[CrossRef](#)]
52. Widatallah, H.M.; Johnson, C.; Al-Harhi, S.H.; Gismelseed, A.M.; Al-Rawas, A.D.; Stewart, S.J.; Elzain, M.E.; Al-Omari, I.A.; Yousif, A.A. A structural and mössbauer study of Y₃Fe₅O₁₂ nanoparticles prepared with high energy ball milling and subsequent sintering. *Hyperfine Interact.* **2008**, *183*, 87–92. [[CrossRef](#)]
53. Niyafar, M.; Mohammadpour, H.; Dorafshani, M.; Hasanpour, A. Size dependence of non-magnetic thickness in YIG nanoparticles. *J. Magn. Magn. Mater.* **2016**, *409*, 104–110. [[CrossRef](#)]
54. Sharma, V.; Saha, J.; Patnaik, S.; Kuanr, B.K. Synthesis and characterization of yttrium iron garnet (YIG) nanoparticles—Microwave material. *AIP Adv.* **2017**, *7*. [[CrossRef](#)]

55. Choi, J.; Cha, J.; Lee, J.K. Synthesis of various magnetite nanoparticles through simple phase transformation and their shape-dependent magnetic properties. *RSC Adv.* **2013**, *3*, 8365–8371. [[CrossRef](#)]
56. Nagrare, B.S.; Kekade, S.S.; Thombare, B.; Reddy, R.V.; Patil, S.I. Hyperfine interaction, Raman and magnetic study of YFeO₃ nanocrystals. *Solid State Commun.* **2018**, *280*, 32–38. [[CrossRef](#)]
57. Popkov, V.I.; Almjashaeva, O.V.; Semenova, A.S.; Kellerman, D.G.; Nevedomskiy, V.N.; Gusarov, V.V. Magnetic properties of YFeO₃ nanocrystals obtained by different soft-chemical methods. *J. Mater. Sci. Mater. Electron.* **2017**, *28*, 7163–7170. [[CrossRef](#)]
58. Jendrzey, S.; Gökce, B.; Amendola, V.; Barcikowski, S. Barrierless growth of precursor-free, ultrafast laser-fragmented noble metal nanoparticles by colloidal atom clusters—A kinetic in situ study. *J. Colloid Interface Sci.* **2016**, *463*, 299–307. [[CrossRef](#)]
59. Siebeneicher, S.; Waag, F.; Castillo, M.E.; Shvartsman, V.V.; Lupascu, D.C.; Gökce, B. Laser fragmentation synthesis of colloidal bismuth ferrite particles. *Nanomaterials* **2020**, *10*, 359. [[CrossRef](#)]

Sample Availability: Samples of the compounds are not available from the authors.



© 2020 by the authors. Licensee MDPI, Basel, Switzerland. This article is an open access article distributed under the terms and conditions of the Creative Commons Attribution (CC BY) license (<http://creativecommons.org/licenses/by/4.0/>).

5 A colloidal additiviation process for polymer powders

Surface-functionalization by colloidal additiviation with surfactant-free laser-generated metal nanoparticles is an established approach for inorganic supports (Chapter 2.5) and also for oxide particles on steel powder for AM [157,267]. Independent of the material combinations, understanding the supporting kinetics is a key requirement for controlling the deposition yield and the dispersion quality, which assures a uniform surface coverage of the nanoparticles [24]. In addition, understanding the support kinetics also enables the development of rules for scale-up.

The following chapter verifies the hypothesis that the colloidal additiviation technique is not limited to inorganic supports but can be transferred to polymer micropowders (organic support), which enables the development of nano-functionalized feedstock materials with outstanding nanoparticle dispersion that are ready for PBF-LB. A proof of concept is shown for the model system PA12-silver in Chapter 5.1 [268]. As silver nanoparticles show a surface plasmon resonance (SPR) in the visible range, which is highly dependent on their size and aggregation state [269], optical properties (SPR intensity and wavelength) are an ideal read-out for particle dispersion and potential aggregation. The nanoparticle deposition process and the surface specific nanoparticle dose during colloidal additiviation of PA12 powder with laser-generated nanoparticles are investigated in Chapter 5.2 , with the objective of achieving high quality dispersion and good yield of colloidal additiviation [270]. This was done without the excessive use of stabilizing agents, which could possibly prevent the supporting process or negatively influence the PBF-LB processing behavior of the functionalized powder. From the state of the art, it was expected that the zeta potential should affect the dispersion quality and the deposition yield and time constant. Therefore, the importance of understanding the interaction between the nanoparticle and a polymer surface, as well as the possibilities to influence this interaction, are highlighted in this

chapter. Results on nano-analytical quantification of the particle dispersion on the polymer surfaces before PBF-LB are shown, with the objective of developing a basic understanding of determinants for colloidal additiviation of polymer powders. Furthermore, this chapter deals with an investigation of the nanoparticle volume dispersion in the polymer matrix after PBF-LB and an analysis of the dispersion quality along the process chain from LAL to PBF-LB, analyzed using SEM and TEM imaging, as well as characterizing the optical properties after each process step.

In order to generate large amounts of functionalized powder for PBF-LB experiments ($\gg 1$ kg per build job), an upscaling of the entire additiviation process chain is required. Therefore, this chapter will not only introduce the colloidal additiviation process (Chapter 5.1 and 5.2) [268,270], but will also show the potential and challenges for upscaling toward kg/h in a continuous process (Chapter 5.3) [271].

5.1 Proof of concept

A new approach to coat PA12 powders with laser-generated nanoparticles for selective laser sintering

Reprinted from Procedia CIRP 74 (2018) 244–248 under CC BY-NC-ND

Highlights:

- Proof of concept for colloidal additivition of a polymer powder based on laser-generated silver nanoparticles
- Introduction of characterization methods for dispersion analysis demonstrated for the model system PA12-silver
- An outstanding dispersion and homogeneous decoration of the polymer particle surface with nanoparticles can be achieved by colloidal additivition
- First indication that the high nanoparticle dispersion is conserved during PBF-LB

10th CIRP Conference on Photonic Technologies [LANE 2018]

A new approach to coat PA12 powders with laser-generated nanoparticles for selective laser sintering

T. Hupfeld^a, T. Laumer^b, T. Stichel^b, T. Schuffenhauer^b, J. Heberle^c,
M. Schmidt^{b,c}, S. Barcikowski^a, B. Gökce^{a*}

^aTechnical Chemistry I and Center for Nanointegration Duisburg-Essen (CENIDE), University of Duisburg-Essen, Universitätsstraße 7, 45141 Essen, Germany

^bBayerisches Laserzentrum GmbH (blz), Konrad-Zuse-Straße 2-6, 91052 Erlangen, Germany

^cInstitute of Photonic Technologies (LPT), Friedrich-Alexander-Universität Erlangen-Nürnberg, Konrad-Zuse-Str. 3-5, 91052, Germany

* Corresponding author. Tel.: +49-201-183-3146; fax: +49-201-183-3049. E-mail address: bilal.goekce@uni-due.de

Abstract

The modification of selective laser sintering (SLS) powder materials by nanoadditives offers the possibility to adapt the powder properties to the laser sintering process or the resulting part properties. To avoid agglomeration of the nanofiller, a new approach in which surfactant-free laser-generated colloidal nanoparticles are adsorbed onto the polymer surface directly in an aqueous solution is demonstrated. Based on this novel approach, polyamide 12 (PA12) powders are decorated with metal and oxide nanoparticles and processed via SLS. Electron microscopy and confocal laser scanning imaging are utilized to analyze the dispersion of the filler.

© 2018 The Authors. Published by Elsevier Ltd. This is an open access article under the CC BY-NC-ND license

(<https://creativecommons.org/licenses/by-nc-nd/4.0/>)

Peer-review under responsibility of the Bayerisches Laserzentrum GmbH.

Keywords: polymer powders; selective laser sintering; nanoparticles; laser additive manufacturing; pulsed laser ablation in liquids

1. Introduction

Polymer powders for laser additive manufacturing (LAM) have become increasingly important even for small-scale industrial fabrication [1]. However, the availability of powder materials for selective laser sintering (SLS) is extremely limited [2]. Since engineering measures cannot fully compensate the difficulties in powder quality [3, 4], there is a significant need for material development to create new powders for SLS production processes [5].

A common route to modify SLS-powder properties is the introduction of additives such as carbon black [6], titania or silica [7] with mass fractions of up to 5 wt%. Inorganic nanoparticles such as carbon nanotubes [8] and ceramics [9] provide distinct advantages for improved SLS processing through significantly affecting sintering characteristics and final part properties. In this way, uniformly dispersed fillers can influence the melting and resolidification behavior [10] and cause the melting enthalpy, the relative crystalline content

and the crystallization temperature to increase. Typically, these improvements are caused by the heterogeneous nucleation effect of the filler [11]. Furthermore, a distinct coarse spherulitic morphology with a lower degree of crystallization develops at low cooling rates [12]. Increased thermal nucleation and hindered crystal growth due to a higher number of nuclei in combination with higher cooling rates result in a finer crystal structure [10, 13]. The resulting part properties (e.g., mechanical and tribological properties) are strongly related to the crystallinity and microstructure formed by the polymer molecules [14]. Thus, adapting crystallization behavior through nanoadditives directly affects the powder's SLS processability and thus the properties of the final component.

To include nanoparticles as additives, several methods such as melt compounding [15], milling [16] or ex situ dispersion into polymer solution [17] are reported in the literature. Agglomeration of the filler during the additivization process is a typical problem occurring in most of these methods. A high

degree of agglomeration, in turn, inevitably leads to higher demand for filler to achieve a high surface area of the nanoparticles accessible by the polymer chains and to avoid disadvantages in the processability (by light scattering and inhomogeneous particle quality).

It is evident that increasing the dispersion of the nanoparticles, decreasing the mass fraction of the filler and optimizing the interfacial bonding between polymer and filler [18, 20, 21] is essential. It is also important that filling factors <0.1 wt% are required for the SLS process parameters to remain unchanged [18]. Even at such low filling factors a significant impact of the nanofiller on the mechanical properties of the final part can be observed [19]. Nevertheless, most of today's approaches for additivation show high filling rates and lacking dispersion. Furthermore, the determinants of the degree of nanoparticle dispersion and the surface-specific dose have only rarely been studied in SLS literature.

An alternative way to achieve a homogeneous distribution of nanoparticles on microparticle surfaces is the use of ligand-free, laser-generated nanoparticles directly in an aqueous solution. To generate ligand-free nanoparticles for the supporting on microparticles, laser synthesis and processing of nanoparticles in liquids (LSPC) was established in recent years [22, 23, 24]. LSPC is an economically feasible [25] and scalable method that can achieve nanoparticle productivities of up to several grams per hour, equivalent to 20 l of nanoparticle colloid per hour [26, 27]. Because of its applicability to a variety of materials [28, 29, 30] and fluids [31] laser-generated nanoparticles can easily be combined with different routes to fabricate nanocomposites [32, 33, 34]. The approach of decorating microparticles with colloidal nanoparticles was already established for the formation of heterogeneous catalysts by adsorption of the nanoparticles on ceramic supports such as TiO₂ [23, 24] or for the production of LAM-processable metal powders [35, 36]. This route includes the pH-controlled, colloidal mixing of ligand-free nanoparticles with a suspension of the microparticle support. Note that the yield of this supporting procedure is almost 100% and that the particle size does not change during deposition (no size-selectivity). After the supporting, the suspension is filtered and dried. By this means a homogeneous distribution and high dispersion of nanoparticles on the surface of the support is obtained [23].

The presented route for generating composite materials (supported particles) is not limited to inorganic supports and can be extended to polymer powders to homogeneously coat the powder surface with nanoparticles. In this study, a new approach to decorate PA12 microparticles with inorganic nanoparticles generated by LSPC, directly in an aqueous solution to create new nanocomposite powders with low filling degrees and high dispersion ready to use in SLS is demonstrated.

2. Materials and Methods

Fig. 1a schematically illustrates the route for decorating polymer microparticles with laser-generated colloidal nanoparticles to obtain composite microparticle powders. LSPC was performed with an 8 ns Nd-YAG-laser (1064 nm)

operating at a laser power of 110 W and a repetition rate of 5 kHz. The beam was focused by an f-theta lens on the silver target, which was mounted in a flow chamber setup, resulting in a nanoparticle productivity of approximately 1.1 g/h. After laser ablation, PA12 (EOS PA2200) microparticles were admixed to the colloid, leading to a filling factor of 0.1 wt%. During stirring of the suspension at a pH of 3, adsorption (supporting) of the nanoparticles on the polymer surface takes place within a few seconds, which is indicated by an increasing transparency of the suspension. Filtrating the suspension after supporting leads to a completely colorless filtrate which indicates that the yield of the supporting process is almost 100%. As a reference, PA12 was additivated with 0.1 wt% of a silver nanopowder in a conventional ball milling process. Additivation with iron oxide nanoparticles was performed with commercially available iron oxide nanoparticles (Sigma Aldrich, particle size < 50 nm) and additivation with yttrium oxide nanoparticles was performed with commercial available yttrium oxide (Alfa Aesar, particle size 25-50 nm) which were dispersed in water by ultrasonication. After colloidal supporting, all nanocomposite powders were dried at 50° C and atmospheric pressure for two days to ensure a complete removal of water. Before processing by SLS the powders were sifted with a 100 µm sieve. Rectangular multi-layer specimens with a size of 20 mm x 20 mm x 1 mm were built with an EOSint P385 SLS machine. The parameters used for the melting process of the modified powders were the same as for the conventional PA12 material (build-temperature = 170 - 175 °C, 25 W laser power, 200 mm/s scanning speed, Hatch distance of 0.3 mm). To ensure the formation of homogeneous powder layers during recoating, the layer thickness was set to 0.3 mm.

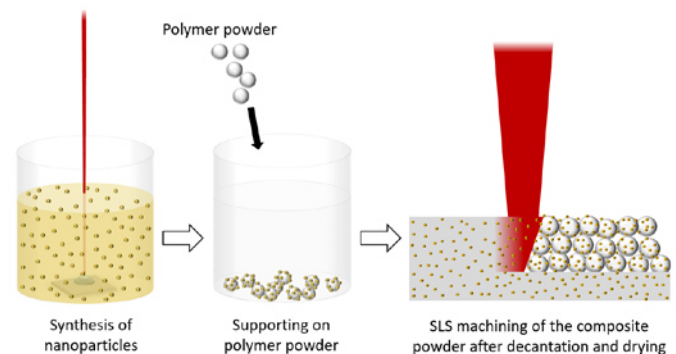


Fig. 1: (a) Schematic illustration of the process steps to support silver nanoparticles on polymer powders, from left to right: Laser synthesis of silver nanoparticles, mixing of polymer particles with the colloid and SLS machining of the composite micropowder.

After processing, cross sections of the specimens were prepared to analyze the dispersion quality of the admixed nanoparticles after the manufacturing process by transmission electron microscopy (TEM). Laser scanning confocal microscopy was used as a complementary method to TEM to characterize dispersion of inorganic nanoparticles in the polymer materials [37]. Confocal laser dark-field scattering can be used to create 3D images of macroscopic polymer parts [37] and even to extract quantitative information [38] with far larger imaging area and better statistics than TEM.

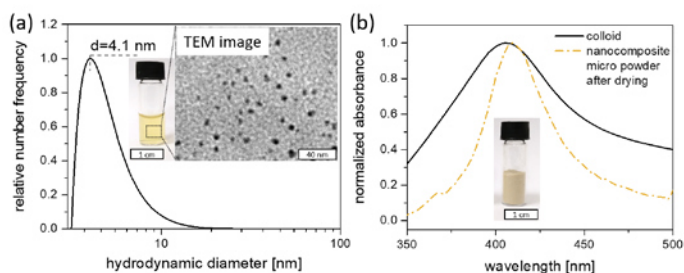


Fig. 2: (a) Size distribution and TEM image of silver nanoparticles generated by LSPC and (b) UV-Vis absorbance spectrum of the colloid and the PA12-Ag-composite.

3. Results and discussion

3.1. Nanoparticle-modified polymer micropowders

Fig. 2b shows a picture of a PA12 powder decorated with 0.1 wt% of silver nanoparticles. The laser-synthesized silver nanoparticles have a monomodal size distribution with a mean diameter of 4.1 nm (Fig. 2a) and show the characteristic plasmon resonance peak (at approx. 405 nm) in the UV-Vis spectrum (Fig. 2b). The support on the polymer powder could be attributed to a pH-dependent electrostatic attraction between the polymer microparticles and the nanoparticles, similar to supporting metal nanoparticles on oxide powders [23] or oxide nanoparticles on metal powders [36]. After drying and sieving, the nanocomposite powder shows the characteristic yellow color of silver nanoparticles. As evident in the image shown in Fig. 2b the sharp surface plasmon resonance peak is conserved indicating that no significant agglomeration occurred during the drying process.

In Fig 3a,b scanning electron microscopy (SEM) images of polymer microparticles additivated with 0.1 wt% of silver are shown. While the SEM analysis of a composite powder obtained by ball milling shows strong agglomeration (Fig. 3a), colloiddally deposited nanoparticles lead to homogeneous distribution on the polymer particle surface (Fig. 3b) with significantly less agglomeration compared to ball milling. This is also confirmed by confocal laser scanning microscopy. The 2D scans in Fig. 3c,d were captured by irradiating the samples at 405 nm, close to the surface plasmon resonance (SPR) peak of silver (see Fig. 2b). For the ball-milled composite powder the scattering signal is much weaker compared to the powder obtained by colloiddal deposition. This can be explained by the higher degree of agglomeration which leads to the absence of surface plasmon resonance (absence of yellow color) and hence to less scattering at 405 nm.

To show the transferability of the presented approach to other nanoparticle materials, PA12 powder was further decorated with Fe_2O_3 nanoparticles (Fig. 4 (a)). The achieved mass fraction for iron oxide on PA12 ranges from 0.1 wt% to 1.0 wt%. Although partial agglomeration is evident (Fig. 4b), the general transferability of the additivation method is confirmed, and the nanoscale aggregates seem to be well dispersed on the surface of the polymer microparticle. Further optimization could be achieved by fine-tuning of the pH, which has been shown to enable better control over the supporting process [39].

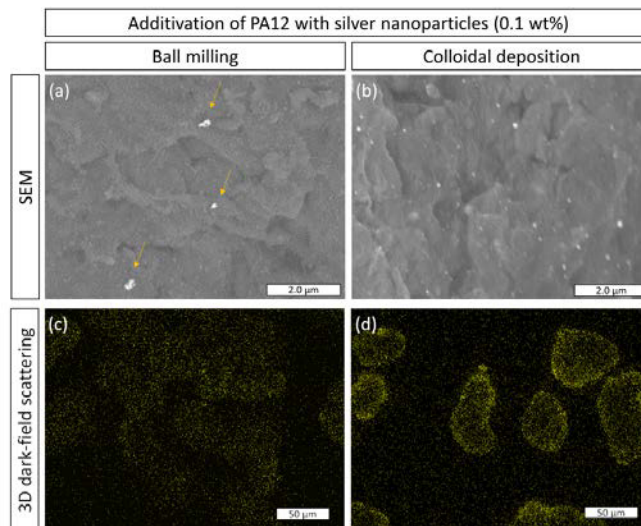


Fig. 3: SEM images (a,b) and laser confocal images (c,d) of Ag nanoparticle-decorated polymer particles. Left column shows composite powders obtained by ball milling of nanoparticles with the polymer powder while right column shows colloiddally deposited laser-generated nanoparticles

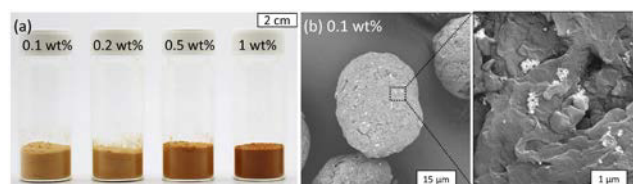


Fig. 4: (a) PA12 powders decorated with different mass fractions of iron oxide nanoparticles ranging from 0.1 to 1 wt% and (b) SEM images of the powder with 0.1 wt%.

3.2. SLS processability

In Fig. 5a the sintered part made from PA12, additivated with a mixture of 0.1 wt% of silver and 0.1 wt% Y_2O_3 is depicted. The plasmon resonance of the silver nanoparticles is conserved in the sintered part, indicating that the particles are mostly homogeneously dispersed in the polymer matrix of the macroscopic sintered part. Their dispersion into the polymer powder is confirmed by TEM images (Fig. 5b) which only show some agglomerates and clearly separated single particles below 50 nm. In Fig. 5c the respective 3D confocal laser scanning microscopy scan is shown. The nanoparticles did not significantly leave the polymer particle surface in the molten state before resolidification, resulting in a web-like macroscopic structure, which is formed by the surfaces of the former polymer microparticles. This has been previously observed by Bai et al. for PA12 decorated with carbon nanotubes [8]. The nanoparticles show a homogeneous particle distribution and only minor agglomeration. A better understanding of the particle supporting procedure and its material dependencies will make optimization feasible. In following studies, a DSC analysis of the micropowder after colloiddal deposition will be performed. Since the particles are very well dispersed, an impact on the resolidification behavior can be expected.

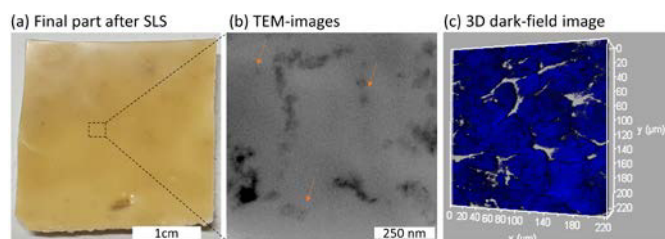


Fig. 5: (a) Picture of a PA12/Ag/Y₂O₃-nanocomposite after SLS machining, (b) TEM images of the part shown in (a). (c) Confocal laser scanning 3D dark-field scattering image of a PA12/Ag-nanocomposite, showing the distribution of the nanoparticles (blue) in the final part.

4. Conclusion

Even though nanoparticles are often used to adjust the properties of polymer powder materials used in SLS, a general understanding of nanoparticle material effects is still lacking. The presented route consisting of laser synthesis of metal and oxide nanoparticle and their colloidal deposition on polymer powders is a feasible way to fabricate SLS-processable composite powders and to understand the nanoparticle effect on the SLS processability. However, influences such as pH effects, nanoparticle material effects (different hydrophilicity of metals, oxides, and carbon) as well as nanoparticle dose considerations need more attention. For further works, it is necessary to analyze the influence of the size and the surface charge, the type and amount of nanoparticle material (metal, oxides, and carbon) as well as their degree of dispersion.

Acknowledgments

We acknowledge Anna Ziefuß from University of Duisburg-Essen for confocal imaging. We further thank the German Research Foundation (DFG) for the financial support of the SLS experiments which are part of the Collaborative Research Center 814 (CRC 814) – Additive Manufacturing, sub-project B6.

References

- [1] Pflöging, W.; Kohler, R.; Suedmeyer, I.; Rohde, M.: Laser micro and nano processing of metals, ceramics, and polymers, Springer Series in Materials Science, 161, 319 (2013)
- [2] Schmid, M.; Amado, A.; Wegener, K.: Materials perspective of polymers for additive manufacturing with selective laser sintering, *J. Mater. Res.*, 29, 1824 (2014)
- [3] Laumer, T.; Stichel, T.; Amend, P.; Roth, S.; Schmidt, M.: Analysis of the Influence of Different Flowability on Part Characteristics Regarding the Simultaneous Laser Beam Melting of Polymers. In: *Physics Procedia*, 83, 937–946 (2016)
- [4] Laumer, T.; Stichel, T.; Schmidt, M.: Optical analysis of polymer powder materials for selective laser sintering. In: *Journal of Polymer Testing*, 56, 207–213 (2016)
- [5] Gökce, B.; Barcikowski, S.; Behrens, P.; Fritsching, U.; Kelbassa, I.; Poprawe, R.; Esen, C.; Ostendorf, A.; Voit, B.: *Materials for Photonics*. In: *Laser+Photonics*, 6-10 (2016)
- [6] Kim, H. C.; Hahn, H. T.; Yang, Y. S.: Synthesis of PA12/functionalized GNP nanocomposite powders for the selective laser sintering process. *Journal of Composite Materials* 47, 4 (2012)
- [7] Lexow, M. M. and Dietmar Drummer: New Materials for SLS: The Use of Antistatic and Flow Agents. *Journal of Powder Technology*, Volume 2016, 9 pages (2016)
- [8] Bai, J.; Goodridge, R.D.; Hague, R.J.M.; Song, M.; Murakami, H.: Nanostructural characterization of carbon nanotubes in laser-sintered polyamide 12 by 3D-TEM. *J. Mater. Res.*, 29, 1817–1823 (2014)
- [9] Qi, F.; Chen, N.; Wang, Q.: Preparation of PA11/BaTiO₃ nanocomposite powders with improved processability, dielectric and piezoelectric properties for use in selective laser sintering. *Materials & Design*, 131, 5, 135-143 (2017)
- [10] Piorkowska, E. and Rutledge, G. C.: *Handbook of Polymer Crystallization*. John Wiley & Sons, New Jersey (2013)
- [11] Wang, Y.; Shi, Y.; Huang, S.: Selective laser sintering of polyamide-rectorite composite *Proceedings of the Institution of Mechanical Engineers, Part L: Journal of Materials: Design and Applications* 219, 1, 11–15 (2005)
- [12] Mollova, A.; Androsch, R.; Mileva, D.; Schick, C.; Benhamida, A.: Effect of supercooling on crystallization of polyamide 11. *Macromolecules*, 46(3), 828 (2013)
- [13] Jungmeier, A., Ehrenstein, G. W., & Drummer, D.: New aspects of process induced properties of microinjection moulded parts. *Plastics, Rubber and Composites*, 39(7), 308-314 (2010)
- [14] Toda, A.; René Androsch, R.; Schick, C.: Insights into polymer crystallization and melting from fast scanning chip calorimetry. *Polymer*, 91, 239-263 (2016)
- [15] Zheng, W.; Lu, X.; Wong, S.C.: Electrical and mechanical properties of expanded graphite-reinforced high-density polyethylene. *J Appl Polym Sci*, 91, 5, 2781–2788 (2004)
- [16] Goodridge, R.D.; Shofner, M.L.; Hague, R.J.M.; McClelland, M.; Schlea, M.R.; Johnson, R.B.; Tuck, C.J.: Processing of a Polyamide-12/carbon nanofibre composite by laser sintering, *Polymer Testing*, 30, 1, 94-100 (2011)
- [17] Wei S.Y., Patil R.H., Sun L.Y., et al.: Ex-situ solvent-assisted prepared magnetic poly(propylene) nanocomposites filled with Fe@FeO nanoparticles. *Macromol Mater Eng.*, 296, 9, 850–857 (2011)
- [18] Kim, H.C.; Hahn, H.T.; Yang, Y.S.: Synthesis of PA12/functionalized GNP nanocomposite powders for the selective laser sintering process *Journal of Composite Materials*, 47, 4, 501–509 (2012)
- [19] Bai, J.; Goodridge, R.D.; Hague, R.J.M.; Song, M.: Improving the Mechanical Properties of Laser-Sintered Polyamide 12 Through Incorporation of Carbon Nanotubes. *Polym. Eng. Sci.*, 53, 1937–1946, (2013)
- [20] Athreya, S.R.; Kalaitzidou, K.; Das, S.: Processing and characterization of a carbon black-filled electrically conductive Nylon-12 nanocomposite produced by selective laser sintering. *Materials Science and Engineering: A*. 527, 10, 2637-2642 (2010)
- [21] Wang, D.; Song, C.; Gu, G.; Hu, Z.: Preparation of Fe₂O₃ microcages from the core/shell structures. *Materials Letters*, 59, 7, 782-785 (2005)
- [22] Zhang, D.; Gökce, B.; Barcikowski, S.: Laser Synthesis and Processing of Colloids: Fundamentals and Applications. In: *Chemical Reviews* 117, 3990-4103 (2017)
- [23] Marzun, G.; Streich, C.; Jendrzzej, S.; Barcikowski, S.; Wagener, P.: Adsorption of Colloidal Platinum Nanoparticles to Supports: Charge Transfer and Effects of Electrostatic and Steric Interactions. In: *Langmuir* 30, 40, 11928-11939 (2014)
- [24] Wagener, P.; Schwenke, A.; Barcikowski, S.: How citrate ligands affect nanoparticle adsorption to microparticle supports. In: *Langmuir* 28, 6132–6140 (2012)
- [25] Jendrzzej, S.; Goekce, B.; Epple, M.; Barcikowski, S.: How Size Determines the Value of Gold - Economic Aspects of Wet Chemical and Laser-Based Metal Colloid Synthesis. In: *Chemical Physics and Physical Chemistry*, 18, 9, 1012-1019 (2017)
- [26] Streubel, R.; Barcikowski, S.; Gökce, B.: Continuous multigram nanoparticle synthesis by high-power, high-repetition-rate ultrafast laser ablation in liquids. *Optics Letters*, 41, 7, 1486 (2016)
- [27] Streubel, R.; Bendt, G.; Gökce, B.: Pilot-Scale Synthesis of Metal Nanoparticles by High-Speed Pulsed Laser Ablation in Liquids. *Nanotechnology* 27, 205602 (2016)
- [28] Gemini, L.; Schmitz, T.; Kling, R.; Barcikowski, S.; Gökce, B.: Upconversion nanoparticles synthesized by ultra-short pulsed laser

- ablation in liquid: effect of stabilizing environment. *ChemPhysChem*, 18, 1210 (2017)
- [29] Schmitz, T.; Wiedwald, U.; Dubs, C.; Gökce, B.: Ultrasmall Yttrium Iron Garnet Nanoparticles with High Coercivity at Low Temperature Synthesized by Laser Ablation and Fragmentation of Pressed Powders, *ChemPhysChem*, 18, 1125 (2017)
- [30] Zhang, D.; Ma, Z.; Spasova, M.; Yelsukova, A. E.; Lu, S.; Farle, M.; Wiedwald, U.; Gökce, B.: Formation Mechanism of Laser-Synthesized Iron-Manganese Alloy Nanoparticles, Manganese Oxide Nanosheets and Nanofibers, *Particle & Particle Systems Characterization*, 34, 1600225 (2017)
- [31] Kalus, M. R.; Bärsch, N.; Streubel, R.; Gökce, E.; Barcikowski, S.; Gökce, B.: How persistent microbubbles shield nanoparticle productivity in laser synthesis of colloids - quantification of their volume, dwell dynamics, and gas composition. *Physical Chemistry Chemical Physics* 19, 7112 (2017)
- [32] Zhang, D. and Gökce, B.: Perspective of laser-prototyping nanoparticle-polymer composites. *Appl. Surf. Sci.* 392, 991–1003 (2017)
- [33] Maurer, E.; Barcikowski, S.; Gökce, B.: Process Chain for the Fabrication of Nanoparticle Polymer Composites by Laser Ablation Synthesis. *Chem. Eng. Technol.* 40, 1535–1543 (2017)
- [34] Barcikowski, S., Baranowski, T., Durmus, Y., Wiedwald, U., Gökce, B.: Solid solution magnetic FeNi nanostrand-polymer composites by connecting-coarsening assembly. *J. Mater. Chem. C* 3, 10699–10704 (2015)
- [35] Streubel, R.; Wilms, M. B.; Doñate-Buendía, C.; Weisheit, A.; Barcikowski, S.; Schleifenbaum, J. H.; Gökce, B.: Depositing laser-generated nanoparticles on powders for additive manufacturing of oxide dispersed strengthened alloy parts via laser metal deposition. *J. Journal of Applied Physics* 57, 040310 (2018)
- [36] Doñate-Buendía, C.; Frömel, F.; Wilms, M.B.; Streubel, R.; Tenkamp, J.; Hupfeld, T.; Nachev, M.; Gökce, E.; Weisheit, A.; Barcikowski, S.; Walther, F.; Schleifenbaum, J.H.; Gökce, B.: Oxide dispersion-strengthened alloys generated by laser metal deposition of laser-generated nanoparticle-metal powder composites. *Materials & Design* (2018), doi: 10.1016/j.matdes.2018.05.044
- [37] Blaeser, A.; Million, N.; Duarte Campos, D.F.; Gamrad, L.; Köpf, M.; Rehbock, C.; Nachev, M.; Sures, B.; Barcikowski, S.; Fischer, H.: Laser-based in situ embedding of metal nanoparticles into bioextruded alginate hydrogel tubes enhances human endothelial cell adhesion. *Nano Research*, 9, 11, 3407–3427 (2016)
- [38] Klein, S.; Petersen, S.; Taylor, U.; Rath, D.; Barcikowski, S.: J. of Biomedical Optics, Quantitative visualization of colloidal and intracellular gold nanoparticles by confocal microscopy, 15, 3, 036015 (2010)
- [39] Barcikowski, S.; Wagener, P.; Schwenke, A.: Process for producing a micro-nano combined effective system. (2018). EP2651593B1, 31.01.2018 (registration: 17th December 2010, No. 102010063342.9)

5.2 Identification of process determinants

How colloidal surface additivition of polyamide 12 powders with well-dispersed silver nanoparticles influences the crystallization already at low 0.01 vol%

Reprinted from Additive Manufacturing 36, 101419 (2020) with the permission of Elsevier

Highlights:

- Detailed investigation and analysis of process determinants for colloidal additivition reveals that nanoparticle adsorption on the polymer surface is driven by pH-dependent repulsive forces
- Definition of the process window for colloidal additivition (particle concentrations, pH, mixing time)
- Introduction of the surface specific dose (surf%) as a meaningful descriptor for nano-additivition
- Silver nanoparticle additivition influences crystallization properties of PA12 at high cooling rates even at 0.01 vol%

Appendix:

- Supporting information (A6)



How colloidal surface additivation of polyamide 12 powders with well-dispersed silver nanoparticles influences the crystallization already at low 0.01 vol%



Tim Hupfeld^a, Alexander Sommereyns^{b,c}, Thomas Schuffenhauer^{c,e}, Evgeny Zhuravlev^d, Moritz Krebs^a, Stan Gann^a, Olaf Keßler^d, Michael Schmidt^{b,c}, Bilal Gökce^{a,*}, Stephan Barcikowski^a

^a Technical Chemistry I and Center for Nanointegration Duisburg-Essen (CENIDE), University of Duisburg-Essen, Universitätsstrasse 7, 45141, Essen, Germany

^b Institute of Photonic Technologies (LPT), Friedrich-Alexander Universität Erlangen-Nürnberg, Konrad-Zuse-Str.3-5, 91052, Erlangen, Germany

^c Erlangen Graduate School in Advanced Optical Technologies (SAOT), Friedrich-Alexander Universität Erlangen-Nürnberg, Germany

^d Chair of Materials Science, University of Rostock, 18051, Rostock, Germany

^e Bayerisches Laserzentrum GmbH (blz), Konrad-Zuse-Straße 2-6, 91052 Erlangen, Germany

ARTICLE INFO

Keywords:

Nanocomposite
Surface functionalization
Electrostatic deposition
Laser ablation in liquid (LAL)
Laser powder bed fusion (PBF-LB)
Selective laser sintering (SLS)
Fast scanning calorimetry (FSC)

ABSTRACT

As Additive Manufacturing (AM) is fast-growing, properties adaption of feedstock materials for AM is becoming more and more relevant due to high quality standards in industrial applications. Compared to traditional manufacturing techniques like injection molding, laser powder bed fusion (PBF-LB) of polymers has a very limited variety of processable materials, which is a major obstacle for future growth. Nanocomposites are an established material class for addressing the limitations in PBF-LB but often show poor dispersion of the nanomaterial in/on the polymer powder. Especially in the context of plasmonic nanomaterials and composites, where the state of aggregation considerably influences the optical properties, dispersion plays an important role. Our study presents a deeper understanding of the colloidal surface additivation of polyamide 12 (PA12) powders with laser-generated plasmonic silver nanoparticles, leading to high dispersion of the nanoparticles on the micropowder surface with good reproducibility. The additivation is ruled by colloidal stability and control of electrostatic forces between particles and resulted in powders that could successfully be processed on a PBF-LB machine to generate plasmonic-functionalized parts. Finally, we introduce the surface specific nanoparticle dose (surf%) as scaling key parameter complementary to the commonly used mass specific dose (wt%) to appropriately describe nanoparticle load, proving the effect of such surface additivation on the recrystallization behavior of PA12. Via flash calorimetry, already at 0.01 vol% silver load, significant nanoparticle-induced heterogeneous nucleation effects are evident, whereas the thermal properties analyzed by conventional calorimetry remain unaffected.

1. Introduction

Laser powder bed fusion (PBF-LB, according to ISO/ASTM DIS 52900:2018) of polymers, metals, or composites has become an important additive manufacturing technique for prototyping [1,2] and also started to approach serial production [3,4] due to its high geometrical flexibility and design freedom [5]. PBF-LB is more and more established in industry and a wide variety of reliable machines is available. Nowadays, the focus is shifting towards material development, since the availability of specialized powders for PBF-LB is a limiting factor for future growth [6–9]. One way of modifying powders

for PBF-LB and to affect their melting and resolidification characteristics and the mechanical properties of the final part is the additivation with inorganic micro- and nanoparticles such as carbon nanostructures [10–13] or oxides [14,15]. Such nanoscale fillers in a low amount can significantly influence the crystallization behavior through heterogeneous nucleation [16] and thus affect the mechanical properties of processed parts [10,17–19]. At the same time, induced crystallization through an increased number of nuclei can negatively affect the thermal processing characteristics of the polymer composites for PBF-LB by reducing the processing window through an increase in crystallization temperatures [20–22]. Therefore, a balanced amount of

* Corresponding author.

E-mail address: bilal.goekce@uni-due.de (B. Gökce).

<https://doi.org/10.1016/j.addma.2020.101419>

Received 9 February 2020; Received in revised form 7 June 2020; Accepted 23 June 2020

Available online 25 June 2020

2214-8604/ © 2020 Elsevier B.V. All rights reserved.

nanoparticles for maintaining a good processability and achieving desired mechanical properties has to be found. During the PBF-LB process, heating rates up to 10^7 K/min by laser radiation [23–25] and cooling rates between 0.2 and 20 K/min [26] can occur, depending on the position of the part in the process chamber. During the cooling step, spherulite (γ -phase) formation of PA12 typically originates by lamellar growth from nuclei, while increasing the overall crystallinity via primary and secondary crystallization [24,27–29]. Next to existing nuclei, the shape and quantity of the crystalline structures are also influenced by cooling rates [27,30].

Besides manipulation of crystallization behaviors, it is also possible to significantly adjust the absorption properties of the powder for wavelengths in the Vis and NIR by the addition of low amounts (0.01 wt%) of plasmonic nanomaterials [31], thus enabling inexpensive and compact diode laser PBF without the characteristic black appearance of a carbon additivated feedstock materials. Similar approaches for development of plasmonic-enhanced feedstock materials were demonstrated for two-photon polymerization [32] or near-field-enhanced laser sintering of semiconductors [33], both based on plasmonic gold nanoparticles. In contrast to gold nanoparticles, silver nanoparticles are factor 40 cheaper and come with a 4-times higher molar absorbance coefficient [34–36]. Their optical properties can further be tuned by alloying [35] and change of particle morphology [37]. In addition, composites based on silver nanostructures are known for a wide range of application [38], e.g. in biomedicine [39], electronics [40] and catalysis [41]. Therefore, the development of silver additivated feedstock materials could lead to novel properties through direct functionalization of final parts.

In this context, however, the dispersion (distribution) of the nanoparticles in the polymer matrix plays a decisive role. The poorer the dispersion and the larger and more aggregated the nanoparticles, the less nanoparticle surface is available at a given mass loading. Therefore, not only the value of the mass loading but also the degree of dispersion plays a crucial role in the nucleation properties [13,42]. The degree of nanoparticle dispersion and the surface coverage have only rarely been studied in the literature. Furthermore, the dispersion quality is deeply related to the additivation method [13,43]. Common additivation methods like dry-coating or melt compounding result in substantial aggregation of the filler after additivation [43–45]. They typically use aggregated nanoparticle, usually fabricated by gas phase synthesis (e.g., SiO_2 flow aid additive), which cannot be fully dispersed during the additivation process.

A promising method to increase the nanoparticle dispersion on microparticle surfaces is the colloidal additivation with surfactant-free laser-generated nanoparticles, which was recently demonstrated for nanoparticles on PA12 [46,68] and steel powders [15,47]. Laser synthesis and processing of colloids (LSPC) [48] can be used to synthesize a variety of nanoparticle materials in liquids. It is an easily scalable [49] and economically feasible [50] method to produce stable colloids for different applications such as composites [51], optics [33], biomedicine [52] or catalysis [53]. Additivation of polymer powders for PBF-LB is performed directly in an aqueous solution, where a laser-generated colloid and the polymer microparticles are simply mixed, followed by filtration and drying. This colloidal additivation route was initially established for the production of heterogeneous catalysts, where typically metal nanoparticles are adsorbed on support particles [54–58]. By controlling the pH during the adsorption an almost 100 % yield of this supporting procedure can be achieved and aggregation of the nanoparticles on the support can be avoided [59]. For the adsorption of nanoparticles on polymer powders, however, the mechanism for supporting is not fully understood. Therefore, influencing factors such as zeta potential, pH dependency and surface specific nanoparticle dosage need more attention.

In the present study we focus on these aspects, analyse the influence of process variables and aim for a better understanding of the particle supporting procedure. In this context, silver nanoparticles will act as a

model material, because the generation of electrostatic stabilized silver colloids by means of laser ablation is well established and the adsorption of plasmonic silver nanoparticles on polymer surfaces allows investigation of dispersion quality and quantity by optical means (characteristic surface plasmon resonance peak) and electron microscopy (good contrast of silver nanoparticles on/in polymer matrix). Since these particles might act as a nucleating agent, an impact on the calorimetric properties is expected. According to this, analysis of the surface-functionalized feedstock material is performed by differential scanning calorimetry (DSC) and fast scanning calorimetry (FSC) in order to investigate the influence of small doses of highly dispersed silver nanoparticles. To highlight the relevance of this surface-functionalized feedstock material for PBF-LB, an exemplary build job will be conducted.

2. Material and methods

2.1. Nanoparticle synthesis and colloidal additivation

Laser ablation in aqueous sodium citrate solution (100 $\mu\text{mol/l}$) was performed with a pulsed Nd:YAG-laser (Edgewave InnoSlab Laser IS400) centered at 1064 nm (8 ns, 110 W, 5 kHz), which was focused with an f-theta lens on a silver target mounted in a flow chamber setup. Small amounts of additives such as sodium citrate are known to increase colloidal stability and the reproducibility of laser-synthesis [60]. With our setup, nanoparticle synthesis by laser ablation resulted in a productivity of 1.1 g nanoparticles per hour, equivalent to more than 20 L of colloid. pH dependent zeta potential of laser-generated silver colloids was measured with PSS-Nicomb 380 ZLS after adjusting the pH with hydrochloric acid or sodium hydroxide solution. For colloidal additivation of PA12 with silver nanoparticles, PA12 (Evonik VESTO-SINT 3D Z2773, $d_{50,3} = 57.8 \mu\text{m}$, see supporting information Fig. S3 for more details) was dispersed in the colloid by mixing for 10 s, followed by stirring for 3 min (if not stated differently). Thereafter, the mixture was filtered with a Büchner funnel and a common blue-ribbon filter. Permeates were analyzed by UV–vis absorbance spectroscopy (Thermo Scientific Evolution 201) in the range of 300–900 nm (1 nm step size). As the most important parameter, the characteristic SPR peak intensity of silver at around 400 nm is analyzed. The efficiency of the supporting process is calculated by comparing the SPR intensity of the educt colloid and the permeate after additivation and filtration. It is defined as:

Supporting efficiency

$$= \frac{\text{SPR peak height (Educt)} - \text{SPR peak height (Permeate)}}{\text{SPR peak height (Educt)}} \cdot 100\% \quad (1)$$

The filter cake was dried at 50 °C for one day before size fractionation with a 125 μm sieve. Surface functionalized powders were characterized by diffuse reflection measurements (Agilent Cary 100 Bi Cricket). Distribution (Dispersion) and size of the nanoparticles on the polymer particle surface were analyzed by scanning electron microscopy (SEM, ESEM Quanta 400 FEG). In addition, transmission electron microscopy (TEM, JEOL 1400 Plus TEM) was used for high-resolution imaging of sliced polymer particles at IMCES, where samples were sliced with an ultramicrotome after being embedded in epoxy resin (EPON). Based on these images, interparticle distance histograms were extracted with the ImageJ open-source software package, counting about 400 particles, to quantify the nanoparticle dispersion [64].

Flowability was tested with a Mercury Scientific REVOLUTION Powder Analyzer and Hausner ratio were determined according to VDI 3405 Part 1.1 with a 100 mL plastic measuring cylinder by repeating the procedure four times, whereas the size of polymer particles was determined by the Camsizer X2 (ISO 13322-2) with compressed air of 50 kPa through the X-Jet extension.

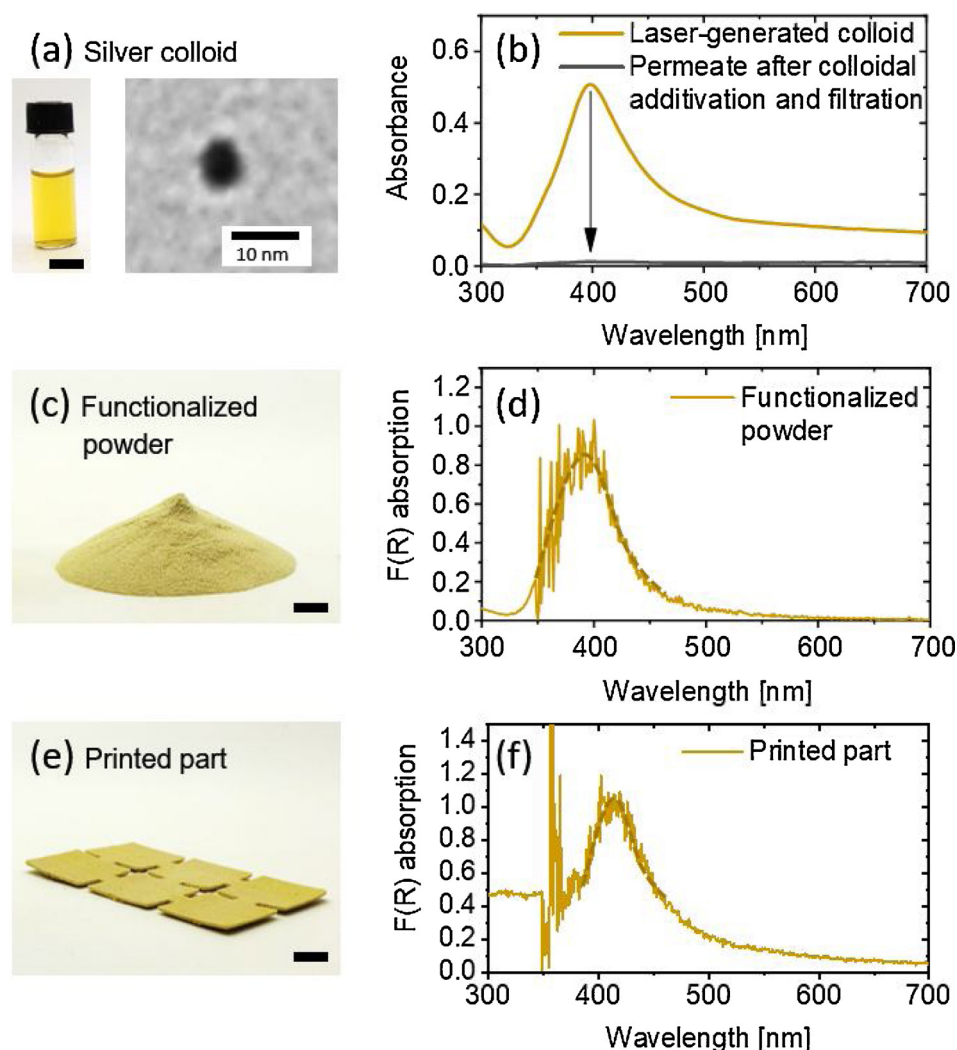


Fig. 1. Preservation of plasmonic properties along the process chain: (a) Laser-generated silver colloid with its characteristic yellow color caused by surface plasmon resonance (SPR) of silver nanoparticles and representative TEM image, and (b) corresponding UV-vis absorbance spectrum of the silver colloid showing the characteristic surface plasmon resonance peak of silver. (c) Surface-functionalized PA12 powder after filtration and drying and (d) its corresponding UV-vis absorption spectrum. (e) Test specimen after processing the powder with a Sharebot Snowwhite PBF-LB machine and corresponding UV-vis absorption spectrum. The black bar measures 1 cm.

2.2. Differential scanning calorimetry (DSC)

Surface functionalized powders were analyzed non-isothermally with a Mettler Toledo DSC 822e under nitrogen purge of 40 mL/min. Powder samples of approx. 12 mg were placed in 40 μ L aluminum pans with covers. The measurement went from 25 $^{\circ}$ C to 250 $^{\circ}$ C in a nitrogen atmosphere (nitrogen purge of 40 mL/min) with a heating rate of 10 K/min. At this temperature the samples were held for 3 min to fully melt all remaining crystals, leading to a thermal equilibrium. Afterwards, the samples were cooled down to 80 $^{\circ}$ C with a cooling rate of 10 K/min, held again for 3 min and heated up to 250 $^{\circ}$ C with 10 K/min. This way, the melting behavior of previously grown crystals as well as the sample's crystallinity can be measured. For statistical evaluation, each powder was measured three times. The evaluation of the results was performed with the Mettler Toledo STARe Evaluation Software 16.10. For the calculation of the relevant enthalpies, an integral tangential baseline was used.

2.3. Fast scanning calorimetry (FSC)

Fast scanning calorimetry was performed at the University of Rostock FSC. To cover a larger range of scanning rates which are relevant for PBF-LB and beyond, two different sensor and sample sizes were used. The calorimetric sensor XI395 with a heated area of $60 \times 80 \mu\text{m}^2$ with sample of approx. 4 ng was used to cover heating and cooling rates from 20,000–100 K/s. Heating and cooling rates from 0.1–100 K/s

were analyzed using a slower Mettler Toledo UFS 1 sensor with a heated area of 500 μm in diameter and sample masses of approx. 40 ng were used. All measurements were performed in dry nitrogen atmosphere ($-190 \text{ }^{\circ}\text{C}$).

First, samples were molten at 250 $^{\circ}$ C for 0.1 s and cooled to $-190 \text{ }^{\circ}\text{C}$ at 1000 K/s to have a defined thermal history. After that, samples were heated and cooled to 250 $^{\circ}$ C applying different heating and cooling rates between 0.1 and 20,000 K/s. Vitrification of pure PA12 sample occurs at cooling rates above ca. 5000 K/s – no crystallization peak and only glass transition is observed. For additivated material the critical cooling rate (cooling rate at which material becomes amorphous) was 1000 K/s. This observation is in line with larger undercooling of the additivated materials with increasing cooling rate, compared to pure PA12. As all samples showed crystallization on cooling at 1,000 K/s, the melting peak can be observed at all available heating rates up to 20,000 K/s.

After cooling at each different cooling rate, samples were reheated at 20,000 K/s to observe melting of previously formed crystals. Peak shape, temperatures, as well as enthalpy of crystallization and melting were analyzed. The absence of confinement and surface influences was confirmed by comparison of melting peaks at different heating rates (100 to 20,000 K/s) of samples with different masses.

Isothermal studies were performed using the reheating method, described in e.g. Wurm et al. [61]. Sensors XI395 with approx. 4 ng was used and samples were first molten for 0.1 s at 250 $^{\circ}$ C and then quenched to crystallization temperature at 20,000 K/s. After crystallization

for desired time it was quenched to $-190\text{ }^{\circ}\text{C}$ at maximum possible uncontrolled cooling rate (ca. $70,000\text{ K/s}$ at glass transition temperature) to freeze in the results of crystallization. Time of crystallization was increased logarithmically from 0.001 to 100 s . After that, reheating at $20,000\text{ K/s}$ was performed for melting of crystallized material. Giving the fast heating rate, reorganization of crystals was suppressed, and the overall enthalpy change during heating is equal to the previous crystallization enthalpy change. Crystallization enthalpy was compared for different temperature and time of crystallization for pure and surface-functionalized material.

3. Results and discussion

3.1. Process determinants for colloidal additivation

The colloidal additivation process starts with a laser-generated silver colloid, characterized by its yellow color, caused by the surface plasmon resonance (SPR) peak at a wavelength of 398 nm (Fig. 1a,b). The peak maximum of the number weighted particle size distribution is 4.1 nm , based on TEM particle size analysis. A representative TEM image is shown in the inset of Fig. 1a. After mixing the silver colloid with PA12 microparticles and after filtration of the mixed suspension, the permeate does not show any SPR peak (Fig. 1b) and a yellow powder remains in the filter. UV-vis absorption measurement of the dried functionalized powder (Fig. 1c) shows the characteristic SPR peak (Fig. 1d), proving the presence of nanosilver. The SPR peak wavelength of the powder is similar to the colloid and no shoulder is visible at high wavelength, indicating a successful prevention of aggregation of the silver, which would cause red-shift of SPR peak. The absence of the surface plasmon resonance peak in the permeate indicates a quantitative/high yield adsorption (supporting) of the silver nanoparticles on the surface of the polymer microparticles. Even after processing on a PBF-machine (Sharebot Snowwhite), the characteristic yellow color and the SPR peak are preserved (Fig. 1e,f). Thus, we show that the final parts were successfully functionalized with a high dispersion of plasmonic silver nanoparticles.

A deeper understanding about the kinetics of the colloidal additivation process could lead to better process control, especially in the context of upscaling towards kg-scale of functionalized powder. Since laser-generated metal colloids usually bear a high electrostatic charge with strong, pH-dependent zeta potentials [60], the pH during mixing with the polymer particles and the mixing time are suspected to be important factors for the additivation process. In a first experiment, time-dependent pH measurements were performed after mixing PA12 powder with 25 mL ultrapure water under vigorous stirring. Interestingly, the pH of the suspension changes significantly over time (Fig. 2a). Within 30 s after immersing the PA12 in water, the pH drops from $\text{pH} = 6.1$ to $\text{pH} = 5.4$, which causes the absolute zeta potential value of the silver colloid to drop from -40 mV to less than -20 mV for the silver colloid (Inset of Fig. 2a). Since the zeta potential is below an absolute value of $\pm 30\text{ mV}$, the stability of the colloid is significantly reduced, resulting in slow precipitation of the silver on the surface of the polymer microparticles. However, the pH value of the suspension is still high enough to avoid instant aggregation and a complete vanishing of the SPR peak, which is confirmed by the yellow color of the surface-functionalized. Nonetheless, the origin of the pH-shift resulting after immersing the PA12 in water remains unclear. Dissolved additives [62] like carbon acids added to the polymer powder during its processing are likely to have influence on the pH. Further results of pH measurements are provided in supporting information S1.

From Fig. 2a,b it is evident that the supporting is very fast and a supporting efficiency of $> 90\%$ is reached after less than 60 s . This was also confirmed by ICP-MS of a permeate after filtration, where approx. 10% of the initial silver content of the educt colloid was found after supporting. Note that silver nanoparticles release ions over time which will not contribute to the SPR peak of the surface-functionalized

powders or permeates and can just be found by ICP-MS of the permeate. Further XRF analysis confirmed a silver content of $0.086 \pm 0.0015\text{ wt}\%$ in the surface-functionalized powder. A slightly smaller supporting efficiency is measured for mixing times $< 30\text{ s}$ compared to the maximum at 60 s (Fig. 2b). It is evident for our stirring conditions that supporting is faster than the change of pH, so that a critical pH range where the nanoparticles' electrostatic repulsion is almost zero is avoided. However, the necessary mixing time for $> 90\%$ supporting efficiency is likely to be affected by the batch size and stirring conditions, which is important for scale-up in order to meet the needs for PBF-LB parameter studies and build jobs. If longer mixing times were necessary, the pH value would drop further and increase the probability for aggregation.

The supporting process is also influenced by nanoparticle concentration as it is shown in Fig. 2c for the supporting efficiency and the corresponding absorption of the surface-functionalized powder (intensity of the SPR peak) at constant nanoparticle loading of $0.1\text{ wt}\%$. Supporting efficiency is above 95% for all tested nanoparticle concentrations except for 10 mg/l , where the efficiency drops below 80% and shows poor reproducibility. This could be explained by a higher stability of the colloid, since the rate of aggregation is proportional to the square of nanoparticle concentration [63]. Furthermore, smaller nanoparticle concentrations mean smaller polymer concentration in order to achieve the same polymer to nanoparticle mass ratio. As a result, the pH is higher, and the colloid is more stable, which leads to smaller supporting efficiency (see supporting information Fig. S1 information for the influence of polymer concentration on pH value). When increasing the nanoparticle concentration above 50 mg/l , supporting efficiency and powder absorption remain stable, but the probability increases to observe a complete failure of the supporting process and complete aggregation of the silver colloid. In this case the SPR peak vanishes and a greyish, almost white powder is produced, which is shown in the inset of Fig. 2c. This reproducibility issue could be explained by higher nanoparticle concentration resulting in smaller interparticle distances and weaker colloidal stability at low pH value, where repulsive forces are weaker. Two exemplary powders are depicted in the inset of Fig. 2c to illustrate the weak reproducibility. For the additivation process, especially on a larger scale, the processed volume should be as small as possible to allow smaller setups, faster filtration, and saving water. The nanoparticle concentration should, therefore, be as large as possible. As a compromise to ensure good reproducibility, a nanoparticle concentration of 50 mg/l and 60 s mixing time was used for the following experiments, which gives a polymer microparticle concentration of 50 g/l and a nanoparticle loading of $0.1\text{ wt}\%$ ($0.01\text{ vol}\%$) at $> 95\%$ yield.

3.2. Nanoparticle surface dose and dispersion

An essential parameter for the applications and mechanical properties of surface-functionalized powders in PBF-LB is the nanoparticle load, typically given in terms of $\text{wt}\%$. But this value might be misleading, since the effect of nanoparticles can also be driven by their volume fraction ($\text{vol}\%$), degree of dispersion, and surface coverage ($\text{surf}\%$) on the polymer microparticle surface. The connection between $\text{wt}\%$, $\text{vol}\%$, $\text{surf}\%$ and nanoparticle size is illustrated in Fig. 3 for silver nanoparticles adsorbed on PA12 microparticles. Based on the $\text{wt}\%$, the $\text{vol}\%$ can be calculated under consideration of the polymer and nanoparticle densities. From the $\text{wt}\%$ the theoretical $\text{surf}\%$ can be calculated as follows.

$$\begin{aligned} \text{theo. surf}\% &= \frac{\text{total nanoparticle footprint}}{\text{total polymer particle surface}} \\ &= \frac{3 \cdot \text{wt}\%}{2 \cdot A_{\text{pp}} (100 - \text{wt}\%) \cdot \delta_{\text{NP}} \cdot d_{\text{NP}}} \cdot 100\% \end{aligned}$$

A_{pp} stands for the specific surface of the polymer powder, which was calculated from the particle size distribution measured by laser

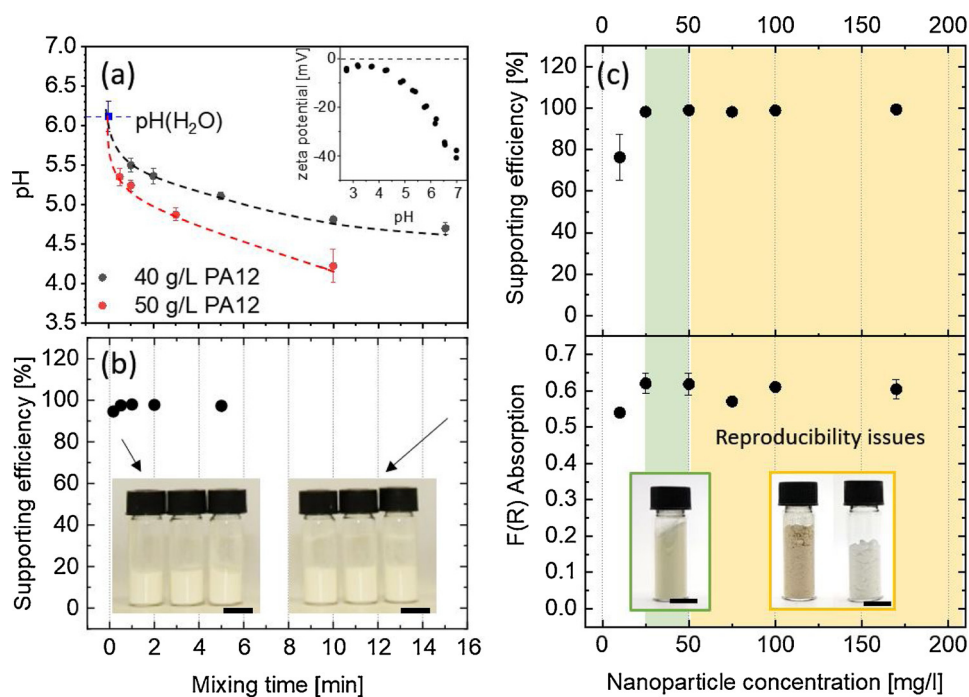


Fig. 2. Colloidal addition process characteristics: (a) pH value as a function of stirring time for PA12 dispersed in water. The inset shows the pH-dependent zeta potential of silver nanoparticles. (b) Supporting efficiency as a function of mixing time. (c) Supporting efficiency and absorption at the SPR peak of the surface-functionalized powder after drying as a function of nanoparticle concentration at a constant nanoparticle loading of 0.1 wt% (0.01 vol%). The green marked area corresponds to efficient supporting and high reproducibility, whereas the yellow area shows weaker supporting and high reproducibility.

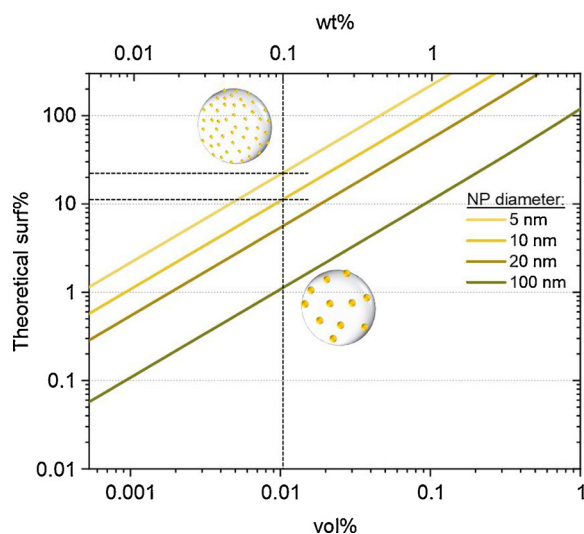


Fig. 3. Scaling graph illustrating the connection between wt%, vol%, surface coverage (surf%) and nanoparticle size for PA12 powder with a specific surface of $0.114 \text{ m}^2/\text{g}$ which was determined based on the polymer microparticle size distribution (Size distribution and different scale graphs are available in the supporting information S2). The dotted vertical line and marked range indicate a theoretical surface coverage between 10 and 20 surf% for 0.01 vol% (0.1 wt%) and nanoparticles in the range of 5 to 10 nm.

diffraction (see supporting information Fig. S2) and was equal to $0.114 \text{ m}^2/\text{g}$. δ_{NP} is the density of the nanomaterial and d_{NP} is the nanoparticle diameter. The scaling graph in Fig. 3 illustrates that far less than 1 wt% (or 0.1 vol%) of silver nanoparticles in the size of 5 nm are necessary to reach 100% of theoretical surface coverage. If larger nanoparticles are used or if the nanomaterial aggregates on the polymer microparticle surface, the surface coverage decreases by magnitudes. This makes the surface coverage highly dependent on the dispersion and thus on the nanoadditivation process itself.

The effect of high surface coverage can be observed if the wt% of nanoparticles is altered. Fig. 4a,b shows the connection between experimental supporting efficiency and theoretical surf% for a variation of

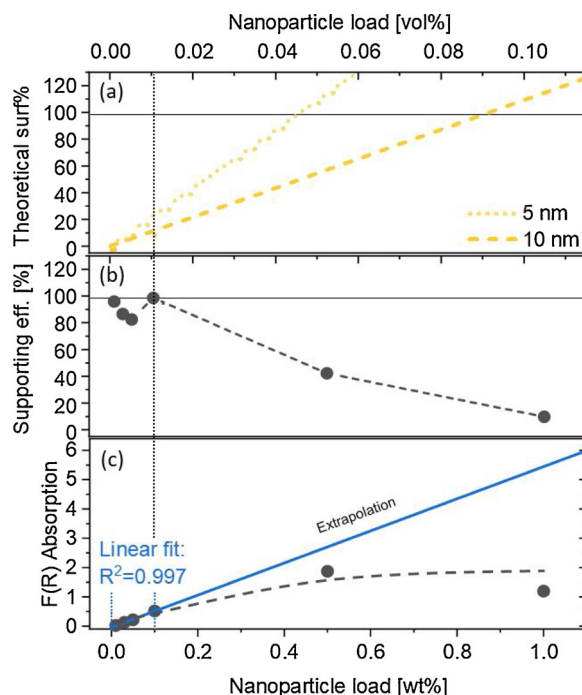


Fig. 4. (a) Theoretical surf%, (b) Supporting efficiency and SPR peak intensity (F(R) absorption) of the surface-functionalized powder as a function of nanoparticle loading during colloidal addition. The dotted vertical line at 0.01 vol% mark the loading until which a linear correlation between supporting efficiency, powder absorption and nanoparticle load is observed and where a change in absorption kinetics happens.

nanoparticle loading between 0.01 and 1 wt%. The nanoparticle loading represents the ratio of silver nanoparticles and polymer microparticle during addition. If the supporting efficiency is above 80%, which is the case until 0.1 wt%, the nanoparticle loading is approximately equal to the effective nanoparticle loading, since almost all nanoparticles are deposited on the polymer surface. This is also reflected in a linear correlation between SPR peak intensity of the powder

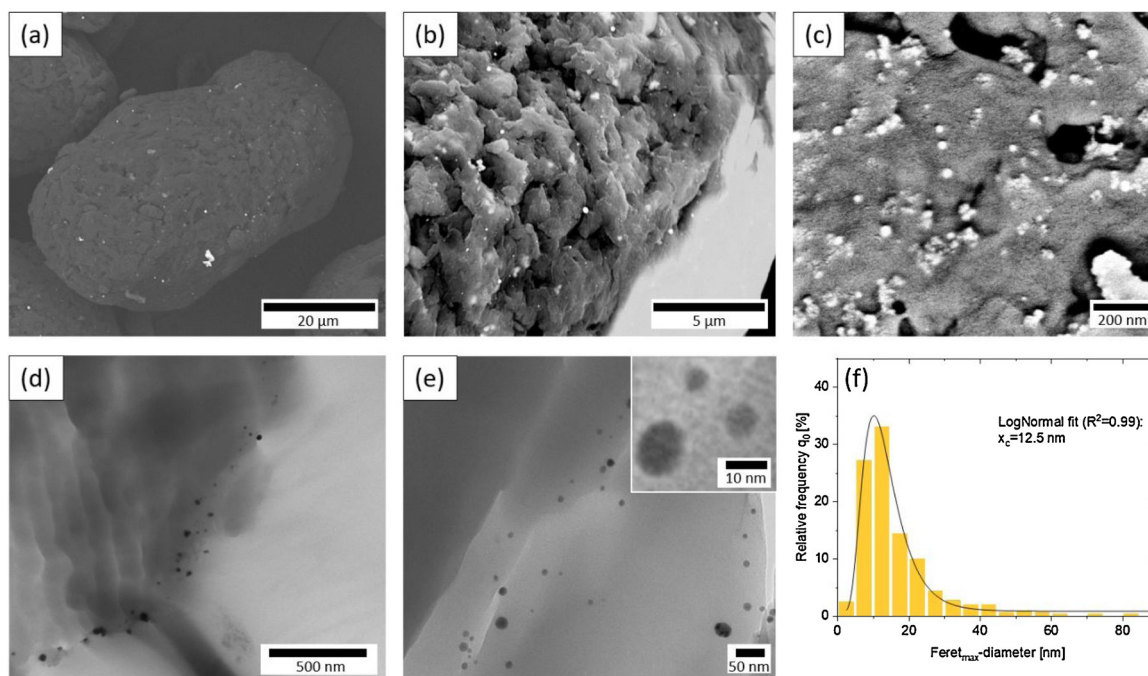


Fig. 5. (a, b, c) SEM images of PA12 microparticles decorated with 0.1 wt% silver nanoparticles. (d,e) TEM images of sliced PA12 microparticle and (f) corresponding particle size distribution ($n = 400$).

(F(R) absorption) and mass loading until 0.1 wt% (indicated by a dotted line in Fig. 4a–c). Interestingly, at higher mass loadings of 0.5 wt% and 1 wt%, the supporting efficiency decreases to 20–40 % and therefore the effective nanoparticle loading is much smaller than the theoretical value, which also results in a saturation of SPR peak intensity. For 1.0 wt% the SPR peak intensity is approximately reduced by 80 % compared to the expected value from a linear extrapolation. As expected, the decrease in supporting efficiency correlates with the threshold of maximal theoretical surface coverage which reaches 100 surf% at 0.5 wt%. This correlation can be attributed to less space on the polymer microparticle surface and hence indicates a change in absorption kinetics which results in a hindered deposition of the nanoparticles. Therefore, an increase in nanoparticle loading to more than 0.1 wt% (0.01 vol%) is not useful for the given material combination since more and more of the silver colloid would be wasted without being supported. At loadings of up to 0.1 wt% (20–40 theoretical surf%) high supporting efficiency and SPR absorption of the powder is reached.

For the additivation with 0.1 wt% nanoparticles, Fig. 5a–c shows SEM images of polymer microparticles after colloidal additivation, indicating a homogeneous distribution of nanoparticles. Silver nanoparticles exhibit only minor aggregation on the polymer microparticle surface. We also observe a high surface porosity of the PA12 microparticles which most likely results in an underestimation of the polymer particle surface assumed for the calculation of surf%. Furthermore, under consideration of the limited resolution of the SEM of approx. 10 nm, it could be possible that a significant number of nanoparticles on the polymer surface is too small to be detected by SEM. To check this hypothesis, the polymer particles were sliced and imaged via TEM. The results in Fig. 5d,e confirm the presence of small particles below 10 nm, which contribute 30 % to the total particle number (Fig. 5f, $x_c=12.5$ nm). Thus, the primary particle diameter has not changed during additivation, which is in accordance with the conservation of the surface plasmon resonance peak. Furthermore, the polymer particle size distribution, as well as the Hausner ratio and the avalanche angle of the powder, are also not significantly influenced by additivation (Table 1), pointing at the applicability of the nano-additivated powder for PBF-LB.

3.3. Calorimetric properties

As it was shown in Fig. 3, the nanoparticle size has a significant impact on the surface coverage. Moreover, the number of small particles is of particular interest for possible effects on heterogeneous nucleation, which should depend on the particle size, especially on the presence of small non-aggregated particles with a high total surface area. Dynamic DSC analysis allows the examination and a first evaluation of the effect of nanoparticles on the thermal behavior of polymers and their influence on the relevant process window for PBF-LB. During the first heating cycle, the position of the peak, the onset and the endset, as well as its sharpness and the overall form of the melting curve show no significant difference (n.s.) between PA12 with and without silver nanoparticles (Fig. 6). Respectively, the melting peak temperature of PA12 at 185.7 ± 0.2 °C remains at 185.6 ± 0.2 °C with the addition of the silver nanoparticles. This unchanged melting behavior shows that the initial melting properties of the base polymer have not been altered through the adhesion of silver nanoparticles onto the polymer particle surface. For PBF-LB the crystallization after melting is of high interest as a read-out of the final part properties [10,64].

Nanoscale impurities inside a polymer melt are initiating a heterogeneous nucleation of spherulites during cooling [16]. Therefore, nanoparticles in the size of a crystal nuclei within a polymer melt should be able to induce a premature crystallization due to the availability of several new nucleation sites. Thermoplastic PA12 shows its typical crystallization behavior with a crystallization onset at 150.3 ± 0.3 °C (Fig. 6b). In the case of a potential nucleation effect of silver nanoparticles an earlier crystallization can be expected, and the exothermic peak should shift towards higher temperatures. Interestingly, this does not occur in our experiments (Fig. 6a). The crystallization onset of the surface-functionalized powder with 0.1 wt% silver nanoparticles lies at 150.6 ± 0.2 °C, which is not significantly different (n.s.) to the PA12 without silver nanoparticles (Fig. 6b). Respectively, the peak and the endset temperature do not significantly change with the addition of silver nanoparticles either. As a result, the addition of silver nanoparticles to PA12 retains a processing window for PBF-LB of 30 K, which is defined by the difference of the onset of the first melting and the onset of the first crystallization. Therefore, changes in crystalline

Table 1

Polymer powder particle sizes for neat PA12 and PA12 after colloidal additivition with 0.1 wt% of silver nanoparticles. dx values are given for Q0 and Q3. Powders were sieved with a 125 μm sieve before measurements. Flowability is characterized by the avalanche angle and Hausner ratio.

Samples	Particle size distribution (xarea; area of particle projection)						Avalanche angle	Hausner ratio
	x10,3	x50,3	x90,3	x10,0	x50,0	x90,0		
PA12 (washed)	42.4	57.8	72.5	0.9	4.0	8.2	48.7 \pm 0.30	1.15 \pm 0.02
PA12 + 0.1 wt% Ag	41.6	56.6	72.1	0.9	3.8	8.0	49.0 \pm 0.15	1.13 \pm 0.01

phases or nucleation effects would be detectable with a change of the overall crystallinity X_c of the samples, which can be calculated according to Eq. (2).

$$X_c = \frac{\Delta H_m}{\Delta H_{100}} \quad (2)$$

The enthalpy of fusion of the sample ΔH_m can be extracted by the data of the melting curves, while the enthalpy of fusion of a perfect PA12 crystal ΔH_{100} is given by theoretical extrapolation ($\Delta H_{100} = 209,3 \frac{\text{J}}{\text{g}}$) [65].

When heating the sample a second time, the melting peak is shifted to lower temperatures in comparison to the first melting peak due to different crystalline phases, which develop during the fabrication process of the polymer powder [27]. As a result of an isotropic crystallization during the previous cooling cycle, the enthalpy decreases from $99.5 \pm 0.5 \text{ J/g}$ to $35.25 \pm 0.1 \text{ J/g}$ and consequently, the crystallinity decreases from $47.5 \pm 0.2 \%$ to $16.8 \pm 0.1 \%$ (Fig. 6a). By adhesion of silver nanoparticles onto the PA12 powder surface, the enthalpy of fusion remains almost constant at $35.3 \pm 0.2 \text{ J/g}$ with a sample crystallinity of $16.9 \pm 0.1 \%$ and thus exhibiting no visible change in crystallization behavior from the nanoparticles at 10 K/min. In order to further investigate possible nucleation effects of silver nanoparticles within the PA12 matrix, calorimetric analysis with higher heating and cooling rates (FSC) outside of PBF conditions was conducted.

Crystallization at 150 $^{\circ}\text{C}$ occurs in the region of heterogeneous nucleation [66]. When increasing the cooling rate beyond 100 K/s, the PA 12 is crystallizing homogeneously below 100 $^{\circ}\text{C}$. It is known, that certain nucleating agents disturbs homogeneous nucleation, slowing down crystallization. To investigate the influence of additives on PA12 at faster cooling, FSC was applied. In order to extend scanning rate range, two sample sizes were used in FSC: ca. 40 ng samples cover the range 0.1–100 K/s and ca. 4 ng samples cover the range from 100 to 20,000 K/s. Fig. 7a summarizes conventional and fast scanning DSC results.

Fig. 7a shows the peak temperature for melting (dashed lines) and

crystallization (solid lines) at different heating and cooling rates. Melting was performed after cooling at cooling rate 1000 K/s. Melting peaks after 1000 K/s are almost coinciding for all samples, indicating that the thermal lag is comparable and not causing the difference for melting below 10,000 K/s. This confirms the validity of temperature measurements through all different samples in the range of scanning rates. Solid lines on Fig. 7a indicate that nanoparticle-nucleated samples crystallize at approx. 20 $^{\circ}\text{C}$ lower temperature on fast cooling compared to neat PA12. This significantly lower temperature crystallization is almost independent of the amount of nucleation agent.

PA12 shows bimodal solidification with at least two peaks (Fig. 7b). Due to DSC principles, comparison of the subtle peak development is difficult during cooling at different rates. Therefore, the reheating at 20,000 K/s was done after each cooling. The resulting heating scans for pure and 1 wt% surface-functionalized PA12 is shown in Fig. 7b. Curves shows glass transition around 52 $^{\circ}\text{C}$, followed by cold crystallization peaks at around 120 $^{\circ}\text{C}$ and melting at ca. 150 $^{\circ}\text{C}$. The melting peaks enthalpies correspond to the peak area and are comparable for the pure sample and the surface-functionalized sample, e.g. for 200 K/s cooling. But the low temperature shoulder at around 120 $^{\circ}\text{C}$ appears to be wider for the surface-functionalized PA 12. This can be interpreted as a similar crystallinity, but wider size distribution of the crystals for functionalized material.

Eventually an isothermal crystallization was performed by FSC on small samples (4 ng). Three characteristic temperatures are shown in Fig. 7c: 150 $^{\circ}\text{C}$ – temperature in the region of heterogeneous nucleation, 40 $^{\circ}\text{C}$ – temperature in the region of homogeneous nucleation and 100 $^{\circ}\text{C}$ - interplay between homogeneous and heterogeneous nucleation. Only the pure PA12 and highest nanoparticle loaded PA12 are shown here. Curves show typical sigmoidal shape with exponentially developing primary crystallization and secondary crystallization after that (for interpretation see e.g. [61]). When possible, data were fitted using Kolmogorov-Johnson-Mehl-Avrami (KJMA) kinetics [67], superimposed with linear secondary crystallization kinetics [61].

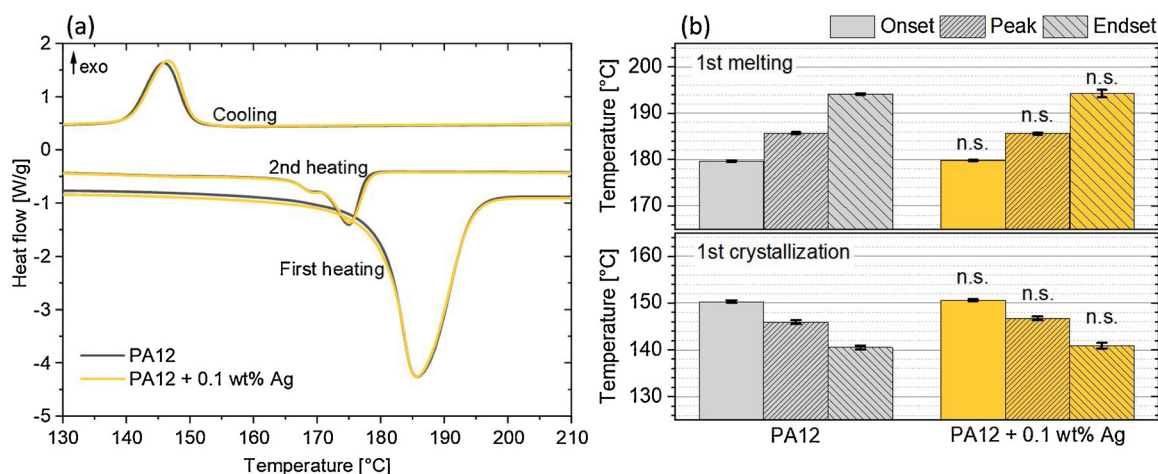


Fig. 6. Melting and crystallization curves of PA12 with and without 0.1 wt% silver nanoparticles, averaged over three runs by conventional DSC at 10 K/min. (b) Corresponding thermal values obtained from DSC of PA12 and its additivated counterpart with 0.1 wt% silver nanoparticles, based on three runs with its standard deviations and results of a significance analysis (n.s. stands for values which show no significant difference to PA12 without silver).

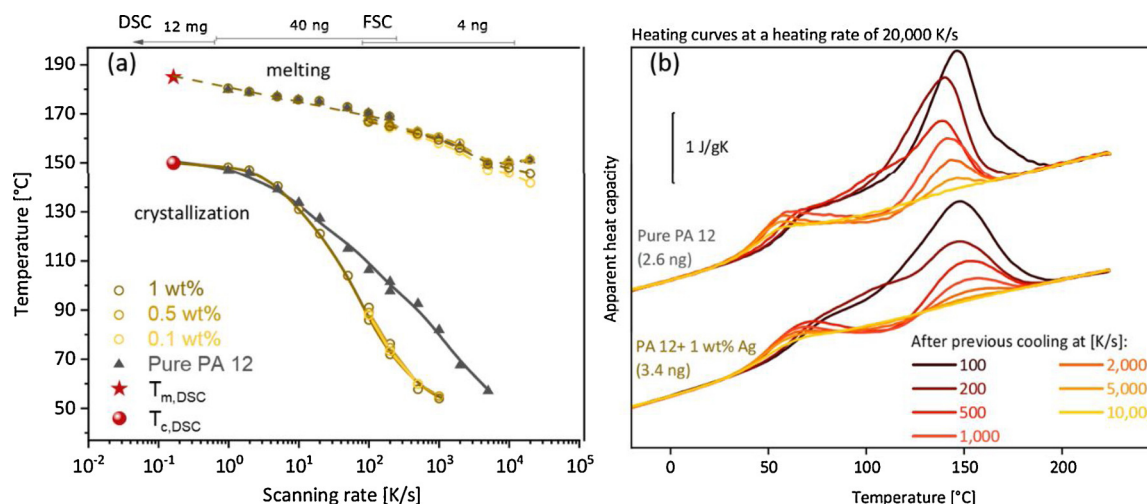


Fig. 7. Fast scanning calorimetry analysis of crystallization at low temperatures for different nanoparticle loadings. (a) Crystallization and melting peak maximum temperatures at different cooling and heating rates from 0.1 to 20,000 K/s. Melting was performed at different heating rates after cooling at 1000 K/s. Additionally, the melting and crystallization point for standard DSC measurements are highlighted in red. (b) Reheating of pure and additivated PA12 at 20,000 K/s after cooling at different rates.

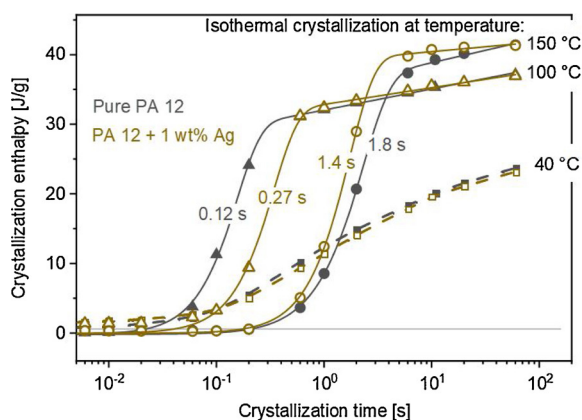


Fig. 8. Isothermal crystallization development of pure and nanoparticle-functionalized samples at three characteristic and PBF-LB relevant temperatures. Solid curves show Kolmogorov-Johnson-Mehl-Avrami (KJMA) fit and the half-time of crystallization.

Crystallization below glass transition temperature expectedly not follows Avrami kinetics and therefore were not fitted. As already observed during non-isothermal crystallization, the high temperature crystallization (150 °C in Fig. 8) shows no obvious influence of nucleation agent on crystallization half-time. In the region of homogeneous nucleation below glass transition temperature (40 °C in Fig. 8) crystallization occurs even more identically. In between (100 °C) the functionalized material is more than 2 times slower than pure PA 12. This supports the idea that as soon as the heterogeneous nucleation start to compete with homogeneous nucleation, the overall crystallization slows down.

A possible difference in the polymer-microparticle interaction could be expected for other nanoparticle material like oxides, e.g. it is known that the Hamaker constant is far lower for oxides compared to metals.

4. Conclusion

For the development of new polymer nanoparticle-composite powder materials for additive manufacturing, homogenous and fine dispersion of the nanoparticles is a key factor, which can be addressed by colloidal surface additivation. During this process, adsorption (Supporting) of silver nanoparticles on semi-crystalline PA12 powder

(Evonik VESTOSINT 3D Z2773) is a very fast process, driven by electrostatic destabilization of the colloid. Immersing the polymer powder in a laser-generated silver colloid results in a pH decrease and a supporting efficiency of more than 90 % in less than 60 s. Within this time frame, colloidal stability is still high enough to avoid aggregation effects. This is confirmed by preservation of the plasmonic properties along the process chain from the laser-generated colloid to the surface-functionalized powder and the generated test specimen after successful PBF-LB. Ideal nanoparticle and polymer concentrations were found for this process leading to high dispersion and good reproducibility. Surface coverage (surf%) of nanoparticles on the polymer surface is highly dependent on the dispersion and thus on the nano-addition process. Saturation of plasmon resonance intensity above 0.1 wt%, can be explained with high surface coverage, more aggregation and a decrease in supporting efficiency at high mass loadings. Based on the results of the thermal analysis, silver nanoparticles clearly influence crystallization of PA12 already at 0.01 vol% (100 ppm by volume) due to the excellent dispersion of the nanoparticles, resulting in 20-40 surf %. At high temperatures and fast cooling, small amounts of silver nanoparticles preserve crystallization. However, at temperatures and cooling rates within the range of PBF-LB of polymers, silver nanoparticles show no significant effects on the crystallization behavior and thus maintain the optimal thermal properties of pure PA12 for PBF-LB. All in all, our study points a way towards a better understanding of the influence of nanoparticle surface additivation and outstanding dispersion on the functionalization of polymer powders for PBF-LB.

CRediT authorship contribution statement

Tim Hupfeld: Conceptualization, Methodology, Software, Writing - original draft, Writing - review & editing. **Alexander Sommereyns:** Methodology, Software, Writing - original draft, Writing - review & editing. **Thomas Schuffenhauer:** Data curation, Investigation. **Evgeny Zhuravlev:** Methodology, Software, Writing - original draft, Writing - review & editing. **Moritz Krebs:** Data curation, Visualization. **Stan Gann:** Data curation, Methodology. **Olaf Keßler:** Supervision, Funding acquisition, Writing - review & editing. **Michael Schmidt:** Supervision, Funding acquisition, Writing - review & editing. **Bilal Gökce:** Conceptualization, Supervision, Visualization, Funding acquisition, Writing - original draft, Writing - review & editing. **Project administration.** **Stephan Barcikowski:** Supervision, Funding acquisition, Writing - review & editing.

Declaration of Competing Interest

The authors declare that they have no known competing financial interests or personal relationships that could have appeared to influence the work reported in this paper.

Acknowledgements

We thank Evonik Industries for providing the PA12 powder, Smail Boukercha and Kateryna Loza (AK Epple, University of Duisburg-Essen) for SEM imaging of the polymer powders and IMCES (Imaging Center Essen, University Hospital Essen) for TEM analysis of the sliced polymer samples and fruitful discussions on nanoparticle imaging in and on polymers. The authors also thank Marc Labusch for size measurements of polymer microparticles, Milen Nachev for ICP-MS measurements of permeates and Simon Siebeneicher for his support during XRF analysis. Tim Hupfeld thanks Elisavet Papadopoulou, Leyla Carkir, Philipp P. May, Simon Nieskens and Vladyslav Sharov for their assistance during the experiments. Stan Gann thanks Markus Piechotta (Institut für Produkt Engineering, University of Duisburg-Essen) for his help during powder floability tests. The authors thank Matthias Krause (FH Dortmund, Prof. Sinnemann) for prociding first nanofunctionalized PBF-LB test specimen. Tim Hupfeld acknowledge Evonik Industries for financial support. Alexander Sommereyns gratefully acknowledges funding of the Erlangen Graduate School in Advanced Optical Technologies (SAOT) by the German Research Foundation (DFG) in the framework of the German excellence initiative. The authors gratefully acknowledge the funding by the German Research Foundation (DFG) within the priority program (SPP) 2122 "Materials for Additive Manufacturing (MATframe, BA 3580/27-1 + SCHM 2115/78-1). Bilal Gökce additionally acknowledges funding from the DFG, project GO 2566/10-1. Bilal Gökce additionally acknowledges funding from the DFG, project GO 2566/10-1.

Appendix A. Supplementary data

Supplementary material related to this article can be found, in the online version, at doi:<https://doi.org/10.1016/j.addma.2020.101419>.

References

- [1] Wohlers Associates, Wohlers Report 2019, (2019), p. 369.
- [2] T.D. Ngo, A. Kashani, G. Imbalzano, K.T.Q. Nguyen, D. Hui, Additive manufacturing (3D printing): a review of materials, methods, applications and challenges, *Compos. Part B Eng.* 143 (2018) 172–196, <https://doi.org/10.1016/j.compositesb.2018.02.012>.
- [3] Trends Appear on the Gartner Hype Cycle for Emerging Technologies, Gartner, 2019, p. 2019 (Accessed 27 September 2019), <https://www.gartner.com/smarterwithgartner/5-trends-appear-on-the-gartner-hype-cycle-for-emerging-technologies-2019/>.
- [4] P. Basiliere, 3D Printing Accelerates, 4D Printing Gets Started, Gartner, (2019) <https://blogs.gartner.com/pete-basiliere/2019/01/03/3d-printing-accelerates-4d-printing-gets-started/>.
- [5] A. Paolini, S. Kollmannsberger, E. Rank, Additive manufacturing in construction: a review on processes, applications, and digital planning methods, *Addit. Manuf.* 30 (2019) 100894, <https://doi.org/10.1016/j.addma.2019.100894>.
- [6] W. Pfleging, R. Kohler, I. Südmeyer, M. Rohde, Laser Micro and nano processing of metals, ceramics, and polymers, *Laser-Assisted Fabr. Mater.* 161 (2013) 319–374, <https://doi.org/10.1007/978-3-642-28359-8>.
- [7] F.P.W. Melchels, M.A.N. Domingos, T.J. Klein, J. Malda, P.J. Bartolo, D.W. Huttmacher, Additive manufacturing of tissues and organs, *Prog. Polym. Sci.* 37 (2012) 1079–1104, <https://doi.org/10.1016/j.progpolymsci.2011.11.007>.
- [8] Nationale Akademie der Wissenschaften Leopoldina, Deutschen Akademie der Technikwissenschaften Acatech, Additive Fertigung, Munich, 2017.
- [9] M. Schmid, A. Amado, K. Wegener, Materials perspective of polymers for additive manufacturing with selective laser sintering, *J. Mater. Res.* 29 (2014) 1824–1832, <https://doi.org/10.1557/jmr.2014.138>.
- [10] J. Bai, R.D. Goodridge, R.J.M. Hague, M. Song, Improving the mechanical properties of laser-sintered polyamide 12 through incorporation of carbon nanotubes, *Polym. Eng. Sci.* 53 (2013) 1937–1946, <https://doi.org/10.1002/pen.23459>.
- [11] R.D. Goodridge, M.L. Shofner, R.J.M. Hague, M. McClelland, M.R. Schlea, R.B. Johnson, C.J. Tuck, Processing of a Polyamide-12/carbon nanofibre composite by laser sintering, *Polym. Test.* 30 (2011) 94–100, <https://doi.org/10.1016/j.polymertesting.2010.10.011>.
- [12] T. Wagner, T. Höfer, S. Knies, P. Eyerer, Laser sintering of high temperature resistant polymers with carbon black additives, *Int. Polym. Process.* 19 (2004) 395–401, <https://doi.org/10.3139/217.1846>.
- [13] H.C. Kim, H.T. Hahn, Y.S. Yang, Synthesis of PA12/functionalized GNP nanocomposite powders for the selective laser sintering process, *J. Compos. Mater.* 47 (2012) 501–509, <https://doi.org/10.1177/0021998312441812>.
- [14] M.M. Lexow, D. Drummer, New materials for SLS: the use of antistatic and flow agents, *J. Powder Technol.* 2016 (2016) 1–9, <https://doi.org/10.1155/2016/4101089>.
- [15] C. Doñate-Buendía, F. Frömel, M.B. Wilms, R. Streubel, J. Tenkamp, T. Hupfeld, M. Nachev, E. Gökce, A. Weisheit, S. Barcikowski, F. Walther, J.H. Schleifenbaum, B. Gökce, Oxide dispersion-strengthened alloys generated by laser metal deposition of laser-generated nanoparticle-metal powder composites, *Mater. Des.* 154 (2018) 360–369, <https://doi.org/10.1016/j.matdes.2018.05.044>.
- [16] E. Piorkowska, G.C. Rutledge, Handbook of Polymer Crystallization, (2013), <https://doi.org/10.1002/9781118541838>.
- [17] S.R. Athreya, K. Kalaitzidou, S. Das, Mechanical and microstructural properties of Nylon-12/carbon black composites: selective laser sintering versus melt compounding and injection molding, *Compos. Sci. Technol.* 71 (2011) 506–510, <https://doi.org/10.1016/j.compscitech.2010.12.028>.
- [18] S. Fu, Z. Sun, P. Huang, Y. Li, N. Hu, Some basic aspects of polymer nanocomposites: a critical review, *Nano Mater. Sci.* 1 (2019) 2–30, <https://doi.org/10.1016/j.nanoms.2019.02.006>.
- [19] Y. Wang, Y. Shi, S. Huang, Selective laser sintering of polyamide-rectorite composite, *Proc. Inst. Mech. Eng. Part L J. Mater. Des. Appl.* 219 (2005) 11–16, <https://doi.org/10.1243/146442005X10229>.
- [20] D. Eiras, L.A. Pessan, Influence of calcium carbonate nanoparticles on the crystallization of polypropylene, *Mater. Res.* 12 (2009) 523–527, <https://doi.org/10.1590/S1516-14392009000400024>.
- [21] Y. Wang, C.M. Dinapoli, G.A. Tofig, R.W. Cunningham, R.A. Pearson, Selective Laser Sintering Processing Behavior of Polyamide Powders, n.d.
- [22] C. Huang, X. Qian, R. Yang, Thermal conductivity of polymers and polymer nanocomposites, *Mater. Sci. Eng. R Rep.* 132 (2018) 1–22, <https://doi.org/10.1016/j.mser.2018.06.002>.
- [23] D. Drummer, M. Drexler, K. Wudy, Impact of heating rate during exposure of laser molten parts on the processing window of PA12 powder, *Phys. Procedia* 56 (2014) 184–192, <https://doi.org/10.1016/j.phpro.2014.08.162>.
- [24] T. Laumer, K. Wudy, M. Drexler, P. Amend, S. Roth, D. Drummer, M. Schmidt, Fundamental investigation of laser beam melting of polymers for additive manufacture, *J. Laser Appl.* 26 (2014) 042003, <https://doi.org/10.2351/1.4892848>.
- [25] L. Lanzl, K. Wudy, M. Drexler, D. Drummer, Laser-high-speed-DSC: process-oriented thermal analysis of PA 12 in selective laser sintering, *Phys. Procedia* 83 (2016) 981–990, <https://doi.org/10.1016/j.phpro.2016.08.103>.
- [26] M. Zhao, K. Wudy, D. Drummer, Crystallization kinetics of polyamide 12 during Selective laser sintering, *Polymers (Basel)* 10 (2018), <https://doi.org/10.3390/polym10020168>.
- [27] M. Schmid, Laser sintering with plastics, Technology, Processes, and Materials, (2018), <https://doi.org/10.3139/9781569906842.fm>.
- [28] D. Hui, R.D. Goodridge, C.A. Scotchford, D.M. Grant, Laser sintering of nano-hydroxyapatite coated polyamide 12 powders, *Addit. Manuf.* 22 (2018) 560–570, <https://doi.org/10.1016/j.ADDMA.2018.05.045>.
- [29] F.J. Baltá-Calleja, T.A. Ezquerro, Polymer crystallization: general concepts of theory and experiments, *Encycl. Mater. Sci. Technol.* (2001) 7244–7252, <https://doi.org/10.1016/B0-08-043152-6/01289-4> Elsevier.
- [30] N.L.A. McFerran, C.G. Armstrong, T. McNally, Nonisothermal and isothermal crystallization kinetics of nylon-12, *J. Appl. Polym. Sci.* 110 (2008) 1043–1058, <https://doi.org/10.1002/app.28696>.
- [31] A.W. Powell, A. Stavrinadis, I. De Miguel, G. Konstantatos, R. Quidant, White and brightly colored 3D printing based on resonant photothermal sensitizers, *Nano Lett.* 18 (2018) 6660–6664, <https://doi.org/10.1021/acs.nanolett.8b01164>.
- [32] L. Jonušauskas, M. Lau, P. Gruber, B. Gökce, S. Barcikowski, M. Malinauskas, A. Ovsianikov, Plasmon assisted 3D microstructuring of gold nanoparticle-doped polymers, *Nanotechnology* 27 (2016) 154001, <https://doi.org/10.1088/0957-4484/27/15/154001>.
- [33] M. Lau, R.G. Niemann, M. Bartsch, W. O'Neill, S. Barcikowski, Near-field-enhanced, off-resonant laser sintering of semiconductor particles for additive manufacturing of dispersed Au-ZnO-micro/nano hybrid structures, *Appl. Phys. A Mater. Sci. Process.* 114 (2014) 1023–1030, <https://doi.org/10.1007/s00339-014-8270-1>.
- [34] Z. Yan, R.A. Shah, G. Chado, S.K. Gray, M. Pelton, N.F. Scherer, Guiding spatial arrangements of silver nanoparticles by optical binding interactions in shaped light fields, *ACS Nano* 7 (2013) 1790–1802, <https://doi.org/10.1021/nn3059407>.
- [35] A. Neumeister, J. Jakobi, C. Rehbock, J. Moysig, S. Barcikowski, Monophasic ligand-free alloy nanoparticle synthesis determinants during pulsed laser ablation of bulk alloy and consolidated microparticles in water, *Phys. Chem. Chem. Phys.* 16 (2014) 23671–23678, <https://doi.org/10.1039/C4CP03316G>.
- [36] S. Link, Z.L. Wang, M.A. El-Sayed, Alloy formation of gold-silver nanoparticles and the dependence of the plasmon absorption on their composition, *J. Phys. Chem. B* 103 (1999) 3529–3533, <https://doi.org/10.1021/jp990387w>.
- [37] V. Amendola, O.M. Bakr, F. Stellacci, A study of the surface plasmon resonance of silver nanoparticles by the discrete dipole approximation method: effect of shape, size, structure, and assembly, *Plasmonics* 5 (2010) 85–97, <https://doi.org/10.1007/s11468-009-9120-4>.
- [38] I. Pastoriza-Santos, C. Kinnear, J. Pérez-Juste, P. Mulvaney, L.M. Liz-Marzán, Plasmonic polymer nanocomposites, *Nat. Rev. Mater.* 3 (2018) 375–391, <https://doi.org/10.1038/s41578-018-0050-7>.

- [39] Y.H. Lim, K.M. Tiemann, G.S. Heo, P.O. Wagers, Y.H. Rezenom, S. Zhang, F. Zhang, W.J. Youngs, D.A. Hunstad, K.L. Wooley, Preparation and in vitro antimicrobial activity of silver-bearing degradable polymeric nanoparticles of polyphosphoester-block-poly(l-lactide), *ACS Nano* 9 (2015) 1995–2008, <https://doi.org/10.1021/nn507046h>.
- [40] R. Zhu, C.H. Chung, K.C. Cha, W. Yang, Y.B. Zheng, H. Zhou, T. Bin Song, C.C. Chen, P.S. Weiss, G. Li, Y. Yang, Fused silver nanowires with metal oxide nanoparticles and organic polymers for highly transparent conductors, *ACS Nano* 5 (2011) 9877–9882, <https://doi.org/10.1021/nn203576v>.
- [41] N. Karak, Silver Nanomaterials and Their Polymer Nanocomposites, *Nanomater. Polym. Nanocomposites*, (2019), pp. 47–89, <https://doi.org/10.1016/b978-0-12-814615-6.00002-3>.
- [42] S.R. Athreya, K. Kalaitzidou, S. Das, Processing and characterization of a carbon black-filled electrically conductive Nylon-12 nanocomposite produced by selective laser sintering, *Mater. Sci. Eng. A* 527 (2010) 2637–2642, <https://doi.org/10.1016/j.msea.2009.12.028>.
- [43] S. Yuan, F. Shen, C.K. Chua, K. Zhou, Polymeric composites for powder-based additive manufacturing: materials and applications, *Prog. Polym. Sci.* 91 (2019) 141–168, <https://doi.org/10.1016/j.progpolymsci.2018.11.001>.
- [44] C. Blümel, M. Sachs, T. Laumer, B. Winzer, J. Schmidt, M. Schmidt, W. Peukert, K.E. Wirth, Increasing flowability and bulk density of PE-HD powders by a dry particle coating process and impact on LBM processes, *Rapid Prototyp. J.* 21 (2015) 697–704, <https://doi.org/10.1108/RPJ-07-2013-0074>.
- [45] J. Yang, A. Sliva, A. Banerjee, R.N. Dave, R. Pfeffer, Dry particle coating for improving the flowability of cohesive powders, *Powder Technol.* 158 (2005) 21–33, <https://doi.org/10.1016/j.powtec.2005.04.032>.
- [46] T. Hupfeld, T. Laumer, T. Stichel, T. Schuffenhauer, J. Heberle, M. Schmidt, S. Barcikowski, B. Gökce, A new approach to coat PA12 powders with laser-generated nanoparticles for selective laser sintering, *Procedia CIRP* 74 (2018) 244–248, <https://doi.org/10.1016/j.procir.2018.08.103>.
- [47] R. Streubel, M.B. Wilms, C. Doñate-Buendía, A. Weisheit, S. Barcikowski, J.H. Schleifenbaum, B. Gökce, Depositing laser-generated nanoparticles on powders for additive manufacturing of oxide dispersed strengthened alloy parts via laser metal deposition, *J. Appl. Phys.* 57 (2018), <https://doi.org/10.7567/JJAP.57.040310>.
- [48] D. Zhang, B. Gökce, S. Barcikowski, Laser synthesis and processing of colloids: fundamentals and applications, *Chem. Rev.* 117 (2017) 3990–4103, <https://doi.org/10.1021/acs.chemrev.6b00468>.
- [49] R. Streubel, G. Bendt, B. Gökce, Pilot-scale synthesis of metal nanoparticles by high-speed pulsed laser ablation in liquids, *Nanotechnology* 27 (2016) 205602, <https://doi.org/10.1088/0957-4484/27/20/205602>.
- [50] S. Jendzej, B. Gökce, M. Epple, S. Barcikowski, How size determines the value of gold: economic aspects of wet chemical and laser-based metal colloid synthesis, *ChemPhysChem* 18 (2017) 1012–1019, <https://doi.org/10.1002/cphc.201601139>.
- [51] D. Zhang, B. Gökce, Perspective of laser-prototyping nanoparticle-polymer composites, *Appl. Surf. Sci.* 392 (2017) 991–1003, <https://doi.org/10.1016/j.apsusc.2016.09.150>.
- [52] A. Blaeser, N. Million, D.F.D. Campos, L. Gamrad, M. Köpf, C. Rehbock, M. Nachev, B. Sures, S. Barcikowski, H. Fischer, Laser-based in situ embedding of metal nanoparticles into bioextruded alginate hydrogel tubes enhances human endothelial cell adhesion, *Nano Res.* 9 (2016) 3407–3427, <https://doi.org/10.1007/s12274-016-1218-3>.
- [53] J. Zhang, M. Chaker, D. Ma, Pulsed laser ablation based synthesis of colloidal metal nanoparticles for catalytic applications, *J. Colloid Interface Sci.* 489 (2017) 138–149, <https://doi.org/10.1016/j.jcis.2016.07.050>.
- [54] S. Reichenberger, G. Marzun, M. Muhler, S. Barcikowski, Perspective of surfactant-free colloidal nanoparticles in heterogeneous catalysis, *ChemCatChem* 11 (2019) 4489–4518, <https://doi.org/10.1002/cctc.201900666>.
- [55] S. Barcikowski, P. Wagener, A. Schwenke, Method for producing micro-nano combined active systems, US9403160B2, 2016. doi:10.1016/j.(73).
- [56] G. Marzun, J. Nakamura, X. Zhang, S. Barcikowski, P. Wagener, Size control and supporting of palladium nanoparticles made by laser ablation in saline solution as a facile route to heterogeneous catalysts, *Appl. Surf. Sci.* 348 (2015) 75–84, <https://doi.org/10.1016/j.apsusc.2015.01.108>.
- [57] M. Lau, A. Ziefuss, T. Komossa, S. Barcikowski, Inclusion of supported gold nanoparticles into their semiconductor support, *Phys. Chem. Chem. Phys.* 17 (2015) 29311–29318, <https://doi.org/10.1039/c5cp04296h>.
- [58] P. Wagener, A. Schwenke, S. Barcikowski, How citrate ligands affect nanoparticle adsorption to microparticle supports, *Langmuir* 28 (2012) 6132–6140, <https://doi.org/10.1021/la204839m>.
- [59] E. Bertin, A. Münzer, S. Reichenberger, R. Streubel, T. Vinnay, H. Wiggers, C. Schulz, S. Barcikowski, G. Marzun, Durability study of platinum nanoparticles supported on gas-phase synthesized graphene in oxygen reduction reaction conditions, *Appl. Surf. Sci.* 467–468 (2019) 1181–1186, <https://doi.org/10.1016/j.apsusc.2018.10.061>.
- [60] V. Merk, C. Rehbock, F. Becker, U. Hagemann, H. Nienhaus, S. Barcikowski, In situ non-DLVO stabilization of surfactant-free, plasmonic gold nanoparticles: effect of Hofmeister's anions, *Langmuir* 30 (2014) 4213–4222, <https://doi.org/10.1021/la404556a>.
- [61] A. Wurm, E. Zhuravlev, K. Eckstein, D. Jehnichen, D. Pospiech, R. Androsch, B. Wunderlich, C. Schick, Crystallization and homogeneous nucleation kinetics of poly(ϵ -caprolactone) (PCL) with different molar masses, *Macromolecules* 45 (2012) 3816–3828, <https://doi.org/10.1021/ma300363b>.
- [62] S. Monsheimer, M. Grebe, F.E. Baumann, W. Christoph, T. Schiffer, H. Scholten, *Laser-Sinter-Pulver mit verbesserten Recyclingeigenschaften, Verfahren zu dessen Herstellung und Verwendung des Laser-Sinter-Pulvers*, EP1413594A2, (2004).
- [63] N. Kallay, S. Žalac, Stability of nanodispersions: a model for kinetics of aggregation of nanoparticles, *J. Colloid Interface Sci.* 253 (2002) 70–76, <https://doi.org/10.1006/jcis.2002.8476>.
- [64] S. Dupin, O. Lame, C. Barrès, J.Y. Charneau, Microstructural origin of physical and mechanical properties of polyamide 12 processed by laser sintering, *Eur. Polym. J.* 48 (2012) 1611–1621, <https://doi.org/10.1016/j.eurpolymj.2012.06.007>.
- [65] S. Gogolewski, Effect of annealing on thermal properties and crystalline structure of polyamides, *Colloid Polym. Sci.* 257 (1979) 811–819 <http://www.springerlink.com/content/tu119881u5545674/>.
- [66] F. Paolucci, M.J.H. van Mook, L.E. Govaert, G.W.M. Peters, Influence of post-condensation on the crystallization kinetics of PA12: from virgin to reused powder, *Polymer (Guildf.)* 175 (2019) 161–170, <https://doi.org/10.1016/j.polymer.2019.05.009>.
- [67] A.T. Lorenzo, M.L. Arnal, J. Albuerno, A.J. Müller, DSC isothermal polymer crystallization kinetics measurements and the use of the Avrami equation to fit the data: guidelines to avoid common problems, *Polym. Test.* 26 (2007) 222–231, <https://doi.org/10.1016/j.polymertesting.2006.10.005>.
- [68] Tim Hupfeld, et al., Plasmonic seasoning: Giving color to desktop laser 3D-printed polymers by highly dispersed nanoparticles, *Adv. Opt. Mater.* (2020), <https://doi.org/10.1002/adom.202000473>.

5.3 Upscaling of nano-functionalization towards kg/h

Scaling up colloidal surface additivation of polymer powders for laser powder bed fusion

Reprinted from Procedia CIRP 94, 110-115 (2020) under CC BY-NC-ND

Highlights:

- Analysis of the colloidal additivation process chain and its current bottlenecks
- Comparison of a stirred-tank reactor and a continuous process design based on a static mixer
- Successful scale-up of colloidal additivation to 750 g of functionalized powder per hour in a continuous setup, based on the process determinants identified in chapter 5.3
- Outlook on automatization and further increasing the technology readiness level

Appendix:

- Drying procedure of powders after colloidal additivation (A7)

11th CIRP Conference on Photonic Technologies [LANE 2020] on September 6-10, 2020

Scaling up colloidal surface additivation of polymer powders for laser powder bed fusion

Tim Hupfeld^a, Carlos Doñate-Buendía^a, Matthias Krause^b, Alexander Sommereyns^{c,d}, Andreas Wegner^e, Thorsten Sinnemann^b, Michael Schmidt^{c,d}, Bilal Gökce^a, Stephan Barcikowski^{a*}

^aTechnical Chemistry I and Center for Nanointegration Duisburg-Essen (CENIDE), University of Duisburg-Essen, Universitätsstrasse 7, 45141 Essen, Germany

^bFachhochschule Dortmund, Department for mechanical engineering, Sonnenstrasse 96, 44139 Dortmund, Germany

^cInstitute of Photonic Technologies (LPT), Friedrich-Alexander Universität Erlangen-Nürnberg, Konrad-Zuse-Str.3-5, 91052 Erlangen, Germany

^dErlangen Graduate School in Advanced Optical Technologies (SAOT), Friedrich-Alexander Universität Erlangen-Nürnberg, Germany

^eChair for Manufacturing Technology, University of Duisburg-Essen, Lotharstrasse 1, 47057 Duisburg, Germany

* Corresponding author. Tel.: +49-201-183-3150; fax: +49-0201-183-3049. E-mail address: stephan.barcikowski@uni-due.de

Abstract

Nanoadditivation of polymer materials has high potential to meet the needs of material modification for laser powder bed fusion (PBF-LB/P), e.g. by tuning optical or mechanical properties. Colloidal additivation of polymer powders has proven to avoid aggregation of nanofillers on the polymer surface during additivation. In our study, we demonstrate kg-scale, continuous colloidal surface additivation of polymer powders to generate sufficient amounts for PBF-LB/P process development and manufacturing of test specimens. Furthermore, colloidal additivation achieves a high surface coverage even at low wt% and allows PBF-LB/P with CO₂ and diode lasers to form parts preserving the superior nanoparticle dispersion within TPU and PA12.

© 2020 The Authors. Published by Elsevier B.V.

This is an open access article under the CC BY-NC-ND license (<http://creativecommons.org/licenses/by-nc-nd/4.0/>)

Peer review statement: Peer-review under responsibility of the Bayerisches Laserzentrum GmbH

Keywords: nanocomposites; laser powder bed fusion (PBF-LB); selective laser sintering (SLS); Laser synthesis and processing of colloids; upscaling, colloidal additivation; deposition

Introduction

Laser powder bed fusion (PBF-LB/P, according to ISO/ASTM DIS 52900:2018) has become an important prototyping and manufacturing technique over the last years [1]. Extending the variety of polymer powder feedstock materials is an important step to unlock PBF-LB/P's potentials for industrial applications [2], e.g. in fields of aerospace and automotive. Developing new materials, however, is challenging, due to the complex processing conditions during PBF-LB/P [3]. Additivation of polymer powders with nanomaterials for PBF-LB/P has proven to be a versatile approach for enhancing the powder processability and to

introduce new part properties and functionalization [4–7]. A high dispersion and homogeneous distribution of nanoparticles in/on the polymer matrix poses a key feature for the fabrication of nanoparticle-composites, but cannot be reached easily by conventional additivation methods like dry coating [8–10]. Colloidal additivation can overcome this challenge and can lead to extraordinary dispersion of nanoparticles on the polymer surface [11–13]. Nanoparticles are generated by flexible and scalable laser synthesis and processing of colloids (LSPC) [14] in aqueous solution and adsorbed onto the polymer surface by pH-controlled mixing with the polymer powder, followed by filtration and drying. This process is also well known for fabrication of heterogeneous catalysts [15–17]

2212-8271 © 2020 The Authors. Published by Elsevier B.V.

This is an open access article under the CC BY-NC-ND license (<http://creativecommons.org/licenses/by-nc-nd/4.0/>)

Peer review statement: Peer-review under responsibility of the Bayerisches Laserzentrum GmbH

and additivation of steel powders for additive manufacturing [18,19].

In order to generate sufficient amounts of nanoparticle-polymer composite powders for statistically validated PBF-LB/P experiments and process developments (> 3 kg), upscaling of the colloidal additivation process is of central importance. Hence, laser-generated nanoparticles in the gram-scale will be needed for each experiment, e.g. 3 g of colloidal nanoparticles are necessary to fabricate 3 kg of polymer composite powder with 0.1 wt% loading. The scalability of laser synthesis, namely the employed technique laser ablation in liquids (LAL), can be achieved by using a flow chamber setup in combination with high power, high repetition rate lasers and advanced scanning strategies [20] to result in a productivity of more than 1 g/h. Since the colloidal additivation of polymer powders is governed by colloidal stability and is therefore dependent on the interplay of particle concentration, electrostatic forces and mixing conditions [11,13], upscaling requires precise control of these parameters.

Our study focuses on upscaling of colloidal additivation towards kg-scale for fundamental PBF-LB/P studies and the influence of different upscaling strategies on the overall process duration as well as on the reproducibility and quality of the composite powders. Examples will be given for the PA12 (Evonik Vestosint 1115) and TPU (AM POLYMERS Rolaserit PB01) polymer powders decorated with silver nanoparticles as model systems, since optical powder analysis can be used on the surface plasmon resonance (SPR) peak to investigate the dispersion quantity and quality of nanoparticles on the polymer surface [13].

Strategies for upscaling

The process of colloidal additivation can be divided into five steps. LSPC, mixing, and filtration represent the “liquid part” in which the nanoparticle adsorption onto the powder takes place, whereas drying and sifting represent the “dry part”. A long duration for a specific process step, however, does not automatically mean that it is labor intensive, e.g. compared to the liquid part, the dry part requires a relatively small number of man-hours, although it makes up most of the overall process duration (Figure 1). Moreover, process duration and man-hours required for drying and sifting of a specific amount of polymer powder are independent of the individual batch size. However, several parameters with high influence on the liquid part and the overall process duration can be identified. For a certain mass of composite powder, the nanoparticle load governs the LSPC process duration. The higher the targeted nanoparticle load (wt%), the more nanoparticles are needed and the longer lasts the LSPC process. With increasing batch size, process duration of colloidal additivation decreases, because fewer batches are necessary for the same powder mass, resulting in fewer cleaning and preparation cycles (Figure 1a). For example, batches with 50 g each result in a total process duration of 11 hours for the liquid part, corresponding to 12 man-hours for preparation and operating the setup, whereas mixing in a 1 kg batch reduces the process duration and the required man-hours in the liquid part to 3 h and 4 h, respectively.

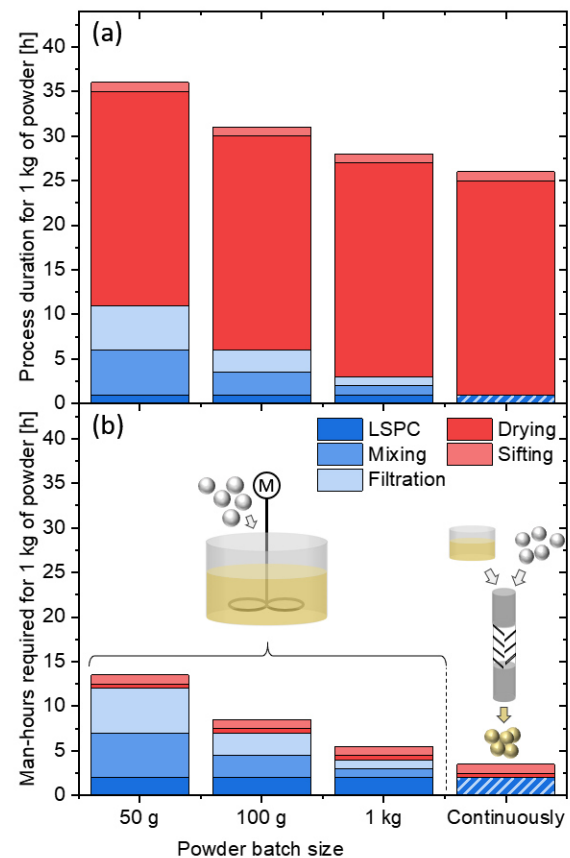


Figure 1: Processing steps (liquid part and dry part) for colloidal additivation. Share of each process step on (a) the overall process duration and on (b) the required man-hours. The example is given for processing of 1 kg of polymer powder with 0.1 wt% of nanoparticles for different powder batch sizes compared to continuous processing. Fluid volumes scale linearly with the polymer amount and range from 1 l to 20 l for batch sizes of 50 g to 1 kg.

Either the colloid can be collected during LSPC and mixed with the polymer afterwards (Figure 2a), or a semi-continuous process can be established to support the nanoparticles on the polymer in parallel to LSPC (Figure 2b). In both cases stirring of the suspension is required for 60 minutes after adding the last portion of colloid to ensure complete mixing and high supporting efficiency (depending on the stirring conditions and material system).

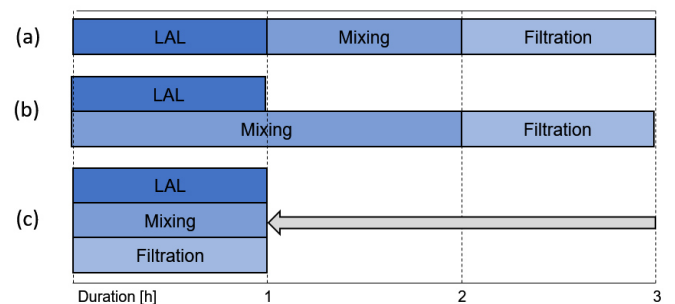


Figure 2: Different procedures for upscaling towards 1 kg of polymer powder at 0.1 wt% of silver. (a) Batch wise and (b) Semi-continuous colloidal additivation in a stirred-tank reactor (1 kg batch) and (c) continuous processing with a static mixer.

Up-scaling of a stirred-tank process always needs adaption of the stirring conditions (geometry and rotation speed) for turbulent flow (high Reynolds number Re) and fast mixing to minimize the size of single fluid elements and to shorten the necessary diffusion length between polymer and nanoparticle. In order to decrease the mixing time and increase the process control, a static mixer can be utilized instead of a stirred-tank reactor. This also enables shortening the overall process duration (Figure 2c) by fully continuous operation of LSPC, mixing/supporting and filtration in parallel. Variation of reactor geometry and volume flow would also require further adaption to the colloidal addition process for various nanoparticle-polymer systems and nanoparticle loadings. As a disadvantage, the more complex setup for continuous processing might not be useful for small batch fabrication with just a few grams of material.

Results and discussion

1.1. Batch wise colloidal addition in a stirred-tank reactor

100 g batches in a stirred-tank reactor are the first step towards upscaling, since it delivers a sufficient amount for powder characterization, e.g. measurement of Hausner ratio, powder spreading tests on a PBF-LB/P machine or for first PBF-LB/P experiments.

As it was shown for silver nanoparticles on commercial PA12 powder (Evonik Vestosint 1115), the dispersion of PA12 powder in water induces a significant decrease in pH (buffer effect) during colloidal addition in a stirred-tank reactor [13]. The longer the mixing duration and residence time, the lower the pH value of the suspension. This will affect the colloidal stability and the adsorption process. Moreover, different polymer-nanoparticle systems require different procedures for pH adjustment to perform colloidal addition. Whereas the used PA12 powder comes with an intrinsic pH shift caused by the buffer effect, the TPU powder (AM POLYMERS Rolaserit PB01) does not change the pH of the suspension and needs external pH adjustment for successful colloidal addition with silver nanoparticles [11]. If further pH-adjustment is needed during mixing, stirring conditions become even more important, because a long stirring time at a low pH close to the isoelectric point increases the probability for aggregation of the nanoparticles. This is not an issue for small batches of up to 100 g, where the mixing time for complete supporting of the nanoparticles on the polymer is still in the range of minutes to reach high supporting efficiency, as it is shown in Figure 3 for TPU microparticles additivated with silver nanoparticles. After stirring for 15 minutes under constant shifting of the pH by addition of hydrochloric acid (1 ml/min of 1 mol/l, total volume: 5 ml), the surface plasmon resonance (SPR) peak intensity of the permeate completely vanishes (Figure 3a), corresponding to a reproducible supporting efficiency of $99.80 \pm 0.12 \%$. This is confirmed by UV-Vis absorption analysis of the powder (Figure 3c). The SPR peak of silver was successfully transferred to the polymer powder (Figure 3b) and the SPR peak position only slightly changes for upscaling from 1 g to 50 g or 100 g batches (Figure 3d). However, 100 g batches show a 20 % reduced SPR peak absorption with higher fluctuations, indicated by larger error

bars. The influence of long mixing time becomes even more obvious when increasing the batch size to 1 kg of TPU powder. As expected, this results in much longer stirring time and a higher risk for complete aggregation of silver and loss of plasmonic properties of the powder (Figure 3c,d). After 60 minutes of stirring, the supporting efficiency is reduced and powder and permeates tend to a green/grey color, instead of yellow color of non-aggregated Ag nanoparticles. Although this issue might be less pronounced for PA12-Ag, which does not need external pH adjustment and is a more robust system with less degree of freedom, these experiments highlight the potential problems during upscaling in a stirred-tank.

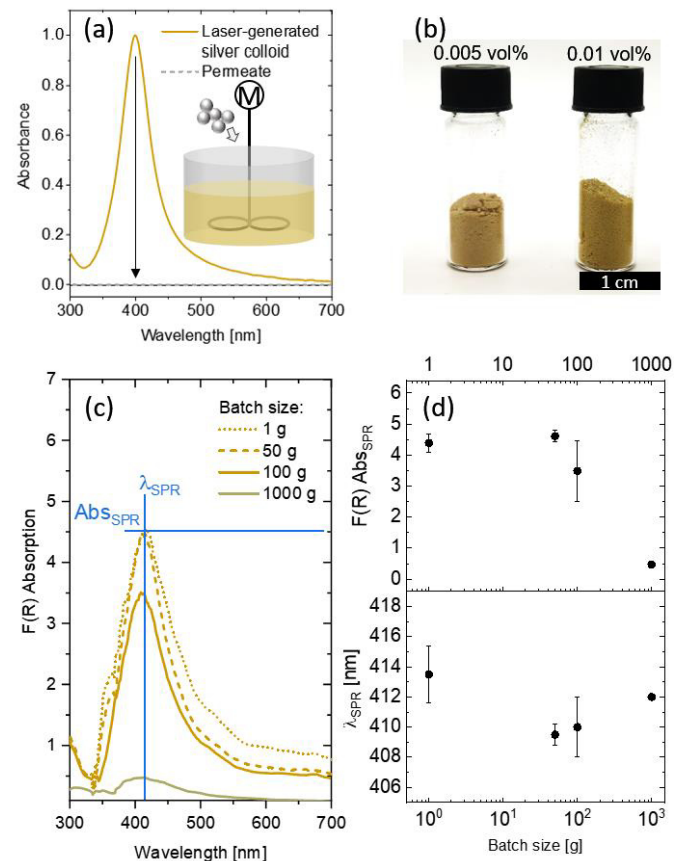


Figure 3: (a) UV-Vis absorbance spectra of a silver colloid and the permeate before/after colloidal addition in a 100 g batch of TPU, (b) exemplary powders, (c) absorption spectra of the functionalized powders made in different batch sizes and (d) corresponding SPR peak intensity ($F(R)$ absorption) and SPR peak wavelength. For the 1 kg batches, permeates come with high instability, which makes exact determination of supporting efficiency impossible

1.2. Continuous colloidal addition with a static mixer

In order to shorten the mixing time and increase the process control, a static mixer can be utilized instead of a stirred-tank reactor for larger batch sizes. It also enables shortening the overall process duration as it was shown in Figure 2c by fully continuous operation of LSPC, mixing/supporting and filtration in parallel. To prove the concept for continuous colloidal addition, a static mixer cascade was constructed based on the requirements regarding the necessary residence time as well as the polymer powder and nanoparticle

concentrations given for the PA12-silver-system [13]. 2 m of tubing (inner diameter 13 mm) were mounted on a base plate and filled with static mixer elements (ESSKA, PTFE elements) to create a static mixer with a total volume of 350 ml (Figure 4a,b). The volume flow of the colloid ($c = 50 \text{ mg/l}$) and the microparticle suspension ($c = 50 \text{ g/l}$) were both 250 ml/min. Operating at a total volume flow rate of 500 ml/min, equivalent to an average residence time of 40 s. The laser-generated silver colloid and the polymer suspension were stored in reservoirs of 2 l, which were refilled regularly. With respect to the previous experiments and under assumption of good mixing quality, a dwell time of 40 s is expected to achieve at least 90 % of supporting efficiency [13]. After the whole tubing was filled with suspension, samples of the suspension at the output of the static mixer cascade were taken every 2 minutes and directly filtered to allow calculations of supporting efficiency from the remaining SPR peak intensity of the permeate. The process runs for ten minutes in total and the complete product suspension was filtered directly at the output of the mixer.

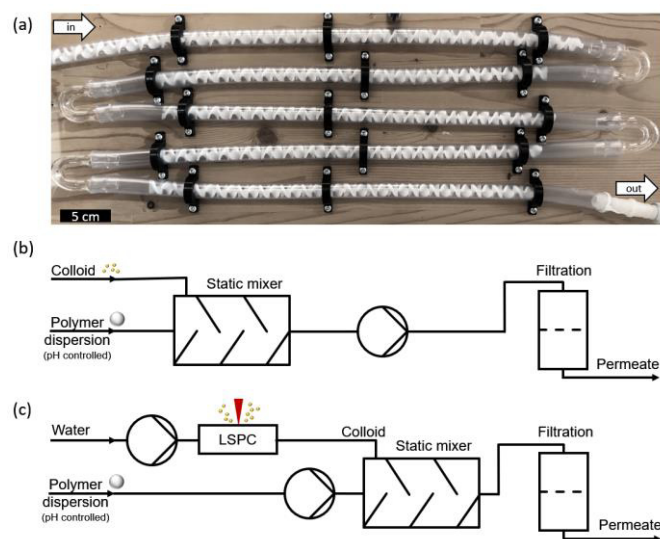


Figure 4: (a) Image of the static mixer setup. (b) Schematic illustration of the used set-up operating with one sucking pump and (c) illustration of the proposed additivition system with two pumps, one of them directly attached to the LAL setup with further potential for fully automated continuous colloidal additivition of nanoparticles on polymer powders.

As expected, the SPR peak intensity of the permeate decreases significantly compared to the educt colloid and the supporting efficiency is constantly between 90 and 95 % throughout the process (Figure 5a). After filtration and drying, the homogeneously yellow-colored powders were investigated by diffuse reflectance spectroscopy, where a pronounced SPR peak can be observed (Figure 5b). The intensity at the SPR peak as a function of time in Figure 5b confirms only minor fluctuations and a steady state of the process. The SPR peak position at around 400 nm and the SPR intensity are similar to batch-wise processed silver-functionalized PA12 powder [12]. Compared to TPU powder, the SPR peak position is blue-shifted by 10-15 nm, indicating an even better dispersion of the nanoparticles on the PA12. Within 10 min a total liquid volume of 5 l flowed through the setup, equivalent to a productivity of 750 g/h (3 kg in 4 h), proving the concept of

downstream colloidal supporting. To increase productivity to an even higher extend, the volume flow rate and the length of the static mixer could be increased, resulting in a similar residence time but a more intense mixing. An increase of the reactor diameter is also an option but comes with decreasing velocity and therefore a less turbulent flux (lower Re), which should be avoided to ensure good mixing quality at the given residence time [21].

In future studies, the setup schematically illustrated in Figure 4c directly attached to a LSPC setup could allow even better control over the separate volume flows, for example to allow adjustment of pH values and nanoparticle load. Inline process monitoring, e.g. UV-Vis spectrometer, flowmeter, and pH-meter would allow full automatization and further increase of productivity and process stability. In order to influence the nanoparticle size, the setup could further be extended with inline centrifugation of the colloids before entering the static mixer [22].

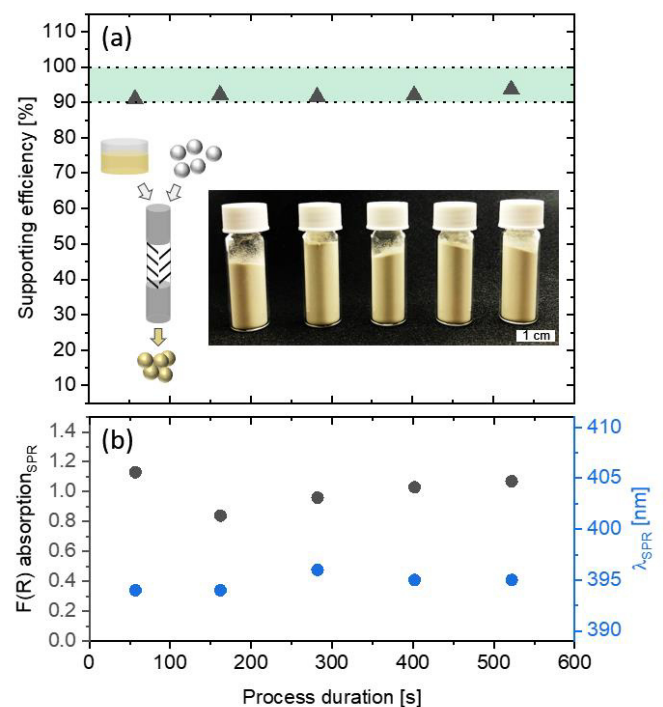


Figure 5: (a) Supporting efficiency as a function of process duration during continuous colloidal supporting of colloidal nanoparticles on polymer powders with a static mixer at a volume flow rate of 500 ml/min and a powder throughput of 750 g/h (0.1 wt% silver). The inset shows dried functionalized powders collected during the process. (b) Exemplary F(R) absorption spectra of a functionalized powder and corresponding SPR peak absorption as a function of process duration.

1.3. Nanoparticle dispersion and powder processability

Colloidal additivated powders were sifted ($125 \mu\text{m}$) after drying. In addition, TPU powder was additivated with a flow aid (0.4 wt%, AM POLYMERS AC1) to enhance flowability. The functionalized powders showed a Hausner ratio of 1.14 (TPU-Ag with flow aid) and 1.13 (PA12-Ag) according to VDI 3405 sheet 1.1 norm, with matches the Hausner ratio of the base polymer powders without silver nanoparticle additivation

(Table 1). Finally, both feedstock materials were successfully processed through PBF-LB/P. TPU-Ag was processed on a diode laser machine (Sintratec S1, $\lambda = 445$ nm, more information in Table 2), whereas PA12 powder was processed on a Sharebot Snowwhite ($\lambda = 10.6$ μm , layer height of 300 μm , building platform temperature of 192 $^{\circ}\text{C}$). An overview of the materials and resulting parts is given in Figure 6. The preservation of the yellow color caused by the SPR of silver nanoparticles proves the outstanding nano-dispersion of silver along the whole process chain, which is the key feature of colloidal additivition and is also supported by TEM images of the final PA12 part (inset Figure 6f)

Table 1. Hausner ratio of the silver functionalized powders (0.01 vol%) compared to the powders without silver functionalization.

	Hausner ratio
TPU + flow aid	1,20
TPU-Ag + flow aid	1,14
PA12	1,15
PA12-Ag	1,13

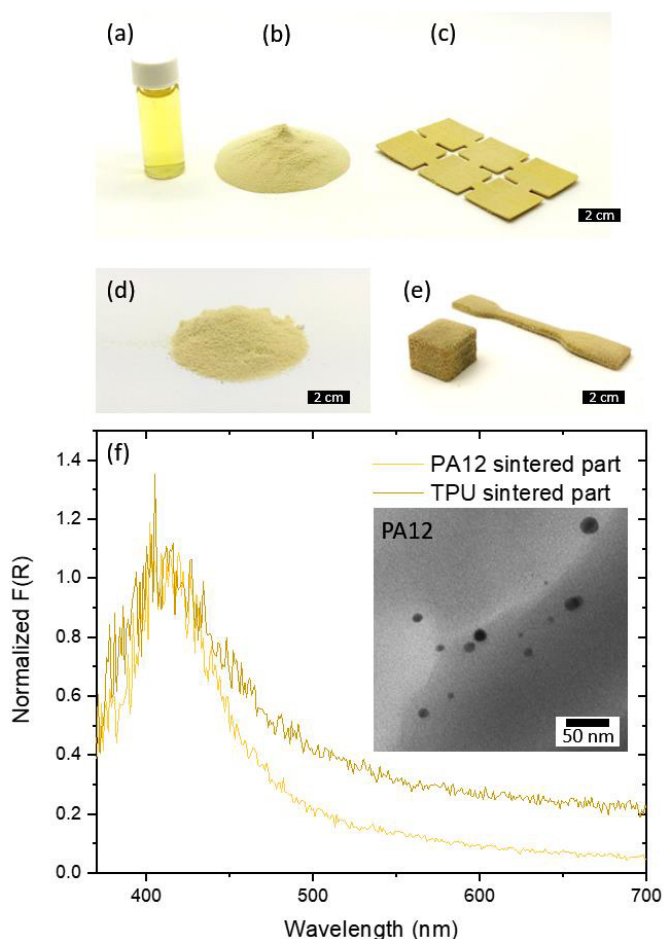


Figure 6: Conservation of the surface plasmon resonance along the process chain for colloidal additivition of PA12 and TPU powders with silver nanoparticles, indicated by its characteristic yellow color. (a) Laser-generated silver colloid, (b) silver additivited PA12 powder, (c) test structures built from PA12-Ag powder by CO₂-laser PBF-LB/P and (d) TPU powder with (e) corresponding TPU-Ag test structures built by diode laser PBF-LB/P, exploiting the enhanced powder absorption by the plasmon resonance at the diode laser wavelength of 445 nm. (f) Absorption measurement of printed parts with the inset showing a TEM image of a sliced PA12 part.

Table 2. Parameters for diode laser PBF of silver functionalized TPU powder with a silver nanoparticle loading of 0.01 vol%.

	Powder bed temperature [°C]	Laser power [W]	Hatch distance [mm]	Scan speed [mm/s]	Volume energy density [J/mm ³]
Sintratec S1 (445 nm laser)	94	2	0.05	200	2.0

Conclusion

In conclusion, the process of colloidal additivition of nanoparticles on polymer powders was successfully scaled-up towards kg-scale. Since drying and sifting are relatively easy to scale to kg/day, the liquid-phase processing is identified as the current bottleneck with highest optimizing potential to reduce the amount of man-hours/kg. For small batch sizes of up to 100 g of functionalized powder, a batch process in a stirred-tank reactor is a feasible method, whereas a continuous processing with a static mixer leads to high throughput in the kg-scale, which is necessary for using the nanoparticle-functionalized powder for PBF-LB/P part fabrications. Besides, along the whole process chain, nanoparticle properties are preserved. Whilst productivity is enhanced by this continuous approach, process control could profit from it as well. The fast mixing and narrow residence time distribution of a static mixer could enable precise control over nanoparticle adsorption and dispersion on the polymer particle surface by fine tuning pH values, volume flow rates and concentrations of the mixed fluids. Nanoparticles could be supported just a few seconds after LSPC under constant conditions. Encouraged by the results presented here, future studies should focus on process optimization and investigation of the deposition yield, kinetics and nanoparticle dispersion in steady state conditions for various polymer-nanoparticle systems. Through automatization, this continuous colloidal additivition approach has high potential to meet the needs for upscaling towards the multi-kg and thus increasing the technology readiness level (TRL), which is a common measure for evaluation of the technology development status [23] and was demonstrated by Maurer et al. for laser-based nanoparticle-polymer composite fabrication [24].

Acknowledgements

Tim Hupfeld thanks Vladyslav Sharov for his help during experiments. Tim Hupfeld also acknowledges Evonik Industries for financial support of his work. Alexander Blasczyk gratefully acknowledges funding of the Erlangen Graduate School in Advanced Optical Technologies (SAOT) by the German Research Foundation (DFG) in the framework of the German excellence initiative. The authors gratefully acknowledge the funding by the German Research Foundation (DFG) within the priority program (SPP) 2122 “Materials for Additive Manufacturing (MATframe, BA 3580/27-1 + SCHM 2115/78-1).

References

- [1] Wohlers Associates, Wohlers Report 2019, (2019) 369.
- [2] Nationale Akademie der Wissenschaften Leopoldina, Deutschen Akademie der Technikwissenschaften Acatech, Additive Fertigung, Munich, 2017.
- [3] A. Wegner, New polymer materials for the laser sintering process: Polypropylene and others, *Phys. Procedia*. 83 (2016) 1003–1012. doi:10.1016/j.phpro.2016.08.105.
- [4] S. Yuan, F. Shen, C.K. Chua, K. Zhou, Polymeric composites for powder-based additive manufacturing: Materials and applications, *Prog. Polym. Sci.* 91 (2019) 141–168. doi:10.1016/j.progpolymsci.2018.11.001.
- [5] S.R. Athreya, K. Kalaitzidou, S. Das, Processing and characterization of a carbon black-filled electrically conductive Nylon-12 nanocomposite produced by selective laser sintering, *Mater. Sci. Eng. A*. 527 (2010) 2637–2642. doi:10.1016/j.msea.2009.12.028.
- [6] A.W. Powell, A. Stavrinadis, I. De Miguel, G. Konstantatos, R. Quidant, White and Brightly Colored 3D Printing Based on Resonant Photothermal Sensitizers, *Nano Lett.* 18 (2018) 6660–6664. doi:10.1021/acs.nanolett.8b01164.
- [7] M.M. Lexow, D. Drummer, New Materials for SLS: The Use of Antistatic and Flow Agents, *J. Powder Technol.* 2016 (2016) 1–9. doi:http://dx.doi.org/10.1155/2016/4101089.
- [8] H.C. Kim, H.T. Hahn, Y.S. Yang, Synthesis of PA12/functionalized GNP nanocomposite powders for the selective laser sintering process, *J. Compos. Mater.* 47 (2012) 501–509. doi:10.1177/0021998312441812.
- [9] C. Blümel, M. Sachs, T. Laumer, B. Winzer, J. Schmidt, M. Schmidt, W. Peukert, K.E. Wirth, Increasing flowability and bulk density of PE-HD powders by a dry particle coating process and impact on LBM processes, *Rapid Prototyp. J.* 21 (2015) 697–704. doi:10.1108/RPJ-07-2013-0074.
- [10] J. Yang, A. Sliva, A. Banerjee, R.N. Dave, R. Pfeffer, Dry particle coating for improving the flowability of cohesive powders, *Powder Technol.* 158 (2005) 21–33. doi:10.1016/j.powtec.2005.04.032.
- [11] T. Hupfeld, A. Wegner, M. Blanke, C. Doñate-Buendía, V. Sharov, S. Nieskens, M. Piechotta, M. Giese, S. Barcikowski, B. Gökce, Plasmonic seasoning: Giving color to desktop laser 3D-printed polymers by highly dispersed nanoparticles, *Adv. Opt. Mater.* (2020). doi:10.1002/adom.202000473.
- [12] T. Hupfeld, T. Laumer, T. Stichel, T. Schuffenhauer, J. Heberle, M. Schmidt, S. Barcikowski, B. Gökce, A new approach to coat PA12 powders with laser-generated nanoparticles for selective laser sintering, *Procedia CIRP*. 74 (2018) 244–248. doi:10.1016/j.procir.2018.08.103.
- [13] T. Hupfeld, A. Blaszcyk, T. Schuffenhauer, E. Zhuravlev, M. Krebs, S. Gann, O. Keßler, M. Schmidt, B. Gökce, S. Barcikowski, How colloidal surface addition of polyamide 12 powders with well-dispersed silver nanoparticles influences the crystallization already at low 0.01 vol%, *Submitt. to Addit. Manuf.* (2020).
- [14] D. Zhang, B. Gökce, S. Barcikowski, Laser Synthesis and Processing of Colloids: Fundamentals and Applications, *Chem. Rev.* 117 (2017) 3990–4103. doi:10.1021/acs.chemrev.6b00468.
- [15] S. Reichenberger, G. Marzun, M. Muhler, S. Barcikowski, Perspective of Surfactant-Free Colloidal Nanoparticles in Heterogeneous Catalysis, *ChemCatChem*. 11 (2019) 4489–4518. doi:10.1002/cctc.201900666.
- [16] D. Zhang, J. Liu, P. Li, Z. Tian, C. Liang, Recent Advances in Surfactant-Free, Surface-Charged, and Defect-Rich Catalysts Developed by Laser Ablation and Processing in Liquids, *ChemNanoMat*. 3 (2017) 512–533. doi:10.1002/cnma.201700079.
- [17] J. Zhang, M. Chaker, D. Ma, Pulsed laser ablation based synthesis of colloidal metal nanoparticles for catalytic applications, *J. Colloid Interface Sci.* 489 (2017) 138–149. doi:10.1016/j.jcis.2016.07.050.
- [18] C. Doñate-Buendía, F. Frömel, M.B. Wilms, R. Streubel, J. Tenkamp, T. Hupfeld, M. Nachev, E. Gökce, A. Weisheit, S. Barcikowski, F. Walther, J.H. Schleifenbaum, B. Gökce, Oxide dispersion-strengthened alloys generated by laser metal deposition of laser-generated nanoparticle-metal powder composites, *Mater. Des.* 154 (2018) 360–369. doi:10.1016/j.matdes.2018.05.044.
- [19] R. Streubel, M.B. Wilms, C. Doñate-Buendía, A. Weisheit, S. Barcikowski, J.H. Schleifenbaum, B. Gökce, Depositing laser-generated nanoparticles on powders for additive manufacturing of oxide dispersed strengthened alloy parts via laser metal deposition, *Jpn. J. Appl. Phys.* 57 (2018). doi:10.7567/JJAP.57.040310.
- [20] R. Streubel, S. Barcikowski, B. Gökce, Continuous multigram nanoparticle synthesis by high-power, high-repetition-rate ultrafast laser ablation in liquids, *Opt. Lett.* 41 (2016) 1486–1489. doi:10.1364/OL.41.001486.
- [21] M.H. Pahl, E. Muschelkautz, Einsatz und Auslegung statischer Mischer, *Chemie Ing. Tech.* 51 (1979) 347–364. doi:10.1002/cite.330510504.
- [22] S. Kohnowski, F. Seiser, J.P. Wiederrecht, S. Reichenberger, T. Vinnay, S. Barcikowski, G. Marzun, Effective size separation of laser-generated, surfactant-free nanoparticles by continuous centrifugation, *Nanotechnology*. 31 (2020). doi:10.1088/1361-6528/ab55bd.
- [23] M. Héder, From NASA to EU: The evolution of the TRL scale in Public Sector Innovation, *Innov. J.* 22 (2017).
- [24] E. Maurer, S. Barcikowski, B. Gökce, Process Chain for the Fabrication of Nanoparticle Polymer Composites by Laser Ablation Synthesis, *Chem. Eng. Technol.* 40 (2017) 1535–1543. doi:10.1002/ceat.201600506.

6 3D printing of nanoparticle-functionalized powders

Nanoparticles generated by laser synthesis enable colloidal additivition of polymer microparticles to create nanoparticle-functionalized feedstock material that are ready for PBF-LB. After focusing on the colloidal additivition process and its upscaling potential for providing sufficient powder amounts, this chapter will closely evaluate the influence of highly dispersed nanoparticles on the PBF-LB process. As discussed in Chapter 2, powder spreading, laser absorption, and melting and resolidification behavior of the polymer govern PBF-LB. The nanoparticle size and dispersion could potentially influence all these factors simultaneously. For example, nanoparticles on the surface of polymer microparticles affect the van der Waals forces between the microparticles, thereby altering the powder flowability and recoating behavior [19,20,135]. Nanoparticles also influence the beam-matter interaction; e.g., light scattering or absorption [22,136,138,139]. Instead of using a broad band absorber such as carbon black to increase the light absorption of polymers for diode laser PBF; absorbers with narrow wavelength ranges are of particular interest [128,129]. This is shown in Chapter 6.1 for thermoplastic polyurethane (TPU) powder, whose adsorption properties in the blue spectral region can be tuned by homogeneous decoration with just 0.01 vol% of plasmonic silver nanoparticles, which act as photothermal sensitizer during processing with a 445 nm diode laser PBF-machine [272]. Finally, highly dispersed nanoparticles also modify the melting and resolidification behaviors and may act as nuclei during cooling of the polymer after laser-induced melting [16,113,131]. Even at small nanoparticle loadings well below 1 wt%, high dispersion and small nanoparticle size may affect crystallization. Since heterogeneous nucleation can also manipulate the microstructure of the printed part, which also affects the mechanical properties [18,138–140,145,146], an investigation of calorimetric properties and microstructure is shown in Chapter 6.2 .

6.1 Tuning the laser absorption of polymer powders

Plasmonic Seasoning: Giving Color to Desktop Laser 3D Printed Polymers by Highly Dispersed Nanoparticles

Reprinted from *Advanced Optical Materials* 2000473 (2020) under CC BY

Highlights:

- Detailed study of the nanoparticle adsorption kinetics on polymer powders, highlighting the important role of stirring conditions
- The pH-dependent zeta potential affects supporting efficiency (quantity) and dispersion (quality)
- Dispersion quality determines the optical properties of plasmonic TPU powders
- Highly dispersed silver nanoparticles delay TPU melting during heating
- Ag nanoparticles act as photothermal sensitizers and enable PBF-LB with compact diode laser machines already at 0.01 vol% to create 3D objects

Appendix:

- Supporting information (A8)
- Spray drying of TPU powder suspensions for nanoparticle-functionalization (A9)

Plasmonic Seasoning: Giving Color to Desktop Laser 3D Printed Polymers by Highly Dispersed Nanoparticles

Tim Hupfeld, Andreas Wegner, Meik Blanke, Carlos Doñate-Buendía, Vladyslav Sharov, Simon Nieskens, Markus Piechotta, Michael Giese, Stephan Barcikowski,* and Bilal Gökce

Material development is key for continuing the exponential growth in the field of 3D printing. However, 3D printing of polymers by laser powder bed fusion (PBF-LB) still is limited to a few polymer powder materials, which restricts the range of applications. Tailoring the chemical, rheological, mechanical, or optical properties of the feedstock powder to the requirements of the laser printing process poses a significant challenge. In order to meet global trends in the commercialization of desktop 3D printers, the use of inexpensive and compact diode lasers for PBF-LB in the visible or near-infrared range is highly desired. However, at present, only black objects can be printed by desktop laser printers since only commercial carbon black-based composite powders meet their laser absorption requirements. In this study, a route for tuning the absorption properties of thermoplastic polyurethane polymers and incorporating color into printed objects by using minute amounts (i.e., 0.01 vol%) of highly dispersed plasmonic silver nanoparticles is reported, presenting a new way for colored parts to be produced through laser 3D printing.

shape-shifted 4D printing.^[5] In line with this development, the demand emerged for new materials suitable for additive manufacturing. In the field of laser powder bed fusion of polymers (PBF-LB/P) (a method defined by ISO/ASTM 52900) ≈90% of all polymer powders currently in use are polyamide powders.^[6] Thus, there is a great effort to develop new processable materials for this particular method.^[7,8] However, suitable new powders are being introduced to the market very slowly, and they often must struggle to match industrial quality standards, such as sufficient flowability, optical absorption, and melting and resolidification characteristics.^[9–11] For example, thermoplastic polyurethane (TPU) is a versatile material,^[12,13] and it is interesting for laser powder bed fusion (PBF-LB) because it has high resistance against wear or chemicals^[14] and exhibits adjustable mechanical

1. Introduction

With the increasing need for more sustainable use of raw materials and the demand for higher complexity in design, the interest in additive manufacturing (colloquially: 3D printing) has grown exponentially in development and application^[1–3] as well as in society,^[4] and new responsive materials even have given rise to

properties by a combination of soft, amorphous elastomers and hard, ordered thermoplastic domains.^[15,16] Goodridge et al.^[11] and Ziegelmeier et al.^[17] showed that TPU can be processed successfully by PBF-LB. However, apart from its extrinsic properties, such as the flowability of the powder, the unfavorable thermal properties inhibit the use of TPU powders in PBF-LB processes.^[18] The soft, amorphous portion of the structure results in TPU not having a sharp melting and crystallization peak; rather, it has broad phase transitions that are difficult to define. In addition, the peaks are relatively close to each other, resulting in only a narrow process window for PBF-LB. For this reason, process temperature and especially the preheating temperature for TPU can be adjusted only to a limited extent; thus, to date, these temperatures have been approximated by complex, empirical “trial & error” optimization.^[18] Also, TPU has an increased tendency to coalescence during heating (caking), and this reduces the recyclability of the powder.^[17] So far, these problems have been compensated by complicated and expensive adaptations of the process parameters. Thus, it is of great interest to modify the intrinsic properties of TPU powder for PBF-LB and aim for a sharp melt transition, which would allow high preheating temperatures without caking.

The development of PBF-LB processable polymers, such as TPU, is limited further by its weak absorption in the visible and near-infrared ranges, so expensive CO₂ lasers are required to heat and fuse the powders. Studies of process parameter studies would be facilitated^[19] if desktop PBF-LB machines could be used with smaller build volumes, simpler beam guidance systems, and diode laser sources. Carbon-based photothermal

T. Hupfeld, Dr. C. Doñate-Buendía, V. Sharov, S. Nieskens, Prof. S. Barcikowski, Dr. B. Gökce
Technical Chemistry I and Center for Nanointegration
Duisburg-Essen (CENIDE)
University of Duisburg-Essen
Universitaetsstrasse 7, Essen 45141, Germany
E-mail: stephan.barcikowski@uni-due.de

Dr. A. Wegner, M. Piechotta
Chair for Manufacturing Technology
University of Duisburg-Essen
Lotharstrasse 1, Duisburg 47057, Germany
M. Blanke, Prof. M. Giese
Institute of Organic Chemistry and CENIDE
University of Duisburg-Essen
Universitaetsstraße 7, Essen 45141, Germany

 The ORCID identification number(s) for the author(s) of this article can be found under <https://doi.org/10.1002/adom.202000473>.

© 2020 The Authors. Published by WILEY-VCH Verlag GmbH & Co. KGaA, Weinheim. This is an open access article under the terms of the Creative Commons Attribution License, which permits use, distribution and reproduction in any medium, provided the original work is properly cited.

DOI: 10.1002/adom.202000473

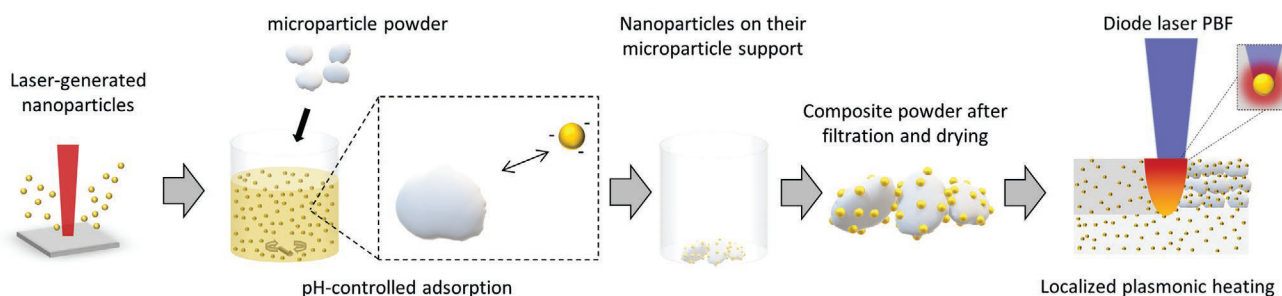


Figure 1. Process chain for the colloidal addition of polymer powder with laser-generated silver nanoparticles: Laser ablation liquids, pH-controlled mixing with polymer microparticles resulting in adsorption of nanoparticles on the polymer surface (supporting), filtration, and drying. This process enables achieving an extraordinary dispersion of nanoparticles on the composite powder for plasmon-enhanced powder bed fusion of the polymer powder with a diode laser operating at 445 nm.

sensitizers, such as carbon black, graphene, or carbon nanotubes, can overcome this issue and result in strong absorption in the visible and near-infrared spectrum, which makes diode laser sintering possible but also results in the final parts having a black color. Thus, the parts can only be colored in post processing, which is a drawback compared to material extrusion or binder jetting, both of which can work with different colors in the 3D printing process. To overcome this issue, the use of a nanosized photothermal sensitizer with an absorption range tuned to a specific wavelength is a promising approach. Gold nanorods have been demonstrated to achieve this aim,^[20] but silver nanoparticles are a factor of 40 cheaper than gold, and they have a molar absorption coefficient that is four times higher at the surface plasmon resonance (SPR) peak.^[21] While nano- and microparticulate additives often are used to enhance the optical, mechanical, and calorimetric properties of powders for PBF-LB,^[22] the typically high amounts of the additives that are required ($\gg 1$ wt%) often lead to agglomeration and a lack of dispersion. Therefore, small mass loadings, that is, < 0.1 wt%,^[23] and a fine, homogeneous dispersion of the nanoparticles are needed. A scalable additivition method that can fulfil these needs is colloidal additivition with surfactant-free nanoparticles, which was shown for polyamide (PA) 12^[24] and steel powder^[25,26] in the context of PBF-LB. In this process, colloidal nanoparticles and polymer microparticles are mixed, and a homogeneous decoration of the surfaces of the polymer microparticles with nanoparticles is achieved. Analogous to the generation of heterogeneous catalysts by electrostatic controlled supporting,^[27–31] the colloidal additivition of polymers features a high dispersion with only minor aggregation of nanoparticles during the process. In particular, nanoparticles generated by laser synthesis and processing of colloids (LSPC)^[32] are suitable for colloidal supporting since they do not have any surfactants and often have enhanced adsorption (supporting) behavior on micropowders. Since LSPC is a versatile,^[33,34] scalable,^[35,36] and economically feasible^[37] method to generate colloids, it is compatible with the production of powder for additive manufacturing.

The aim of our study was to enhance the light absorption of TPU powders in a small spectral region in order to perform PBF-LB with a diode laser at 445 nm by using a small mass fraction of silver nanoparticles ($\ll 1$ wt%). This approach of developing plasmonic-functionalized raw materials for 3D printing has been shown successfully before for plasmonic resins in two-photon polymerization^[38,39] as well as in the near-

field-enhanced laser sintering of semiconductors.^[40] Due to their high coefficient of molar absorbance,^[21,41,42] silver nanoparticles are suited ideally for use as photothermal sensitizers. The colloidal additivition route depicted in **Figure 1** was used to achieve a high dispersion and high surface coverage of plasmonic silver nanoparticles on TPU micropowders to absorb light at 445 nm during PBF-LB without the final part's having a black or grey color after processing. In addition, silver nanoparticle-polymer composites show high potential for applications in the fields of biology,^[43] catalysis,^[44] and electronics.^[45,46]

2. Results and Discussion

2.1. Adsorption Kinetics during Surface Functionalization of Powders

2.1.1. pH-Controlled Dispersion of Nanoparticles on Polymer Powders

Silver nanoparticles generated by LSPC in aqueous solution have a distinct SPR peak at 397 nm (**Figure 2a**) due to their small size of $d_{50} = 5.3$ nm (**Figure 2b**), which leads to the yellow color of the colloid (see inset of **Figure 2a**). Relevant parameters for further characterization are the SPR peak maximum wavelength and intensity, as well as the intensity at a wavelength of 445 nm ($\lambda_{\text{diode laser}}$). The SPR peak intensity is used below to calculate the supporting efficiency of the silver nanoparticles on the polymer powders. The supporting efficiency is defined as

$$\text{Supporting efficiency} = \frac{(\text{Abs}_{\text{SPR, educt}} - \text{Abs}_{\text{SPR, product}})}{\text{Abs}_{\text{SPR, educt}}} \times 100\% \quad (1)$$

where $\text{Abs}_{\text{SPR, educt}}$ is the absorbance of the laser-generated educt colloid at the SPR wavelength, and $\text{Abs}_{\text{SPR, product}}$ is the corresponding absorbance of the functionalized powder. The higher the absorbance at 445 nm, the higher the potential absorption of the powder will be after additivition and the lesser the laser energy will be needed during PBF-LB. Since the SPR wavelength and its intensity are dependent on the size and aggregation of the nanoparticles, colloidal stability has a crucial role during the additivition of the polymer powders in the liquid phase.

After performing LSPC, the silver colloids show high stability, characterized by their electrokinetic potential (zeta potential ζ) of about -35 mV at pH = 6. Ripening effects typically change the

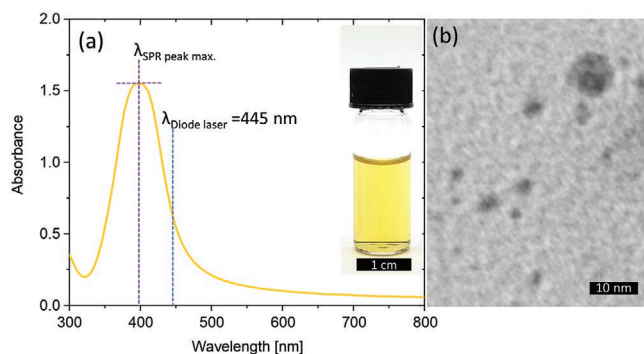


Figure 2. a) UV-vis spectrum of a laser-generated silver colloid stabilized by sodium citrate at a concentration of $100 \mu\text{mol L}^{-1}$ in water. The characteristic SPR peak wavelengths $\lambda_{\text{SPR peak max}}$ and the wavelength of the diode laser used for PBF-LB ($\lambda_{\text{diode laser}}$) are marked on the graph. The inset depicts a typical laser-generated silver colloid with its characteristic yellow color. b) Representative TEM image of the particles ($d_{50} = 5.3 \text{ nm}$). Figure S1, Supporting Information provides more information concerning the particle size distributions.

size of the nanoparticles and the zeta potential, especially within the first day after synthesis,^[47] and this could lead to fluctuations in the additivation process and in the quality of the nanoparticle composite after additivation. In addition, storing silver colloids over a long period of time, such as days or weeks, also could result in instability and insufficient reproducibility. In order to ensure reproducibility, colloidal supporting on the TPU microparticles was performed 1 day after the synthesis of the nanoparticles. (Also, see Figure S4, Supporting Information for the influence of the colloid aging effects.) The literature indicates that colloids with ζ values that range from -30 to $+30 \text{ mV}$ tend to have a higher degree of agglomeration,^[48] and the literature also indicates that the stability of colloids is highly dependent on temperature,^[43] which makes normalization of the zeta potential to the thermal energy $k_{\text{B}}T$ useful. **Figure 3** shows the supporting efficiency as a function of normalized colloidal stability. The green area corresponds to a supporting efficiency $>90\%$, and it indicates the process window ($2.5 \leq \text{pH} \leq 3.0$) for supporting silver nanoparticles on TPU microparticles. This was confirmed by the X-ray fluorescence (XRF) analysis of the powder that was generated, in which 86% of the expected silver was found. Note that a small amount of silver ions is dissolved in the permeate and does not contribute to the plasmon peak. In Figure 3, the yellow shaded area indicates that the supporting efficiencies range from 0% to 90% (for pH values between 3 and 6). In general, for $e|\zeta| \leq k_{\text{B}}T$ (note that at room temperature, this corresponds to an absolute value of 26 mV or smaller for the zeta potential), the colloidal stability is low, and the supporting efficiency increases. In the inset of Figure 3, representative suspensions are shown immediately after mixing. Colloids turn clear and powders turn yellow for low colloidal stability, whereas no supporting can be observed for $e|\zeta| > k_{\text{B}}T$, and the suspension conserves its yellow color.

In agreement with the measured supporting efficiencies shown in Figure 3, we observed no significant change in the color of the powder after drying and sifting when no supporting occurred (**Figure 4d**); this was due to the fact that almost no plasmonic particles are adsorbed on the surface of the polymer. In contrast, a change from the pure TPU (white

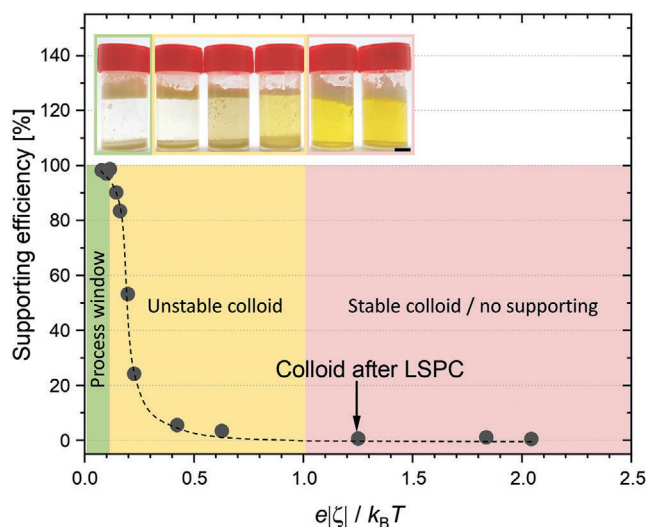


Figure 3. Supporting efficiency as a function of colloidal stability, defined by the zeta potential normalized to $k_{\text{B}}T$. For $e|\zeta| \leq k_{\text{B}}T$, the colloidal stability is low, and adsorption occurs. The green marked area corresponds to a supporting efficiency of $>90\%$ and indicates the process window ($2.5 \leq \text{pH} \leq 3.0$) for supporting silver nanoparticles on TPU microparticles. In the yellow area, supporting efficiencies range from 0% to 90% (for pH values between 3 and 6). See Figure S3, Supporting Information for more details.

powder) to the bright yellow powder, Ag-TPU, occurs when the pH is in the range of 2.5 to 3.0, indicating a high supporting efficiency (Figure 4e). If supporting was successful, the SPR peak of the colloid would have been conserved in the dried composite powder (Figure 4a). However, the composite powders show significant differences in their absorption spectra depending on the colloidal stability (normalized zeta potential) during additivation. Figure 4b shows the absorption at different characteristic wavelengths as a function of colloidal stability. As expected, the highest SPR peak intensity can be found for the highest supporting efficiencies ($e|\zeta| < k_{\text{B}}T$). At very low colloidal stability ($e|\zeta| \ll k_{\text{B}}T$), which corresponds to a $\text{pH} < 2.5$, a strong increase in the absorption at 600 nm can be observed without any significant change in supporting efficiency or SPR intensity. The wavelength of the SPR peak and the ratio of the intensity of the SPR peak and the intensity at 600 nm ($\text{Abs}_{\text{SPR}}/\text{Abs}_{600}$) can be used to determine the degree of aggregation. The shift in $\text{Abs}_{\text{SPR}}/\text{Abs}_{600}$ identifies an aggregation effect. The lower the colloidal stability, the lower the $\text{Abs}_{\text{SPR}}/\text{Abs}_{600}$ ratio becomes and the larger the relative amount of aggregates becomes that no longer show a SPR in the visible range but have a strongly damped SPR and mainly a characteristic grey color like bulk silver (Figure 4f). There is a significant shift in the SPR maximum from 397 nm (laser-generated colloid) to 410 nm (composite powder, $0.2 < e|\zeta| < k_{\text{B}}T$). For an additional decrease of colloidal stability ($e|\zeta| < 0.2$), the SPR shift of the powder is even more prominent (up to 417 nm). This also could be explained by minor nanoparticle aggregation. Based on the literature, we expect an aggregate size of 24 nm for a SPR peak at 410 nm and a size of 36 nm for a SPR peak centered at 417 nm^[49–51] (Figure S5, Supporting Information). Since the plasmon

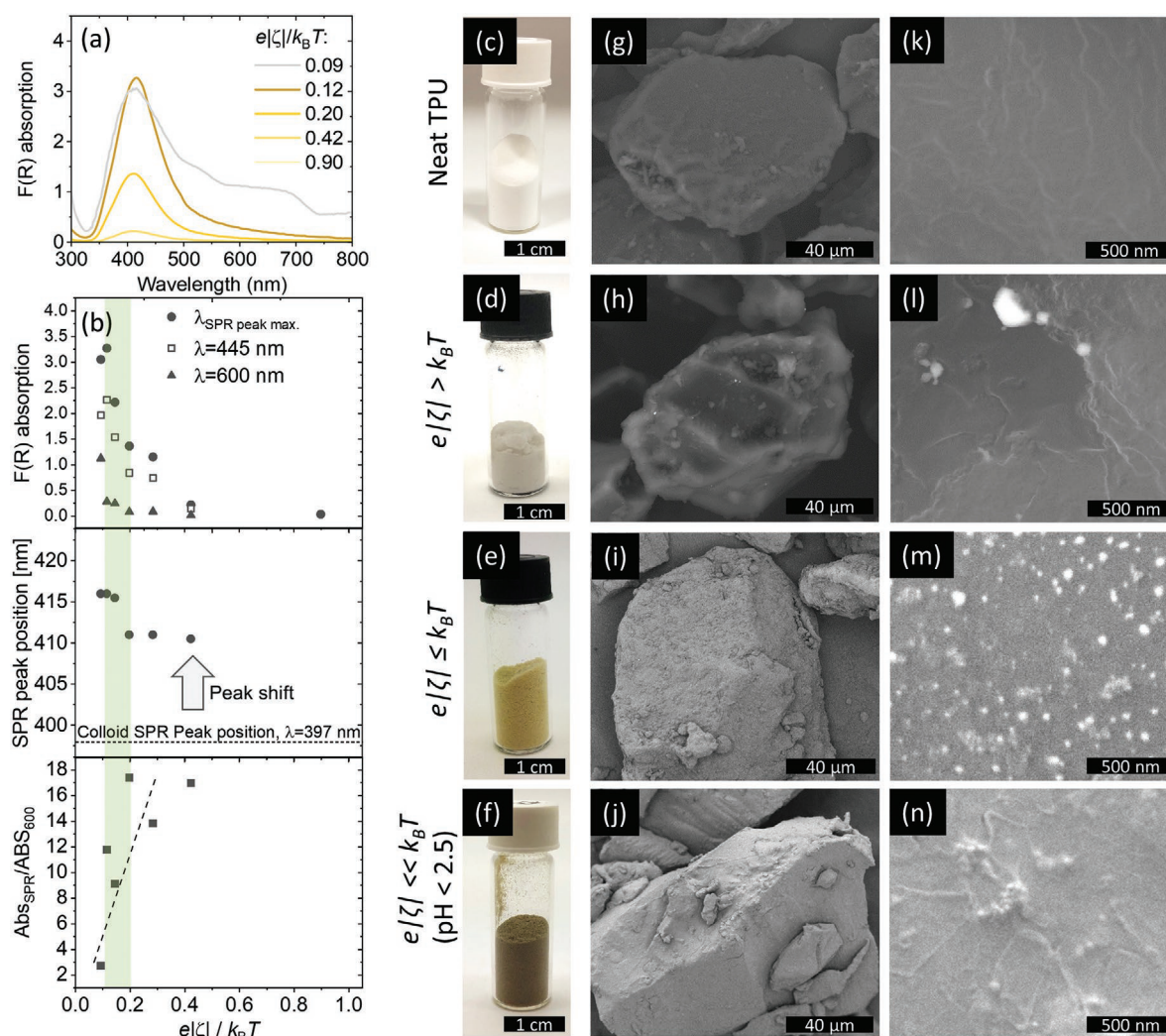


Figure 4. a) Powder absorption spectra of the nano-additivated plasmonic TPU powders produced at different colloidal stabilities (normalized zeta potential). b) Powder absorption at the characteristic wavelength (SPR peak, at 445 and 600 nm) as a function of colloidal stability (normalized zeta potential). c–f) Images of powders after colloidal additivation. g–n) Corresponding SEM images in two magnifications showing the nanoparticle dispersion on the surface of the TPU.

resonance still is conserved in the composite powder, a homogeneous nanoparticle coating of the polymer surface can be expected. This was confirmed by scanning electron microscope (SEM) imaging of the powders (Figure 4g–n). At a low supporting efficiency, only scattered silver particles can be found on the surfaces of the TPU microparticles (Figure 4h,l). The surface looks similar to the SEM images of neat TPU particles (Figure 4g,k). After successful colloidal additivation ($e|\zeta| < k_B T$), the surface of TPU microparticles is decorated homogeneously with nanoparticles (Figure 3i,m), resulting in a plasmonic TPU powder. As expected, the distribution of nanoparticles is homogeneous, and only minor aggregation can be observed. In contrast, strong aggregation occurs for $e|\zeta| \ll k_B T$ (Figure 4j,n).

Figure 5 shows the particle size distributions for homogeneous dispersion and aggregation in order to quantify the influence of colloidal stability on the aggregation of the nanoparticles on the surface of the TPU. In accordance with the size estimation from the SPR peak position, the maximum

size distribution occurred around 25 nm ($x_c = 25.3$ nm). Composite powders with aggregated silver nanoparticles have a broader size distribution, which is shifted toward larger Ferret diameters. The polydispersity index (PDI), which is a measure of the dispersion and shifts from 0.14 (monodisperse < 0.3) to 0.41 (polydisperse), also is in agreement with the results of powder spectroscopy. These results underline the capabilities of spectroscopic analysis and its potential as a characterization method for fast parameter screening during plasmonic functionalization.

Since the resolution of SEM is limited to ≈ 15 nm for the analysis of the surfaces of the polymer particles, transmission electron microscopy (TEM) images of the sliced polymer particles were used to analyze the primary size of the particles after colloidal additivation (Figure 6). With an x_c value of 8.7 nm, the primary particle size lies in the range of colloidal particle sizes of the educt shown in Figure 2, further featuring a very narrow size distribution (PDI = 0.05).

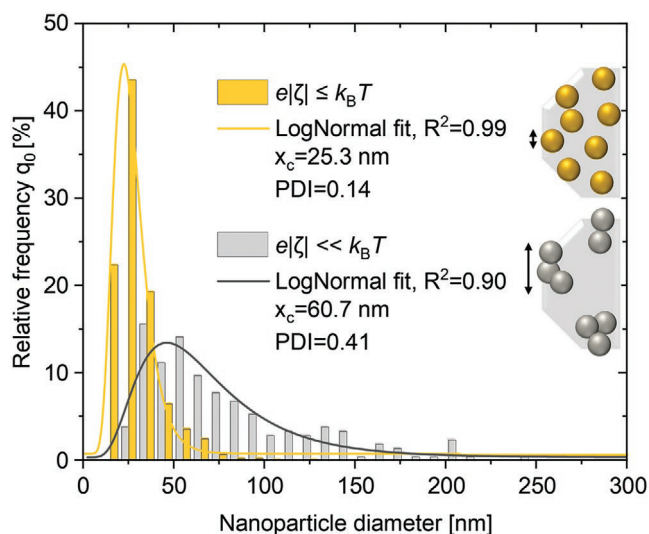


Figure 5. Particle size distribution based on the SEM images of homogeneously dispersed silver nanoparticles on the surface of the TPU micro-particle (0.1 wt%) at optimum process conditions ($e|\zeta| < k_B T$) and at a very low colloidal stability ($e|\zeta| \ll k_B T$).

2.1.2. Nanoparticle Concentration and Mixing Dependency

Colloidal stability is governed by both the zeta potential and the concentration of the nanoparticles. The mixing time of the suspension plays a crucial role in the supporting process. Both parameters are key factors for scaling up the colloidal addition process toward 1 kg of composite powder. **Figure 7a** shows the supporting efficiency as a function of the stirring time, t , and the initial concentration of the nanoparticles, $c_{NP,0}$. Even for very short stirring times of a few seconds, high supporting efficiencies of $>70\%$ were reached. The speed of the process is related directly to the initial concentration of the nanoparticles,

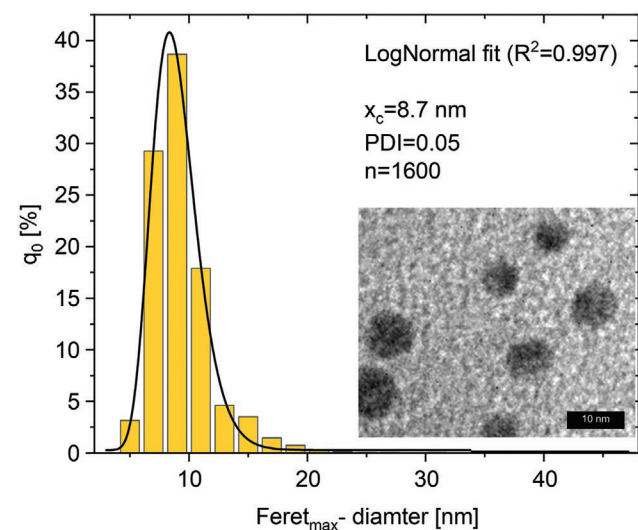


Figure 6. Particle size distribution as extracted from the TEM images of homogeneously dispersed silver nanoparticles on TPU microparticles (0.1 wt%) at optimum process conditions ($e|\zeta| < k_B T$) (1600 particles were counted.) Before imaging, particles were embedded in a resin and sliced with a microtome.

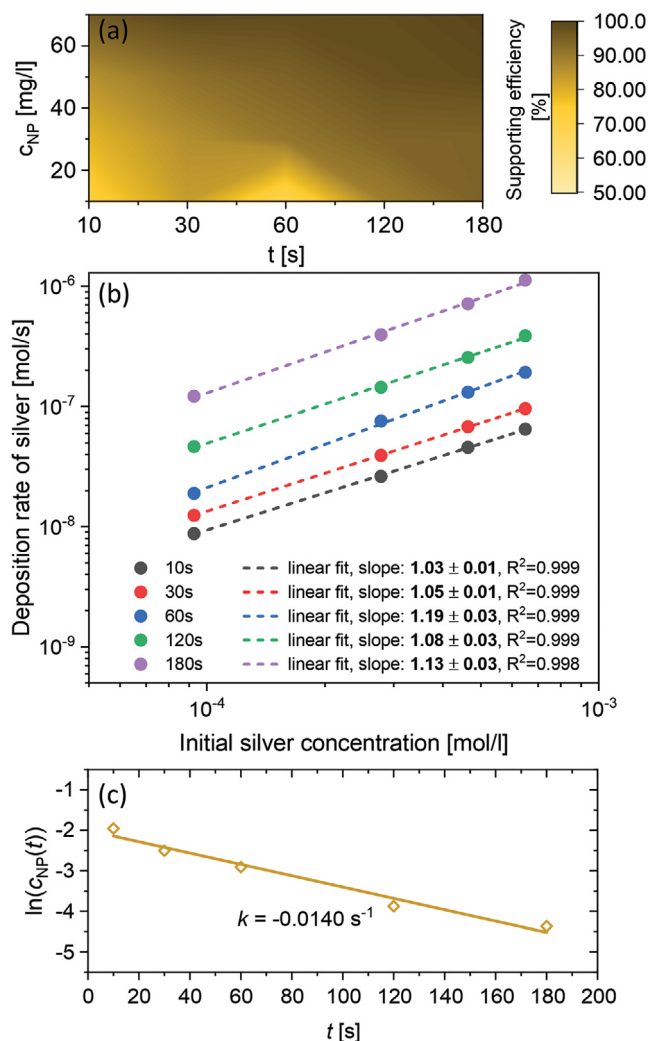


Figure 7. a) Contour plot illustrating the connection between the initial concentration of nanoparticles, c_{NP} , mixing time, t , and the supporting efficiency of the colloidal nanoparticles on the TPU microparticles. b) Double logarithmic plot of deposition rate over initial silver concentration of 50 mg L^{-1} . The dashed lines are linear fits ($R^2 = 0.972$) with the slopes given in the diagram. A slope of ≈ 1 indicates a first-order kinetic, which only depends on the concentration of the nanoparticles. c) $\ln(c_{NP}(t))$ as a function of mixing time for $c_{NP} = 50 \text{ mg L}^{-1}$ to calculate the deposition constant, k .

that is, the higher the initial concentration of nanoparticles is, the faster the process becomes. Independent from the concentration of nanoparticles that was used in our experiments, the process is completed in 3 min with a supporting efficiency of $>95\%$. However, nanoparticle concentrations above 50 mg L^{-1} are not suitable because colloidal stability, $\text{Abs}_{\text{SPR}}/\text{Abs}_{600}$, and the SPR peak intensity of the composite powder decrease. Reproducibility also is an issue for high concentrations (Figure S6, Supporting Information). For a concentration of 50 mg L^{-1} , a supporting efficiency of 95% is reached in a mixing time of 1 min. Plotting the adsorption rate as a function of initial nanoparticle concentration in Figure 7b gives a linear correlation and a slope of 1 ($R^2 = 0.999$), which corresponds to first-order kinetics with the deposition rate, d , given by

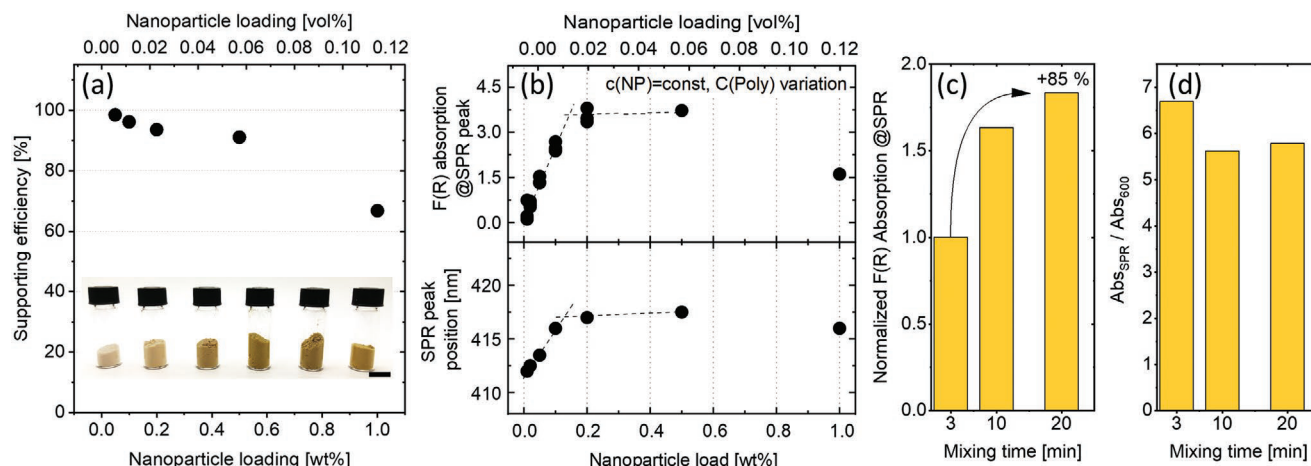


Figure 8. a) Supporting efficiency as a function of nanoparticle loading: The inset shows the powders at different loadings of nanoparticles. The black bar measures 1 cm. b) TPU powder SPR peak absorption and SPR peak wavelength as a function of nanoparticle load, which was achieved by keeping the nanoparticle concentration constant and varying the polymer particle concentration. c) Normalized SPR peak absorption at 1.0 wt%. d) $\text{Abs}_{\text{SPR}} / \text{Abs}_{600}$ as a function of mixing time.

$$d = k \cdot c(\text{Ag}) \quad (1)$$

Under the assumption of a constantly high number of adsorption spots on the surfaces of the microparticles, which is true only for small loadings of nanoparticles, there is no dependency on the concentration of the microparticles. The value of r is dependent only on the concentration, $c(\text{Ag})$, of the nanoparticles and the deposition rate constant, k . The value of k can be extracted from the slope in Figure 7c, where $\ln(c_{\text{NP},0})$ is plotted as a function of t . In a stirred-tank reactor, the mixing time depends on both macroscopic and microscopic mixing. The latter is driven by diffusion, whereas macroscopic mixing depends strongly on the stirring conditions. Good macroscopic mixing shortens the diffusion time that is necessary on the microscopic scale, and it requires turbulent flow that is characterized by a large Reynolds number, Re_R , of the stirrer. Re depends on the density, ρ , and the viscosity, η , of the fluid, the diameter, d , and the rotation velocity, n , of the stirrer.

$$Re_R = \frac{\rho n d^2}{\eta} \quad (2)$$

For the setup used in this study, the value of Re_R was around 2100, which is in the transition regime between laminar and turbulent flow. The necessary mixing time, θ , which typically is defined as the mixing time for 95% homogeneity, is a function of Re_R and the constant, c , which represents a correction factor for the geometry of the tank.

$$\theta = \frac{\eta}{\rho n^2 d^2} c \quad (3)$$

The larger the dimensions of the stirrer and its velocity are, the faster the mixing occurs, but the mixing time also depends on the size of the reactor. Since the tasks of the stirring system are to minimize the sizes of the segregated fluid elements and to shorten the distances over which diffusion takes place, this system must be adjusted if the dimensions of the reactor and

the Re_R change in order to upscale the supporting process. Therefore, θ must be measured empirically for any new setup. In considering the supporting process that is being driven by colloidal destabilization (Figures 3 and 4), it is important to be aware that an increased mixing time at a constant pH value inevitably results in more aggregation since the nanoparticles have more time to aggregate before they are deposited on the surface of the polymer. Also, the dosing with acid to adjust the pH must be adjusted if the mixing time increases to avoid a large pH gradient within the suspension, which, again, would lead to stronger aggregation and, in the worst case, even to a complete loss of the SPR. The importance of mixing will be even more significant in the context of varying the loading of nanoparticles.

2.1.3. Variation of the Loading of Nanoparticles

A possible way to adjust the absorption of the composite powder at the wavelength of 445 nm is to vary the loading of nanoparticles. This, in turn, can be achieved either by varying the concentration of the nanoparticles at a constant colloid volume or by varying the volume of the colloid at a constant concentration of nanoparticles (Figure S7, Supporting Information). In both cases, the mass of the polymer is fixed. However, varying the concentration of the colloid is not useful since it would have significant effects on the stability of the colloid, the supporting efficiency, and the necessary mixing time. Therefore, the volume of the colloid was varied, and, thus, only the batch size was changed. In Figure 8a,b, the supporting efficiency, the absorption of powder at the SPR peak, and the wavelength of the SPR peak are plotted as functions of nanoparticle loading. We observed a high supporting efficiency, that is, greater than 90%, for nanoparticle loadings of up to 0.2 wt% and a strong decrease in supporting efficiency (i.e., 60%) for a mass loading of 1.0 wt% (Figure 8a). The absorption of powder and the SPR peak wavelength had

similar trends (Figure 8b). Both were linearly dependent on the nanoparticle loading until a loading of 0.1 wt%. Above a mass loading of 0.2 wt% both curves saturate. This could be attributed to the decreasing distances between the nanoparticles on the surface of the polymer surface and a trend toward a higher degree of aggregation. The batch size increased with wt% (larger colloid volume), and this increased the mixing time that was necessary (Figure 8c,d) as well as the probability of the aggregation of the nanoparticles on the surface of the polymer. When the mixing time was increased from 3 to 20 min, a positive effect (+85%) on the absorption of the powder was observed. However, this positive effect was limited to a relatively small extent, and it did not compensate fully for the deviation from the expected absorption of the powder based on the linear extrapolation of the values below 0.1 wt%. Therefore, we concluded that a low or moderate nanoparticle loading leads to a low probability of the agglomeration of the nanoparticles on the surface of the polymer due to the lower density of the packing, resulting in plasmonic-functionalized TPU powder with homogeneous coverage of the surface by Ag nanoparticles.

2.2. Characteristics of the Functionalized Powder for Laser 3D Printing

2.2.1. Powder Melting Behavior

The presence of highly dispersed nanoparticles on the surface of the polymer was expected to influence the melting behavior of the powder. When placed on a heating stage, the samples that had been additivated with silver nanoparticles had higher melting temperatures. Instead of melting around 120 °C and forming a uniform layer at 126 °C, additivation with 0.1 wt% of silver nanoparticles shifted the formation of a uniform layer to 150 °C (Figure 9a). The differential scanning calorimetry (DSC) results confirmed this trend and showed a change in the melting temperature from 115 to 123 °C. In addition, the melting peak appeared sharper (Figure 9b). Interestingly, the melting temperature did not show any further shift above 0.2 wt% (Figure 9c), which correlates with the saturation of the absorption during the variation of the nanoparticle loading in Figure 8. Hence, it was indicated that 0.1 to 0.2 wt%, which is equivalent to 0.01 to 0.02 vol%, was an efficient amount for additivation.

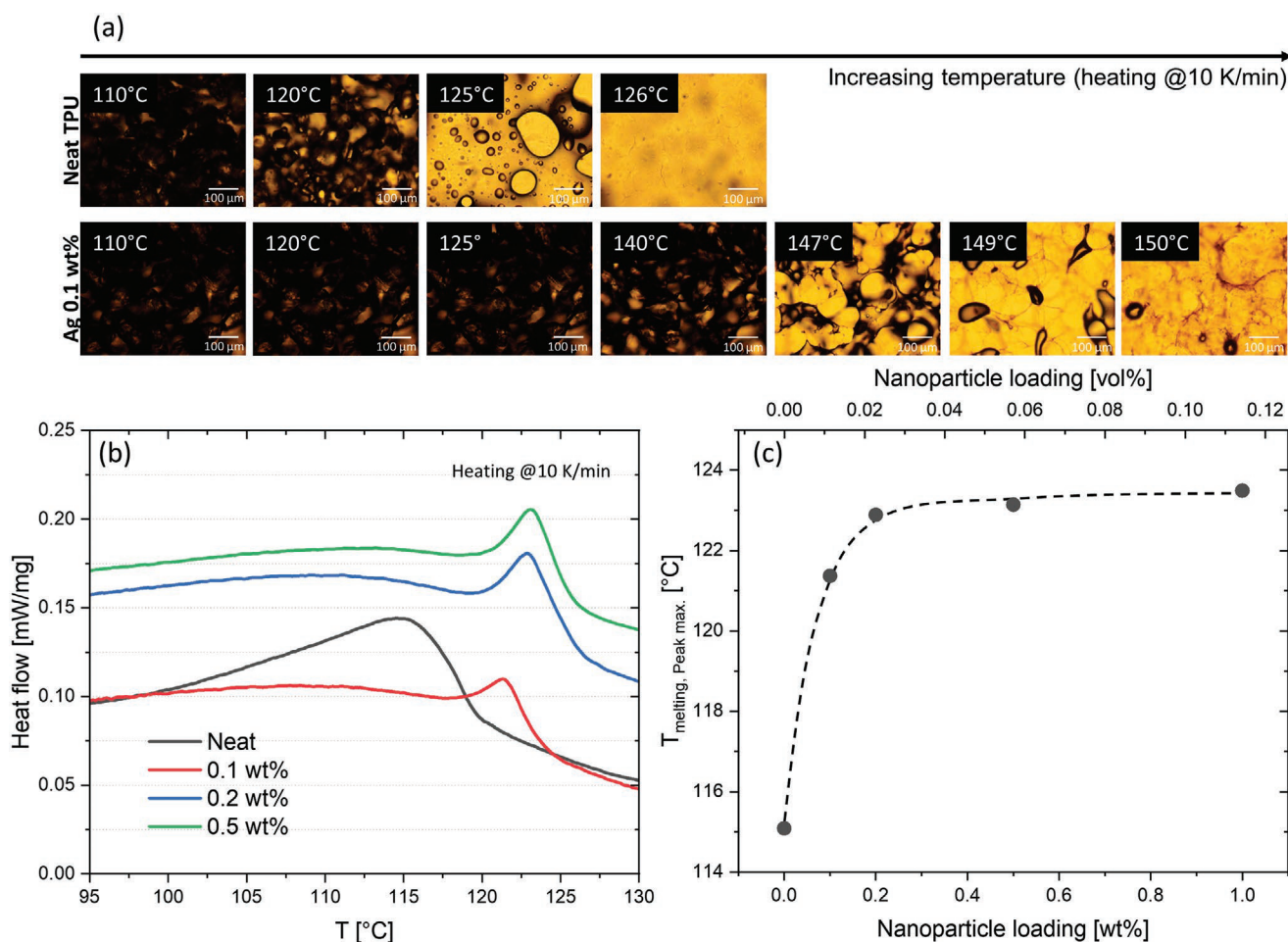


Figure 9. a) Optical microscopy images of the TPU powders on a heating stage heated at the rate of 10 K min^{-1} . b) Heat flow as a function of temperature during the melting of the silver nanoparticle-additivated TPU powder heated at 10 K min^{-1} as measured by DSC. c) Corresponding temperature at the onset of melting as a function of the loadings of nanoparticles.

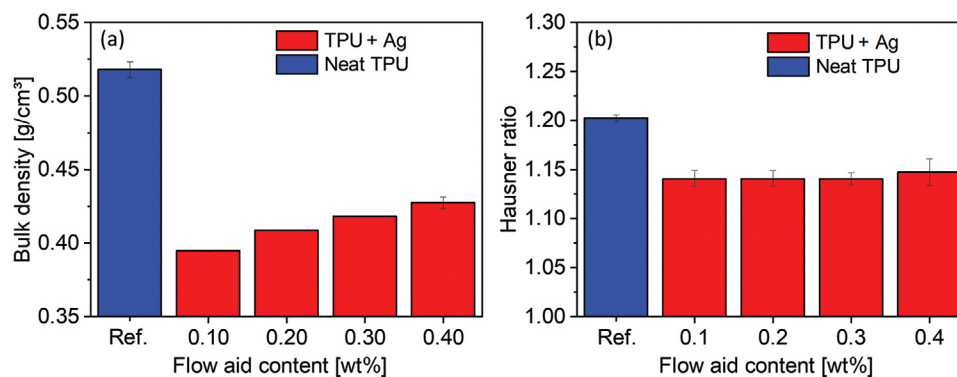


Figure 10. a) Bulk density. b) Effect of the content of the flow aid on the Hausner ratio of the silver nanoparticle-additivated TPU powders.

2.2.2. Powder Rheology

The processing behavior was investigated based on the nano-additivated powder with 0.1 wt% silver. In order to meet the need for high productivity of the powder additivation, the colloidal additivation process was scaled up successfully to the kg scale by 100 g batches of polymer powder in 2 L of colloid. The properties of the powder were investigated to determine its suitability for PBF-LB with a diode laser at 445 nm. It was found that the powder had suitable optical properties. (For more details, see Figure S8, Supporting Information.) The bulk density and the Hausner ratio were measured. Also, the influence of a flow aid on the composite powder properties was investigated to ensure a fair comparison with the unfunctionalized commercial TPU powder. All laser sintering powders usually are modified using flow aids in order to improve processability, which is a standard procedure for commercial powders. **Figure 10** shows the results. With regard to the bulk density, the powders functionalized with silver nanoparticles always had lower values than the raw material that was used for the tests. To improve the bulk density, an additive was placed in the functionalized TPU powder to improve the flow properties. As the proportion that was added increased, the bulk density increased significantly from 0.39 to 0.43 g cm⁻³. Even so, the values of the reference still were just over 20% higher than those of the TPU powder loaded with silver. Thus, the nano-functionalization led to a decrease in the bulk density. Comparative studies that investigated the storage of the TPU powder in citric acid with subsequent drying in a vacuum furnace showed that the bulk density after the citric acid treatment decreased to ≈0.46 g cm⁻³ after only 1 h. After 12 h, the bulk density had decreased further, to 0.43 g cm⁻³. However, the colloidal additivation process cannot fully explain the decrease since the TPU powder was in contact with the acidic environment only for a few minutes.

The Hausner ratio shows the opposite behavior. The reference value is 1.2, which is in the range of a free-flowing powder (Hausner ratio <1.25). In comparison, the Hausner ratio is somewhat lower for powders loaded with silver, that is, the values are between 1.14 and 1.15. The proportion of the flow aid only has a minor influence. The results seem to indicate that the modified powders have better flowability than the reference. The Hausner ratio measures the compaction of a powder that was poured earlier. It indicates the extent to which the powder can be compacted further. According to the VDI 3405 sheet 1.1 norm, the compaction is caused by knocking. A powder that flows very well directly forms dense packing during pouring, and it only can be compressed a little further. In a poorly flowing powder, there are numerous cavities in the bulk powder, and some of them can be eliminated by tapping. However, it has been found that, in some cases, even poorly flowing materials have low compaction. In this case, the Hausner ratio is not always a clear evidence. In the present case, a worse flowability can be assumed to be due to the very low bulk density as well as due to the fact that the flow aid hardly has any influence on the Hausner ratio.

Measurements also were carried out with the REVOLUTION Powder Analyzer (RPA). For reference reasons, additional measurements were performed with the commercial TPU powder type AM POLYMERS Rolaserit PBGR01. The measurements were performed on the silver nanoparticle additivated TPU powder with the addition of 0.4% flow aid. Both the virgin powder and powder from the part cake after processing were analyzed. The results in **Table 1** show that, for the avalanche angle, the reference material is in the range of 52°, while the angle for the modified powders with silver nanoparticles was between 60° and 62°, and ageing only had a slight effect. The optimal values for the avalanche angle are as low as possible. However, for the surface linearity, values close to one are optimal. The results that were obtained showed a slightly higher

Table 1. REVOLUTION Powder Analyzer measurements for reference materials and silver nanoparticle additivated TPU powders in dependency of the content of flow aid and material aging.

	Avalanche angle [deg]	Surface linearity	Surface fractal
TPU + carbon black (AM POLYMERS ROLASERIT PBGR01)	51.70 ± 0.38	0.971 ± 0.001	4.50 ± 0.15
TPU + 0.4% flow aid	61.62 ± 0.60	0.966 ± 0.002	3.53 ± 0.20
TPU + 0.4% flow aid; used	60.90 ± 0.41	0.966 ± 0.001	4.68 ± 0.20

Table 2. PBF-LB processing parameters.

	Laser power [W]	Hatch distance [mm]	Scan speed [mm s ⁻¹]	Volume energy density [J mm ⁻³]
Parameter set 1	2	0.05	200	2.0
Parameter set 2	2	0.05	175	2.3

value for the reference material. Also, aging had no significant effect. The optimal surface fractal is in the range between 2 and 4. While the reference material and the aged material with 0.4% flow aid are outside this interval, the unaged composite powder with silver nanoparticles was within the range. In general, the clearest difference between new and used powder can be seen here, that is, the values for the used powder are always higher. However, it is difficult to make a clear statement about the quality of the powders at this point due to the different characteristics of the values.

2.3. Plasmonic-Enhanced Laser 3D Printing

2.3.1. Processing of Functionalized TPU Powder

Based on the measured results and the first test with a 0.3 wt% flow aid, all further PBF processing tests were conducted with the highest amount of flow aid, that is, 0.4 wt%. It is evident that the application of the powder, especially on the components, was insufficient (**Figure 11a**). This also indicates poor flow behavior, but the processing was reliable. The laser energy input provided good melting and the formation of a melt film of the material. Thus, it was proven that the functionalization of the TPU powder with silver nanoparticles provided sufficient absorption for PBF-LB using lasers with visible light. For comparison, two different energy inputs, that is, 2.0 and 2.3 J mm⁻³, were investigated (**Table 2**). These two energy inputs led to suitable melting behaviors in the process, but the energy input that was required was almost ten times greater than that in PBF systems with CO₂ lasers.^[52] Also, compared to typical carbon black additivated TPU powder (with an energy input of 0.42 J mm⁻³), almost five times as much energy input was required. Compared to carbon black additivation, this results in a significantly slower process with small scan speeds, since the laser energy is fixed, and the area-normalized energy dose only can be increased by decreasing the scanning speed. As Powell et al.^[20] stated, a balance must be found between effective heating and coloring the material the same color as the photothermal sensitizers. Since the silver additivated powders are much brighter than the carbon black additivated powders, additional coloring

of the plasmonic Ag-TPU powders could be possible, but not if carbon black is used. Furthermore, the process control was suitable for producing different specimens (**Figure 11b**).

2.3.2. Investigation of the Properties of the Printed Part

Density cubes and tension bars were generated, and they were examined to determine their respective properties. After measuring and weighing the parts, the Archimedes method was used to calculate the densities of the parts (**Figure 12a**). For manual measurements, the density values were in the range of 0.82–0.93 g cm⁻³, which clearly were less than the usual density of the material, which is about 1.07 g cm⁻³. The Archimedes measurement indicated that the densities were 1.10 or 1.06 g cm⁻³. It was noted that the density seemed to decrease at the higher energy density in contrast to the manual measurements. This effect can be explained by the general density values. Since the parts have significant porosity, their densities generally are rather low. From the measurement according to Archimedes, it is known that, with laser-sintered parts, the measuring medium can penetrate the part thereby decreasing its porosity.^[53] When this occurs, the measured density is greater than the actual density. Since the porosity is higher at 2.0 J mm⁻³ than it is at 2.3 J mm⁻³ due to the lower density (manual measurement), the described effect also occurs when measuring according to Archimedes. Therefore, the density appears higher.

The stress–strain curves for two exemplary tension bars for the two energy inputs (**Figure 12b**) show that a higher energy density leads to both a higher breaking stress and a higher elongation at break. For comparison purposes, the results of the tensile tests that were conducted are summarized in **Figure 13**. The characteristic values increased significantly in each case for a higher energy input. The Young's modulus was between 22 and 32 MPa, so the value for 2.3 J mm⁻³ was 46% higher than it was for an energy input of 2.0 J mm⁻³. The values of the tensile strength were 2.6 and 3.2 MPa, with the latter being 23% higher. In the case of elongation at break, the difference was the smallest, that is, only 7%. The values were 195% and 209%, respectively. Thus, it was apparent that the characteristic

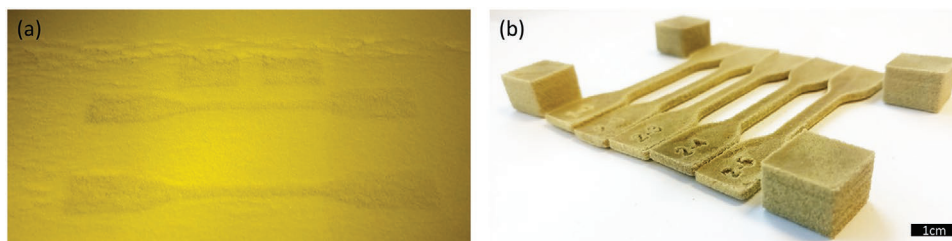


Figure 11. Visible (445 nm) diode laser powder bed fusion: a) image of the powder bed during processing; b) resulting parts of the silver nanoparticle additivated (0.1 wt%) TPU powders.

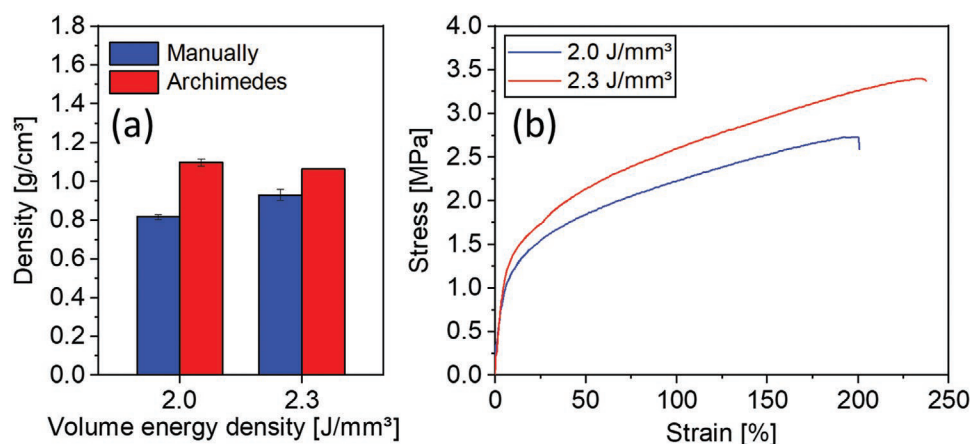


Figure 12. a) PBF-LB processed part density of the silver nanoparticle-additivated (0.1 wt%) TPU powders after diode laser PBF-LB in dependency of volume energy density. b) Stress–strain curves.

values were increased by increasing the volume energy density. Although these values still are below the reference values for the Sintratec S1 with TPU using carbon black as an absorber (8 MPa tensile strength and elongations at break of over 400%), further optimizations of the dosage and dispersion of the silver nanoparticles and tuning the parameters of the machine most likely will improve the processing and quality of the parts in the future.

3. Conclusion

Plasmonic feedstock materials could facilitate the ability of the 3D printing method of laser PBF to penetrate the market of desktop 3D printers. A colloidal addition process was established successfully to decorate commercial TPU powders with silver nanoparticles at the kg scale, followed by processing via PBF in the visible range with a 445 nm diode laser desktop machine. The silver nanoparticle TPU composite powder has a bright yellow color due to the SPR of the silver nanoparticles. Supporting efficiency is found to be a function of colloid concentration and mixing time, and the process must be considered as two parallel processes, that is, 1) controlled destabilization of colloidal nanoparticles and 2) adsorption

of nanoparticles or aggregates on polymer surfaces. Stirring conditions are very important for the time constant of supporting of nanoparticles, which is of special interest for further upscaling of our method. Under optimum conditions, the adsorption of nanoparticles on polymer surfaces dominates the aggregation of nanoparticles in the destabilized colloid. Since the deposition process follows first-order kinetics, upscaling is facilitated, but a static mixer could be used for better control of the process during upscaling. Nanoparticles are well distributed on the surface of the TPU. Also, the optical properties of the plasmonic TPU powders strongly correlate with the dispersion quality and adsorption quantity of the nanoparticles on the surface of the polymer, which makes the analysis of the optical powder a powerful method for the rapid screening of parameters. The location of the nanoparticles on the surface is beneficial for the local heating of the surface during diode laser PBF. The nanoparticles act as photothermal sensitizers and enable sintering with a diode laser close to the plasmon resonance frequency of the silver nanoparticles. The nano-functionalized TPU powders was processed in PBF with 2 J mm^{-3} , and this led to parts with measurable mechanical properties. Note that only 0.01 vol% (100 ppm volume weighted) silver was required to allow PBF processability in the visible laser range, making it about 98% less expensive than the Au nanoparticles

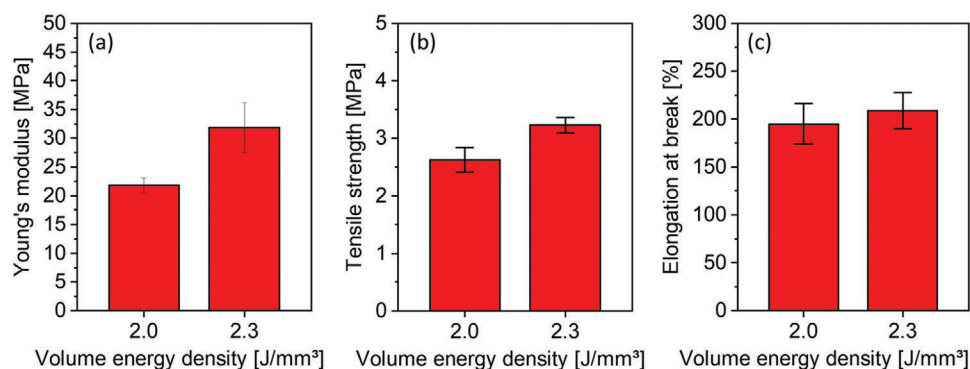


Figure 13. Mechanical properties of diode laser PBF-LB processed, nano-additivated TPU powders (0.1 wt% silver) in dependency of the volume energy density.

that have been used to date. The investigations showed that the functionalized powder materials have sufficient spreading behavior for the laser sintering process. The resulting properties of the component show good sintering with elongation at break of up to 200%, and they offer extensive potential for further optimization. Overall, this study emphasizes the potential of colloidal additivation in terms of modifying the properties of optical powder with ultra-small amounts of highly dispersed nanoparticles. In the future, by fine tuning of the SPR position to 445 nm, for example, by using AgAu alloy nanoparticles,^[42] higher absorption of the powder at specific wavelengths could be accessible at small nanoparticle loadings, for example, Ag₇₃Au₂₇ alloys exhibit a shift of the SPR peak toward 425 nm, and, thus, they also exhibit a significantly higher absorption at 445 nm.^[21] (More information is available in Figure S9, Supporting Information.) Since plasmonic nanoparticle composites also are known for their relevance in many different applications,^[54] the colloidal additivation of polymer powders with silver nanoparticles also could lead to the direct functionalization of final parts.

4. Experimental Section

Preparation of Nanoparticle-Functionalized Powders: For the additivation of the TPU powders (AM POLYMERS Rolaserit PB01), silver nanoparticles were generated by LSPC. A pulsed Nd:YAG laser (10 ns, 15 kHz) centered at 1064 nm was focused on a silver target (99.9%) mounted in a flow chamber, through which deionized water with 100 μmol L⁻¹ of sodium citrate was pumped at a flow rate of 20 mL min⁻¹. (See Figure S2, Supporting Information for more details.) Colloidal additivation of TPU was performed by pH-controlled mixing of the colloid in the presence of TPU microparticles. If not stated differently, 0.1 wt% (0.01 vol%) silver nanoparticles (relative to TPU) at a polymer concentration of 50 g L⁻¹ were mixed, and the pH of the mixture was adjusted to 2.7, followed by further stirring for 3 min. The pH values were varied by adding different amounts of hydrochloric acid. In addition, the nanoparticle concentration, mixing time, and nanoparticle load were varied to investigate the kinetics of the supporting process. After filtration, UV-vis absorbance spectroscopy of the permeates was performed to calculate the supporting efficiency, which is defined as the absorbance of the permeates divided by the initial absorbance of the colloid after LSPC.

Characterization of Nanoparticles and Functionalized Powder: Characterization of the particle sizes of the nanoparticle colloids was performed by analytical disc centrifugation and TEM before mixing the colloid with the TPU powder. Dried and sifted powders (<200 μm) were imaged by a SEM and sliced composite particles were imaged via TEM size analytics. The optical properties of the composite powders were analyzed by reflectance spectroscopy to check the suitability for diode laser sintering at 445 nm. The composition of the polymer powder was investigated by XRF. Transition temperatures and energies were measured by DSC (Metler Toledo DSC3+) for which 2–5 mg of polymer powder were heated and cooled in an aluminum crucible at a heating and cooling rate of 10 K min⁻¹ (flushing gas: argon at 20 mL min⁻¹). The melting process was followed by microscopy for which the samples were heated and cooled at a rate of 10 K min⁻¹.

The flowability of the nanoparticle-micropowder composite was optimized by adding different amounts (between 0.1 and 0.4 wt%) of the flow aid, AM POLYMERS AC1. The bulk density was measured according to DIN EN ISO 60, and the Hausner factor was measured according to VDI 3405 sheet 1.1 norm. Flowability was tested using the Mercury Scientific RPA. The RPA measurements were performed at 25 °C with a rotating speed of 10 rpm and a 100 mL volume of powder. Six measurements were conducted for each powder that was analyzed.

Laser 3D Printing of Functionalized Powder: 3D printing by PBF-LB processing were conducted on a Sintratec S1 printer emitting laser radiation at a wavelength of 445 nm. The thickness of the layer was chosen to be 100 μm, and the temperature of the powder bed was optimized to 94 °C. Two different test jobs were built while varying the parameter settings (Table 2), and test specimens for further testing were built.

Mechanical Testing of the Printed Parts: Tensile bars according to DIN 53504 S2 were produced in the x-direction with three specimens each. The tensile tests were performed in compliance with DIN 53504 using a Zwick Z020 M evo (MultiXtense) and a testing speed of 200 mm min⁻¹. The densities of the parts were measured for cubes using the Archimedes method according to DIN 1183 as well as by measuring the volume and weight using a micrometer gauge and an analytical balance according to VDI 3405 sheet 7 norm. The results for both measuring techniques were compared and discussed.

Supporting Information

Supporting Information is available from the Wiley Online Library or from the author.

Acknowledgements

The authors thank S. Boukercha, K. Loza (AK Epple, University of Duisburg-Essen) and IMCES (Imaging Center Essen, University Hospital Essen) for SEM imaging of nanocomposite powders and J. Jacobi for TEM imaging of laser-generated nanoparticles. The authors also thank IMCES (Imaging Center Essen, University Hospital Essen) for TEM analysis of sliced polymer samples. The authors thank C. Streich and L. Berg for their preliminary work on polymer micropowder additivation. T.H. thanks L. Cakir, E. Papadopoulou, and P. May for their support during experiments and F. Stein for fruitful discussions on tuning the SPR peak through AgAu alloys. T.H. also thanks Evonik industries for financial support of this work. M.B. and M.G. are thankful for generous financial support by the Professor-Werdemann Foundation. The authors gratefully acknowledge funding from the German Research Foundation (DFG) within the priority program (SPP) 2122 "Materials for Additive Manufacturing (MATframe)," BA 3580/27-1 and within the grant GO 2566/10-1.

Conflict of Interest

The authors declare no conflict of interest.

Keywords

additive manufacturing, laser ablation in liquids, laser sintering, powder bed fusion, surface plasmon resonance

Received: March 18, 2020

Revised: April 21, 2020

Published online:

[1] S. C. Ligon, R. Liska, J. Stampfl, M. Gurr, R. Mülhaupt, *Chem. Rev.* **2017**, *117*, 10212.

[2] D. Kokkinis, M. Schaffner, A. R. Studart, *Nat. Commun.* **2015**, *6*, 8643.

[3] A. Camposeo, L. Persano, M. Farsari, D. Pisignano, *Adv. Opt. Mater.* **2019**, *7*, 1800419.

- [4] R. Jiang, R. Kleer, F. T. Piller, *Technol. Forecast. Soc. Change* **2017**, *117*, 84.
- [5] J. del Barrio, C. Sánchez-Somolinos, *Adv. Opt. Mater.* **2019**, *7*, 1900598.
- [6] K. Wudy, D. Drummer, *Addit. Manuf.* **2019**, *25*, 1.
- [7] A. Wegner, *Phys. Procedia* **2016**, *83*, 1003.
- [8] M. M. Lexow, D. Drummer, *J. Powder Technol.* **2016**, *2016*, 4101089.
- [9] M. Schmid, A. Amado, K. Wegener, *J. Mater. Res.* **2014**, *29*, 1824.
- [10] M. Schmid, K. Wegener, *Proc. Eng.* **2016**, *149*, 457.
- [11] R. D. Goodridge, C. J. Tuck, R. J. M. Hague, *Prog. Mater. Sci.* **2012**, *57*, 229.
- [12] L. Verbelen, S. Dadbakhsh, M. Van den Eynde, D. Strobbe, J. P. Kruth, B. Goderis, P. Van Puyvelde, *Addit. Manuf.* **2017**, *15*, 12.
- [13] C. Xiang, P. J. Cox, A. Kukovecz, B. Genorio, D. P. Hashim, Z. Yan, Z. Peng, C. C. Hwang, G. Ruan, E. L. G. Samuel, P. M. Sudeep, Z. Konya, R. Vajtai, P. M. Ajayan, J. M. Tour, *ACS Nano* **2013**, *7*, 10380.
- [14] J. G. Drobny, *Handbook of Thermoplastic Elastomers*, 2nd ed., Elsevier, Amsterdam **2014**.
- [15] S. M. Liff, N. Kumar, G. H. McKinley, *Nat. Mater.* **2007**, *6*, 76.
- [16] B. Finnigan, D. Martin, P. Halley, R. Truss, K. Campbell, *J. Appl. Polym. Sci.* **2005**, *97*, 300.
- [17] S. Ziegelmeier, F. Wöllecke, C. J. Tuck, R. D. Goodridge, R. J. M. Hague, *J. Mater. Res.* **2014**, *29*, 1841.
- [18] S. Yuan, F. Shen, J. Bai, C. K. Chua, J. Wei, K. Zhou, *Mater. Des.* **2017**, *120*, 317.
- [19] A. Silver, *Nature* **2019**, *565*, 123.
- [20] A. W. Powell, A. Stavrinadis, I. De Miguel, G. Konstantatos, R. Quidant, *Nano Lett.* **2018**, *18*, 6660.
- [21] S. Link, Z. L. Wang, M. A. El-Sayed, *J. Phys. Chem. B* **1999**, *103*, 3529.
- [22] S. Yuan, F. Shen, C. K. Chua, K. Zhou, *Prog. Polym. Sci.* **2019**, *91*, 141.
- [23] H. C. Kim, H. T. Hahn, Y. S. Yang, *J. Compos. Mater.* **2013**, *47*, 501.
- [24] T. Hupfeld, T. Laumer, T. Stichel, T. Schuffenhauer, J. Heberle, M. Schmidt, S. Barcikowski, B. Gökce, *Proc. CIRP* **2018**, *74*, 244.
- [25] C. Doñate-Buendía, F. Frömel, M. B. Wilms, R. Streubel, J. Tenkamp, T. Hupfeld, M. Nachev, E. Gökce, A. Weisheit, S. Barcikowski, F. Walther, J. H. Schleifenbaum, B. Gökce, *Mater. Des.* **2018**, *154*, 360.
- [26] R. Streubel, M. B. Wilms, C. Doñate-Buendía, A. Weisheit, S. Barcikowski, J. H. Schleifenbaum, B. Gökce, *Jpn. J. Appl. Phys.* **2018**, *57*, 040310.
- [27] S. Reichenberger, G. Marzun, M. Muhler, S. Barcikowski, *ChemCatChem* **2019**, *11*, 4489.
- [28] G. Marzun, A. Levish, V. Mackert, T. Kallio, S. Barcikowski, P. Wagener, *J. Colloid Interface Sci.* **2017**, *489*, 57.
- [29] W. Dong, S. Reichenberger, S. Chu, P. Weide, H. Ruland, S. Barcikowski, P. Wagener, M. Muhler, *J. Catal.* **2015**, *330*, 497.
- [30] T. Mizutaru, G. Marzun, S. Kohsakowski, S. Barcikowski, D. Hong, H. Kotani, T. Kojima, T. Kondo, J. Nakamura, Y. Yamamoto, *ACS Appl. Mater. Interfaces* **2017**, *9*, 9996.
- [31] S. Barcikowski, P. Wagener, A. Schwenke, *US Patent US9403160B2*, **2016**.
- [32] D. Zhang, B. Gökce, S. Barcikowski, *Chem. Rev.* **2017**, *117*, 3990.
- [33] P. Liu, Y. Liang, X. Lin, C. Wang, G. Yang, *ACS Nano* **2011**, *5*, 4748.
- [34] A. V. Kabashin, A. Singh, M. T. Swihart, I. N. Zavestovskaya, P. N. Prasad, *ACS Nano* **2019**, *13*, 9841.
- [35] R. Streubel, S. Barcikowski, B. Gökce, *Opt. Lett.* **2016**, *41*, 1486.
- [36] R. Streubel, G. Bendt, B. Gökce, *Nanotechnology* **2016**, *27*, 205602.
- [37] S. Jendrzzej, B. Gökce, M. Epple, S. Barcikowski, *ChemPhysChem* **2017**, *18*, 1012.
- [38] L. Jonušauskas, M. Lau, P. Gruber, B. Gökce, S. Barcikowski, M. Malinauskas, A. Ovsianikov, *Nanotechnology* **2016**, *27*, 154001.
- [39] A. P. Haring, A. U. Khan, G. Liu, B. N. Johnson, *Adv. Opt. Mater.* **2017**, *5*, 1.
- [40] M. Lau, R. G. Niemann, M. Bartsch, W. O'Neill, S. Barcikowski, *Appl. Phys. A* **2014**, *114*, 1023.
- [41] Z. Yan, R. A. Shah, G. Chado, S. K. Gray, M. Pelton, N. F. Scherer, *ACS Nano* **2013**, *7*, 1790.
- [42] A. Neumeister, J. Jakobi, C. Rehbock, J. Moysig, S. Barcikowski, *Phys. Chem. Chem. Phys.* **2014**, *16*, 23671.
- [43] Y. H. Lim, K. M. Tiemann, G. S. Heo, P. O. Wagers, Y. H. Rezenom, S. Zhang, F. Zhang, W. J. Youngs, D. A. Hunstad, K. L. Wooley, *ACS Nano* **2015**, *9*, 1995.
- [44] N. Karak, *Nanomaterials and Polymer Nanocomposites*, Elsevier, Amsterdam **2019**, p. 47.
- [45] R. Zhu, C. H. Chung, K. C. Cha, W. Yang, Y. B. Zheng, H. Zhou, T. Bin Song, C. C. Chen, P. S. Weiss, G. Li, Y. Yang, *ACS Nano* **2011**, *5*, 9877.
- [46] S. Nam, H. W. Cho, S. Lim, D. Kim, H. Kim, B. J. Sung, *ACS Nano* **2013**, *7*, 851.
- [47] S. Jendrzzej, B. Gökce, V. Amendola, S. Barcikowski, *J. Colloid Interface Sci.* **2016**, *463*, 299.
- [48] S. Bhattacharjee, *J. Controlled Release* **2016**, *235*, 337.
- [49] T. Tsuji, D.-H. Thang, Y. Okazaki, M. Nakanishi, Y. Tsuboi, M. Tsuji, *Appl. Surf. Sci.* **2008**, *254*, 5224.
- [50] R. M. Tilaki, A. Irajizad, S. M. Mahdavi, *Appl. Phys. A* **2006**, *84*, 215.
- [51] S. D. Solomon, M. Bahadory, A. V. Jeyarajasingam, S. A. Rutkowsky, C. Boritz, L. Mulfinger, *J. Chem. Educ.* **2007**, *84*, 322.
- [52] A. Wegner, T. Ünlü, *JOM* **2018**, *70*, 419.
- [53] A. Wegner, M. Oehler, T. Ünlü, *Proc. CIRP* **2018**, *74*, 254.
- [54] I. Pastoriza-Santos, C. Kinnear, J. Pérez-Juste, P. Mulvaney, L. M. Liz-Marzán, *Nat. Rev. Mater.* **2018**, *3*, 375.

6.2 Calorimetric properties and microstructure

Analysis of the Nanoparticle Dispersion and its Effect on the Crystalline Microstructure in Carbon-Additivated PA12 Feedstock Material for Laser Powder Bed Fusion

Reprinted from Materials 13, 3312 (2020) under CC BY

Highlights:

- Investigation of dispersion and fragmentation of carbon nanoparticles in water by LPP
- Decoration of the PA12 polymer surface with a homogeneous layer of carbon nanoparticles
- Carbon nanoparticles (CB-NP) act as nucleation seeds, even at only 0.005 vol%, and significantly increase the crystallization temperature.
- Influence of minute amounts of carbon nanoparticles on the lamellar dimensions of the crystalline structure

Appendix:

- Supporting efficiency as a function of polymer concentration (A10)

Article

Analysis of the Nanoparticle Dispersion and Its Effect on the Crystalline Microstructure in Carbon-Additivated PA12 Feedstock Material for Laser Powder Bed Fusion

Tim Hupfeld ¹, Alexander Sommereyns ^{2,3}, Farbod Riahi ¹, Carlos Doñate-Buendía ¹, Stan Gann ¹, Michael Schmidt ^{2,3}, Bilal Gökce ¹ and Stephan Barcikowski ^{1,*}

¹ Technical Chemistry I and Center for Nanointegration Duisburg-Essen (CENIDE), University of Duisburg-Essen, Universitaetsstrasse 7, 45141 Essen, Germany; tim.hupfeld@uni-due.de (T.H.); farbod.riahi@uni-due.de (F.R.); carlos.donate-buendia@uni-due.de (C.D.-B.); stan.gann@uni-due.de (S.G.); bilal.goekce@uni-due.de (B.G.)

² Institute of Photonic Technologies (LPT), Friedrich-Alexander Universität Erlangen-Nürnberg, Konrad-Zuse-Str.3-5, 91052 Erlangen, Germany; Alexander.Blaszyk@lpt.uni-erlangen.de (A.S.); michael.schmidt@lpt.uni-erlangen.de (M.S.)

³ Erlangen Graduate School in Advanced Optical Technologies (SAOT), Friedrich-Alexander Universität Erlangen-Nürnberg, 91052 Erlangen, Germany

* Correspondence: stephan.barcikowski@uni-due.de

Received: 16 June 2020; Accepted: 17 July 2020; Published: 24 July 2020



Abstract: Driven by the rapid development of additive manufacturing technologies and the trend towards mass customization, the development of new feedstock materials has become a key aspect. Additivation of the feedstock with nanoparticles is a possible route for tailoring the feedstock material to the printing process and to modify the properties of the printed parts. This study demonstrates the colloidal additivation of PA12 powder with laser-synthesized carbon nanoparticles at >95% yield, focusing on the dispersion of the nanoparticles on the polymer microparticle surface at nanoparticle loadings below 0.05 vol%. In addition to the descriptors “wt%” and “vol%”, the descriptor “surf%” is discussed for characterizing the quantity and quality of nanoparticle loading based on scanning electron microscopy. The functionalized powders are further characterized by confocal dark field scattering, differential scanning calorimetry, powder rheology measurements (avalanche angle and Hausner ratio), and regarding their processability in laser powder bed fusion (PBF-LB). We find that heterogeneous nucleation is induced even at a nanoparticle loading of just 0.005 vol%. Finally, analysis of the effect of low nanoparticle loadings on the final parts’ microstructure by polarization microscopy shows a nanoparticle loading-dependent change of the dimensions of the lamellar microstructures within the printed part.

Keywords: additive manufacturing; colloidal additivation; laser fragmentation in liquids; Nanocomposites; 3D printing; selective laser sintering SLS; polyamide

1. Introduction

Additive manufacturing (AM) causes a transformation of design, manufacturing, and business models [1]. However, the range of polymer materials available for AM on an industrial scale is limited. In the field of powder bed fusion of polymers (PBF-LB/P, according to ISO/ASTM DIS 52900:2018), the market is dominated by polyamide powders with a market share of ~90% [2]. Much effort is spent on extending the range of materials in PBF-LB/P, and hereby also widen the range of potentials applications [3–8]. One approach for tailoring the polymer powder properties is additivation with

nanomaterials [9,10]. Carbon-based nanomaterials, such as carbon dots [11], tubes [12–14], fibers [15,16] or graphene [17,18], are already known for their applicability in various fields [19–21] and can also be used as fillers in polymer powders for PBF-LB/P [10,22]. They significantly affect PBF-LB/P processing behavior in terms of light absorptivity adjustment for diode laser 3D printing [23–26], modify the mechanical properties [24,25,27–30], and introduce new functionalities to the printed part, e.g., electrical conductivity [23,31]. Nevertheless, the complex influence of nanofillers, related to the nanoparticle–polymer interaction during rapid heating and slow cooling of the polymer in the PBF-LB/P process, is yet not fully understood.

As nanoparticles act as nuclei during polymer crystallization and hereby strongly affect the microstructure of the printed part, it can be expected that not only the mass loading of the nanofiller, but also its dispersion (polymer surface coverage and particle size) significantly influence the powder processability and part properties. For example, high filler loadings in the range of 4 wt% of carbon nanoparticles can decrease the flexural modulus, caused by nanoparticle agglomeration [23]. On the other hand, no effects on the melt flow and the polymer crystallization were observed for loadings in the range of 0.1 wt% and low dispersion quality [30,32]. However, the degree of nanoparticle dispersion is typically not investigated in detail. One exception is a study of Meyer and Zimmerman [33], who highlighted the influence of oxide nanoparticle dispersion on the powder flowability. They found that the dispersion affects the surface roughness of the microparticles and hereby the particle adhesion, which governs the powder rheology in accordance with an earlier study by Rumpf [34]. Nevertheless, the scarce literature makes it hard to systematically correlate the processing behavior and part properties in PBF-LB to the nanoparticle dispersion. The variety of additivation methods aggravates this problem since the dispersion quality is strongly related to the nanoparticle synthesis and polymer additivation method [30,35,36], e.g., insufficient dispersion of aggregated gas phase-synthesized nanoparticles after dry coating of polymer powder or enhanced dispersion after wet coating [37].

Therefore, our study focuses on the preparation method of the feedstock material, starting with the preparation of a highly dispersed carbon colloid by laser synthesis and processing of colloids (LSPC) [38]. LSPC has become an established approach for the formation of metal and metal oxide nanoparticles [39] and was also reported by several researchers for the preparation of carbon colloids [40–46]. In the next step, a colloidal additivation process is used to adsorb the as-prepared laser-generated carbon nanoparticles on PA12 microparticles, directly in an aqueous dispersion. Besides a deep characterization of the nanoparticle dispersion on the polymer particle surface, we focus on investigating the heterogeneous nucleation effect caused by the nanoparticles in the polymer matrix during resolidification. Our study aims at an understanding of the influence of carbon nanoparticles especially at small nanoparticle loadings (<0.1 wt%), which are already high enough to have a high potential for influencing the polymer microstructure and the mechanical properties of the final part.

2. Materials and Methods

2.1. Colloidal Surface Additivation

The process chain for colloidal surface additivation of a polyamide 12 powder (EVONIK VESTOSINT 1115, Evonik Industries, Essen, Germany) is depicted in Figure 1. In a first step, 50 mg/L carbon nanoparticles (CARBON BLACK, Orion Engineered Carbons, Senningerberg, Luxemburg) is dispersed in water by ultrasonication (Hielscher, Ultrasonics, Teltow, Germany, UP200S, 200 W and 24 kHz, alternating between on and off for 0.5 s each), directly followed by laser irradiation through a cylindrical lens with a 3 ps laser system operating at 515 nm (Amphos 500flex, Herzogenrath, Germany, 5 MHz, 170 W, max. 36 mJ/cm², 34 µJ/pulse, 0.094 mm² spot size) or with a 10 ps laser system operating at 532 nm and much higher fluence (Edgewave PX400-3-GH, Edgewave PX400-3-GH, Würselen, Germany, 80 kHz, 30 W 150 mJ/cm², 375 µJ/pulse, 0.25 mm² spot size). A liquid jet set-up with a flow rate of 60 mL/min and a liquid jet diameter of 1.3 mm was utilized for laser postprocessing (LPP) [47,48]. At the given spot size and repetition rate of the laser system, this leads to multiple laser

pulses per volume element [49]. The applied fluence can be tuned by varying the distance between the cylindrical lens and the liquid jet so that the mass-specific energy dose can be tuned by repeating the irradiation cycle several times, which is referred to as “number of passages”. Due to self-focusing effects in the round contour of the liquid jet, approximately 12% of the liquid jet is unirradiated [50]. To ensure that >99% of the particles are illuminated, at least three passages are necessary. However, the net throughput decreases with the increasing number of passages. Therefore, only one passage was applied to the colloids in the following experiments if not stated otherwise. Hereby, 180 mg in 3.6 L of colloid can be processed per hour. After the last passage, the irradiated colloid is either analyzed via UV–Vis absorbance spectroscopy (Thermo Scientific Evolution 201, Waltham, MA, USA, 1 nm bandwidth, 0.8 nm resolution), dynamic light scattering (DLS, PSS-Nicomb 380 ZLS, Entegris, Billerica, MA, USA), or dried to perform transmission electron microscopy (TEM, Zeiss EM 910, Oberkochen, Germany), Raman spectroscopy (Renishaw InVia, Wotton-under-Edge, UK), and Fourier-transform infrared spectroscopy (FTIR, JASCO FT/IR-430, Easton, MD, USA). SEM and TEM samples were prepared by dripping 20 μ L of the nanoparticle dispersion on a TEM grid or an SEM specimen mount, followed by drying for one day. To perform colloidal additivation, the colloid is directly mixed with an aqueous suspension of PA12 powder (50 g/L) under constant stirring. After irradiation, the mixture is stirred for 5 min to ensure complete supporting. The typical mass load for additivation ranged between 0.01 and 0.1 wt% (equivalent to 0.005 vol%–0.05 vol%). The concentration of 50 g/L was chosen to ensure efficient colloidal additivation. Subsequently, the mixture is filtered, dried at 50 °C for 24 h, and sifted with a 125 μ m sieve before powder analysis. The educt colloids as well as the permeates after filtration were analyzed by UV–Vis absorbance spectroscopy to calculate the residual carbon nanoparticles in the permeate and the supporting efficiency, defined as

$$\text{Supporting efficiency} = \frac{Abs_{600}(\text{Educt}) - Abs_{600}(\text{Permeate})}{Abs_{600}(\text{Educt})} 100\% \quad (1)$$

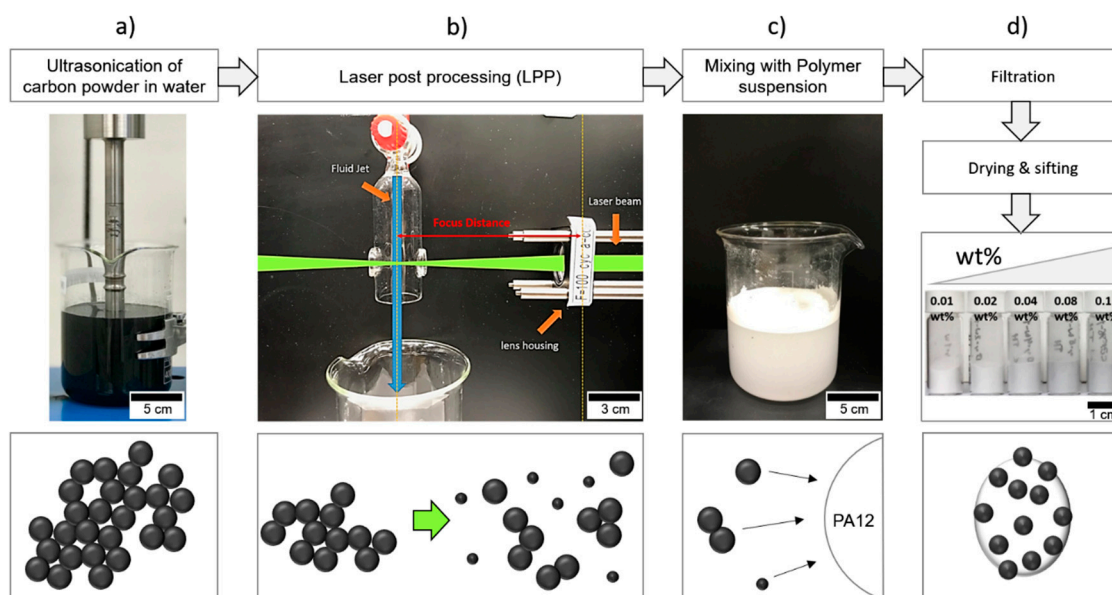


Figure 1. Process chain for colloidal additivation of PA12 micropowder with carbon nanoparticles: (a) Dispersion of aggregated carbon nanoparticle powder in water by ultrasonication. (b) Laser postprocessing (LPP) with a high power, high repetition rate laser, focused on the nanoparticle dispersion in a liquid jet. (c) Fixing of the irradiated colloid with the polymer powder and adsorption of nanoparticles on the polymer particles. (d) Filtration, drying, and sifting to yield dry nanofunctionalized PA12 powder.

2.2. Polymer Powder Analysis

The distribution of nanoparticles on the surface of the polymer particles is investigated by laser scanning confocal dark-field imaging (Leica TCS SP8, Leica Microsystems, Wetzlar, Germany) and scanning electron microscopy (SEM, ESEM Quanta 400 FEG, ThermoFisher Scientific, Waltham, MA, USA). Hausner ratio measurements were conducted according to VDI 3405 Part 1.1. The tapped volume has been determined manually with a 100 mL plastic cylinder for 5 times for statistical evaluation. The dynamic flow properties of powders were estimated by using a rotating drum analyzer (Revolution Powder Analyzer, Mercury Scientific, Newtown, CT, USA), which is known for good correlation with PBF-LB/P processing conditions due to the evaluation of particle cohesiveness during flow under elevated temperatures [8,51,52]. Avalanche angles were measured at 20 °C and 100 °C and a rotating speed of 10 rpm with a sample quantity of 100.0 ± 0.5 mL. Measurements of 150 avalanches were averaged for each sample. The dynamic image analysis (ISO 13322-2) of the PA12 powder compositions was conducted via the Camsizer X2 (Microtrac RETSCH, Haan, Germany) with compressed air of 50 kPa through the X-Jet extension to get rid of possible agglomerations. The amounts of analyzed powder per run were a few grams, which equals to around 500,000 detectable particles. The range of detection of this machine is between 0.8 μm and 8 mm, with a resolution of up to 0.8 $\mu\text{m}/\text{pixel}$. The number-weighted and volume-weighted distributions were directly calculated by the device and are based on the projected area of a sphere. The procedure has been repeated 3 times for statistical analysis.

2.3. Differential Scanning Calorimetry (DSC)

The PA12 powders and their composites were analyzed non-isothermally with a DSC 822e (Mettler Toledo, Columbus, OH, USA) under a nitrogen purge of 40 mL/min. The machine has a temperature accuracy of ± 0.2 °C, reproducibility of ± 0.1 °C, and a resolution of 0.04 μW . Powder samples of 12 mg were placed in 40 μL aluminum pans with covers. The measurements were performed from 25 °C to 250 °C with a heating rate of 20 K/min. At 80 °C, the powders were held for 3 min to ensure the same starting conditions for every powder sample. At 250 °C, the samples were held again for 3 min to fully melt all residual crystals and to assure a thermal equilibrium. Afterward, the samples were cooled down to 80 °C with a cooling rate of 10 K/min, held for 3 min, and heated up to 250 °C with 10 K/min. Thus, an analysis of the crystallization behavior and the melting behavior of previously emerged crystals as well as the sample's crystallinity were possible. For statistical evaluation, each powder composition was analyzed 3 times, leading to a total of 9 samples. The evaluation of the results was performed with the Mettler Toledo STARe Evaluation Software 16.10. For the calculation of the relevant enthalpies, an integral tangential baseline was used.

2.4. Microscopic Analysis

After cooling down the DSC samples at a rate of 10 K/min, the crystalline structures were analyzed through transmitted light as well as reflected light for bright field illumination by the microscope Metalloplan from Leitz (Leica Microsystems, Wetzlar, Germany) with a magnification of 400 and 256, respectively. For this, the samples were sliced to 10 μm specimens with a microtome and embedded in oil on microscope slides. With the use of two polarizers, the birefringence of the crystals was made visible. The evaluation of the aspect ratio of the crystal forms has been performed manually by measuring the longest to shortest dimension of at least 20 crystalline structures of 3–5 DSC slices per sample, with a value of 1 being equivalent to a circle.

3. Results and Discussion

3.1. Preparation of Carbon Nanoparticles by Laser Synthesis

Ps-laser irradiation with a high repetition rate laser system (3 ps, 5 MHz, max. 36 mJ/cm²) significantly decreases the hydrodynamic diameter of carbon nanoparticles, which is confirmed by

DLS measurements (Figure 2a). The higher the fluence, the smaller the nanoparticle size (Figure 2b). The best results were found for a fluence of 36 mJ/cm^2 , leading to a hydrodynamic particle size reduction from 157 nm to 36 nm . A similar trend can be found for the zeta potential, which decreases from -40 to -60 mV through irradiation (Figure 2c). This effect indicates a higher surface charge of the irradiated particles and has also been reported for laser irradiation of other materials, such as gold [53,54]. In accordance with the literature, the isoelectric point (IEP, Figure 2d) lies between pH values of 3.5 to 4 [55,56] and slightly shifts from 4.1 pH before LPP is to 3.3 pH through laser irradiation. Although the high absolute zeta potential value of more than 30 mV nominally indicates good colloidal stability, colloids exhibit only short time stability and show high activity for aggregation. This happens within minutes after laser irradiation (Figure 2d), indicated by hydrodynamic particles diameters in the range of a few hundreds of nm. However, the short time stability was high enough for reliable DLS and zeta potential measurements. In order to further reduce the size of the nanoparticles, another laser system with a higher fluence was utilized (10 ps , 80 kHz , 150 mJ/cm^2). The synthesized colloid also showed very weak colloidal stability and aggregation within minutes. In both cases, the weak colloidal stability could be explained by the successful disaggregation and fragmentation of carbon nanoparticles. The smaller the nanoparticles at a given concentration, the smaller the volumetric interparticle distance, and the higher the probability for aggregation (which scales with the square root of particle number concentration).

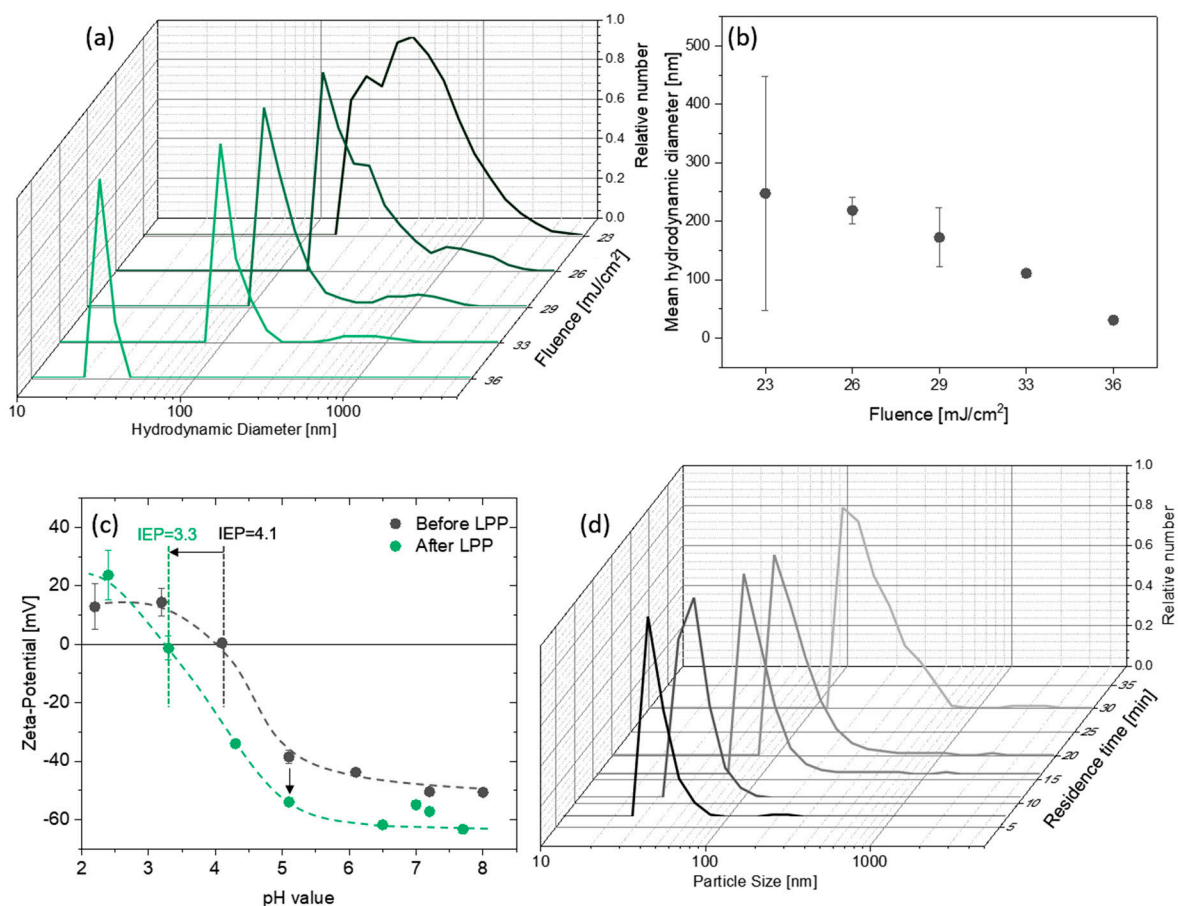


Figure 2. Laser postprocessing of carbon black with a high repetition rate laser system: (a,b) Hydrodynamic nanoparticle diameter (mass weighted) measured by dynamic light scattering (DLS) as a function of laser fluence. (c) Zeta potential as a function of the pH value of the dispersion before and after LPP. (d) Temporal evolution of the hydrodynamic particle size after laser irradiation. The error bars in panels (b,c) represent the standard deviation and are based on at least 3 samples each.

TEM images (Figure 3) confirm pronounced disaggregation for the low fluence laser system (Figure 3b) compared to the educt particles (Figure 3a), whereas the high fluence laser system also results in fragmentation of the primary particles (Figure 3c) and appearance of strongly aggregated nanoparticles in the sub-10 nm scale (inset of Figure 3c). Laser synthesis is known to produce such small nanoparticles with a size below 10 nm [40–46]. Due to the high instability of the aqueous colloid and the fast aggregation after LPP, statistical evaluation of particle size and degree of dispersion based on TEM images is not meaningful as the TEM grid does not represent the degree of dispersion and the aggregate size right after laser irradiation, but the size after preparation of the TEM grid and drying of the colloid. Note that particle ripening and aggregation is much faster than drying of the colloid on the TEM grid. Despite the fraction of small particles, which is likely to dominate the number-weighted particle size distribution, a significant fraction of the educt volume material remains unchanged by laser irradiation. This is indicated by larger educt particles and aggregates on the TEM grid. In agreement with this observation, a volume-sensitive Raman shift analysis (Figure 4) does not reveal any significant changes of the ratio of the relevant peaks at 1590 cm^{-1} (G-Band) and 1350 cm^{-1} (D-Band), which result from the sp^2 -hybridization of planar carbon (graphite) and defect structure in the graphite, respectively. The investigation of the carbon particle's surface by Fourier-transform infrared spectroscopy (Figure 4b) reveals the presence of C=C, C-H, C-O, and O-H bonds in the material before and after irradiation [57]. The preservation of the chemical surface groups composition after laser irradiation is associated to the employment of water as solvent, therefore no other element apart from C, H, and O are expected even after irradiation. A closer look to the spectra reveals slight differences after laser irradiation, as a higher absorption of the C-O peak at 1060 cm^{-1} and the C-H peaks at 2860 cm^{-1} and 1470 cm^{-1} . This fact indicates the increased presence of C-OH and CH_2 surface groups, which can be explained due to the higher surface area after particle size reduction and the generation of molecular O and H based radicals or molecules from water splitting during laser irradiation [58].

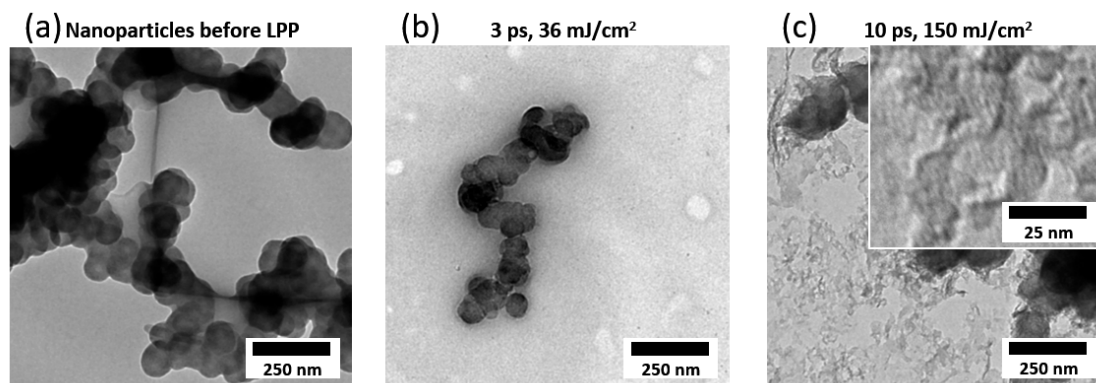


Figure 3. TEM analysis of (a) the raw carbon nanoparticles dispersed in water by ultrasonication and (b,c) colloids produced by irradiation with (b) a low fluence (36 mJ/cm^2) and (c) a high fluence laser system (150 mJ/cm^2). LPP with a high fluence laser system results in many small particles, but the colloid is more unstable against aggregation than at low fluence.

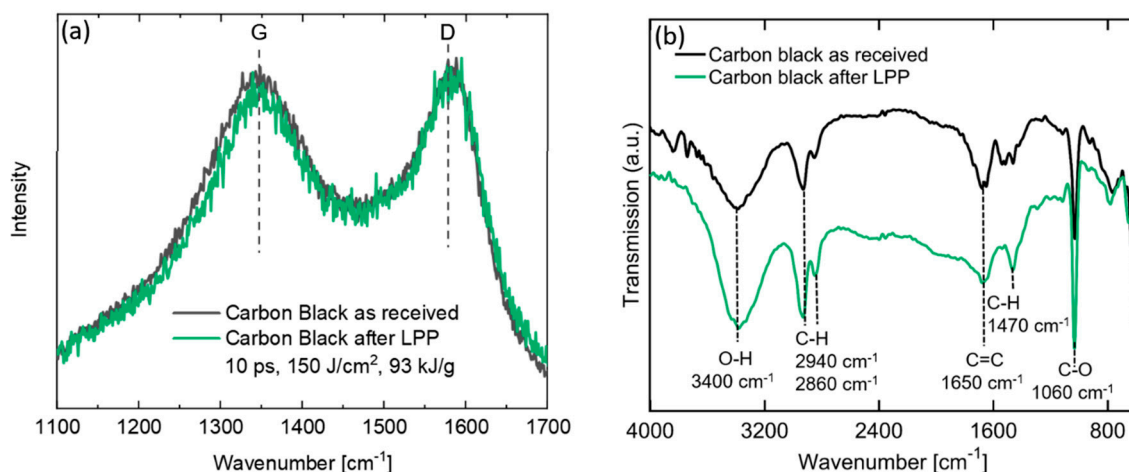


Figure 4. (a) Representative spectra from samples analyzed by Raman spectroscopy (3 measurements each), showing the two relevant peaks at 1590 cm^{-1} (G-Band) and 1350 cm^{-1} (D-Band) for carbon nanoparticles before and after irradiation with the highest fluence (10 ps , 150 mJ/cm^2). (b) Fourier transform infrared spectroscopy (FTIR) spectra of the as-received and laser-irradiated carbon black, where the surface bonds identified by the absorption peaks are marked with a dotted line. In both cases the spectra displayed represent carbon nanoparticles before and after irradiation with the highest fluence (10 ps , 150 mJ/cm^2).

3.2. Nanoparticle Dispersion on PA12 Microparticle Surface

After irradiation of the nanoparticles, a fast aggregation of the carbon nanoparticles within minutes can be observed. However, if a support (PA12 powder) is provided under constant stirring during this phase, efficient and fast adsorption of nanoparticles on the support occurs in less than one minute. As we know from a previous study for nanoparticle adsorption on a polymer surface, constant stirring is an important factor once the colloid is unstable and starts to aggregate [59]. A good mixture reduces the necessary diffusion distance between a nanoparticle and the polymer surface. The supporting efficiency of the nanoparticles on the polymer microparticles determined by UV-Vis absorbance spectroscopy of the permeate is larger than 95%, independent of the used laser for laser synthesis. Permeates show a clear color and powders exhibit a black or grey color depending on the mass load of carbon nanoparticles. As the nanoparticles completely adsorb on the polymer powder in less than one minute under constant stirring (supporting efficiency > 95%), nanoparticle adsorption is likely to dominate aggregation.

Laser scanning confocal microscopy of the decorated polymer particles reveals a homogeneous distribution of nanoparticles (Figure 5). It is a reference method adapted from Blaesser/Million et al. [60] and Klein et al. [61], which has also shown its potential for analyzing the distribution of fillers in polymer matrixes [62,63]. The bright-field images of the additivated and unadditivated powders look similar (Figure 5, upper row), but confocal dark-field imaging reveals much higher scattering intensity for 0.05 vol% compared to 0.005 vol%, whereas only minor scattering can be observed for the unloaded polymer powder. However, even the scattering signal from 0.005 vol% is high enough to clearly distinguish the additivated from unadditivated polymer particles.

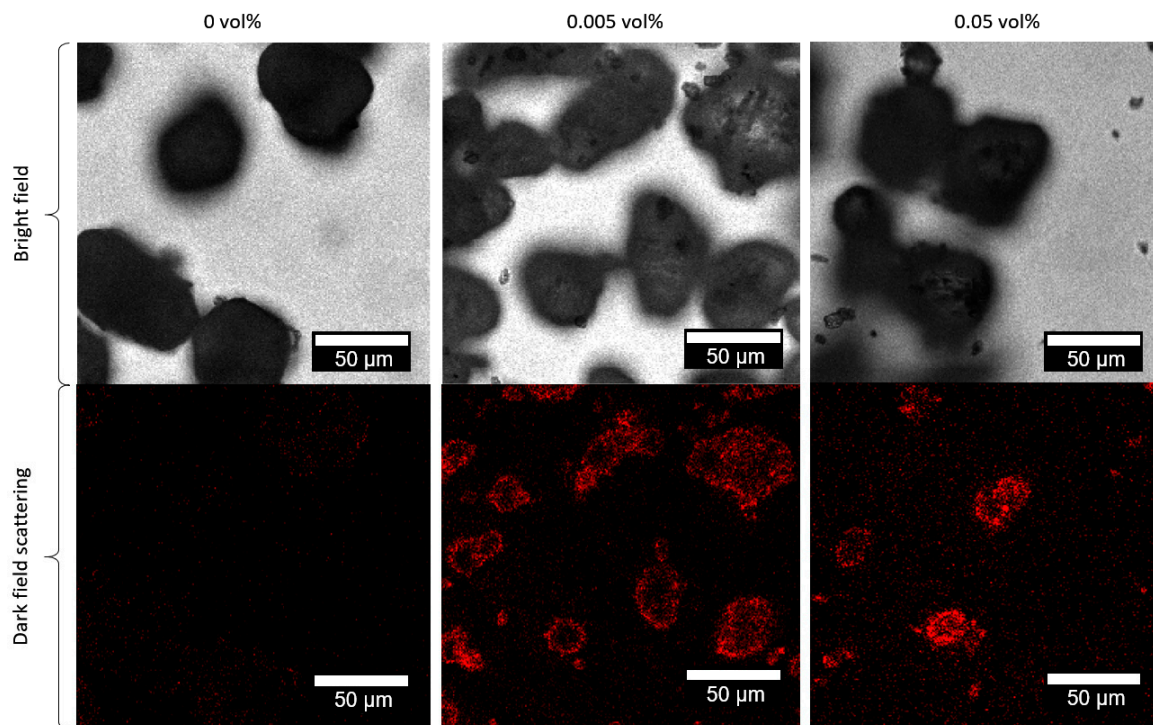


Figure 5. Representative confocal bright field images and laser scanning dark field images of pure PA12 and PA12 colloidal additivated with 0.005 and 0.05 vol% of laser irradiated carbon nanoparticles, respectively. For dark-field imaging, the sample was excited at a wavelength of 500 nm and the detection wavelength was set to 507–587 nm.

SEM images confirm the homogeneous distribution and high dispersion of the nanoparticles on the polymer particle surface (Figure 6a–c). As expected from the colloidal analysis, small aggregates appear. The effect of dispersion and nanoparticle size on the surface coverage on the polymer particle surface is described in the scaling graphs in Figure 6d,e. Reducing the particle size by one magnitude, e.g., from 500 nm to 50 nm, also results in an increase of theoretical surface coverage by one magnitude. This is shown exemplarily in the scaling graphs in Figure 6d,e. If the particle size is dropping further to 10 nm, even 0.01 vol% of carbon nanoparticles would be enough to completely cover the polymer particles with 10 surf%. Therefore, the surface coverage could be an interesting parameter to quantify the dispersion quality and quantity, instead of just using wt% to describe the nanoparticle loading. However, for practical usage it is difficult to use this value, due to the limited resolution of SEM imaging of carbon nanoparticles on a polymer surface. This can be explained by the low contrast between nanoparticle and polymer. Especially, ultra-small carbon nanoparticles in the sub-10 nm-scale, which are generated during LPP, cannot be resolved. Eventually, the primary particle diameter cannot be determined exactly. In addition, surf% was also calculated from the polymer particle size distributions, neglecting any surface porosity of the polymer particles. Especially, the latter will highly influence a calculation of the surface coverage. However, the general scaling graphs in Figure 6d,e outline the importance of high dispersion and small nanoparticle sizes in order to reach a high surface coverage at small nanoparticle loadings.

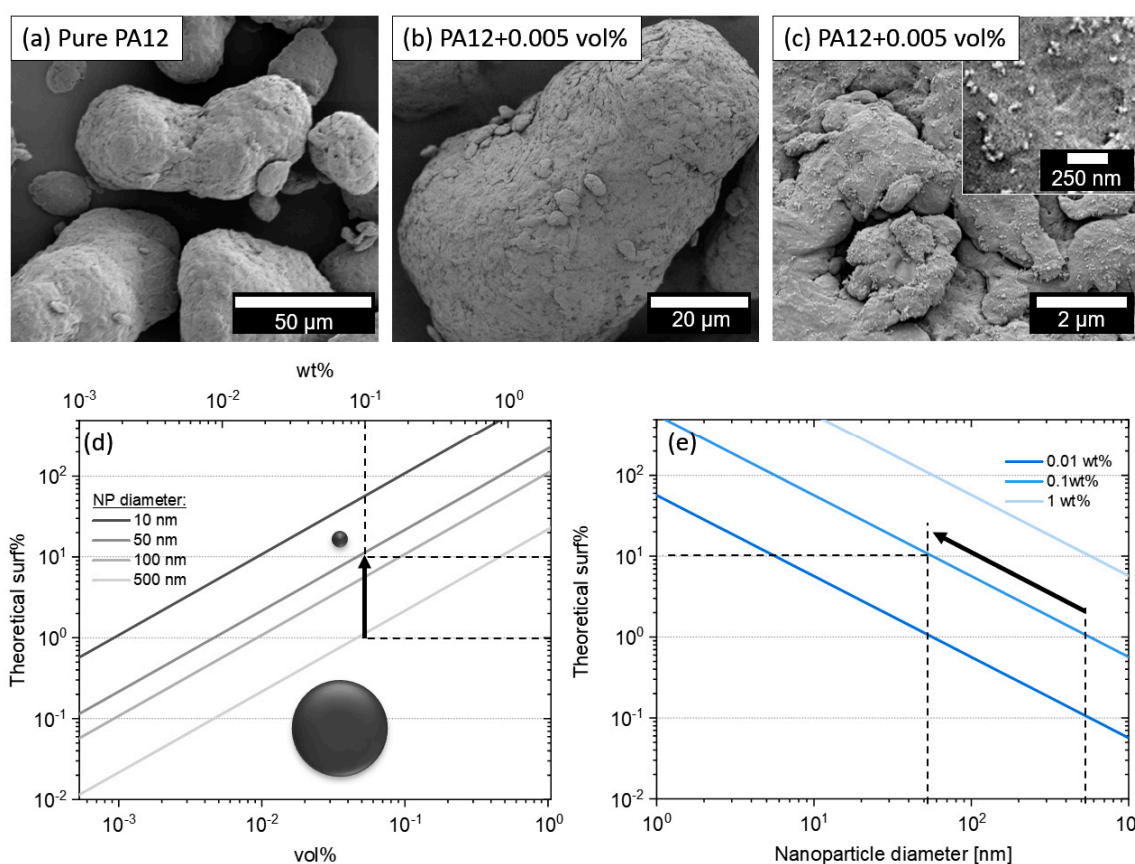


Figure 6. (a) SEM images of PA12 particles (a) before and (b) after colloidal addition with 0.005 vol% (0.01 wt%) of carbon nanoparticles (LPP at highest fluence). (c) Zoom in shows the homogeneous distribution of carbon nanoparticles on the surface of the polymer microparticle. (d,e) Scaling graphs illustrating the connection between vol%, wt%, and surface coverage (surf%) for different nanoparticles sizes on PA12 polymer powder (The specific surface area of PA12 was 0.114 m²/g, calculated from the particle size distribution, assuming spherical particles.). The dotted lines give an example of downsizing of the nanoparticle diameter and its effect on the theoretical surface coverage.

Although the high activity of the colloids for aggregation is a drawback for particle size analysis of the colloids, this property can be utilized to vary the dispersion of the nanoparticles on the polymer surface by variation of agglomeration after LPP. Our experimental set-up allows mixing the carbon nanoparticles with the polymer microparticles directly after laser irradiation or after a specific residence time. The hydrodynamic diameter (Figure 7a) shows a linear dependence on the waiting time between sample preparation and measurement (residence time). Comparing a direct measurement and a measurement after 30 min reveals a mean difference of more than 100 nm, which is an increase in hydrodynamic particle size of more than 200%. This reproducible effect is also reflected in the Feret diameter of the adsorbed particles and aggregates on the polymer surface (Figure 7b), and the polydispersity index (PDI; Figure 7c). The Feret diameter shifts from 25 to 80 nm, whereas the PDI increases from below 0.3 (monodisperse < 0.3) to ~0.4 after a residence time of 30 min. Please note that these measurements were just conducted once for each data point, since all SEM images needed to be analyzed manually. In addition, as mentioned before, SEM imaging of carbon nanoparticles on polymer is limited in its resolution due to low contrast between nanoparticle and polymer surface, especially on the sub-10 nm-scale. However, samples can be compared to each other, and the results in Figure 7a–c show clear tendency.

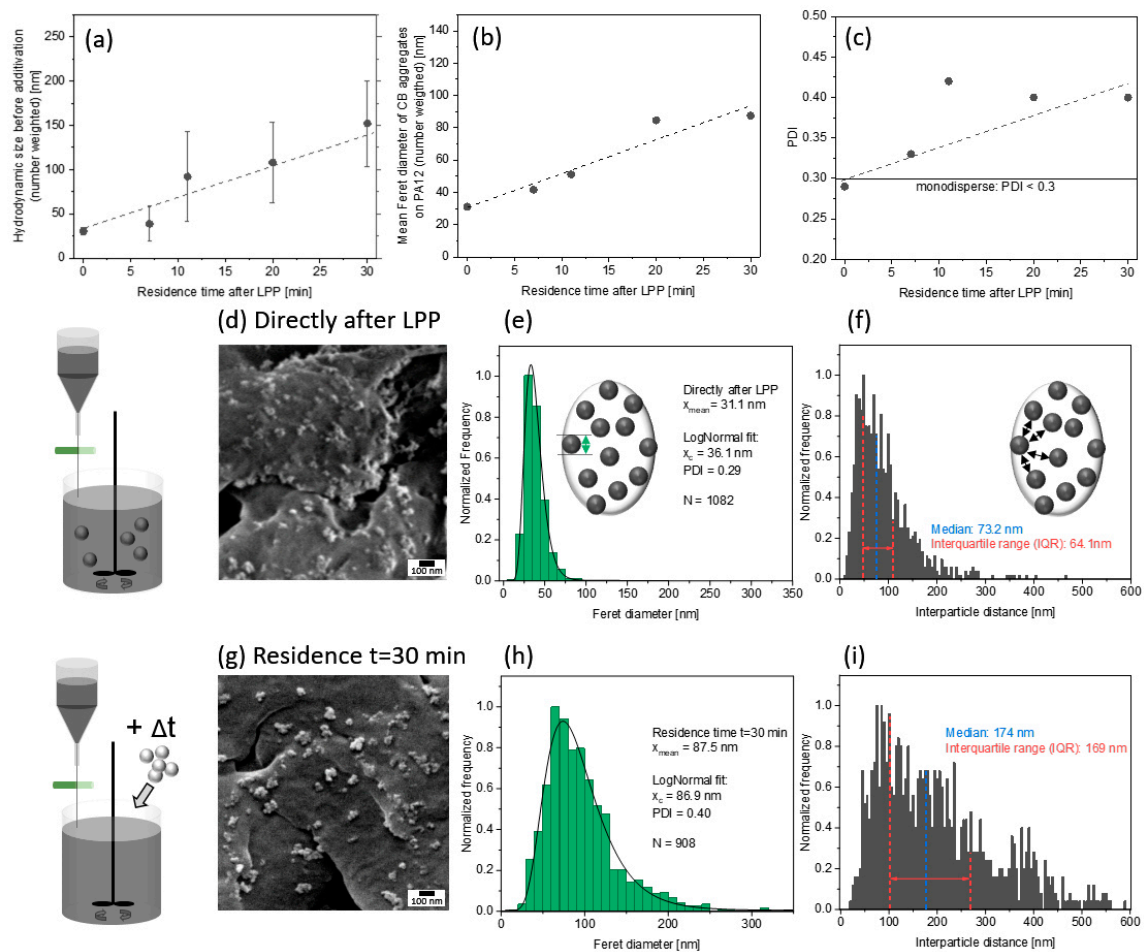


Figure 7. Comparison of (a) the hydrodynamic diameter after LPP with (b) the achieved $\text{Feret}_{\text{max}}$ diameters (primary particle diameter) of carbon nanoparticles on the polymer particle surface; (c) the corresponding polydispersity index (PDI) of carbon nanoparticles on the polymer particle surface at 0.005 vol%. SEM image of the PA12 particle surfaces after (d,g) colloidal additivation. (e,h) Corresponding number-weighted $\text{Feret}_{\text{max}}$ size distribution of carbon nanoparticles on the surface of PA12 particles and (f,i) interparticle distance distribution. For the comparison of particle size and interparticle distance, several images were taken for each sample at the same resolution. Nanoparticles and distances were analyzed for at ~1000 nanoparticles, e.g., $N=1082$ in panel (e) and $N=908$ in panel (h).

Our presented set-up allows a flexible additivation of polymer micropowders via the liquid-flow LPP and colloidal downstream supporting process. At a throughput of 180 mg of carbon nanoparticles per hour, equivalent to 3.6 L of colloid, it is capable to additivate 1.8 kg/h of polymer powder at a loading of 0.005 vol%, which is a sufficient amount for powder production to allow PBF-LB/P parameter studies and 3D printing of test structures. Equipped with a static mixer instead of a stirred tank reactor, this approach has an even higher potential for fully automated, continuous colloidal additivation.

3.3. PA12 Powder Characteristics

To ensure the processability of the nanoparticle–polymer composite powder in terms of powder recoating/spreading during PBF-LB/P, colloidal additivation should not worsen the morphology and geometry of the base particles, preserving the extraordinary flowability of the base powder material. Therefore, particle size distribution before and after colloidal additivation is analyzed. The addition of 0.05 and 0.005 vol% carbon nanoparticles (CB) does not show significant differences (n.s.; $P > 0.05$) in the $x_{10,3}$, $x_{50,3}$ and $x_{90,3}$ of volume-weighted distribution (Figure 8a). Furthermore, all particle size

distributions are located within the desired average particle size of 10 and 120 μm for PBF-LB/P [64]. Minor changes of particle size distribution are only significant for the number-weighted distribution. However, the total impact is rather minimal and should not negatively influence the flowability of the powders. This hypothesis could be validated by measuring the Hausner ratio (HR). Here, the addition of small amounts of CB does not significantly (n.s.; $P > 0.05$) affect the good flowability (< 1.25) of the base powder (Figure 8b), which shows a Hausner ratio similar to typical PA12 powders used for PBF-LB/P [65]. This is also confirmed by dynamic flow properties, characterized by the unchanged avalanche angle (Figure 8c).

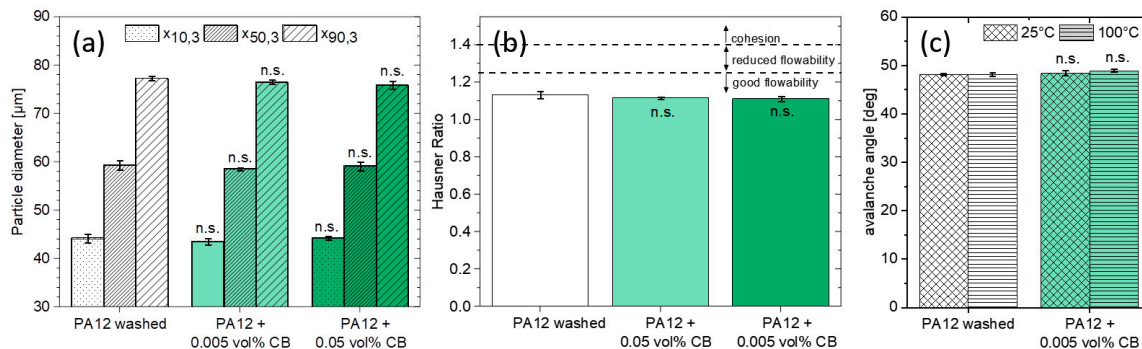


Figure 8. (a) Polymer microparticle size distribution, (b) Hausner ratio, and (c) avalanche angle before and after colloidal addition for 3 samples each. Particle sizes are based on the projected area of a sphere \times_{area} . The significance analysis shows no significant differences (n.s.) through the addition of different amounts of CB.

3.4. Analysis of the Crystallization Behavior

Particles of nanoscale dimensions can significantly influence the melting enthalpy and act as heterogeneous nucleation seeds, increasing the crystallization temperature and initiating crystal growth during cooling [66–68]. Even small amounts (0.005 vol%) of CB induce a change of the crystallization, and subsequent melting behavior as shown in the DSC analysis (Figure 9a,b). The crystallization onset, peak, and endset temperatures shift significantly (****; $P \leq 0.0001$) to 3 $^{\circ}\text{C}$ higher temperature values (Figure 9c). The addition of 0.05 vol% CB increases the onset and the peak temperature even further (+5 $^{\circ}\text{C}$) compared to the base material. Based on these thermal results, CB seem to act as heterogeneous nucleation seeds already at a minute amount of nanoadditive. By subsequently heating the DSC samples, the melting behavior of the crystalline structures can be analyzed (Figure 9b,d).

The addition of CB leads to an increase in the heat of fusion ΔH_m at ~ 172 $^{\circ}\text{C}$ (Figure 10), displayed by a larger peak area (Figure 10b), which indicates an increasing number of thinner lamellar crystalline structures [69]. From the heat of fusion, the crystallinity X_c of the samples was calculated according to Equation (2) [70,71]:

$$X_c = \frac{\Delta H_m}{\Delta H_{100} \cdot (1 - w_f)} = \frac{\Delta H_m}{209.3 \frac{\text{J}}{\text{g}} \cdot (1 - w_f)} \quad (2)$$

where the enthalpy of fusion of a 100% crystalline PA12 crystal ΔH_{100} is given in the literature [72], and w_f is the weight percentage of the nanofiller in the composite. At higher amounts of CB (0.05 vol%), the overall heat of fusion shows a significant (**; $p \leq 0.01$) decrease compared to the base material, while the crystallinity increases significantly (***; $p \leq 0.001$) (Figure 10b). Based on these measurements, higher amounts of CB seem to promote the crystal growth at a cooling rate of 10 K/min. This correlates with the fact that more CB lead to more nucleation sites, increasing the amount of crystalline structures.

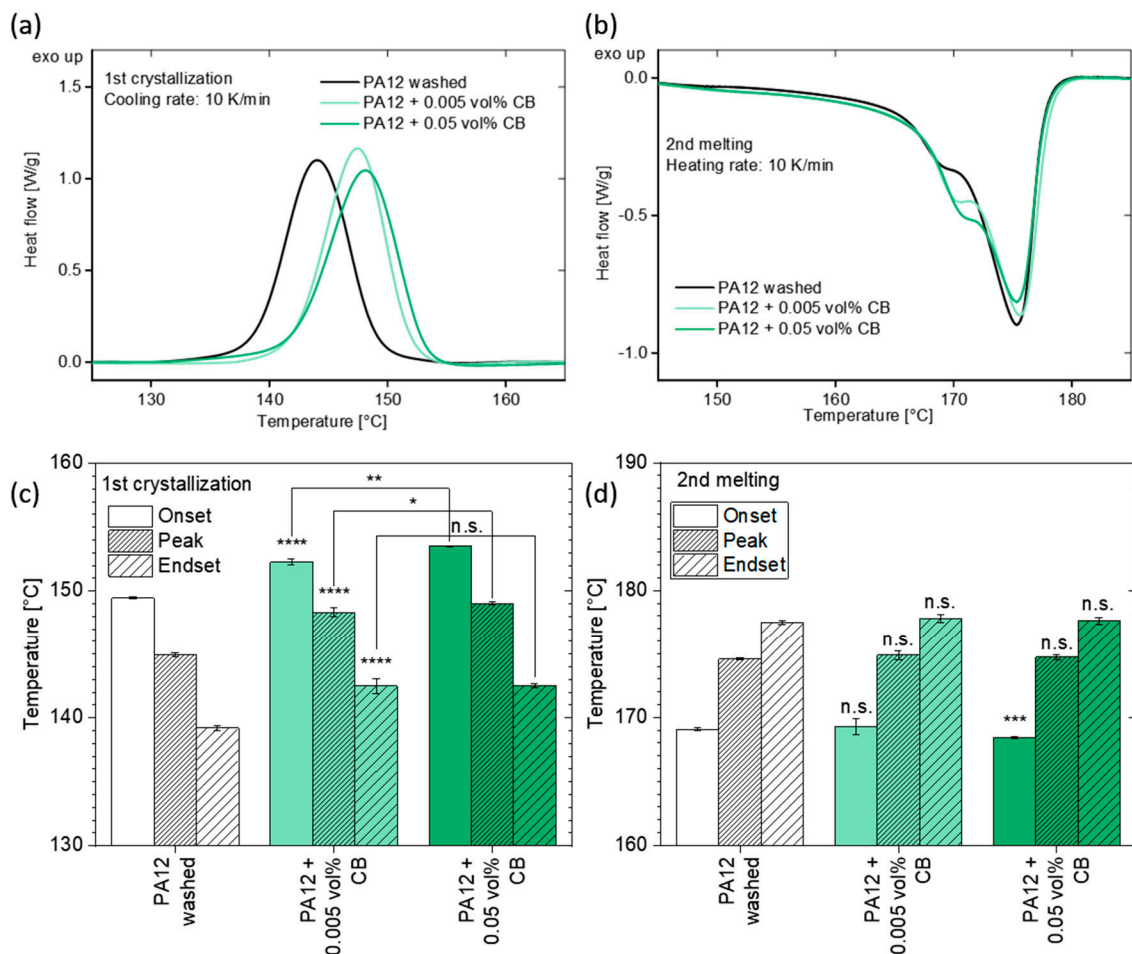


Figure 9. DSC analysis of PA12 powder before and after colloidal addition with the laser-generated carbon nanoparticles: (a) 1st crystallization and (b) 2nd heating curves, based on the average of 3 runs. (c,d) Extracted onset, peak, and endset temperatures with corresponding error bars. The analysis of statistical significance either shows no significant difference (n.s.; $p > 0.05$) or a significant difference, where the p -values decrease with the increasing number of asterisks.

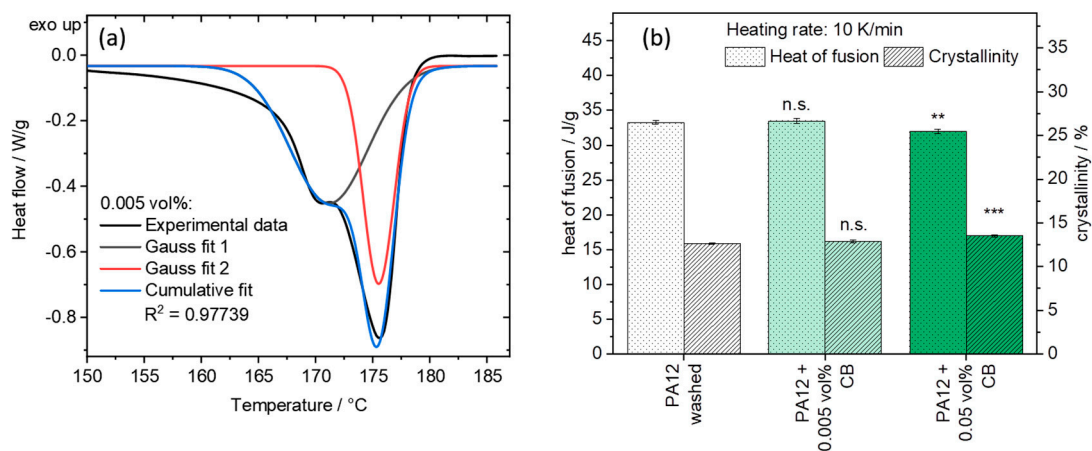


Figure 10. (a) Exemplary determination of the heat of fusion of both peak areas from the DSC second heating curve and (b) heat of fusion and crystallinity of PA12 and its composites after colloidal addition calculated from the DSC data. No significant changes are visualized with n.s. ($p > 0.05$) and significant differences with asterisks ** ($p \leq 0.01$) and *** ($p \leq 0.001$).

For a more detailed analysis of the nucleation effects of CB, an evaluation of the area underneath the two peaks of the heat of fusion curve of Figure 9b was conducted in Figure 10a. The deconvolution of two Gaussian curves ($R^2 > 0.97$) shows that the left area increases with increasing amounts of CB from 18.10 to 21.38 and finally to 22.57 J/g, while the right area sank from 16.18 to 13.57 and finally to 11.01 J/g, accordingly. This leads to the conclusion that the addition of CB increases the amount of thinner lamellar crystals while decreasing the amount of thicker crystalline structures [69]. Further proof for different crystal dimensions can come from polarization microscopy imaging of sliced DSC samples. Pure PA12 samples show the typical spherulite structures of a Maltese cross (Figure 11a) with an aspect ratio of 1.04 ± 0.04 . The origin of these crystals is located in their center. The addition of 0.005 vol% CB leads to different crystalline structures instead. Some of the typical round spherulite structures are replaced by oval shapes at 0.005 vol% CB (Figure 11b) with an aspect ratio of 1.48 ± 0.38 . This phenomenon becomes further evident when increasing the amount of CB to 0.05 vol% and thereby the density of the carbon nanoparticles on the polymer matrix. In this case, oval structures dominate the crystalline areas in the sample (Figure 11c), resulting in an even higher aspect ratio of 1.71 ± 0.35 (Figure 11d). The transition point between solely spherulites and only oval lamellar structures seems to lie between 0.005 and 0.05 vol% CB in PA12.

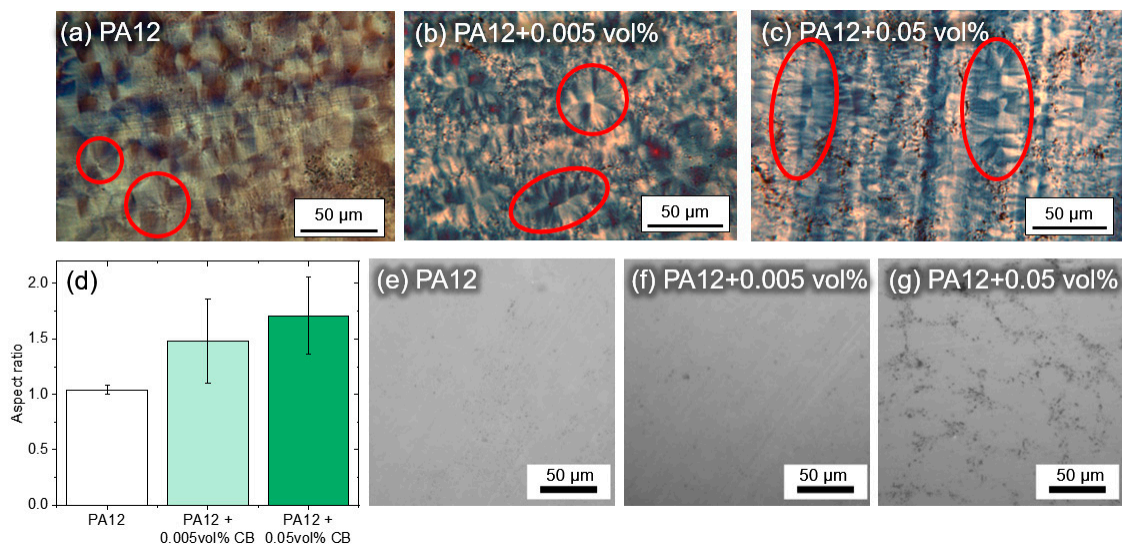


Figure 11. (a–c) Polarization microscopy images of PA12 with different carbon nanoparticles loading, showing representative crystalline structures of different dimensions. (d) Corresponding aspect ratio of observed crystalline shapes at different carbon nanoparticles loadings. (e–g) Bright-field images of PA12 with carbon nanoparticles, depicted as black dots. Samples were analyzed after sizing to 10 μm films.

An explanation for the change of crystal structure could lie in the nanoparticle dispersion within the polymer matrix. Incident bright-field images of the sample slices are shown in Figure 11e–g. Increasing the amount of CB to 0.05 vol% clearly shows the CB distribution throughout the polymer matrix. The CB, which were initially adhered to the surface of the powder particles, are distributed on former polymer powder particle surface, creating a superstructure on the former surface of the polymer particles, visible as chain formation in the sliced samples. As a result, spherulites which originate on these nucleation seeds show highly anisotropic growth. This transition in crystal structures could have an effect on mechanical properties of final parts and should be examined in future studies. To prove that PA12 powders additivated with 0.005 vol% of colloidal nanoparticles can be processed on a PBF-LB/P machine, a test sample of 10 layers was successfully printed on an EOSINT P385 (150 μm layers, 13 × 13 mm²) (Figure 12), indicating high potential for generating test structures of refined parameters for an optimal layer bonding in follow-up studies on the influence of a very low carbon nanoparticle dose on the microstructure and properties of printed polymer parts.

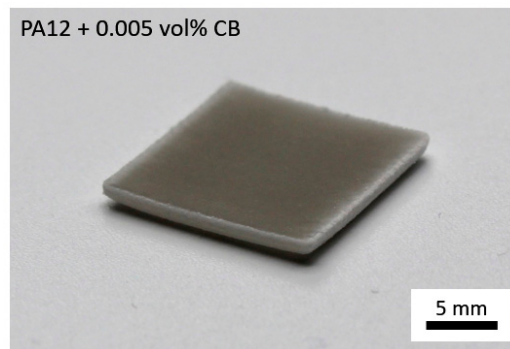


Figure 12. Test sample generated by PBF-LB/P of PA12 powder additivated with 0.005 vol% carbon nanoparticles.

4. Conclusions

Carbon nanoadditives are often applied at high weight doses in polymer feedstock powder for PBF-LB/P. This limits the dispersion and decreases the number of nuclei for heterogeneous nucleation of the polymer. Alternatively to chemical ligands as dispersion aids, which might hinder the polymer–nanoparticle bonding significantly, lower additive doses could be applied in case a good dispersion on the polymer surface is achieved. Hence, the influence of the degree of nanoparticle dispersion is an important aspect for the application of nanofunctionalized polymer powders in PBF-LB/P. By colloidal additivation of PA12 with carbon nanoparticles in an aqueous dispersion at comparable small loadings, we were able to coat the polymer particles with a homogenous layer of carbon nanoparticles. Colloidal nanoparticles were dispersed and fragmented in water by laser postprocessing (LPP), prior to colloidal additivation. Our experiments reveal that the dispersion of the carbon nanoparticles on the polymer surface can be tailored by the waiting time between sample preparation and measurement (residence time). If direct mixing was performed immediately after laser irradiation, the nanofunctionalized PA12 shows a high carbon nanoparticle dispersion on its surface with a polydispersity index $PDI < 0.3$.

As-prepared feedstock materials trigger heterogeneous nucleation effects even at just 0.005 vol% of carbon nanoparticles, underlining the value of high dispersion. Through their high surface coverage (surf%) and their small interparticle distances of 50–100 nm, the carbon nanoparticles form a superstructure after melting the polymer matrix. Hereby, they affect the lamellar dimensions of the crystalline structures. The form of the crystals changes from typical round spherulites to oval lamellar structures with the addition of more carbon nanoparticles. Exemplary PBF-LB/P experiments show that the modified PA12 powder with 0.005 vol% CB can be processed like the raw PA12 powder. A deeper understanding of nanoparticle influence on polymer crystallization at small nanoparticle doses will facilitate a precise modification of the microstructure and could have significant effects on the mechanical properties of printed parts.

Author Contributions: Conceptualization, T.H., B.G., and S.B. Methodology, T.H., F.R., and A.S., formal analysis, T.H., A.S., and F.R., investigation, T.H., A.S., F.R., S.G., and C.D.-B, data curation, T.H. and A.S., writing—original draft preparation, T.H. and A.S., writing—review and editing, T.H., A.S., F.R., S.G., and B.G., M.S., S.B., and C.D.-B, visualization, T.H., F.R., A.S., and C.D.-B, supervision, B.G., S.B., and M.S., funding acquisition, S.B., M.S., and B.G. All authors have read and agreed to the published version of the manuscript.

Funding: Tim Hupfeld thanks Evonik industries for financial support. Alexander Sommereyns gratefully acknowledges the funding of the Erlangen Graduate School in Advanced Optical Technologies (SAOT) by the German Research Foundation (DFG) in the framework of the German excellence initiative. The authors gratefully acknowledge the funding by the German Research Foundation (DFG) within the priority program (SPP) 2122 “Materials for Additive Manufacturing” (MATframe, BA 3580/27-1 and SCHM 2115/78-1). Bilal Gökce additionally acknowledges funding from the DFG, project GO 2566/10-1.

Acknowledgments: We acknowledge Jurij Jacobi for TEM imaging of nanoparticles. Furthermore, we thank S. Boukercha (Group of Matthias Epple, University of Duisburg-Essen) and IMCES (Imaging Center Essen, University Hospital Essen) for SEM imaging of polymer powders, and we thank Yaya Li for confocal imaging

of powder samples. We thank Tobias Kolb (Robert Bosch GmbH Nürnberg) for providing the possibility of powder measurements with the Camsizer X2. We also acknowledge Sven Reichenberger and Swen Zerebecki for performing Raman measurements. Stan Gann thanks Markus Piechotta for his support during analysis of dynamic flowability.

Conflicts of Interest: The authors declare no conflicts of interest.

References

1. Savolainen, J.; Collan, M. How Additive Manufacturing Technology Changes Business Models?—Review of Literature. *Addit. Manuf.* **2020**, *32*, 101070. [[CrossRef](#)]
2. Wudy, K.; Drummer, D. Aging effects of polyamide 12 in selective laser sintering: Molecular weight distribution and thermal properties. *Addit. Manuf.* **2019**, *25*, 1–9. [[CrossRef](#)]
3. Dechet, M.A.; Baumeister, I.; Schmidt, J. Development of polyoxymethylene particles via the solution-dissolution process and application to the powder bed fusion of polymers. *Materials* **2020**, *13*, 1535. [[CrossRef](#)] [[PubMed](#)]
4. Dechet, M.A.; Demina, A.; Römling, L.; Gómez Bonilla, J.S.; Lanyi, F.J.; Schubert, D.W.; Bück, A.; Peukert, W.; Schmidt, J. Development of poly(L-lactide) (PLLA) microspheres precipitated from triacetin for application in powder bed fusion of polymers. *Addit. Manuf.* **2020**, *32*, 100966. [[CrossRef](#)]
5. Wu, H.; Fahy, W.P.; Kim, S.; Kim, H.; Zhao, N.; Pilato, L.; Kafi, A.; Bateman, S.; Koo, J.H. Recent developments in polymers/polymer nanocomposites for additive manufacturing. *Prog. Mater. Sci.* **2020**, *111*, 100638. [[CrossRef](#)]
6. Schmid, M.; Wegener, K. Thermal and molecular properties of polymer powders for Selective Laser Sintering (SLS). *AIP Conf. Proc.* **2016**, *1779*, 100003. [[CrossRef](#)]
7. Lexow, M.M.; Drummer, D. New Materials for SLS: The Use of Antistatic and Flow Agents. *J. Powder Technol.* **2016**, *2016*, 1–9. [[CrossRef](#)]
8. Schmid, M. Laser Sintering with Plastics. In *Laser Sintering with Plastics—Technology, Processes, and Materials*; Carl Hanser Verlag GmbH & Co. KG: Munich, Germany, 2018; pp. I–XIII. ISBN 978-1-56990-683-5.
9. Yuan, S.; Shen, F.; Chua, C.K.; Zhou, K. Polymeric composites for powder-based additive manufacturing: Materials and applications. *Prog. Polym. Sci.* **2019**, *91*, 141–168. [[CrossRef](#)]
10. Yi, X.; Tan, Z.J.; Yu, W.J.; Li, J.; Li, B.J.; Huang, B.Y.; Liao, J. Three dimensional printing of carbon/carbon composites by selective laser sintering. *Carbon N. Y.* **2016**, *96*, 603–607. [[CrossRef](#)]
11. Sahu, S.; Behera, B.; Maiti, T.K.; Mohapatra, S. Simple one-step synthesis of highly luminescent carbon dots from orange juice: Application as excellent bio-imaging agents. *Chem. Commun.* **2012**, *48*, 8835–8837. [[CrossRef](#)]
12. Tzounis, L.; Petousis, M.; Grammatikos, S.; Vidakis, N. 3D Printed Thermoelectric Polyurethane/Multiwalled Carbon Nanotube Nanocomposites: A Novel Approach towards the Fabrication of Flexible and Stretchable Organic Thermoelectrics. *Materials* **2020**, *13*, 2879. [[CrossRef](#)] [[PubMed](#)]
13. Yuan, S.; Chua, C.K.; Zhou, K. 3D-Printed Mechanical Metamaterials with High Energy Absorption. *Adv. Mater. Technol.* **2019**, *4*, 1–9. [[CrossRef](#)]
14. Blackburn, J.L.; Ferguson, A.J.; Cho, C.; Grunlan, J.C. Carbon-Nanotube-Based Thermoelectric Materials and Devices. *Adv. Mater.* **2018**, *30*, 1–35. [[CrossRef](#)] [[PubMed](#)]
15. Manufacturing, A. Performance of Short Fiber Interlayered Reinforcement Thermoplastic Resin in Additive Manufacturing. *Materials* **2020**, *13*, 2868.
16. Ponnamma, D.; Sadasivuni, K.K.; Grohens, Y.; Guo, Q.; Thomas, S. Carbon nanotube based elastomer composites—an approach towards multifunctional materials. *J. Mater. Chem. C* **2014**, *2*, 8446–8485. [[CrossRef](#)]
17. Guan, L.Z.; Zhao, L.; Wan, Y.J.; Tang, L.C. Three-dimensional graphene-based polymer nanocomposites: Preparation, properties and applications. *Nanoscale* **2018**, *10*, 14788–14811. [[CrossRef](#)]
18. Lawal, A.T. Graphene-based nano composites and their applications. A review. *Biosens. Bioelectron.* **2019**, *141*, 111384. [[CrossRef](#)]
19. Xiao, L.; Sun, H. Novel properties and applications of carbon nanodots. *Nanoscale Horiz.* **2018**, *3*, 565–597. [[CrossRef](#)]
20. Liu, K.; Yu, J.; Li, Y.; Yan, X.; Bai, D.; Liao, X.; Zhou, Z.; Gao, Y.; Yang, X.; Li, L. Carbon Black from Diesel Soot for High-Performance Wearable Pressure Sensors. *Adv. Mater. Technol.* **2019**, *4*, 1–7. [[CrossRef](#)]

21. Jian, M.; Xia, K.; Wang, Q.; Yin, Z.; Wang, H.; Wang, C.; Xie, H.; Zhang, M.; Zhang, Y. Flexible and Highly Sensitive Pressure Sensors Based on Bionic Hierarchical Structures. *Adv. Funct. Mater.* **2017**, *27*. [[CrossRef](#)]
22. Jing, W.; Hui, C.; Qiong, W.; Hongbo, L.; Zhanjun, L. Surface modification of carbon fibers and the selective laser sintering of modified carbon fiber/nylon 12 composite powder. *Mater. Des.* **2017**, *116*, 253–260. [[CrossRef](#)]
23. Athreya, S.R.; Kalaitzidou, K.; Das, S. Processing and characterization of a carbon black-filled electrically conductive Nylon-12 nanocomposite produced by selective laser sintering. *Mater. Sci. Eng. A* **2010**, *527*, 2637–2642. [[CrossRef](#)]
24. Goodridge, R.D.; Shofner, M.L.; Hague, R.J.M.; McClelland, M.; Schlea, M.R.; Johnson, R.B.; Tuck, C.J. Processing of a Polyamide-12/carbon nanofibre composite by laser sintering. *Polym. Test.* **2011**, *30*, 94–100. [[CrossRef](#)]
25. Salmoria, G.V.; Paggi, R.A.; Lago, A.; Beal, V.E. Microstructural and mechanical characterization of PA12/MWCNTs nanocomposite manufactured by selective laser sintering. *Polym. Test.* **2011**, *30*, 611–615. [[CrossRef](#)]
26. Wagner, T.; Höfer, T.; Knies, S.; Eyerer, P. Laser sintering of high temperature resistant polymers with carbon black additives. *Int. Polym. Process.* **2004**, *19*, 395–401. [[CrossRef](#)]
27. Bai, J.; Goodridge, R.D.; Hague, R.J.M.; Song, M. Improving the Mechanical Properties of Laser-Sintered Polyamide 12 Through Incorporation of Carbon Nanotubes. *Polym. Eng. Sci.* **2013**, *53*, 1937–1946. [[CrossRef](#)]
28. Ivanova, O.; Williams, C.; Campbell, T. Additive manufacturing (AM) and nanotechnology: Promises and challenges. *Rapid Prototyp. J.* **2013**, *19*, 353–364. [[CrossRef](#)]
29. Bai, J.; Goodridge, R.D.; Hague, R.J.M.; Song, M.; Murakami, H. Nanostructural characterization of carbon nanotubes in laser-sintered polyamide 12 by 3D-TEM. *J. Mater. Res.* **2014**, *29*, 1817–1823. [[CrossRef](#)]
30. Kim, H.C.; Hahn, H.T.; Yang, Y.S. Synthesis of PA12/functionalized GNP nanocomposite powders for the selective laser sintering process. *J. Compos. Mater.* **2012**, *47*, 501–509. [[CrossRef](#)]
31. Zheng, W.; Lu, X. Wong S-C. Electrical and mechanical properties of expanded graphite-reinforced high density polyethylene. *J. Appl. Polym. Sci.* **2004**, *91*, 2781–2788. [[CrossRef](#)]
32. Jain, P.K.; Pandey, P.M.; Rao, P.V.M. Selective laser sintering of clay-reinforced polyamide. *Polym. Compos.* **2010**, *31*, 732–743. [[CrossRef](#)]
33. Meyer, K.; Zimmermann, I. Effect of glidants in binary powder mixtures. *Powder Technol.* **2004**, *139*, 40–54. [[CrossRef](#)]
34. Rumpf, H. Die Wissenschaft des Agglomerierens. *Chem. Ing. Tech.* **1974**, *46*, 1–11. [[CrossRef](#)]
35. Blümel, C.; Sachs, M.; Laumer, T.; Winzer, B.; Schmidt, J.; Schmidt, M.; Peukert, W.; Wirth, K.E. Increasing flowability and bulk density of PE-HD powders by a dry particle coating process and impact on LBM processes. *Rapid Prototyp. J.* **2015**, *21*, 697–704. [[CrossRef](#)]
36. Yang, J.; Sliva, A.; Banerjee, A.; Dave, R.N.; Pfeffer, R. Dry particle coating for improving the flowability of cohesive powders. *Powder Technol.* **2005**, *158*, 21–33. [[CrossRef](#)]
37. Chen, B.; Davies, R.; Liu, Y.; Yi, N.; Qiang, D.; Zhu, Y.; Ghita, O. Laser sintering of graphene nanoplatelets encapsulated polyamide powders. *Addit. Manuf.* **2020**, *35*, 101363. [[CrossRef](#)]
38. Zhang, D.; Gökce, B.; Barcikowski, S. Laser Synthesis and Processing of Colloids: Fundamentals and Applications. *Chem. Rev.* **2017**, *117*, 3990–4103. [[CrossRef](#)]
39. Amans, D.; Cai, W.; Barcikowski, S. Status and demand of research to bring laser generation of nanoparticles in liquids to maturity. *Appl. Surf. Sci.* **2019**, *488*, 445–454. [[CrossRef](#)]
40. Amans, D.; Diouf, M.; Lam, J.; Ledoux, G.; Dujardin, C. Origin of the nano-carbon allotropes in pulsed laser ablation in liquids synthesis. *J. Colloid Interface Sci.* **2017**, *489*, 114–125. [[CrossRef](#)]
41. Tabatabaie, N.; Dorrani, D. Effect of fluence on carbon nanostructures produced by laser ablation in liquid nitrogen. *Appl. Phys. A* **2016**, *122*, 558. [[CrossRef](#)]
42. Castro, H.P.S.; Souza, V.S.; Scholten, J.D.; Dias, J.H.; Fernandes, J.A.; Rodembusch, F.S.; Dos Reis, R.; Dupont, J.; Teixeira, S.R.; Correia, R.R.B. Synthesis and Characterisation of Fluorescent Carbon Nanodots Produced in Ionic Liquids by Laser Ablation. *Chem. A Eur. J.* **2016**, *22*, 138–143. [[CrossRef](#)] [[PubMed](#)]
43. De Giacomo, A.; De Bonis, A.; Dell’Aglia, M.; De Pascale, O.; Gaudiuso, R.; Orlando, S.; Santagata, A.; Senesi, G.S.; Taccogna, F.; Teghil, R. Laser Ablation of Graphite in Water in a Range of Pressure from 1 to 146 atm Using Single and Double Pulse Techniques for the Production of Carbon Nanostructures. *J. Phys. Chem. C* **2011**, *115*, 5123–5130. [[CrossRef](#)]

44. Doñate-Buendia, C.; Torres-Mendieta, R.; Pyatenko, A.; Falomir, E.; Fernández-Alonso, M.; Mínguez-Vega, G. Fabrication by Laser Irradiation in a Continuous Flow Jet of Carbon Quantum Dots for Fluorescence Imaging. *ACS Omega* **2018**, *3*, 2735–2742. [[CrossRef](#)] [[PubMed](#)]
45. Baidakova, M.V.; Kukushkina, Y.A.; Sitnikova, A.A.; Yagovkina, M.A.; Kirilenko, D.A.; Sokolov, V.V.; Shestakov, M.S.; Vul', A.Y.; Zousman, B.; Levinson, O. Structure of nanodiamonds prepared by laser synthesis. *Phys. Solid State* **2013**, *55*, 1747–1753. [[CrossRef](#)]
46. Korepanov, V.I.; Hamaguchi, H.O.; Osawa, E.; Ermolenkov, V.; Lednev, I.K.; Etzold, B.J.M.; Levinson, O.; Zousman, B.; Epperla, C.P.; Chang, H.C. Carbon structure in nanodiamonds elucidated from Raman spectroscopy. *Carbon N. Y.* **2017**, *121*, 322–329. [[CrossRef](#)]
47. Schmitz, T.; Wiedwald, U.; Dubs, C.; Gökce, B. Ultrasmall Yttrium Iron Garnet Nanoparticles with High Coercivity at Low Temperature Synthesized by Laser Ablation and Fragmentation of Pressed Powders. *ChemPhysChem* **2017**, *18*, 1125–1132. [[CrossRef](#)]
48. Lau, M.; Barcikowski, S. Quantification of mass-specific laser energy input converted into particle properties during picosecond pulsed laser fragmentation of zinc oxide and boron carbide in liquids. *Appl. Surf. Sci.* **2015**, *348*, 22–29. [[CrossRef](#)]
49. Ziefuß, A.R.; Barcikowski, S.; Rehbock, C. Synergism between Specific Halide Anions and pH Effects during Nanosecond Laser Fragmentation of Ligand-Free Gold Nanoparticles. *Langmuir* **2019**, *35*, 6630–6639. [[CrossRef](#)]
50. Waag, F.; Gökce, B.; Kalapu, C.; Bendt, G.; Salamon, S.; Landers, J.; Hagemann, U.; Heidelmann, M.; Schulz, S.; Wende, H.; et al. Adjusting the catalytic properties of cobalt ferrite nanoparticles by pulsed laser fragmentation in water with defined energy dose. *Sci. Rep.* **2017**, *7*, 13161. [[CrossRef](#)]
51. Amado, A.; Schmid, M.; Levy, G.; Wegener, K. Advances in SLS powder characterization. *Group* **2011**, *7*, 12.
52. Ziegelmeier, S.; Wollecke, F.; Tuck, C.; Goodridge, R.; Hague, R. Characterizing the Bulk & Flow Behaviour of LS Polymer Powders. In Proceedings of the SFF Symposium, Austin, TX, USA, 12–14 August 2013; pp. 354–367.
53. Ziefuß, A.R.; Reichenberger, S.; Rehbock, C.; Chakraborty, I.; Gharib, M.; Parak, W.J.; Barcikowski, S. Laser Fragmentation of Colloidal Gold Nanoparticles with High-Intensity Nanosecond Pulses is Driven by a Single-Step Fragmentation Mechanism with a Defined Educt Particle-Size Threshold. *J. Phys. Chem. C* **2018**, *122*, 22125–22136. [[CrossRef](#)]
54. Sylvestre, J.P.; Poulin, S.; Kabashin, A.V.; Sacher, E.; Meunier, M.; Luong, J.H.T. Surface chemistry of gold nanoparticles produced by laser ablation in aqueous media. *J. Phys. Chem. B* **2004**, *108*, 16864–16869. [[CrossRef](#)]
55. Xu, R.; Wu, C.; Xu, H. Particle size and zeta potential of carbon black in liquid media. *Carbon N. Y.* **2007**, *45*, 2806–2809. [[CrossRef](#)]
56. Boehm, H.P. Some aspects of the surface chemistry of carbon blacks and other carbons. *Carbon N. Y.* **1994**, *32*, 759–769. [[CrossRef](#)]
57. George, S. *Infrared and Raman Characteristic Group Frequencies. Tables and Charts*; John Wiley & Sons: Hoboken, NJ, USA, 2004; ISBN 978-0-470-09307-8.
58. Kalus, M.-R.; Lanyumba, R.; Lorenzo-Parodi, N.; Jochmann, M.A.; Kerpen, K.; Hagemann, U.; Schmidt, T.C.; Barcikowski, S.; Gökce, B. Determining the role of redox-active materials during laser-induced water decomposition. *Phys. Chem. Chem. Phys.* **2019**, *21*, 18636–18651. [[CrossRef](#)]
59. Hupfeld, T.; Wegner, A.; Blanke, M.; Doñate-Buendía, C.; Sharov, V.; Nieskens, S.; Piechotta, M.; Giese, M.; Barcikowski, S.; Gökce, B. Plasmonic seasoning: Giving color to desktop laser 3D-printed polymers by highly dispersed nanoparticles. *Adv. Opt. Mater.* **2020**, 202000473. [[CrossRef](#)]
60. Blaeser, A.; Million, N.; Campos, D.F.D.; Gamrad, L.; Köpf, M.; Rehbock, C.; Nachev, M.; Sures, B.; Barcikowski, S.; Fischer, H. Laser-based in situ embedding of metal nanoparticles into bioextruded alginate hydrogel tubes enhances human endothelial cell adhesion. *Nano Res.* **2016**, *9*, 3407–3427. [[CrossRef](#)]
61. Klein, S.; Petersen, S.; Taylor, U.; Rath, D.; Barcikowski, S. Quantitative visualization of colloidal and intracellular gold nanoparticles by confocal microscopy. *J. Biomed. Opt.* **2010**, *15*, 036015. [[CrossRef](#)]
62. Kashiwagi, T.; Fagan, J.; Douglas, J.F.; Yamamoto, K.; Heckert, A.N.; Leigh, S.D.; Obrzut, J.; Du, F.; Lin-Gibson, S.; Mu, M.; et al. Relationship between dispersion metric and properties of PMMA/SWNT nanocomposites. *Polymer (Guildf)* **2007**, *48*, 4855–4866. [[CrossRef](#)]

63. Hupfeld, T.; Laumer, T.; Stichel, T.; Schuffenhauer, T.; Heberle, J.; Schmidt, M.; Barcikowski, S.; Gökce, B. A new approach to coat PA12 powders with laser-generated nanoparticles for selective laser sintering. *Procedia CIRP* **2018**, *74*, 244–248. [[CrossRef](#)]
64. Chatham, C.A.; Long, T.E.; Williams, C.B. A review of the process physics and material screening methods for polymer powder bed fusion additive manufacturing. *Prog. Polym. Sci.* **2019**, *93*, 68–95. [[CrossRef](#)]
65. Schmid, M.; Amado, F.; Levy, G.; Wegener, K. Flowability of powders for Selective Laser Sintering (SLS) investigated by Round Robin Test. In *High Value Manufacturing: Advanced Research in Virtual and Rapid Prototyping*; CRC Press: Boca Raton, FL, USA, 2013; pp. 95–99.
66. Yan, C.Z.; Shi, Y.S.; Yang, J.S.; Liu, J.H. An organically modified montmorillonite/nylon-12 composite powder for selective laser sintering. *Rapid Prototyp. J.* **2011**, *17*, 28–36. [[CrossRef](#)]
67. Piorkowska, E.; Rutledge, G.C. *Handbook of Polymer Crystallization*; Piorkowska, E., Rutledge, G.C., Eds.; John Wiley & Sons, Inc.: Hoboken, NJ, USA, 2013; ISBN 9781118541838.
68. Wang, Y.; Shi, Y.; Huang, S. Selective laser sintering of polyamide-rectorite composite. *Proc. Inst. Mech. Eng. Part L J. Mater. Des. Appl.* **2005**, *219*, 11–16. [[CrossRef](#)]
69. Schmid, M.; Amado, A.; Wegener, K. Materials perspective of polymers for additive manufacturing with selective laser sintering. *J. Mater. Res.* **2014**, *29*, 1824–1832. [[CrossRef](#)]
70. Pigliaru, L.; Rinaldi, M.; Ciccacci, L.; Norman, A.; Rohr, T.; Ghidini, T.; Nanni, F. 3D printing of high performance polymer-bonded PEEK-NdFeB magnetic composite materials. *Funct. Compos. Mater.* **2020**, *1*, 1–17. [[CrossRef](#)]
71. Rwei, S.P.; Ranganathan, P.; Lee, Y.H. Isothermal crystallization kinetics study of fully aliphatic PA6 copolyamides: Effect of novel long-chain polyamide salt as a comonomer. *Polymers* **2019**, *11*, 472. [[CrossRef](#)]
72. Gogolewski, S. Effect of annealing on thermal properties and crystalline structure of polyamides. *Colloid Polym. Sci.* **1979**, *257*, 811–819. [[CrossRef](#)]



© 2020 by the authors. Licensee MDPI, Basel, Switzerland. This article is an open access article distributed under the terms and conditions of the Creative Commons Attribution (CC BY) license (<http://creativecommons.org/licenses/by/4.0/>).

7 Application potential of 3D printed functionalized parts

AM provides designers with increased macroscopic design freedom through 3D CAD and a layer-by-layer manufacturing approach, which allow for complex geometries ranging from biomedical applications to bionic lightweight construction [65–67]. Beyond this, nanomaterial additivation of feedstock material adds the dimension of microscopic design freedom (Figure 13) [16,17]. As highlighted in the previous chapters, scalable colloidal additivation of polymer powders enables the generation of nanoparticle-functionalized feedstock material with outstanding dispersion, which could influence the processing

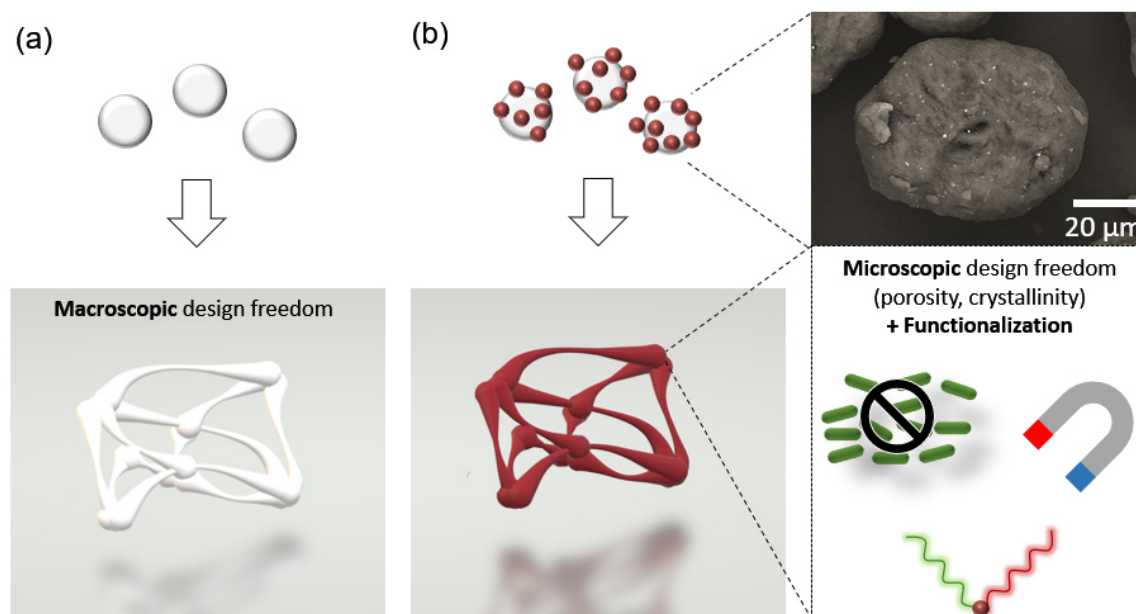


Figure 13: Design freedom in AM: (a) schematic illustration of a bionic 3D structure made from a powder feedstock that illustrates the macroscopic design freedom through 3D CAD and AM. (b) Nanoparticle-additivation of the feedstock material, adding microscopic design freedom (e.g. microstructure, crystallinity, porosity) and introducing new functionality (e.g. anti-bacterial, magnetical, plasmonic properties). The SEM image in (b) shows an exemplary PA12 particle decorated with silver nanoparticles.

behavior and could alter polymer microstructure after resolidification. In addition, the wide variety of materials, nanoparticle sizes, and phase compositions from which nanoparticles can be generated by laser-synthesis enables a further extension of applications.

Chapter 7.1 provides an example of the material class of magnetical functionalized polymers, which has attracted increasing attention over the last several years caused by 4D printing [39,45], active shape-changing structures [44,260,273], and printed parts with specific magnetic field distributions [43,274–276]. Magnetic functionalization of PA12 through colloidal additivation with iron oxide nanoparticles generated by LPP emphasizes the flexibility and transferability of the colloidal additivation approach to oxide nanoparticles (Chapter 7.1). Furthermore, this study investigates the robustness of magnetic performance and structural properties of the nanoparticle-functionalized feedstock materials along the process chain.

Due to their intrinsic material characteristics, laser generated nanoparticles could also enable novel applications with plasmonic and medical devices, where the dispersion of the nanomaterial is a crucial parameter that strongly influences the functionality of the part. For example, aggregation of plasmonic nanoparticles causes a shift of plasmon frequency and intensity. Therefore, Chapter 7.2 focuses on tunable plasmonic properties of gold-silver alloy nanoparticles and shows promising results for anti-bacterial applications of printed parts made from silver nanoparticle-functionalized feedstock materials that were successfully printed by PBF-LB.

7.1 Magnetic functionalization

3D Printing of Magnetic Parts by Laser Powder Bed Fusion of Iron Oxide Nanoparticle Functionalized Polyamide Powders

Reproduced from Journal of Materials Chemistry C 8, 12204-12217 (2020) with permission from the Royal Society of Chemistry

Highlights:

- Laser fragmentation of γ -Fe₂O₃ suspension with 355 nm Nd:YAG laser leads to monomodal size distribution of superparamagnetic iron oxide nanoparticles
- Mössbauer spectroscopy confirms reduction of approx. 25 % of the γ -Fe₂O₃ educt material to Fe₃O₄, caused by laser irradiation
- Production of a magnetic feedstock material by colloidal additivation of PA12 powder with synthesized iron oxide particles, processable by PBF-LB
- Nanoparticle size as well as magnetical and structural properties of laser irradiated iron oxide are transferred from the colloid to the feedstock material and the printed part

Appendix:

- Comparison of ns- and ps-LPP of iron oxide (A11)



Cite this: DOI: 10.1039/d0tc02740e

3D printing of magnetic parts by laser powder bed fusion of iron oxide nanoparticle functionalized polyamide powders

Tim Hupfeld,^a Soma Salamon,^b Joachim Landers,^b Alexander Sommereyns,^{cd} Carlos Doñate-Buendía,^{ae} Jochen Schmidt,^f Heiko Wende,^b Michael Schmidt,^{cd} Stephan Barcikowski^a and Bilal Gökce^{ib}*^a

The development of new feedstock materials is a central prerequisite for advances in Additive Manufacturing (AM). To increase the breadth of potential applications for 3D and 4D printing of polymers, micro- and nano-additives incorporated into the feedstock material play an important role. In this context, magnetic materials are of great interest. Our study describes a way to fabricate polymer powders for laser powder bed fusion (PBF-LB) with a homogeneous, well-dispersed coating of iron oxide nanoparticles. Without the addition of chemical precursors, spherical superparamagnetic FeO_x nanoparticles with monomodal size distribution below 10 nm are generated from FeO_x micropowder by laser fragmentation in liquid. The adsorption of the nanoparticles on polyamide (PA12) powder is conducted directly in an aqueous dispersion after laser fragmentation, followed by drying, powder analysis and PBF-LB processing. Via Mössbauer spectroscopy and magnetometry, we determined that the saturation magnetization and structure of the iron oxide nanoparticles were not influenced by PBF-LB processing, and the magnetic properties were successfully transferred to the final 3D-printed magnetic part.

Received 9th June 2020,
Accepted 22nd July 2020

DOI: 10.1039/d0tc02740e

rsc.li/materials-c

1. Introduction

Iron oxide (FeO_x) nanoparticles are known for their wide range of applications, such as *in vitro* diagnostics via magnetic resonance imaging,¹ magnetic hyperthermia in cancer therapy by magnetic heating,^{2–4} catalysis^{5,6} and targeted drug delivery.¹ FeO_x nanoparticles can also be incorporated into polymer matrices that can be processed to manufacture scaffolds for advanced bone tissue engineering.⁷ New applications arise from the field of 3D printing (Additive Manufacturing, AM) where mass customization and industrialization result in fast growth rates and the need for material variety.^{8,9} Nano-functionalized

magnetic materials can provide increased variety and represent a key towards new applications in 3D printing. FeO_x nanoparticles, for example, can be used for 3D printing of magnetic actuators for lab on a chip applications¹⁰ or force sensors.¹¹ Further, they can be used to produce 4D active shape-changing structures^{12,13} made by 3D printing of magnetic polymers. An external magnetic field is then used to trigger a change in the structure's shape over time (*i.e.* 4th dimension).^{14–16} This approach has high potential in creating flexible robotics and biomedical devices. For permanent magnetic objects, AM provides the opportunity to manufacture a magnetic 3D object based on a calculated structure that fulfills specific magnetic properties, such as a specific magnetic field distribution.^{17–20}

Typically, polymer materials for AM are magnetically functionalized by dispersing the nanomaterial in a polymer matrix and using it for well-established extrusion-based AM.^{13,21–23} Löwa *et al.* also reported a magnetically functionalized resin for AM by photopolymerization to manufacture phantoms for magnetic particle imaging.²⁴ Another widely used AM technique for industrial applications is laser powder bed fusion (PBF-LB) of polymers.^{25,26} Typically, mechanical, optical, or electrical functionalization of powders for PBF-LB by nano-materials often leads to aggregation of the nano-additive.^{27–29} A potential solution to this problem is the utilization of a

^a Technical Chemistry I and Center for Nanointegration Duisburg-Essen (CENIDE), University of Duisburg-Essen, Universitätsstrasse 7, 45141 Essen, Germany. E-mail: bilal.goekce@uni-due.de

^b Faculty of Physics and Center for Nanointegration Duisburg-Essen (CENIDE), University of Duisburg-Essen, Lotharstr. 1, 47057 Duisburg, Germany

^c Institute of Photonic Technologies (LPT), Friedrich-Alexander Universität Erlangen-Nürnberg, Konrad-Zuse-Str. 3-5, 91052 Erlangen, Germany

^d Erlangen Graduate School in Advanced Optical Technologies (SAOT), Friedrich-Alexander Universität Erlangen-Nürnberg, Germany

^e GRO-C-UJI, Institute of New Imaging Technologies, Universitat Jaume I, Avda. Sos Baynat sn, 12071 Castellón, Spain

^f Institute of Particle Technology (LFG), Friedrich-Alexander Universität Erlangen-Nürnberg, Cauerstr. 4, 91058 Erlangen, Germany

colloidal additivation route that typically leads to increased dispersion of nanoparticles on the polymer powder surface.^{30–32} In this method, nanoparticles are synthesized in a one-step process *via* laser synthesis and processing of colloids (LSPC) without the use of surfactants and chemical precursors.³³ Thereafter, adsorption of the colloidal particles on polymer microparticles takes place by mixing colloidal nanoparticles and the polymer powder directly in aqueous solution and controlling their electrostatic interaction and colloidal stability.³¹ The filtered and dried nanoparticle functionalized powder can then be used in PBF-LB. Besides the high dispersion of nanoparticles achieved by this process, LSPC also offers high flexibility regarding the nanomaterial, since it offers a broad span of processable materials and liquids.³⁴ Control of particle size^{35–37} and particle composition^{38–40} are strengths of LSPC, broadening different application areas, such as catalysis^{41,42} or biomedicine.⁴³ Oxide nanoparticle synthesis by LSPC has recently been reviewed, highlighting the application potential of laser-generated colloidal oxide, doped oxide, and sub-oxide nanoparticles.⁴⁴ Since FeO_x nanoparticles are featured in a broad variety of applications, their synthesis *via* LSPC has been reported by many researchers. Depending on parameters like educt, solvent, or laser wavelength, different FeO_x phases such as Fe, FeO, Fe₂O₃, and Fe₃O₄ can be synthesized.^{45–52} While laser ablation in liquid (LAL) is already a powerful method in terms of flexibility, subsequent irradiation of the colloid with another laser, referred to as laser fragmentation or melting in liquids (LFL or LML), can further manipulate the particle sizes and properties.^{53,54} This is typically performed in a batch process with a laser beam focused in a vessel filled with the colloid, resulting in a lack of fluence control, scattered particle properties, and low productivity. To achieve better control over the applied laser fluence and increase scalability, which is necessary to generate sufficient colloid amounts for applications in AM, a liquid jet reactor can be used.⁵⁵ Following this route, narrow size distributions can be achieved, enabling interesting magnetic properties of laser-irradiated oxides.⁵⁶

In this study, we demonstrate LFL of FeO_x nanoparticles by laser irradiation with different wavelengths in a liquid jet setup. After synthesis, nanoparticles are used to functionalize polyamide 12 (PA12) micropowders in a colloidal additivation process. After investigation of their dispersion on the polymer surface, the dried composite powder is analysed for its thermal and calorimetric properties and is finally processed by PBF-LB to create a 3D structure with magnetic functionality. Throughout the individual preparation steps from the as-prepared FeO_x nanoparticles to the final 3D structure, the magnetic performance and phase composition of the materials are analyzed.

2. Materials and methods

The processing route presented in this study is shown in Fig. 1. Iron oxide nanopowder (γ -Fe₂O₃) was purchased from Sigma-Aldrich and dispersed in deionized water by ultrasonic treatment for 10 minutes. The colloid concentration was 1 g L⁻¹. After ultrasonic treatment, colloids were irradiated with a Nd:YAG laser (Edgewave PX400-3-GH) in a liquid jet setup, similar to the procedure given in ref. 56. Irradiation was performed with a wavelength of either 355 nm or 532 nm and a repetition rate of 80 kHz (see Table 1).

Colloids were irradiated in multiple cycles (passages) to vary the specific energy dose applied to the colloids.^{55,57} The resulting colloids after LFL were then characterized by UV-Vis absorbance spectroscopy (Thermo Scientific Evolution 201), analytical disc centrifugation (ADC, CPS Instruments) and transmission electron microscopy (TEM, Zeiss EM 910) to evaluate the optimum process parameters (*i.e.* fluence, irradiation wavelength, necessary energy dose) for LFL. With these LFL-parameters, colloids were irradiated multiple times, directly followed by mixing with PA12 (Evonik Vestosint 1115, $d_{50,3} = 58 \mu\text{m}$) at the outlet of the liquid jet reactor. The suspension was then stirred for another five minutes before

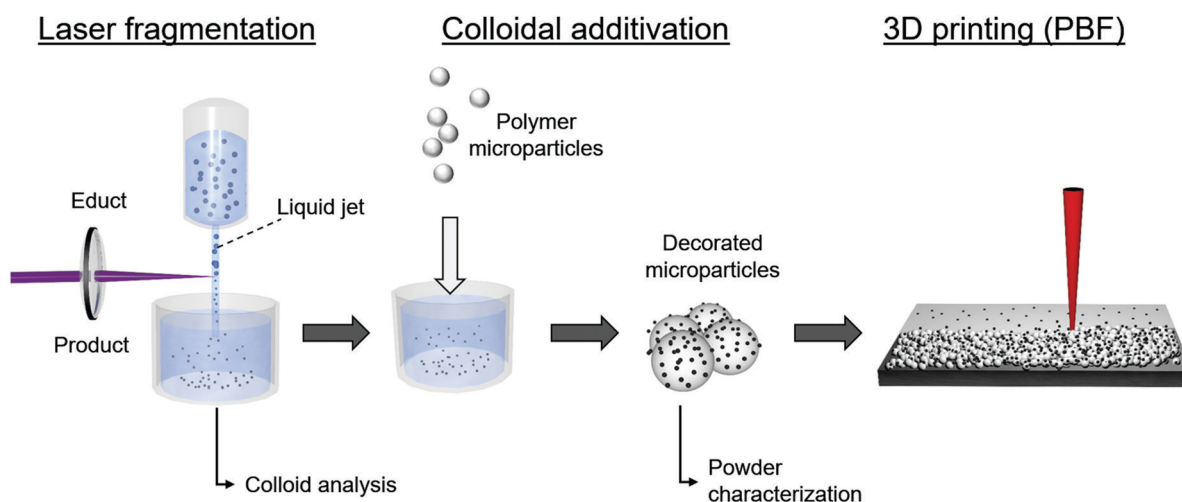


Fig. 1 Liquid jet fragmentation setup during LFL of iron oxide nanoparticles *via* ns irradiation at 355 nm and schematic process chain for FeO_x/polymer nanocomposite powder generation and AM by laser powder bed fusion.

Table 1 Laser parameters employed in the LFL experiments

λ /nm	Pulse duration/ps	Total power/W	Repetition rate/kHz	Pulse energy/mJ
355	10	28	80	0.35
532	10	77	80	0.96

Table 2 Parameter sets for variation of the energy density during PBF-LB (EOSINT P385, layer height of 300 μm)

Sample no.	Hatch distance/mm	Temperature/ $^{\circ}\text{C}$	Laser output power/W	Scan speed/ mm s^{-1}	Energy density/ J mm^{-2}
1	0.3	171	35	4500	0.026
2	0.3	171	37	4500	0.027
3	0.3	171	39	4500	0.029
4	0.3	171	39	4000	0.033
5	0.3	171	39	3500	0.037

filtration. Thereafter, the nano-functionalized PA12 powders were dried at 50 $^{\circ}\text{C}$, similar to the procedure in ref. 30. Powders were characterized by reflectance spectroscopy (Agilent Cary 100 Bi Cricket) and scanning electron microscopy (SEM, ESEM Quanta 400 FEG), and were ultimately processed with a Sharebot Snowwhite desktop PBF-LB machine. In addition, experiments on energy density variation were performed on an industrial PBF-machine (EOSINT P385), which enables a more exact tuning of energy density compared to the Sharebot Snowwhite. Parameters for this machine are given in Table 2. Although the EOS P385 is designed for larger objects (build area = 350 \times 350 mm^2), a build area reduction to 100 \times 350 mm^2 enables processing of smaller powder samples.

To evaluate the effect of the nano-additivation on the thermal material characteristics of PA12, calorimetric experiments and thermogravimetric analyses were conducted. PA12 composites were analyzed dynamically with a Mettler Toledo DSC 822e under nitrogen purge gas flow of 40 mL min^{-1} . Powder samples of approx. 12 mg were placed in 40 μL aluminum pans with covers. The measurement were performed in the temperature range from 25 $^{\circ}\text{C}$ to 250 $^{\circ}\text{C}$ with a heating rate of 20 K min^{-1} . At 80 and 250 $^{\circ}\text{C}$ the samples were held for 3 min to achieve thermal equilibrium. Afterwards, the samples were cooled down to 80 $^{\circ}\text{C}$ at a cooling rate of 20 K min^{-1} and heated up to 250 $^{\circ}\text{C}$ at 20 K min^{-1} . By using an integral tangential baseline, the enthalpy of fusion of the samples of the second heating run ΔH_{m} and thus their crystallinity X_{c} could be calculated according to eqn (1):^{58,59}

$$X_{\text{c}} = \frac{\Delta H_{\text{m}}}{\Delta H_{100} \cdot (1 - w_{\text{f}})} = \frac{\Delta H_{\text{m}}}{209.3 \frac{\text{J}}{\text{g}} \cdot (1 - w_{\text{f}})} \quad (\text{X})$$

with the enthalpy of fusion of a theoretical 100% crystalline PA12 crystal ΔH_{100} ⁶⁰ and w_{f} as the mass fraction of the nanoparticles in the composite.

Each powder composition was measured three times for statistical evaluation (T -test). The evaluation of the results

was performed by the Mettler Toledo STARE Evaluation Software 16.10.

The thermal decomposition behavior of PA12 materials was characterized by means of thermogravimetric analysis (TGA) using a TGA Q50 (TA Instruments). Around 55 to 60 mg of the respective sample were heated at a rate of 10 K min^{-1} from ambient temperature to 1000 $^{\circ}\text{C}$ under synthetic air being fed into the oven at 60 mL min^{-1} . At the end of this temperature ramp the temperature was kept isothermal for 5 minutes to allow for determination of the ash residue at 1000 $^{\circ}\text{C}$.

To determine the magnetic properties, the nanoparticles, the nano-functionalized micropowders, and the sintered bulk samples were characterized by the vibrating sample magnetometer (VSM) option of a Quantum Design PPMS DynaCool. Field-dependent measurements up to 9 T were performed at a temperature of 300 K. Mössbauer spectra were recorded in transmission geometry, using a ⁵⁷Co(Rh) radiation source, mounted on a constant-acceleration Mössbauer drive. Measurements were performed at room temperature as well as at *ca.* 80 K, using a liquid nitrogen bath-cryostat, also allowing us to analyze thermally activated processes, *i.e.* Néel-type superparamagnetism. To compensate for the strongly decreased absorption due to relatively low magnetic nanoparticle concentrations in the additivated micropowder as well as the final test structure, the studied sample mass was increased from *ca.* 20 mg cm^{-2} (FeO_x NPs) to *ca.* 1500 mg cm^{-2} (polymer samples).

3. Results and discussion

3.1 Laser fragmentation and spherification of FeO_x

Independent of the irradiation wavelength, the color of the colloids turns from turbid, rusty red to translucent dark brown or black during laser irradiation, which indicates a phase change or a change in particle size. With increasing specific energy dose, the color further shifts to black. As a quantitative measure of the fragmentation efficiency, the ratio between the absorbance of the product at 350 nm and 600 nm ($\text{Abs}_{350}/\text{Abs}_{600}$) analyzed by UV-Vis absorbance spectroscopy was used. This ratio is similar to the primary particle index (PPI), which is typically correlated to the hydrodynamic nanoparticle size.^{55,61,62} As Fig. 2a and b show, with irradiation of the educt at a wavelength of 355 nm, the $\text{Abs}_{350}/\text{Abs}_{600}$ value linearly scales with the applied specific energy dose (Fig. 2c and d). Alternatively to this approach, a double logarithmic plot of the absorbance spectrum can be used to calculate the Furlong slope, which also correlates to the inverse of particle size,⁶³ and, therefore, with $\text{Abs}_{350}/\text{Abs}_{600}$ (Fig. 2c and d). To compare the effect of laser wavelengths at their corresponding maximum fragmentation efficiency, the laser fluences were varied by focal displacement relative to the liquid jet. Exemplary results for 355 nm are shown in a 2D contour plot in Fig. 2e with special focus on the 3rd passage in Fig. 2f. As expected, the efficiency increases until a maximum, before the optical breakdown significantly reduces the efficiency (red marked area).⁵⁵ For both wavelengths, the distance between liquid jet and lens was

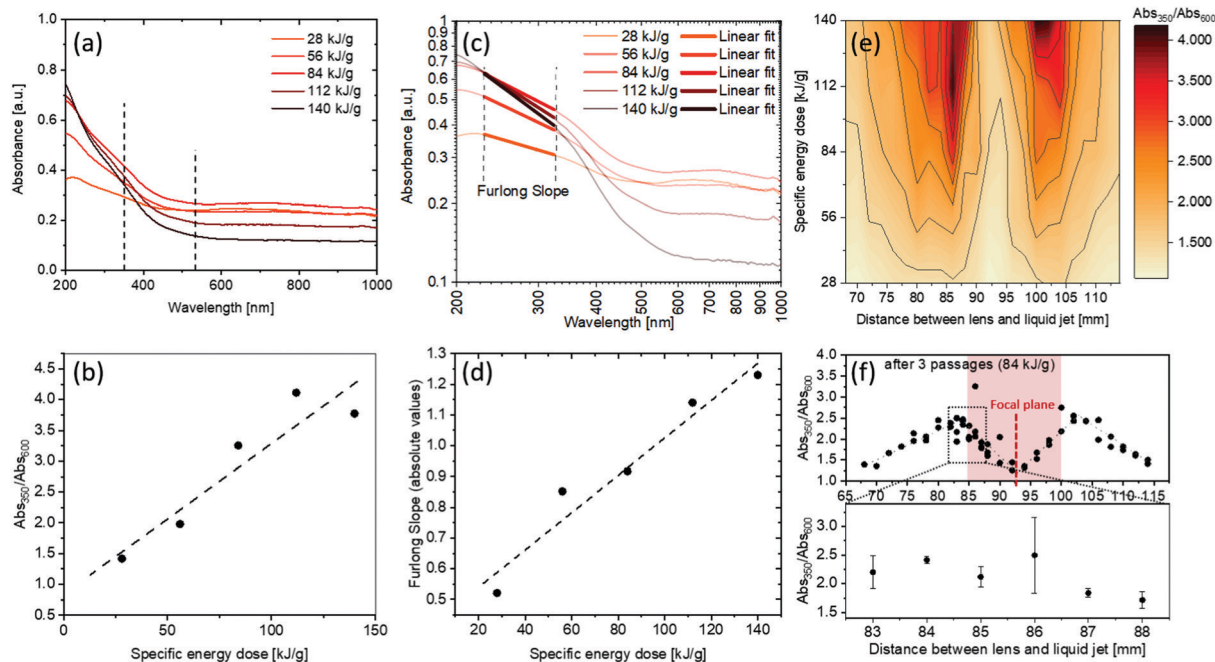


Fig. 2 Exemplary optimization of the laser fluence and influence of the specific energy input during irradiation with 355 nm. (a) UV-Vis spectra of FeO_x colloids. Dashed lines indicate the calculation of the $\text{Abs}_{350}/\text{Abs}_{600}$ ratio, where (b) correlates with the specific energy dose. (c and d) Respective double logarithmic plot of the UV-Vis spectra with the calculation of the Furlong slope. (e) 2D contour plot with the $\text{Abs}_{350}/\text{Abs}_{600}$ ratio as a function of the specific energy dose and the distance between the lens and liquid jet. (f) $\text{Abs}_{350}/\text{Abs}_{600}$ ratio after three passages as a function of distance between the lens and the liquid jet and magnification in the transition regime optical breakdown (red shaded area).

finally set to a value at the transition to optical breakdown to maximize the fragmentation efficiency.

To compare the effect of irradiation at 355 nm and 532 nm in terms of fragmentation efficiency, the change in $\text{Abs}_{350}/\text{Abs}_{600}$ with increasing specific energy dose is depicted in Fig. 3a. Although the used laser system offers almost three times higher laser power at 532 nm compared to 355 nm, UV laser fragmentation with 355 nm can overcompensate this disadvantage with five times higher efficiency (Fig. 3a), as indicated by the slope of $\text{Abs}_{350}/\text{Abs}_{600}$ (specific energy dose) (Fig. 3b). Fig. 3c and d reflect this trend in the hydrodynamic particle diameter. Both wavelengths lead to significant fragmentation and a decrease in hydrodynamic particle size. Size distributions show a sharp peak for 355 nm irradiation and a broader peak for 532 nm (Fig. 3c) with a secondary maximum at the educt particle size of 200–300 nm. In the case of LFL with a wavelength of 355 nm, there are almost no particles larger than 40 nm left. Corresponding d_{10} , d_{50} , d_{90} values are displayed in Fig. 3d (diameter d_x at which $x\%$ of the total nanoparticle mass in the sample is 'contained'). The d_{90} value significantly decreases compared to 532 nm, due to the sharp distributive peak.

From an economic point of view, it is important to consider the costs of creating laser photons at wavelengths of 355 nm and 532 nm. Second harmonic generation (SHG, 532 nm) is at least twice as efficient as third harmonic generation (THG, 355 nm). Presently, both laser power outputs are generated from a common Nd:YAG laser source (1064 nm) by harmonic generation, and 355 nm, instead of 532 nm output, limits the maximum available powder to less than half. This can only be

compensated with better absorption of the irradiated material at 355 nm, which is the case for iron oxide.⁶⁴ Therefore, an assessment of the absorption properties is important for each material that should be fragmented, e.g. one could expect a different outcome for the fragmentation of nanoparticles with an absorption maximum around 530 nm.

Although there is a clear correlation between the PPI and the hydrodynamic size distribution, a critical assessment of the data is important. A measurement of the hydrodynamic size always comes with an intrinsic overestimation of the particle size compared to primary particle diameters. Moreover, ADC measurements depend on centrifugal forces and, therefore, on the density difference between nanoparticle and liquid phase. The lower the density, the longer the time duration for measurement so that back diffusion occurs, blurring the analytical size discrimination. Most of the oxides have a relatively low density and the diameter limit of detection is therefore in the range of 10–20 nm, compared to high-density materials like gold, which can be precisely analyzed to 5 nm or lower. To support our results, a sample after LFL with 355 nm (highest efficiency) was imaged *via* TEM (Fig. 4b) and compared with the educt particles (Fig. 4a).

Ps-LFL results in significant fragmentation of the educt particles from $x_c = 19.5$ nm to $x_c = 7.7$ nm accompanied by spherification, which are shown by the TEM image analysis (Fig. 4a and b). The polydispersity index (PDI) calculated from σ^2/x_c^2 decreases from 0.92 to 0.47 by LFL processing. Note that a $\text{PDI} < 0.3$ represents a monodisperse size distribution, whereas $\text{PDI} > 0.3$ represents a polydisperse size distribution. Although the size distribution after LFL cannot be called

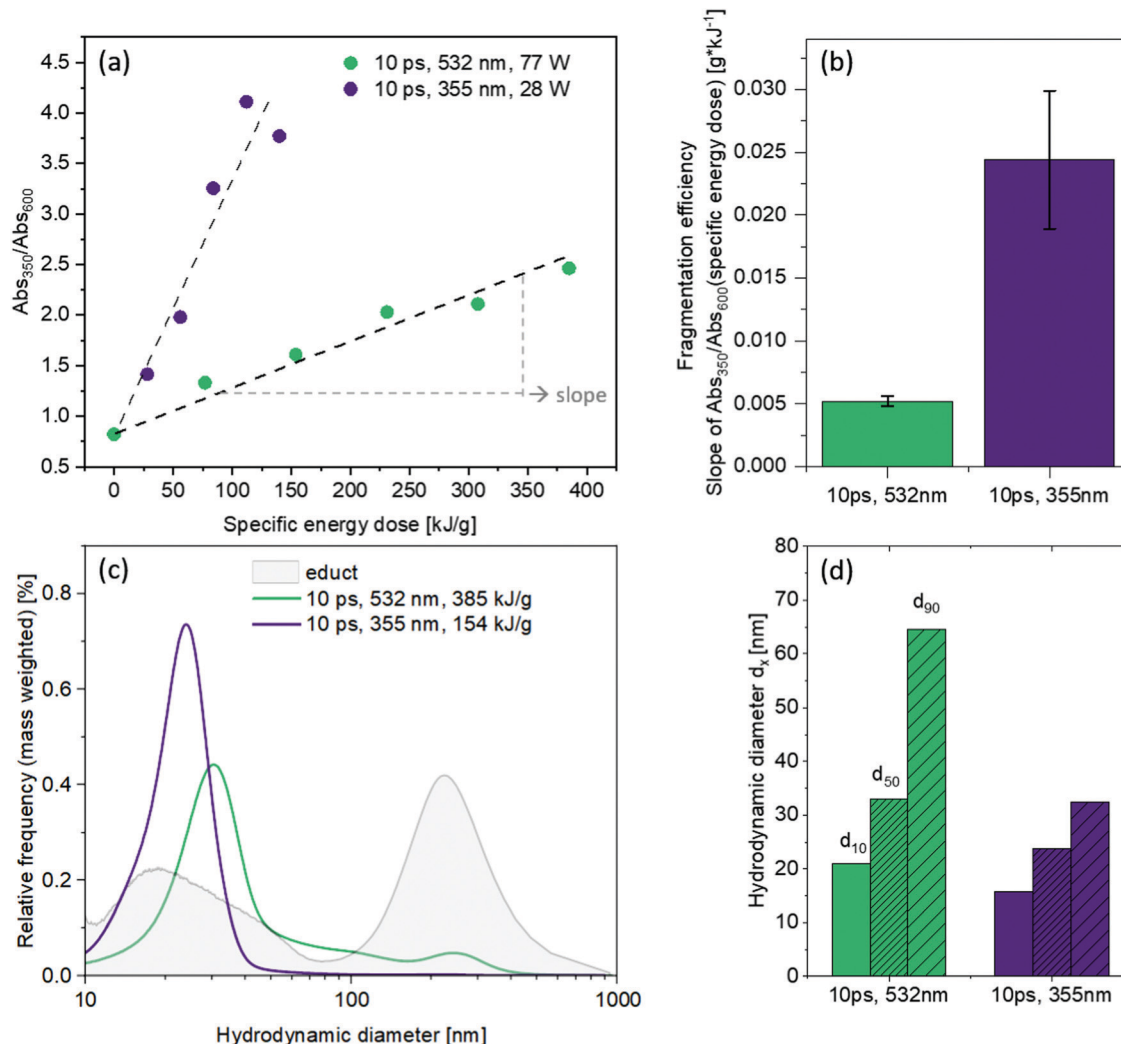


Fig. 3 (a) Abs_{350}/Abs_{600} as a function of the specific energy input by repeating cycles of irradiation at optimized parameters for two laser systems and (b) fragmentation efficiency extracted by the slopes of the fits in (a). (c) Hydrodynamic size distribution (mass-weighted) of iron oxide nanoparticles after LFL for all three laser systems at optimized fluence values compared to the educt size distribution (grey). (d) Corresponding key figures characterizing cumulative size distributions.

monodisperse, TEM measurements confirm the ADC results and show a significant particle size reduction, turning highly polydisperse, bimodal educt iron oxide particles into a significantly narrower, monomodal size distribution after LFL.

3.2 Nano-functionalization of PA12

Following the process route depicted in Fig. 1, laser-generated colloids, processed with parameters at a maximum fragmentation efficiency (355 nm), were adsorbed on the polymer powders to create nano-functionalized magnetic PA12. After colloidal additivition and filtration, permeates did not show absorbance in the UV-Vis, proving complete adsorption of all nanoparticles. Fig. 5 shows the powders obtained after colloidal additivition and subsequent drying. Their appearance darkens with increasing nanoparticle loading (Fig. 5a), which is shown in the absorption spectra. A broad peak between 400 and 800 nm occurs, caused by the FeO_x (Fig. 5b). The integrated absorption scales linearly with nanoparticle loading (Fig. 5c).

SEM images of the powder show a monodisperse distribution of the particles with a $Feret_{max}$ diameter of $x_c = 37$ nm and a PDI of 0.138 (Fig. 6). However, size measurements based on SEM imaging come with the problem of limited resolution, especially for materials with low contrast on polymer surfaces. The smallest particles measure approx. 15 nm, which is larger than the measured particle size of the laser-generated nanoparticles loaded on the PA12. It has been reported that the colloidal adsorption process is not size-selective,³¹ so that particle sizes reported in Fig. 4 should be expected to be unchanged after adsorption on the polymer powder surface. Therefore, it is possible that the actual dispersion of nanoparticles (which are invisible in the SEM picture) on the polymer surface is even better than the one presented in Fig. 6.

3.3 Thermogravimetric analysis and calorimetric properties

The thermal decomposition behavior of pure PA12 powder and PA12 powder being surface-functionalized by iron oxide nanoparticles under air as studied by TGA is depicted in Fig. 7.

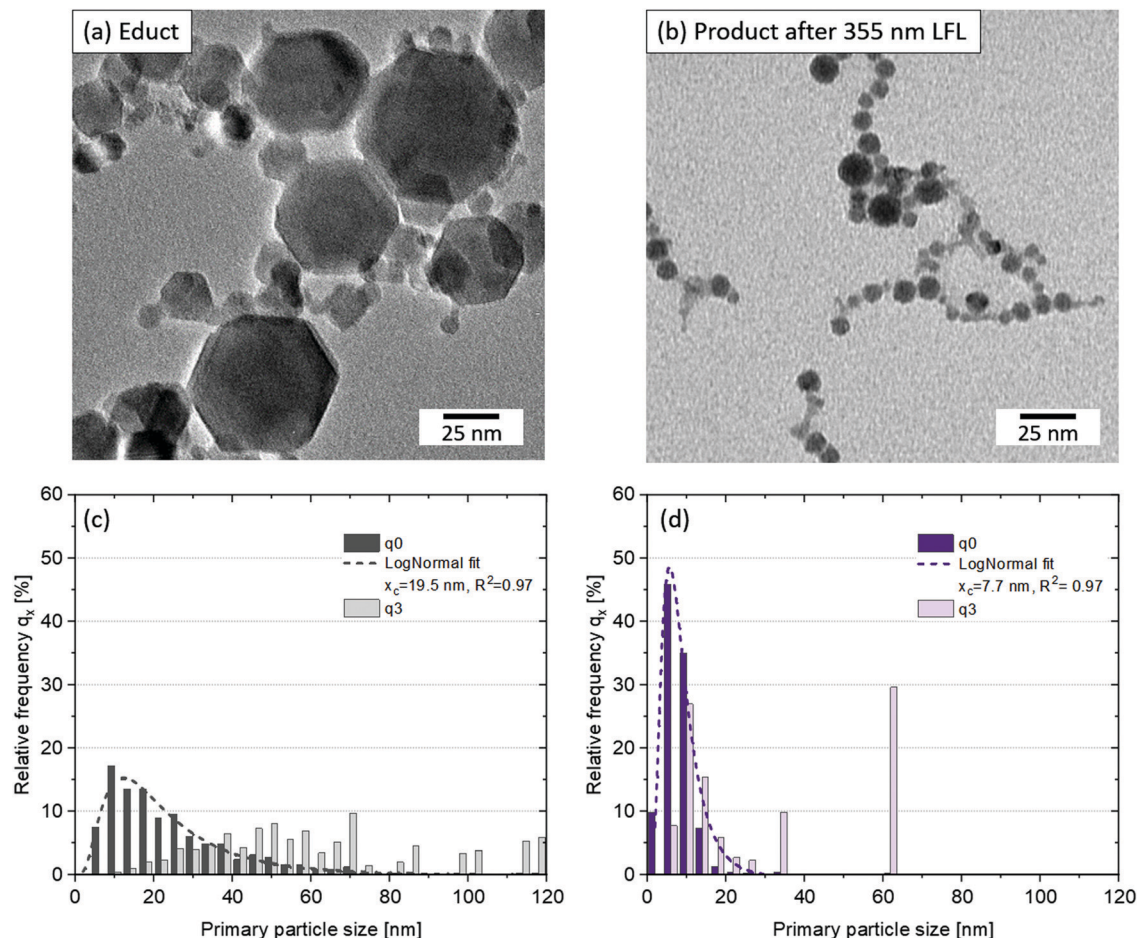


Fig. 4 TEM images of representative (a) educt FeO_x nanoparticles and (b) FeO_x after LFL with a laser wavelength of 355 nm. The corresponding number-weighted (q_0) and mass-weighted (q_3) particle size distributions are shown in (c) and (d).

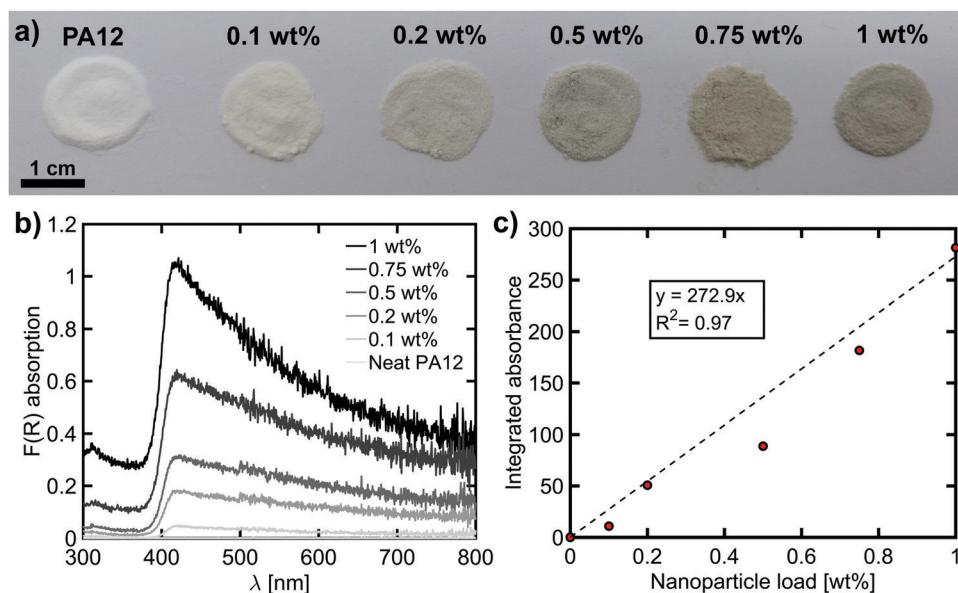


Fig. 5 (a) Dried powders obtained by varying the weight percentage of supported FeO_x nanoparticles on PA12. (b) Absorption spectra obtained from reflection measurements of the powders and (c) integrated absorbance as a function of the nanoparticle load. The integration was performed for the complete wavelength range shown in (b). The dashed line is a linear fit (forced through the origin).

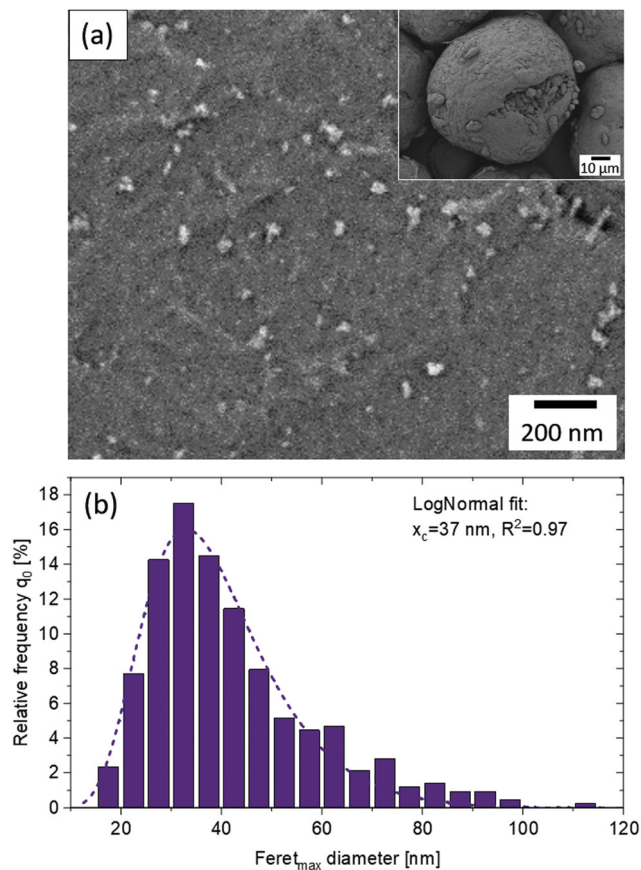


Fig. 6 (a) SEM image of a PA12 polymer microparticle surface (inset shows the whole particle) decorated with laser-generated FeO_x nanoparticles and (b) relative frequency of FeO_x particles on the polymer surface as a function of $\text{Feret}_{\text{max}}$ diameter.

The decomposition of the PA12 (see black solid line in Fig. 7), *i.e.* the temperature where mass loss sets in, starts around 300 °C. At 338 °C, a mass loss of approximately 1 wt%

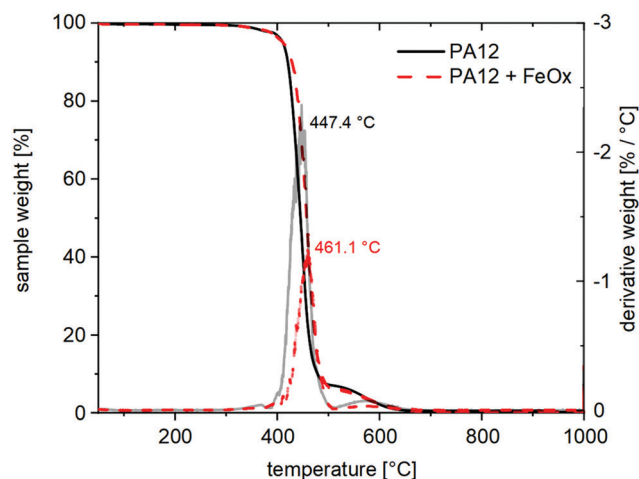


Fig. 7 Thermogravimetric analysis of FeO_x functionalized and non-functionalized PA12 powder (atmosphere: synthetic air (60 ml min^{-1}), heating rate: 10 K min^{-1}).

with respect to the initial sample mass is observed. From there, with further increasing temperature decomposition gradually increases until pronounced oxidation of the sample sets in at 402 °C. This pronounced decomposition of the sample being characterized by a peak mass loss of more than 2% K^{-1} found at 447.8 °C continues up to 488 °C, where about 8.2 wt% of the initial sample weight are left. From there, a gradual further mass loss occurs until 0.5 wt% of the initial sample mass are left as ash residue. The observed thermal degradation for the non-functionalized material is in good agreement with that reported for similar material, *e.g.* by Strobbe *et al.* for PA2200, a commercial PA12 feedstock material for PBF-LB.⁸³

The decomposition behavior of the surface-functionalized powder 'PA12 + FeO_x ' (*cf.* dashed red line in Fig. 7) is very similar to that of the non-functionalized powder. Decomposition sets in at around 300 °C, the mass loss of 1% is found at 338.5 °C, although, from there the oxidation is slightly retarded as compared to the pure PA12, *cf.* a maximum derivative weight loss of around 1.3% K^{-1} is observed at the peak mass loss at 461.1 °C. An ash residue of 0.4 wt% was found for this sample, which is a decrease of 0.14 wt% compared to the pure PA12 powder. In order to simulate the treatment of the PA12 during colloidal addition, the pure PA12 sample was also washed with water and dried before measurement. Nevertheless, small process variation could have caused a difference in partial removal of inorganic flow aids during the process.

For the PBF-LB process, however, not only the mass loading but also the dispersion of nanoparticles is important. During PBF-LB, the process temperatures are usually held below the melting temperature of PA12 of around 180 °C,²⁶ while the laser energy elevates the material temperature beyond the decomposition temperature of around 300 °C.⁶⁵ However, the exposure only lasts for approximately 50 ms which does not necessarily lead to a degradation of the polymer chains.⁶⁶ In this regard, nanoparticles which show a high absorbance at the laser wavelength of the PBF-LB machine can increase the uptake of the laser energy and thus affect the density of otherwise porous parts.^{67,68} During the quasi-isothermal conditions of PBF-LB,⁶⁹ nanoparticles can affect on the one hand the spreadability during the recoating process²⁶ and on the other hand the crystallization kinetics.^{70–72} When cooling down the melt after the process, the morphology and quantity of crystalline structures are typically influenced by a wide range of cooling rates (0.2 to 20 K min^{-1}).^{69,73} The addition of nanoparticles can hereby also change the crystallization behavior of the base polymer through heterogeneous nucleation⁷⁴ by increasing the crystallization temperatures and thus reduce the processing window of PBF-LB.^{75–77} Ideally, PA12 powder for PBF-LB shows a wide process window of approx. 30 K to avoid a premature crystallization of the melt^{78,79} and thus curling or warpage of the parts.^{66,80} However, if the processability is maintained, the addition and ultrafine dispersion of nanoparticles has the potential to change the shape and quantity of crystalline structures in such a way that mechanical properties of processed parts can be manipulated in a desired direction.^{71,81}

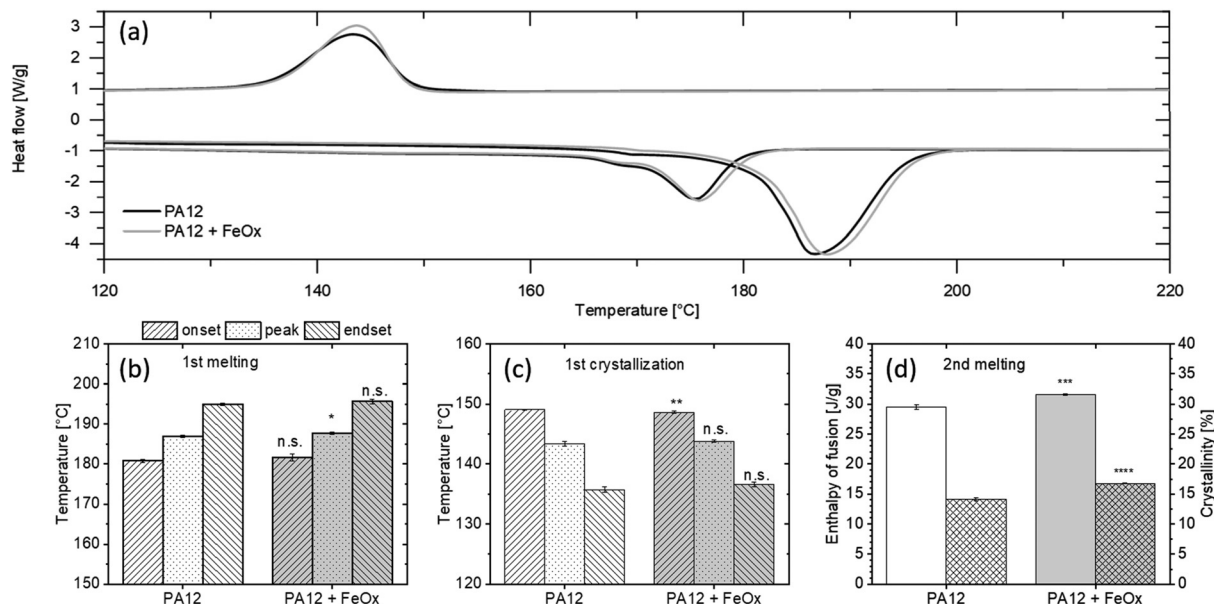


Fig. 8 DSC analysis of PA12 and nanoparticle functionalized PA12: (a) heating curve for melting and resolidification (20 K min⁻¹ heating and cooling rate), (b and c) onset, peak and endset temperature for the 1st melting and resolidification. (d) Enthalpy of fusion and crystallinity after resolidification calculated from the 2nd heating curve. For both powders, curves were averaged over 3 runs.

The addition of highly dispersed FeO_x nanoparticles leads to significant changes in the first and second heating curve (Fig. 8a), where the melting peak temperatures and melting enthalpies are shifted to higher values. Since the nanoparticles are merely on the surface of the PA12 particles, the melting peak-shift of the first heating (Fig. 8b) could originate from an increase in thermal conductivity through the well dispersed FeO_x nanoparticles.⁸² The differences in the second heating can be related to the nucleation effect of nanoparticles on PA12, which increase the crystallization rate and the lamella thickness of the crystalline structures.⁷⁴ This effect becomes apparent by a significant increase of the crystallization enthalpy (***, $P \leq 0.001$) from $45.7 \pm 0.4 \text{ J g}^{-1}$ to $48.1 \pm 0.2 \text{ J g}^{-1}$, which in return results in a significant (**, $P \leq 0.01$) decrease of the onset of the crystallization from $149.1 \pm 0.1 \text{ }^\circ\text{C}$ to $148.6 \pm 0.2 \text{ }^\circ\text{C}$ (Fig. 8c). As expected, the addition of highly dispersed iron oxide nanoparticles significantly increase (****, $P \leq 0.0001$) the crystallinity from $14.1 \pm 0.2\%$ to $16.8 \pm 0.1\%$ (Fig. 8d). On the other hand, the reduction of inorganic material, which was observed in the TGA analysis, does not seem to have a negative influence here.

3.4 Magnetic properties along the process chain

Magnetic properties are highly dependent on the nanoparticle size, which was expected to be influenced along the process chain. The magnetic properties of FeO_x nanoparticles before and after LFL (Fig. 9a) and of nano-functionalized PA12 powder, as well as the 3D part after desktop PBF-LB (Fig. 9b) were investigated. Placed in a magnetic field, the colloidal particles after LFL move rapidly to the magnet as depicted in Fig. 9a. $M(H)$ curves (Fig. 9c) of the educt powder material (black curve) display approx. 67 emu g^{-1} at 1 T and 300 K, comparable to reported values of maghemite powders, while the laser

fragmented particles (red) exhibit a lower magnetization of approx. 49 emu g^{-1} , which is likely caused by stronger frustration of spins close to the particle surface due to the lower average particle diameter as compared to the educt. In general, FeO_x nanoparticles below approx. 15 nm show beginning superparamagnetic behavior at room temperature and a reduced saturation magnetization due to an increased influence of the particle surface.⁸⁴ Their magnetic properties are dependent on their shape and phase composition.^{6,85} For example, Demortière *et al.* reported a saturation magnetization of 43 emu g^{-1} for 5 nm FeO_x particles. Following background correction for the diamagnetic polymer component, the $M(H)$ curves for the functionalized PA12 (green), as well as the 3D part after desktop PBF-LB (blue), are similar in shape as compared to the FeO_x nanoparticles and prove the successful magnetic functionalization of PA12 powder. Based on the magnetization at 1 T given in units of $10^{-3} \text{ emu g}^{-1}$, a magnetic particle concentration of ca. 0.08–0.09 wt% can be estimated for these two samples, matching well with the nominal concentration of 0.1 wt%. From the known FeO_x phases, hematite ($\alpha\text{-Fe}_2\text{O}_3$), maghemite ($\gamma\text{-Fe}_2\text{O}_3$), and magnetite (Fe_3O_4) typically show a temperature-induced phase transition, which can already occur around 250–300 °C.⁸⁶ These temperatures are likely to occur during PBF-LB, since the CO₂ laser heats the powder far above the melting temperature of the polymer for a very short time span of milliseconds before heat propagation.^{87,88} Wegner *et al.*, for example, measured a maximum temperature of 340 °C.⁸⁷ However, the unchanged magnetic properties, as well as the Mössbauer study of the materials throughout the process chain discussed below, indicate that colloidal addition, as well as PBF-LB processing, do not significantly alter the nanoparticle size or phase composition.

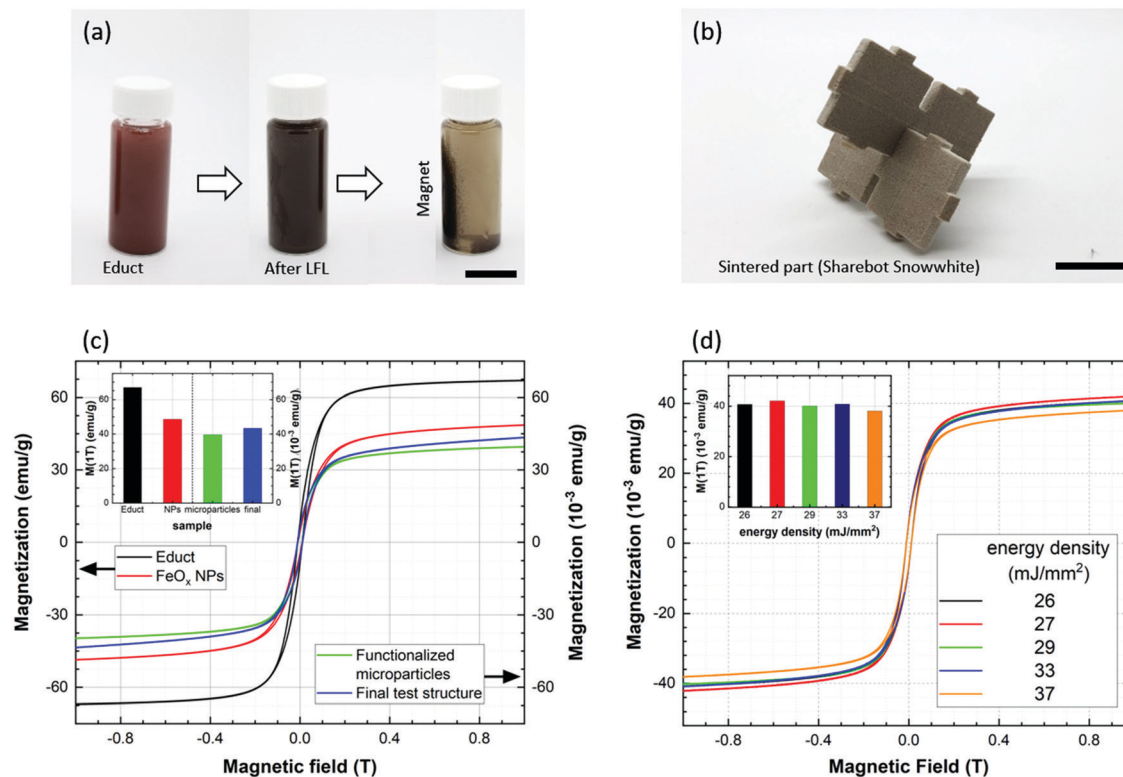


Fig. 9 (a) Educt and laser-irradiated FeO_x-colloid (after LFL with a 355 nm laser) nanoparticles. (b) Assembled 3D part after printing by desktop PBF-LB of the magnetically functionalized PA12 powder with a FeO_x content of 0.1 wt% on a Sharebot Snowwhite Printer. The black bar measures 2 cm. (c) $M(H)$ curves recorded at 300 K for the untreated educt material (black) and laser fragmented FeO_x nanoparticles (red) on the left axis, functionalized PA12 powder (green), and after printing by desktop PBF-LB on a Sharebot Snowwhite (blue) on the right axis. The latter contains only ca. 0.1 wt% of magnetic nanomaterial, where they are given in units of 10⁻³ emu g⁻¹ and are corrected for the minor diamagnetic background of the PA12 polymer powder; magnetization values at 1 T are displayed in the inset. (d) Magnetization $M(H)$ curves recorded at 300 K for parts made from functionalized PA12 powder (0.1 wt%) at different energy densities on a EOS P385 PBF-LB printer. The inset displays magnetization values recorded at 1 T.

This was further investigated by variation of the energy density during PBF-LB from 2.59 to 3.71 J cm⁻² on an EOS P385 (Fig. 9d). In contrast to final part production on a Sharebot Snowwhite, the EOS P385 enables an exact tuning of the energy density, which was necessary for this experiment. However, despite strong layer curling, no influence of the energy density on the magnetic behavior after PBF-LB could be observed, confirming that no structural change occurs in the FeO_x during addition and PBF-LB.

3.5 Nanoparticle structure along the process chain

A deeper investigation of the nanoparticle properties was performed by Mössbauer spectroscopy at 80 K and room temperature to obtain a deeper insight into nanoparticle structure and composition. Sample materials from each step of the processing chain (Fig. 10) were investigated. These include the educt powder (a and b), the FeO_x nanoparticles after LFL (c and d), the functionalized polymer powder (e), and the 3D printed test structure after powder processing (f). The educt spectrum displays a typical spinel/maghemite (γ -Fe₂O₃) structure with two sextet subspectra, representing Fe³⁺ on the octahedral B-sites (blue) and tetrahedral A-sites (green), respectively. No considerable changes are visible between spectra recorded at 80 K and room temperature, except for the appearance of a miniscule doublet, presumably caused by superparamagnetic

relaxation of the smallest educt particles. After LFL, the decrease in average particle diameter is obvious from the change in spectral structure: not only is the superparamagnetic fraction in the room temperature spectrum, which represents smaller particles, increased, but the magnetically blocked sextet fraction at 80 K, as well as at 293 K, also exhibit distinct inner shoulders. These shoulders are caused by beginning thermally excited fluctuation of the particle superspin, not being represented as a superparamagnetic doublet due to the relation of relaxation frequencies in comparison to the Mössbauer time window.^{89,90} The indicator of superparamagnetic behavior in Mössbauer spectroscopy is the crossing of the Larmor precession time (in the range of 5 ns) by the relaxation time, accompanied by the sextet collapse. Still, with the particles showing only approx. 10% doublet area, they can be regarded as primarily magnetically blocked at room temperature, even on longer timescales (> 1 s). It seems reasonable to assume that the LFL-process leads to a (partial) reduction of the maghemite educt material, as an additional minor sextet of smaller nuclear Zeeman splitting and higher isomer shift is visible in Fig. 10 (c, cyan), which we assign to B-site Fe²⁺ in magnetite (Fe₃O₄),^{90,91} also matching the observable change in color from orange (Fe₂O₃) to brown/black (Fe₃O₄). It is unclear whether the particles are only partially reduced

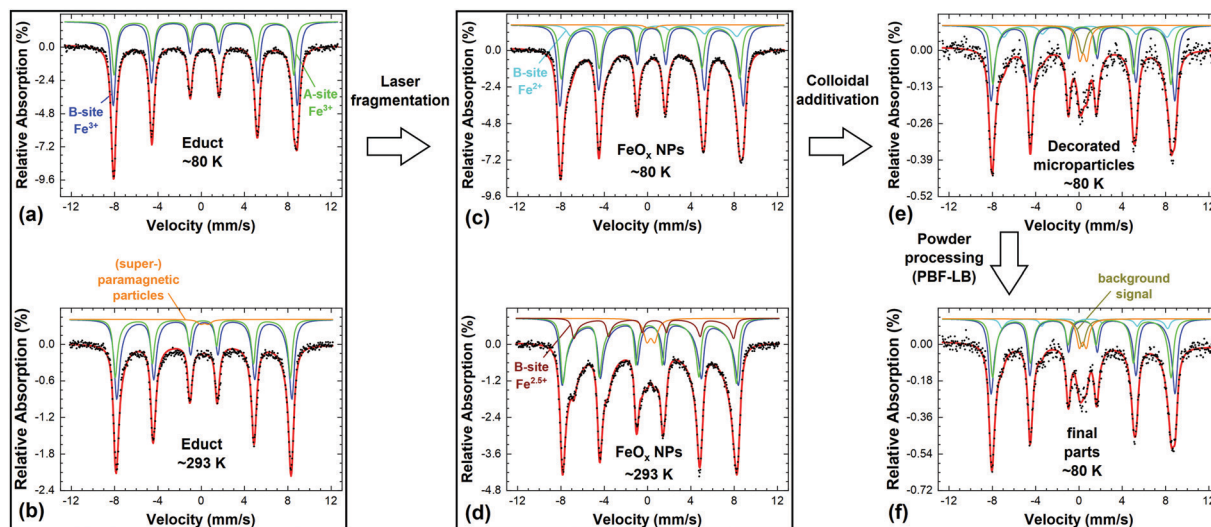


Fig. 10 Mössbauer spectra taken on sample material along the sequence of processing steps at ca. 80 K and 293 K: educt FeO_x powder (a and b), laser fragmented FeO_x nanoparticles (c and d), functionalized polymer powder after colloidal additivition (e), and 3D-printed test structures (f) prepared *via* PBF-LB.

to magnetite in the process or if they are entirely composed of magnetite at some point, followed by the formation of a maghemite oxidation/passivation layer, as is well known from magnetite exposed to oxygen. While at 80 K the Fe^{2+} component is only visible as a minor shoulder, its effect is more pronounced at room temperature, due to the crossing of the Verwey temperature, where fast electron hopping leads to the observation of a mixed-valence state ($\text{Fe}^{2.5+}$, brown), with higher spectral area and an intermediate center shift.⁹⁰ Comparing the relative spectral areas of the Fe^{2+} and $\text{Fe}^{2.5+}$ subspectra to the rest of the spectrum, we can estimate the magnetite fraction in the FeO_x nanoparticles after LFL to ca. 20–25%.

Measuring the spectra of the nano-functionalized polymer powder and the 3D-printed parts, the relatively low concentration of Fe-bearing material of ca. 0.1 wt% was compensated by using higher amounts of sample material (1.5 g instead of ca. 20 mg). Still, the signal intensities in Fig. 10(e and f) are much smaller compared to those of pure iron oxide material, leading to a lower signal-to-noise ratio. However, both spectra display a magnetic structure identical to that of the FeO_x nanoparticles shown in Fig. 10(c and d) within experimental precision, except for the presence of a miniscule paramagnetic contribution with a relative absorption of less than 0.1%, which can be assigned to a background signal of the experimental setup. Therefore, it can be concluded from Mössbauer spectroscopy that FeO_x nanoparticles prepared *via* laser fragmentation consist of a mixture of maghemite and magnetite, are mainly magnetically blocked, and do not show considerable changes in magnetic structure or composition along the processing chain, from the nanoparticles synthesis to the 3D printed parts.

4. Conclusion

Picosecond LFL with an Nd:YAG laser emitting with its third harmonic wavelength is a highly effective method for fragmentation and spherization of FeO_x nanoparticles and

generation of magnetic nanoparticles for use in AM. LFL of a polydisperse FeO_x powder results in a colloidal with a monomodal size distribution of superparamagnetic nanoparticles with diameters below 10 nm. A comparison between LFL with the second harmonic wavelength from the same laser source underlines the importance of choosing a suitable LFL wavelength matching the absorption properties of the raw material. Furthermore, it was shown that during LFL of $\gamma\text{-Fe}_2\text{O}_3$, approx. 25% of the material was reduced to Fe_3O_4 as confirmed by Mössbauer spectroscopy. To generate a powder feedstock material for laser 3D printing, highly dispersed FeO_x nanoparticles were absorbed on a PA12 powder through colloidal additivition. FeO_x nanoparticles on the PA12 microparticle surface show only minor aggregation and homogeneous distribution. Calorimetric properties of PA12 were changed by the FeO_x nanoparticles to higher degrees of crystallinity while maintaining good processability for PBF-LB. The functionalized and non-functionalized PA12 powders showed a comparable thermal degradation behavior at atmosphere, as studied by TGA.

Mössbauer and magnetometry measurements further reveal an unaltered size and structure of magnetic nanoparticles on the PA12 surface and in the final part after PBF-LB, as indicated by the identical behavior in terms of superparamagnetism and Mössbauer spectral structure. Thus, the magnetic properties were successfully transferred to the final part, giving rise to a variety of potential applications for magnetic nano-functionalized feedstock materials, such as 4D AM of magneto-responsive parts.

Conflicts of interest

There are no conflicts to declare.

Acknowledgements

We thank Jurij Jacobi for TEM imaging of nanoparticles and IMCES (Imaging Center Essen, University Hospital Essen) for

SEM analysis of polymer powders. Tim Hupfeld also thanks Evonik industries for financial support. Alexander Sommereyns gratefully acknowledges funding of the Erlangen Graduate School in Advanced Optical Technologies (SAOT) by the German Research Foundation (DFG) in the framework of the German excellence initiative. The authors gratefully acknowledge the funding by the German Research Foundation (DFG) within the priority program (SPP) 2122 “Materials for Additive Manufacturing” (MATframe, BA 3580/27-1+ SCHM 2115/78-1), as well as the Collaborative Research Centre/Transregio (CRC/TRR) 270 (Project-ID 405553726, projects A11, B05 and B08) and 247 (Project-ID 388390466, project B02). Bilal Gökce further thanks the DFG for funding his project GO 2566/10-1.

References

- C. Sun, J. S. H. Lee and M. Zhang, Magnetic nanoparticles in MR imaging and drug delivery, *Adv. Drug Delivery Rev.*, 2008, **60**, 1252–1265, DOI: 10.1016/j.addr.2008.03.018.
- L. P. Singh, N. V. Jadhav, S. Sharma, B. N. Pandey, S. K. Srivastava and R. S. Ningthoujam, Hybrid nanomaterials YVO₄:Eu/Fe₃O₄ for optical imaging and hyperthermia in cancer cells, *J. Mater. Chem. C*, 2015, **3**, 1965–1975, DOI: 10.1039/c4tc02636e.
- C. Bárcena, A. K. Sra and J. Gao, Applications of magnetic nanoparticles in biomedicine, *Nanoscale Magn. Mater. Appl.*, 2009, 591–626, DOI: 10.1007/978-0-387-85600-1_20.
- A. K. Gupta and M. Gupta, Synthesis and surface engineering of iron oxide nanoparticles for biomedical applications, *Biomaterials*, 2005, **26**, 3995–4021, DOI: 10.1016/j.biomaterials.2004.10.012.
- E. Pizzolato, S. Scaramuzza, F. Carraro, A. Sartori, S. Agnoli, V. Amendola, M. Bonchio and A. Sartorel, Water oxidation electrocatalysis with iron oxide nanoparticles prepared via laser ablation, *J. Energy Chem.*, 2016, **25**, 246–250, DOI: 10.1016/j.jechem.2015.12.004.
- W. Wu, C. Jiang and V. A. L. Roy, Recent progress in magnetic iron oxide-semiconductor composite nanomaterials as promising photocatalysts, *Nanoscale*, 2015, **7**, 38–58, DOI: 10.1039/c4nr04244a.
- Z. Yang, H. Peng, W. Wang and T. Liu, Crystallization behavior of poly(ϵ -caprolactone)/layered double hydroxide nanocomposites, *J. Appl. Polym. Sci.*, 2010, **116**, 2658–2667, DOI: 10.1002/app.
- M. Schmid, A. Amado and K. Wegener, Materials perspective of polymers for additive manufacturing with selective laser sintering, *J. Mater. Res.*, 2014, **29**, 1824–1832, DOI: 10.1557/jmr.2014.138.
- M. Schmid and K. Wegener, Additive Manufacturing: Polymers applicable for laser sintering (LS), *Procedia Eng.*, 2016, **149**, 457–464, DOI: 10.1016/j.proeng.2016.06.692.
- B. Zhou, W. Xu, A. A. Syed, Y. Chau, L. Chen, B. Chew, O. Yassine, X. Wu, Y. Gao, J. Zhang, X. Xiao, J. Kosel, X. X. Zhang, Z. Yao and W. Wen, Design and fabrication of magnetically functionalized flexible micropillar arrays for rapid and controllable microfluidic mixing, *Lab Chip*, 2015, **15**, 2125–2132, DOI: 10.1039/c5lc00173k.
- S. B. Kesner and R. D. Howe, Design principles for rapid prototyping forces sensors using 3-D printing, *IEEE/ASME Trans. Mechatron.*, 2011, **16**, 866–870, DOI: 10.1109/TMECH.2011.2160353.
- Y. Kim, H. Yuk, R. Zhao, S. A. Chester and X. Zhao, Printing ferromagnetic domains for untethered fast-transforming soft materials, *Nature*, 2018, 274–279.
- H. Wei, Q. Zhang, Y. Yao, L. Liu, Y. Liu and J. Leng, Direct-write fabrication of 4D active shape-changing structures based on a shape memory polymer and its nanocomposite, *ACS Appl. Mater. Interfaces*, 2017, **9**, 876–883, DOI: 10.1021/acsami.6b12824.
- S. Fusco, M. S. Sakar, S. Kennedy, C. Peters, R. Bottani, F. Starsich, A. Mao, G. A. Sotiriou, S. Pané, S. E. Pratsinis, D. Mooney and B. J. Nelson, An integrated microrobotic platform for on-demand, targeted therapeutic interventions, *Adv. Mater.*, 2014, **26**, 952–957, DOI: 10.1002/adma.201304098.
- M. Wehner, R. L. Truby, D. J. Fitzgerald, B. Mosadegh, G. M. Whitesides, J. A. Lewis and R. J. Wood, An integrated design and fabrication strategy for entirely soft, autonomous robots, *Nature*, 2016, **536**, 451–455, DOI: 10.1038/nature19100.
- F. H. Zhang, Z. C. Zhang, C. J. Luo, I. T. Lin, Y. Liu, J. Leng and S. K. Smoukov, Remote, fast actuation of programmable multiple shape memory composites by magnetic fields, *J. Mater. Chem. C*, 2015, **3**, 11290–11293, DOI: 10.1039/c5tc02464a.
- R. Domingo-Roca, J. C. Jackson and J. F. C. Windmill, 3D-printing polymer-based permanent magnets, *Mater. Des.*, 2018, **153**, 120–128, DOI: 10.1016/j.matdes.2018.05.005.
- C. Huber, C. Abert, F. Bruckner, M. Groenefeld, O. Muthsam, S. Schuschnigg, K. Sirak, R. Thanhoffer, I. Teliban, C. Vogler, R. Windl and D. Suess, 3D print of polymer bonded rare-earth magnets, and 3D magnetic field scanning with an end-user 3D printer, *Appl. Phys. Lett.*, 2016, **109**, 162401, DOI: 10.1063/1.4964856.
- C. Huber, C. Abert, F. Bruckner, M. Groenefeld, S. Schuschnigg, I. Teliban, C. Vogler, G. Wautischer, R. Windl and D. Suess, 3D Printing of Polymer-Bonded Rare-Earth Magnets with a Variable Magnetic Compound Fraction for a Predefined Stray Field, *Sci. Rep.*, 2017, **7**, 1–8, DOI: 10.1038/s41598-017-09864-0.
- C. Abert, C. Huber, F. Bruckner, C. Vogler, G. Wautischer and D. Suess, A fast finite-difference algorithm for topology optimization of permanent magnets, *J. Appl. Phys.*, 2017, **122**, 113904, DOI: 10.1063/1.4998532.
- K. Gandha, L. Li, I. C. Nlebedim, B. K. Post, V. Kunc, B. C. Sales, J. Bell and M. P. Paranthaman, Additive manufacturing of anisotropic hybrid NdFeB-SmFeN nylon composite bonded magnets, *J. Magn. Magn. Mater.*, 2018, **467**, 8–13, DOI: 10.1016/j.jmmm.2018.07.021.
- E. M. Palmero, D. Casaleiz, N. A. Jimenez, J. Rial, J. De Vicente, A. Nieto, R. Altimira and A. Bollero, Magnetic-polymer

- composites for bonding and 3d printing of permanent magnets, *IEEE Trans. Magn.*, 2019, **55**, 2101004, DOI: 10.1109/TMAG.2018.2863560.
- 23 E. M. Palmero, J. Rial, J. de Vicente, J. Camarero, B. Skårman, H. Vidarsson, P. O. Larsson and A. Bollero, Development of permanent magnet MnAlC/polymer composites and flexible filament for bonding and 3D-printing technologies, *Sci. Technol. Adv. Mater.*, 2018, **19**, 465–473, DOI: 10.1080/14686996.2018.1471321.
- 24 N. Löwa, J. M. Fabert, D. Gutkelch, H. Paysen, O. Kosch and F. Wiekhorst, 3D-printing of novel magnetic composites based on magnetic nanoparticles and photopolymers, *J. Magn. Magn. Mater.*, 2019, **469**, 456–460, DOI: 10.1016/j.jmmm.2018.08.073.
- 25 S. Vock, B. Klöden, A. Kirchner, T. Weißgärber and B. Kieback, Powders for powder bed fusion: a review, *Prog. Addit. Manuf.*, 2019, **4**, 383–397, DOI: 10.1007/s40964-019-00078-6.
- 26 C. A. Chatham, T. E. Long and C. B. Williams, A review of the process physics and material screening methods for polymer powder bed fusion additive manufacturing, *Prog. Polym. Sci.*, 2019, **93**, 68–95, DOI: 10.1016/j.progpolymsci.2019.03.003.
- 27 C. Blümel, M. Sachs, T. Laumer, B. Winzer, J. Schmidt, M. Schmidt, W. Peukert and K. E. Wirth, Increasing flowability and bulk density of PE-HD powders by a dry particle coating process and impact on LBM processes, *Rapid Prototyp. J.*, 2015, **21**, 697–704, DOI: 10.1108/RPJ-07-2013-0074.
- 28 J. Yang, A. Sliva, A. Banerjee, R. N. Dave and R. Pfeffer, Dry particle coating for improving the flowability of cohesive powders, *Powder Technol.*, 2005, **158**, 21–33, DOI: 10.1016/j.powtec.2005.04.032.
- 29 S. Yuan, F. Shen, C. K. Chua and K. Zhou, Polymeric composites for powder-based additive manufacturing: Materials and applications, *Prog. Polym. Sci.*, 2019, **91**, 141–168, DOI: 10.1016/j.progpolymsci.2018.11.001.
- 30 T. Hupfeld, T. Laumer, T. Stichel, T. Schuffenhauer, J. Heberle, M. Schmidt, S. Barcikowski and B. Gökce, A new approach to coat PA12 powders with laser-generated nanoparticles for selective laser sintering, *Procedia CIRP*, 2018, **74**, 244–248, DOI: 10.1016/j.procir.2018.08.103.
- 31 T. Hupfeld, A. Wegner, M. Blanke, C. Doñate-Buendía, V. Sharov, S. Nieskens, M. Piechotta, M. Giese, S. Barcikowski and B. Gökce, Plasmonic seasoning: Giving color to desktop laser 3D-printed polymers by highly dispersed nanoparticles, *Adv. Opt. Mater.*, 2020, 2000473, DOI: 10.1002/adom.202000473.
- 32 T. Hupfeld, A. Blasczyk, T. Schuffenhauer, E. Zhuravlev, M. Krebs, S. Gann, O. Keßler, M. Schmidt, B. Gökce and S. Barcikowski, How colloidal surface additivation of polyamide 12 powders with well-dispersed silver nanoparticles influences the crystallization already at low 0.01 vol%, *Addit. Manuf.*, 2020, **36**, 101419.
- 33 D. Zhang, B. Gökce and S. Barcikowski, Laser Synthesis and Processing of Colloids: Fundamentals and Applications, *Chem. Rev.*, 2017, **117**, 3990–4103, DOI: 10.1021/acs.chemrev.6b00468.
- 34 M. R. Kalus, N. Bärsch, R. Streubel, E. Gökce, S. Barcikowski and B. Gökce, How persistent microbubbles shield nanoparticle productivity in laser synthesis of colloids - Quantification of their volume, dwell dynamics, and gas composition, *Phys. Chem. Chem. Phys.*, 2017, **19**, 7112–7123, DOI: 10.1039/c6cp07011f.
- 35 S. Scaramuzza, M. Zerbetto and V. Amendola, Synthesis of Gold Nanoparticles in Liquid Environment by Laser Ablation with Geometrically Confined Configurations: Insights To Improve Size Control and Productivity, *J. Phys. Chem. C*, 2016, **120**, 9453–9463, DOI: 10.1021/acs.jpcc.6b00161.
- 36 C. Rehbock, V. Merk, L. Gamrad, R. Streubel and S. Barcikowski, Size control of laser-fabricated surfactant-free gold nanoparticles with highly diluted electrolytes and their subsequent bioconjugation, *Phys. Chem. Chem. Phys.*, 2013, **15**, 3057–3067, DOI: 10.1039/c2cp42641b.
- 37 F. Mafune, J. Kohno, Y. Takeda, T. Kondow and H. Sawabe, Formation and size control of silver nanoparticles by laser ablation in aqueous solution, *J. Phys. Chem. B*, 2000, **104**, 9111–9117, DOI: 10.1021/jp001336y.
- 38 V. Amendola and M. Meneghetti, What controls the composition and the structure of nanomaterials generated by laser ablation in liquid solution?, *Phys. Chem. Chem. Phys.*, 2013, **15**, 3027–3046, DOI: 10.1039/C2CP42895D.
- 39 S. Scaramuzza, S. Agnoli and V. Amendola, Metastable alloy nanoparticles, metal-oxide nanocrescents and nanoshells generated by laser ablation in liquid solution: influence of the chemical environment on structure and composition, *Phys. Chem. Chem. Phys.*, 2015, **17**, 28076–28087, DOI: 10.1039/C5CP00279F.
- 40 V. Amendola, P. Riello and M. Meneghetti, Magnetic Nanoparticles of Iron Carbide, Iron Oxide, Iron@Iron Oxide, and Metal Iron Synthesized by Laser Ablation in Organic Solvents, *J. Phys. Chem. C*, 2011, **115**, 5140–5146, DOI: 10.1021/jp109371m.
- 41 W. Dong, S. Reichenberger, S. Chu, P. Weide, H. Ruland, S. Barcikowski, P. Wagener and M. Muhler, The effect of the Au loading on the liquid-phase aerobic oxidation of ethanol over Au/TiO₂ catalysts prepared by pulsed laser ablation, *J. Catal.*, 2015, **330**, 497–506, DOI: 10.1016/j.jcat.2015.07.033.
- 42 G. Marzun, J. Nakamura, X. Zhang, S. Barcikowski and P. Wagener, Size control and supporting of palladium nanoparticles made by laser ablation in saline solution as a facile route to heterogeneous catalysts, *Appl. Surf. Sci.*, 2015, **348**, 75–84, DOI: 10.1016/j.apsusc.2015.01.108.
- 43 C. Streich, L. Akkari, C. Decker, J. Bormann, C. Rehbock, A. Müller-Schiffmann, F. C. Niemeyer, L. Nagel-Steger, D. Willbold, B. Sacca, C. Korth, T. Schrader and S. Barcikowski, Characterizing the Effect of Multivalent Conjugates Composed of A β -Specific Ligands and Metal Nanoparticles on Neurotoxic Fibrillar Aggregation, *ACS Nano*, 2016, **10**, 7582–7597, DOI: 10.1021/acs.nano.6b02627.
- 44 V. Amendola, D. Amans, Y. Ishikawa, N. Koshizaki, S. Scirè, G. Compagnini, S. Reichenberger and S. Barcikowski, Room-temperature laser synthesis in liquid of oxide, metal-oxide core-shells and doped oxide nanoparticles,

- Chem. – Eur. J.*, 2020, **26**, 9206–9242, DOI: 10.1002/chem.202000686.
- 45 Y. Ishikawa, N. Koshizaki and A. Pyatenko, Submicrometer-Sized Spherical Iron Oxide Particles Fabricated by Pulsed Laser Melting in Liquid, *Electron. Commun. Jpn*, 2016, **99**, 37–42, DOI: 10.1002/ecj.11898.
- 46 T. Iwamoto and T. Ishigaki, Fabrication of iron oxide nanoparticles using laser ablation in liquids, *J. Phys.: Conf. Ser.*, 2013, **441**(1), DOI: 10.1088/1742-6596/441/1/012034.
- 47 S. F. S. Shirazi, S. Gharehkhani, M. Mehrali, H. Yarmand, H. S. C. Metselaar, N. Adib Kadri and N. A. A. Osman, A review on powder-based additive manufacturing for tissue engineering: Selective laser sintering and inkjet 3D printing, *Sci. Technol. Adv. Mater.*, 2015, **16**, 033502, DOI: 10.1088/1468-6996/16/3/033502.
- 48 V. Amendola, P. Riello, S. Polizzi, S. Fiameni, C. Innocenti, C. Sangregorio and M. Meneghetti, Magnetic iron oxide nanoparticles with tunable size and free surface obtained via a “green” approach based on laser irradiation in water, *J. Mater. Chem.*, 2011, **21**, 18665–18673, DOI: 10.1039/c1jm13680a.
- 49 R. A. Ismail, G. M. Sulaiman, S. A. Abdulrahman and T. R. Marzoug, Antibacterial activity of magnetic iron oxide nanoparticles synthesized by laser ablation in liquid, *Mater. Sci. Eng., C*, 2015, **53**, 286–297, DOI: 10.1016/j.msec.2015.04.047.
- 50 P. Maneeratanasarn, T. Van Khai, S. Y. Kim, B. G. Choi and K. B. Shim, Synthesis of phase-controlled iron oxide nanoparticles by pulsed laser ablation in different liquid media, *Phys. Status Solidi A*, 2013, **210**, 563–569, DOI: 10.1002/pssa.201228427.
- 51 V. Amendola, M. Meneghetti, G. Granozzi, S. Agnoli, S. Polizzi, P. Riello, A. Boscaini, C. Anselmi, G. Fracasso, M. Colombatti, C. Innocenti, D. Gatteschi and C. Sangregorio, Top-down synthesis of multifunctional iron oxide nanoparticles for macrophage labelling and manipulation, *J. Mater. Chem.*, 2011, **21**, 3803–3813, DOI: 10.1039/c0jm03863f.
- 52 A. De Bonis, T. Lovaglio, A. Galasso, A. Santagata and R. Teghil, Iron and iron oxide nanoparticles obtained by ultra-short laser ablation in liquid, *Appl. Surf. Sci.*, 2015, **353**, 433–438, DOI: 10.1016/j.apsusc.2015.06.145.
- 53 T. Hupfeld, F. Stein, S. Barcikowski, B. Gökce and U. Wiedwald, Manipulation of the Size and Phase Composition of Yttrium Iron Garnet Nanoparticles by Pulsed Laser Post-Processing in Liquid, *Molecules*, 2020, **25**(8), 1869, DOI: 10.3390/molecules25081869.
- 54 V. Amendola, P. Riello, S. Polizzi, S. Fiameni, C. Innocenti, C. Sangregorio and M. Meneghetti, Magnetic iron oxide nanoparticles with tunable size and free surface obtained via a “green” approach based on laser irradiation in water, *J. Mater. Chem.*, 2011, **21**, 18665–18673, DOI: 10.1039/c1jm13680a.
- 55 M. Lau and S. Barcikowski, Quantification of mass-specific laser energy input converted into particle properties during picosecond pulsed laser fragmentation of zinc oxide and boron carbide in liquids, *Appl. Surf. Sci.*, 2015, **348**, 22–29, DOI: 10.1016/j.apsusc.2014.07.053.
- 56 T. Schmitz, U. Wiedwald, C. Dubs and B. Gökce, Ultrasmall Yttrium Iron Garnet Nanoparticles with High Coercivity at Low Temperature Synthesized by Laser Ablation and Fragmentation of Pressed Powders, *ChemPhysChem*, 2017, **18**, 1125–1132, DOI: 10.1002/cphc.201601183.
- 57 M. Lau, A. Ziefuss, T. Komossa and S. Barcikowski, Inclusion of supported gold nanoparticles into their semiconductor support, *Phys. Chem. Chem. Phys.*, 2015, **17**, 29311–29318, DOI: 10.1039/c5cp04296h.
- 58 L. Pigliaru, M. Rinaldi, L. Ciccacci, A. Norman, T. Rohr, T. Ghidini and F. Nanni, 3D printing of high performance polymer-bonded PEEK-NdFeB magnetic composite materials, *Funct. Compos. Mater.*, 2020, **1**, 1–17, DOI: 10.1186/s42252-020-00006-w.
- 59 S. P. Rwei, P. Ranganathan and Y. H. Lee, Isothermal crystallization kinetics study of fully aliphatic PA6 copolyamides: Effect of novel long-chain polyamide salt as a comonomer, *Polymers*, 2019, **11**(3), 472, DOI: 10.3390/polym11030472.
- 60 S. Gogolewski, Effect of annealing on thermal properties and crystalline structure of polyamides, *Colloid Polym. Sci.*, 1979, **257**, 811–819.
- 61 S. Jendrzzej, B. Gökce and S. Barcikowski, Colloidal Stability of Metal Nanoparticles in Engine Oil under Thermal and Mechanical Load, *Chem. Eng. Technol.*, 2017, **40**, 1569–1576, DOI: 10.1002/ceat.201600541.
- 62 B. Gökce, D. D. Van't Zand, A. Menéndez-Manjón and S. Barcikowski, Ripening kinetics of laser-generated plasmonic nanoparticles in different solvents, *Chem. Phys. Lett.*, 2015, **626**, 96–101, DOI: 10.1016/j.cplett.2015.03.010.
- 63 B. Y. D. N. Furlong, A. Launikonis and W. H. F. Sasse, Colloidal Platinum Sols, *J. Chem. Soc., Faraday Trans. 1*, 1984, **80**, 571–588.
- 64 M. R. Query, Optical Constants, Contract. Rep. CRDC-CR-85034, 1985.
- 65 J. E. K. Schawe and S. Ziegelmeier, Determination of the thermal short time stability of polymers by fast scanning calorimetry, *Thermochim. Acta*, 2016, **623**, 80–85, DOI: 10.1016/j.tca.2015.11.020.
- 66 A. Wegner and G. Witt, Understanding the decisive thermal processes in laser sintering of polyamide 12, *AIP Conf. Proc.*, 2015, 160004, DOI: 10.1063/1.4918511.
- 67 S. Osswald, K. Behler and Y. Gogotsi, Laser-induced light emission from carbon nanoparticles, *J. Appl. Phys.*, 2008, **104**, 074308, DOI: 10.1063/1.2980321.
- 68 J. Bai, R. D. Goodridge, R. J. M. Hague and M. Song, Improving the Mechanical Properties of Laser-Sintered Polyamide 12 Through Incorporation of Carbon Nanotubes, *Polym. Eng. Sci.*, 2013, **53**, 1937–1946, DOI: 10.1002/pen.23459.
- 69 M. Zhao, K. Wudy and D. Drummer, Crystallization kinetics of polyamide 12 during Selective laser sintering, *Polymers*, 2018, **10**, DOI: 10.3390/polym10020168.
- 70 S. R. Athreya, K. Kalaitzidou and S. Das, Mechanical and microstructural properties of Nylon-12/carbon black

- composites: Selective laser sintering *versus* melt compounding and injection molding, *Compos. Sci. Technol.*, 2011, **71**, 506–510, DOI: 10.1016/j.compscitech.2010.12.028.
- 71 S. Fu, Z. Sun, P. Huang, Y. Li and N. Hu, Some basic aspects of polymer nanocomposites: A critical review, *Nano Mater. Sci.*, 2019, **1**, 2–30, DOI: 10.1016/j.nanoms.2019.02.006.
- 72 Y. Wang, Y. Shi and S. Huang, Selective laser sintering of polyamide-rectorite composite, *Proc. Inst. Mech. Eng., Part L*, 2005, **219**, 11–16, DOI: 10.1243/146442005x10229.
- 73 N. L. A. McFerran, C. G. Armstrong and T. McNally, Non-isothermal and isothermal crystallization kinetics of nylon-12, *J. Appl. Polym. Sci.*, 2008, **110**, 1043–1058, DOI: 10.1002/app.28696.
- 74 E. Piorkowska and G. C. Rutledge, *Handbook of Polymer Crystallization*, 2013, DOI: 10.1002/9781118541838.
- 75 D. Eiras and L. A. Pessan, Influence of calcium carbonate nanoparticles on the crystallization of polypropylene, *J. Mater. Res.*, 2009, **12**, 523–527, DOI: 10.1590/S1516-14392009000400024.
- 76 Y. Wang, C. M. Dinapoli, G. A. Tofig, R. W. Cunningham and R. A. Pearson, Selective laser sintering processing behavior of polyamide powders, Annual Technical Conference – ANTEC, Conference Proceedings, 2017, pp. 112–116.
- 77 C. Huang, X. Qian and R. Yang, Thermal conductivity of polymers and polymer nanocomposites, *Mater. Sci. Eng. R Reports*, 2018, **132**, 1–22, DOI: 10.1016/j.mser.2018.06.002.
- 78 M. Schmid, R. Kleijnen, M. Vetterli and K. Wegener, Influence of the origin of polyamide 12 powder on the laser sintering process and laser sintered parts, *Appl. Sci.*, 2017, **7**, 462, DOI: 10.3390/app7050462.
- 79 D. L. Bourell, T. J. Watt, D. K. Leigh and B. Fulcher, Performance limitations in polymer laser sintering, *Phys. Procedia*, 2014, **56**, 147–156, DOI: 10.1016/j.phpro.2014.08.157.
- 80 F. Neugebauer, V. Ploshikhin, J. Ambrosy and G. Witt, Isothermal and non-isothermal crystallization kinetics of polyamide 12 used in laser sintering, *J. Therm. Anal. Calorim.*, 2016, **124**, 925–933, DOI: 10.1007/s10973-015-5214-8.
- 81 M. Schmid, *Laser Sintering with Plastics – Technology, Processes, and Materials*, Carl Hanser Verlag GmbH & Co. KG, München, 2018, DOI: 10.3139/9781569906842.
- 82 P. Jamilpanah, H. Pahlavanzadeh and A. Kheradmand, Thermal conductivity, viscosity, and electrical conductivity of iron oxide with a cloud fractal structure, *Heat Mass Transfer*, 2017, **53**, 1343–1354, DOI: 10.1007/s00231-016-1891-5.
- 83 D. Strobbe, P. van Puyvelde, J. P. Kruth and B. van Hoorweder, Laser sintering of PA12/PA4,6 polymer composites, Solid Free. Fabr. 2018 Proc. 29th Annu. Int. Solid Free. Fabr. Symp. – An Addit. Manuf. Conf. SFF 2018, 2020, pp. 1550–1559.
- 84 A. Demortière, P. Panissod, B. P. Pichon, G. Pourroy, D. Guillon, B. Donnio and S. Bégin-Colin, Size-dependent properties of magnetic iron oxide nanocrystals, *Nanoscale*, 2011, **3**, 225–232, DOI: 10.1039/c0nr00521e.
- 85 J. Choi, J. Cha and J. K. Lee, Synthesis of various magnetite nanoparticles through simple phase transformation and their shape-dependent magnetic properties, *RSC Adv.*, 2013, **3**, 8365–8371, DOI: 10.1039/c3ra40283e.
- 86 R. M. Cornell and U. Schwertmann, *The Iron Oxides Structure, Properties, Reactions, Occurrences and Uses*, 2003.
- 87 A. Wegner and G. Witt, Understanding the decisive thermal processes in laser sintering of polyamide 12, *AIP Conf. Proc.*, 2015, **1664**, 1–6, DOI: 10.1063/1.4918511.
- 88 K. Wudy, S. Greiner and M. Zhao, D. Drummer, Selective laser beam melting of polymers: In situ and offline measurements for process adapted thermal characterization, *Procedia CIRP*, 2018, **74**, 238–243, DOI: 10.1016/j.procir.2018.08.102.
- 89 S. Mørup, M. F. Hansen and C. Frandsen, Magnetic Nanoparticles, *Comprehensive Nanoscience and Technology*, Elsevier, Amsterdam, 2011, pp. 437–491, DOI: 10.1016/B978-0-12-374396-1.00036-2.
- 90 J. Landers, F. Stromberg, M. Darbandi, C. Schöppner, W. Keune and H. Wende, Correlation of superparamagnetic relaxation with magnetic dipole interaction in capped iron-oxide nanoparticles, *J. Phys.: Condens. Matter*, 2015, **27**, 026002, DOI: 10.1088/0953-8984/27/2/026002.
- 91 F. J. Berry, S. Skinner and M. F. Thomas, ⁵⁷Fe Mössbauer spectroscopic examination of a single crystal of Fe₃O₄, *J. Phys.: Condens. Matter*, 1998, **10**, 215–220, DOI: 10.1088/0953-8984/10/1/024.

7.2 Plasmonic and antibacterial properties

Unpublished results based on a collaboration with:

Carlos Doñate-Buendía^{1,2}, Anna Ziefuß¹, Matthias Krause³, Alexandra Ingendoh-Tsakmakidis⁴, Bernd Sures⁴, Milen Nachev⁵, Bilal Gökce¹

¹ Technical Chemistry I and Center for Nanointegration Duisburg-Essen (CENIDE), University of Duisburg-Essen, Universitaetsstrasse 7, 45141 Essen, Germany

² GROC · UJI, Institute of New Imaging Technologies, Universitat Jaume I, Avda. Sos Baynat sn, 12071 Castellón, Spain

³ FH Dortmund, Chair of Thorsten Sinnemann

⁴ Department of Prosthetic Dentistry and Biomedical Materials Science, Lower Saxony Centre for Biomedical Engineering, Implant Research and Development (NIFE), Hannover Medical School (MHH), Stadtfelddamm 34, 30625 Hannover, Germany

⁵ Department of Aquatic Ecology and Centre for Water and Environmental Research, University of Duisburg-Essen, Universitätsstr. 5, Essen 45141, Germany

Using nano-additives can help overcoming material-related limitations of polymer powders for laser powder bed fusion (PBF-LB), aiming for an expansion of the material variety and adaption of the powder to the PBF-LB process. Besides increasing the processability, also the final part properties are altered and a functionalization of the part can be achieved [16]. Various additivation routes enable the modification of polymer powder materials by nano-additives [16] to increase the flowability and anti-caking, or for electrical conductivity, light absorptivity adjustment [22,128,136,138,139], and enhancement of mechanical properties [13]. However, to achieve this, a deep understanding of the interplay of the PBF-LB process with small mass fractions of nanoparticulate additives is required. Conventional additivation methods typically come with the disadvantage of agglomeration of the nanomaterial, which makes high filling rates necessary to achieve a sufficient surface dose. As an alternative, clean and surfactant-free nanoparticles can be generated using laser ablation and LPP in liquids [33]. Thereafter, these colloidal nanoparticles are deposited on polymer micropowder supports to create and qualify new nanoparticle-composite powders for PBF-LB [268]. Based on this approach polyamide 12 and thermoplastic polyurethane microparticles were already successful decorated with a variety of nanoparticle materials (silver, iron oxide, carbon) and processed via PBF-LB (please see previous chapters). The nanoparticle degree of dispersion on the polymer microparticle surface and the surface coverage can alter the PBF-LB processability and enable functionalization of final parts, as it is presented in the following section for plasmonic and antibacterial properties.

Plasmonic polymer powder materials

Plasmonic metal nanoparticles are known for a broad variety of applications in catalysis, microfluidics, optical data storage, sensing, imaging, and in vivo therapy [277–279]. They respond to external physical triggers and can translate a variable such as temperature, light, refractive index, pH, ionic strength, magnetic fields, ultrasound, humidity or specific molecules into a variation of the nanoparticle optical properties [269,280,281]. By AM, plasmonic-functionalized polymer parts that respond to such external triggers could be generated. Hereby, another dimension of design freedom is added to the AM process. However, the interaction between metal nanoparticles and the applicability of the above-mentioned sensorics properties (plasmonic response) are considerably dependent on the particle size and shape [269,282]. Aggregation of the nanoparticles has therefore a huge effect on optical properties, e.g. surface plasmon resonance (SPR) frequency, and hereby on the functionality of the printed parts.

Preventing agglomeration and conserving dispersion along the process chain for plasmonic-functionalized parts by AM poses a key challenge. Furthermore, low volume fractions are desirable in order to add a nano-functionality with only little impact on the mechanical properties of the part, which could be modified [277], e.g. by influencing the crystallization behavior of the polymer. In addition, also economical aspects (material costs) for additivation with plasmonic particles like gold must be considered and require a low dosage.

By colloidal additivation of polymer powder with laser-generated nanoparticles these requirements can be addressed and considerable plasmonic functionalization can be obtained even at mass loadings of 0.1 wt% or below. For the following investigation, gold and silver nanoparticles have been generated by LSPC and adsorbed on PA12 and TPU powders by pH-controlled colloidal additivation. Due to their plasmonic properties, the dispersion of gold and silver nanoparticle in and on a polymer matrix can easily be analyzed by confocal laser scanning microscopy and UV-Vis spectroscopy. Confocal laser scanning microscopy has been used in previous studies to characterize the dispersion of inorganic nanoparticles in polymer materials, allowing to create 3D images of macroscopic polymer parts [283] and even to extract quantitative information [284] even though nanoparticle diameters are far below Abbe's diffraction limit. However, confocal imaging cannot resolve single nanoparticles in the size of several 10th nm, for which SEM is more suitable (Figure 14a,b). Instead, confocal imaging enables evaluation of the distribution of particles on the surface (Figure 14c). Performing both techniques, SEM imaging and confocal dark field scattering, is therefore an ideal way for investigating the aggregation state of plasmonic nanoparticles

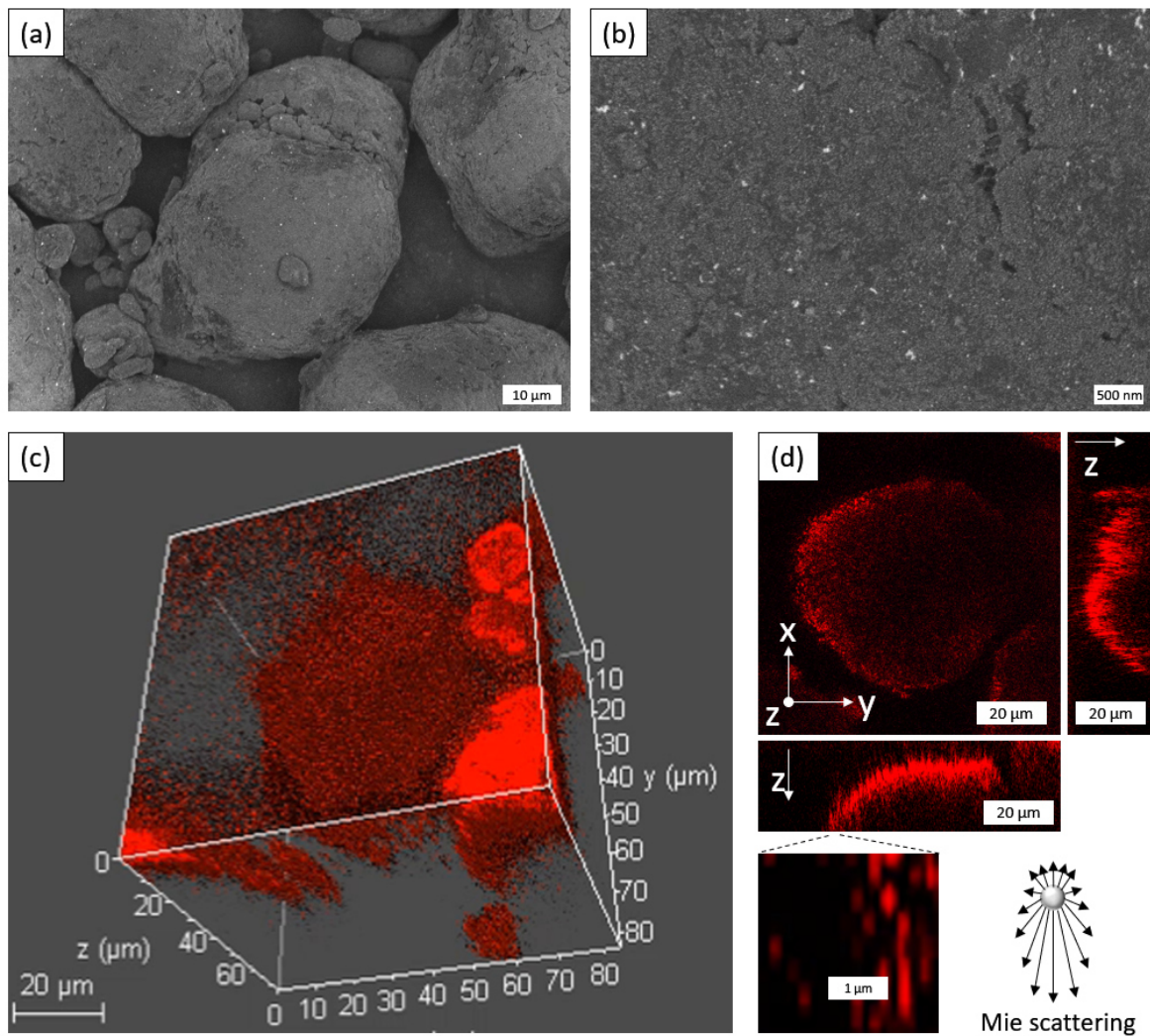


Figure 14: (a,b) SEM images of PA12 polymer particles decorated with 0.1 wt% gold nanoparticles. Laser scanning confocal dark field scattering imaging of PA12 particles coated with gold: (c) 3D image, (d) 2D image in the xy -plane with the corresponding 2D images in the xz - and yz -plane, depicting the Mie scattering of the nanoparticles.

(SEM) and its macroscopic distribution on the particle surface (confocal laser scattering). Since different dispersions and particles sizes result in different scattering intensities, confocal dark field scattering can also distinguish between good and bad dispersion as it was shown for silver nanoparticles [268]. The method is not limited to powders but can also be utilized to analyze previously molten and resolidified polymer.

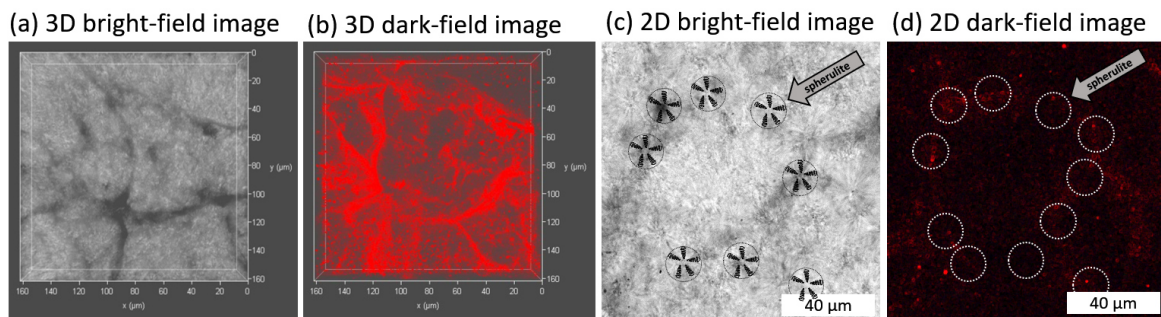


Figure 15: Analysis of the sintered parts made from PA12 micropowders decorated with gold nanoparticles: (a,b) Confocal laser scanning 3D brightfield image and 3D dark-field scattering image of a PA12-Au powder, showing the distribution of the nanoparticles in the final part after sintering. (c, d) Confocal laser scanning 2D bright-field image and 2D dark-field scattering image of a PA12-Au powder, showing the distribution of spherulites (c) relative to the distribution of nanoparticles (d) after sintering.

In Figure 15 (a) a 3D confocal laser scanning microscopy scan of PA12 supported with 0.1 wt% gold nanoparticles is shown after sintering with the respective 3D dark-field scattering image in Figure 15 (b). The plasmonic nanoparticles exhibit a strong scattering signal. It can be observed that the nanoparticles did not significantly leave the polymer particle surface in the molten state before resolidification, resulting in a web-like macroscopic superstructure, which is formed by the contour of the former polymer microparticles. This has been observed in other studies for PA12 decorated with carbon nanotubes or carbon nanoparticles [146,285]. While the nanoparticles show a homogeneous particle distribution, a better understanding of the particle supporting procedure and its material dependencies will make optimization feasible. In Figure 15(c,d), confocal laser scanning 2D bright-field image and 2D dark-field scattering image of a PA12/Au-nanocomposite are shown. It can be observed that the distribution of spherulites (c) correlates with the position of the nanoparticles on the former microparticle surface (d). Hence, we also conclude that the gold nanoparticles act as nuclei for the crystallization of the polymer.

One advantage of plasmonic metal nanoparticles generated by laser synthesis lies in the tunability of properties through alloying. For example, in addition to the widespread way of using pure metal targets for laser ablation, it is also possible to ablate alloy targets or powder targets. The latter can be produced by mixing and pressing powders, which allows target compositions that are not possible by alloying [231][232]. An approach to tune the plasmonic properties of silver and gold alloys is demonstrated in Figure 16. By variation of the gold to silver molar ratio Ag_xAu_y -alloy nanoparticles were generated, which could successfully be supported on PA12 particles, as it is shown in Figure 16 a-e. SEM images further confirms the high dispersion and homogeneous decoration for silver and gold nanoparticles on the PA12 particle surface (Figure 16 g,h). Used as a feedstock material, these plasmonic functionalized PA12 powders allow printing of parts that still exhibit the

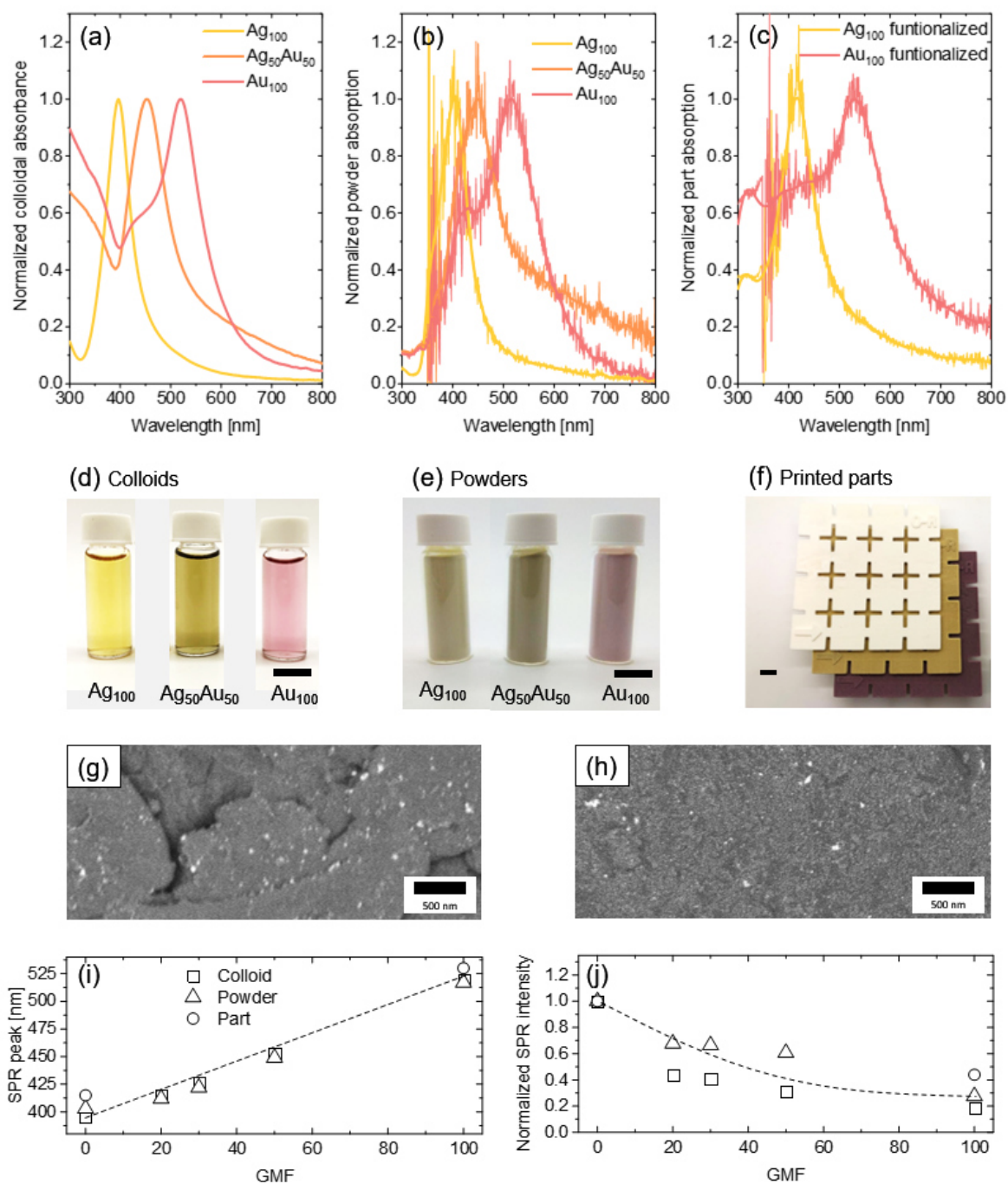


Figure 16: Tuning of plasmonic properties: (a) UV-Vis absorbance spectra of laser-generated colloidal Ag_xAu_y -alloy nanoparticles, (b) corresponding normalized absorbance spectra of functionalized powders measured by UV-Vis reflection spectroscopy and (c) UV-Vis absorbance spectra from printed parts. (d) Laser generated plasmonic metal nanoparticles in water, (e) PA12 powder functionalized with Au_xAg_y nanoparticles and (f) printed parts processed by PBF-LB: Neat PA12 (white), PA12 with 0.1 wt% silver (yellow) and PA12 with 0.1 wt% gold (purple). SEM images of PA12 decorated with (g) silver and (h) gold nanoparticles. (i,j) SPR peak wavelength and normalized SPR intensity as function of the gold molar ratio (GMR) for colloids, powders and printed parts. In all experiments PA12 was functionalized with 0.1 wt% of plasmonic nanoparticles. Please note that due to differences in the density between gold and silver the vol% and surf% are not constant and will decrease with increasing GMR.

original plasmonic properties (Figure 16 f). Plasmonic functionalized PA12 powders and a neat PA12 reference powder were processed on a Desktop PBF-LB machine (Sharebot SnowWhite) equipped with a CO₂ laser. Details on used parameters and optimization of scan speed and powder bed temperature are given in A11. A final comparison of the SPR peak wavelength of the alloy colloid, the functionalized powder and the printed parts is presented in Figure 16 i,j as a function of the gold molar fraction (GMF), underlining the linear between gold content and SPR wavelength and intensity.

Although the addition of gold with its smaller molar absorption coefficient compared to silver [286] results in a 4 times smaller absorption of Au₁₀₀ functionalized parts compared to Ag₁₀₀ functionalized parts, it can be expected that laser generated alloy nanoparticles open up new ways for fine tuning of absorption, catalytical properties or biocompatibility in 3D printed polymer parts. It has already been shown for both, pure gold [128] and silver [272] functionalization, that even small amounts of those particles can be beneficial for PBF-LB processing.

Besides influencing optical properties, plasmonic silver and gold nanoparticles are also known for their use in biomedical applications [287,288]. Silver, for example, features antibacterial properties and can thus be used to generate nanoparticle-composites for manufacturing of implants [259]. Test specimen made from silver-functionalized TPU powder already showed significant silver ion release over a test period of 30 days in deionized water (Figure 17a). In a first anti-bacteria tests, extracts of PBF-LB processed PA12-Ag platelets with 0.1 wt% of silver content have already shown an antibacterial effect against *E. coli*. For this experiment, the platelets were stored in phosphate buffered saline solution

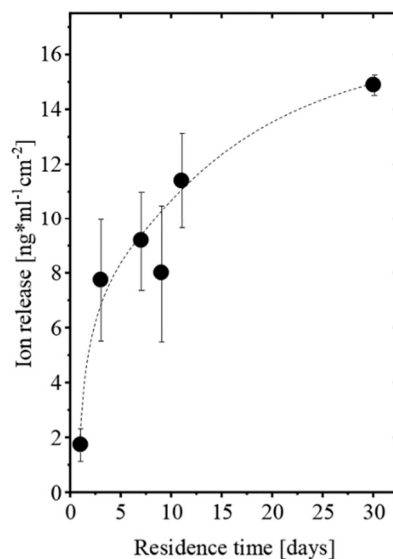


Figure 17: Silver ion release of a silver-functionalized TPU specimen immersed in water over a test period of 30 days. Ion concentrations were normalized to the surface area of the part.

(PBS) for ten days before performing anti-bacteria tests. At an average silver ion concentration of 28 $\mu\text{g}/\text{l}$ the metabolic activity was reduced by more than 90 % relative to a control sample without silver, which was expected from previous studies [289]. Bayraktar *et al.* recently reported on the antibacterial effect of silver functionalized PLA composite material for 3D printing by FDM [290]. They observed a pronounced antibacterial for *S. aureus* and *E. coli* at silver loadings between 1-3 wt%. Furthermore, the silver-functionalization decreased the number of bacteria adhered to the polymer surface, which could not be observed for our study with 0.1 wt% of silver nanoparticle-functionalization of PA12. However, the influence of silver nanoparticle size, dispersion and concentration on the silver ion release and the inhibition of bacteria growth and adhesion has not been systematically investigated, yet.

In summary the wide variety of materials from which nanoparticles can be generated by LPSC, enables a further extension of applications for highly dispersed plasmonic nanoparticles on polymer powders for PBF-LB. On the one hand, nanoparticles can affect the PBF-LB process and the final part (macro- and microstructure), but on the other hand nanoparticles lead to new functionalities due to their intrinsic material characteristics. This will allow new applications of 3D printed functional parts for plasmonics, catalysis or biomedical devices.

8 Summary and Outlook

Development of application specific feedstock materials for AM is important in order to establish AM in industrial processes. For PBF-LB of polymers, nanoparticle-functionalization represents a promising approach for increasing the variety of feedstock materials. Since the PBF-LB process chain is highly dependent on powder surfaces regarding flowability, melting, porosity, or laser absorption, it is important to control the effect of nanoparticle additivation on the polymer surface in order to optimize the properties of the polymer powder. Overall, nanoparticle-functionalization shows great potential but developing a general understanding of nanoparticle effects and interaction with the polymer matrix is challenging, which is attributed to the precise dosing and quantitative analysis of nanoparticle dispersion. Additionally, the established process routes for fabricating composite materials such as dry-coating or melt compounding typically lead to substantial aggregation of the nano-additive and often use pre-aggregated nanoparticles from gas-phase synthesis. In this thesis, colloidal additivation of polymer powders with laser-generated, highly dispersed nanoparticles was introduced as a promising alternative for fabricating nanoparticle-functionalized polymer powders for PBF-LB.

Generating nanoparticles by laser synthesis facilitates a wide variety of materials in almost any liquid in a scalable one-step process, which provides solid foundation for introducing variety to AM feedstock materials. Nevertheless, a profound understanding and control of the processes during laser irradiation and nanoparticle formation, especially in the early phase (plasma, cavitation bubble), is necessary for enhanced productivity and tailored nanoparticle properties. In order to close the knowledge gaps regarding laser ablation in highly viscous liquids, ultrafast imaging experiments of laser induced cavitation bubbles on metal and oxide targets in viscous liquids were performed. It was found that stronger viscous forces alter the shape of cavitation bubbles, lifetime, and damping, and affect the shape and dynamics of persistent microbubbles, independent of the target material.

Laser-generated aqueous colloids were subsequently used to demonstrate the feasibility of colloidal additivation of polymer powders, using the model system PA12-silver nanoparticles. Adsorption of silver nanoparticles on PA12 is a fast process and occurs within seconds under the right conditions due to electrostatic destabilization. Therefore, colloidal additivation needs precise control of particle concentrations, pH, and zeta potential to ensure a reproducible supporting quantity (efficiency/yield) as well as quality (nanoparticle dispersion). The process was also transferred to TPU powder and optimum process parameters for colloidal additivation with laser-generated silver nanoparticles were found for both polymers. The pH needs to be approximately 3-4, which is close to the isoelectric point of the silver colloid, and nanoparticle and polymer concentrations are optimal at approximately 50 mg/l and 50 g/l, respectively. Since the process is driven by electrostatic destabilization, fast mixing is necessary, and the mixing conditions are crucial for successful upscaling. Beyond a simple consideration of the nanoparticle dose by wt%, which is the standard value for comparing nanoparticle filler contents, the nanoparticle volume fraction (vol%), the polymer surface coverage (surf%), and the degree of dispersion were analyzed. Nanoparticle surface per polymer particle surface (surf%) and the distances between nanoparticles on the polymer surface are more relevant for describing the nanoparticle additivation than just wt%. However, these parameters can only be calculated from SEM images, which limits their wide use. After identification and investigation of process determinants for colloidal additivation of polymer powders, a concept for upscaling toward kg/h was presented, which features a continuous static mixer and direct filtration. This setup could process several kg of nanoparticle-composite powders per day, which would be enough for successful PBF-LB processing of test specimens. It can also be expected that further automatization of continuous colloidal additivation will improve process efficiency and throughput.

Silver functionalized polymer powders showed high dispersion and a conservation of surface plasmon resonance after additivation that can be utilized for diode laser sintering at 449 nm, which is close to the absorption maximum of plasmonic silver nanoparticles. It was also shown that fine-tuning of the SPR peak was possible by alloying. Although CO₂ lasers are mostly used for PBF-LB because of high absorption of most of the polymers at the laser wavelength of 10.6 μm, the use of other laser sources has distinct advantages. For example, diode lasers in the visible and NIR range (400-1100 nm) provide higher efficiency and enable the construction of small PBF-LB machines. Furthermore, with diode lasers, highly capable beam shaping devices can be used, which allow a more homogeneous temperature distribution and faster processing. Interestingly, silver additivation had no effect on the melting behavior of PA12 and only affected its crystallization at high cooling rates, which

are not relevant for PBF-LB. In contrast, DSC analysis of silver-functionalized TPU showed an increase and sharpening of the melting peak. The difference in the thermocalorimetric behavior of TPU and PA12 with the same mass loading of silver nanoparticles highlights the importance of understanding nanoparticle-polymer interactions in the melt pool.

Transfer of the additivation route to oxide, carbon, and gold nanoparticles on PA12 was also shown and examples for magnetical and anti-bacterial properties were given, which emphasize the potential of highly dispersed nanoparticle additivation. For generation of nanoparticles from iron oxide, yttrium iron oxide, and carbon, laser post-processing with ps- and ns-lasers was shown to have high potential for manipulating the phase composition and size of nanoparticles. In combination with colloidal additivation, monomodal nanoparticles were produced via ps-LFL, followed by direct mixing with a polymer suspension to generate functionalized powders. Based on the results, future studies should investigate the effects of the nanoparticle material, including different hydrophilicity of metals, oxides, and carbon as well as the influence of nanoparticles on surface roughness, flowability, final part microstructure, mechanical properties, and application specific tests.

In conclusion, even minute amounts (0.01 vol%) of well dispersed nanoparticles can spice up feedstock materials for PBF-LB, as demonstrated for magnetic, plasmonic, and anti-bacterial properties. LSPC and upscaling of colloidal additivation provides us with the opportunity to develop a new family of nanoparticle-functionalized materials and qualify them for PBF-LB, addressing the requirements of the manufacturing process, and finally contribute to increased design freedom.

References

- [1] R. Jiang, R. Kleer, F.T. Piller, Predicting the future of additive manufacturing: A Delphi study on economic and societal implications of 3D printing for 2030, *Technol. Forecast. Soc. Change.* 117 (2017) 84–97, doi.org/10.1016/j.techfore.2017.01.006.
- [2] B. Berman, 3D printing: the new industrial revolution, *IEEE Eng. Manag. Rev.* 41 (2014) 72–80, doi.org/10.1109/emr.2013.6693869.
- [3] Wohlers Associates, *Wohlers Report 2019*, (2019) 369.
- [4] C. Parra-Cabrera, C. Achille, S. Kuhn, R. Ameloot, 3D printing in chemical engineering and catalytic technology: Structured catalysts, mixers and reactors, *Chem. Soc. Rev.* 47 (2018) 209–230, doi.org/10.1039/c7cs00631d.
- [5] A. Paolini, S. Kollmannsberger, E. Rank, Additive manufacturing in construction: A review on processes, applications, and digital planning methods, *Addit. Manuf.* 30 (2019) 100894, doi.org/10.1016/j.addma.2019.100894.
- [6] C. Feng, M. Zhang, B. Bhandari, Materials Properties of Printable Edible Inks and Printing Parameters Optimization during 3D Printing: a review, *Crit. Rev. Food Sci. Nutr.* 59 (2019) 3074–3081, doi.org/10.1080/10408398.2018.1481823.
- [7] I. Gibson, D. Rosen, B. Stucker, *Additive manufacturing technologies: 3D printing, rapid prototyping, and direct digital manufacturing*, second edition, Springer, New York, 2015, doi.org/10.1007/978-1-4939-2113-3.
- [8] B. Jackson, Airbus ramps up 3D printing with Liebherr and Ultimaker, *3dprintingindustry.Com.* (2019). <https://3dprintingindustry.com/news/airbus-ramps-up-3d-printing-with-liebherr-and-ultimaker-148901/> (accessed April 25, 2020).
- [9] G. Wilson, The evolution of 3D printing in manufacturing, *Manuf. Glob.* (2020). <https://www.manufacturingglobal.com/technology/evolution-3d-printing-manufacturing> (accessed April 25, 2020).
- [10] B. Gökce, S. Barcikowski, P. Behrens, U. Fritsching, I. Kelbassa, R. Poprawe, C. Esen, A. Ostendorf, B. Voit, Prozessadaptierte Materialien fuer die Photonik, *Photonik* 1. (2015) 24–28.
- [11] C.A. Chatham, T.E. Long, C.B. Williams, A review of the process physics and material screening methods for polymer powder bed fusion additive manufacturing, *Prog. Polym. Sci.* 93 (2019) 68–95, doi.org/10.1016/j.progpolymsci.2019.03.003.
- [12] J. Schmidt, M. Sachs, S. Fanselow, K.E. Wirth, W. Peukert, New approaches towards production of polymer powders for selective laser beam melting of polymers, *AIP Conf. Proc.* 1914 (2017) 762–769, doi.org/10.1063/1.5016797.
- [13] M.M. Lexow, D. Drummer, New Materials for SLS: The Use of Antistatic and Flow Agents, *J. Powder Technol.* 2016 (2016) 1–9, doi.org/http://dx.doi.org/10.1155/2016/4101089.
- [14] M.A. Dechet, A. Goblirsch, S. Romeis, M. Zhao, F.J. Lanyi, J. Kaschta, D.W. Schubert, D. Drummer, W. Peukert, J. Schmidt, Production of polyamide 11 microparticles for Additive Manufacturing by liquid-liquid phase separation and precipitation, *Chem. Eng. Sci.* 197 (2019) 11–25, doi.org/10.1016/j.ces.2018.11.051.
- [15] J. Schmidt, M. Sachs, C. Blümel, B. Winzer, F. Toni, K.E. Wirth, W. Peukert, A novel process route for the production of spherical LBM polymer powders with small size and good flowability, *Powder Technol.* 261 (2014) 78–86, doi.org/10.1016/j.powtec.2014.04.003.
- [16] S. Yuan, F. Shen, C.K. Chua, K. Zhou, Polymeric composites for powder-based additive manufacturing: Materials and applications, *Prog. Polym. Sci.* 91 (2019) 141–168, doi.org/10.1016/j.progpolymsci.2018.11.001.
- [17] X. Wang, M. Jiang, Z. Zhou, J. Gou, D. Hui, 3D printing of polymer matrix composites: A review and prospective, *Compos. Part B Eng.* 110 (2017) 442–458, doi.org/10.1016/j.compositesb.2016.11.034.
- [18] H.C. Kim, H.T. Hahn, Y.S. Yang, Synthesis of PA12/functionalized GNP nanocomposite powders for the selective laser sintering process, *J. Compos. Mater.* 47 (2012) 501–509, doi.org/10.1177/0021998312441812.
- [19] C. Blümel, M. Sachs, T. Laumer, B. Winzer, J. Schmidt, M. Schmidt, W. Peukert, K.E. Wirth, Increasing flowability and bulk density of PE-HD powders by a dry particle coating process and impact on LBM processes, *Rapid Prototyp. J.* 21 (2015) 697–704, doi.org/10.1108/RPJ-07-2013-0074.

- [20] J. Yang, A. Sliva, A. Banerjee, R.N. Dave, R. Pfeffer, Dry particle coating for improving the flowability of cohesive powders, *Powder Technol.* 158 (2005) 21–33, doi.org/10.1016/j.powtec.2005.04.032.
- [21] D.W. Chae, B.C. Kim, Physical properties of isotactic poly(propylene)/silver nanocomposites: Dynamic crystallization behavior and resultant morphology, *Macromol. Mater. Eng.* 290 (2005) 1149–1156, doi.org/10.1002/mame.200500277.
- [22] T. Wagner, T. Höfer, S. Knies, P. Eyerer, Laser sintering of high temperature resistant polymers with carbon black additives, *Int. Polym. Process.* 19 (2004) 395–401, doi.org/10.3139/217.1846.
- [23] B. Chen, S. Berretta, K. Evans, K. Smith, O. Ghita, A primary study into graphene/polyether ether ketone (PEEK) nanocomposite for laser sintering, *Appl. Surf. Sci.* 428 (2018) 1018–1028, doi.org/10.1016/j.apsusc.2017.09.226.
- [24] S. Reichenberger, G. Marzun, M. Muhler, S. Barcikowski, Perspective of Surfactant-Free Colloidal Nanoparticles in Heterogeneous Catalysis, *ChemCatChem.* 11 (2019) 4489–4518, doi.org/10.1002/cctc.201900666.
- [25] G. Marzun, C. Streich, S. Jendrzzej, S. Barcikowski, P. Wagener, Adsorption of Colloidal Platinum Nanoparticles to Supports: Charge Transfer and Effects of Electrostatic and Steric Interactions, *Langmuir.* 30 (2014) 11928–11936, doi.org/10.1021/la502588g.
- [26] G. Marzun, A. Levish, V. Mackert, T. Kallio, S. Barcikowski, P. Wagener, Laser synthesis, structure and chemical properties of colloidal nickel-molybdenum nanoparticles for the substitution of noble metals in heterogeneous catalysis, *J. Colloid Interface Sci.* 489 (2017) 57–67, doi.org/10.1016/j.jcis.2016.09.014.
- [27] J.H. Yu, X. Liu, K.E. Kweon, J. Joo, J. Park, K.-T. Ko, D.W. Lee, S. Shen, K. Tivakornasithorn, J.S. Son, J.-H. Park, Y.-W. Kim, G.S. Hwang, M. Dobrowolska, J.K. Furdyna, T. Hyeon, Giant Zeeman splitting in nucleation-controlled doped CdSe:Mn²⁺ quantum nanoribbons, *Nat. Mater.* 9 (2010) 47–53, doi.org/10.1038/nmat2572.
- [28] W. Dong, S. Reichenberger, S. Chu, P. Weide, H. Ruland, S. Barcikowski, P. Wagener, M. Muhler, The effect of the Au loading on the liquid-phase aerobic oxidation of ethanol over Au/TiO₂ catalysts prepared by pulsed laser ablation, *J. Catal.* 330 (2015) 497–506, doi.org/10.1016/j.jcat.2015.07.033.
- [29] T. Mizutaru, G. Marzun, S. Kohsakovski, S. Barcikowski, D. Hong, H. Kotani, T. Kojima, T. Kondo, J. Nakamura, Y. Yamamoto, Peptide Cross-linkers: Immobilization of Platinum Nanoparticles Highly Dispersed on Graphene Oxide Nanosheets with Enhanced Photocatalytic Activities, *ACS Appl. Mater. Interfaces.* 9 (2017) 9996–10002, doi.org/10.1021/acsami.6b16765.
- [30] S. Barcikowski, P. Wagener, A. Schwenke, Method for producing micro-nano combined active systems, US9403160B2, 2016.
- [31] M. Lau, A. Ziefuss, T. Komossa, S. Barcikowski, Inclusion of supported gold nanoparticles into their semiconductor support, *Phys. Chem. Chem. Phys.* 17 (2015) 29311–29318, doi.org/10.1039/c5cp04296h.
- [32] P. Wagener, A. Schwenke, S. Barcikowski, How citrate ligands affect nanoparticle adsorption to microparticle supports, *Langmuir.* 28 (2012) 6132–6140, doi.org/10.1021/la204839m.
- [33] D. Zhang, B. Gökce, S. Barcikowski, Laser Synthesis and Processing of Colloids: Fundamentals and Applications, *Chem. Rev.* 117 (2017) 3990–4103, doi.org/10.1021/acs.chemrev.6b00468.
- [34] J.P. Sylvestre, S. Poulin, A. V. Kabashin, E. Sacher, M. Meunier, J.H.T. Luong, Surface chemistry of gold nanoparticles produced by laser ablation in aqueous media, *J. Phys. Chem. B.* 108 (2004) 16864–16869, doi.org/10.1021/jp047134.
- [35] G. Marzun, H. Bönemann, C. Lehmann, B. Spliethoff, C. Weidenthaler, S. Barcikowski, Role of Dissolved and Molecular Oxygen on Cu and PtCu Alloy Particle Structure during Laser Ablation Synthesis in Liquids, *ChemPhysChem.* 18 (2017) 1175–1184, doi.org/10.1002/cphc.201601315.
- [36] J. Jakobi, S. Petersen, A. Menéndez-Manjón, P. Wagener, S. Barcikowski, Magnetic alloy nanoparticles from laser ablation in cyclopentanone and their embedding into a photoresist, *Langmuir.* 26 (2010) 6892–6897, doi.org/10.1021/la101014g.
- [37] A. Menéndez-Manjón, A. Schwenke, T. Steinke, M. Meyer, U. Giese, P. Wagener, S. Barcikowski, Ligand-free gold-silver nanoparticle alloy polymer composites generated by picosecond laser ablation in liquid monomer, *Appl. Phys. A Mater. Sci. Process.* 110 (2013) 343–350, doi.org/10.1007/s00339-012-7264-0.
- [38] M. Lau, F. Waag, S. Barcikowski, Direct Integration of Laser-Generated Nanoparticles into Transparent Nail Polish: The Plasmonic “goldfinger,” *Ind. Eng. Chem. Res.* 56 (2017) 3291–3296, doi.org/10.1021/acs.iecr.7b00039.
- [39] H. Wei, Q. Zhang, Y. Yao, L. Liu, Y. Liu, J. Leng, Direct-write fabrication of 4D active shape-changing structures based on a shape memory polymer and its nanocomposite, *ACS Appl. Mater. Interfaces.* 9 (2017) 876–883, doi.org/10.1021/acsami.6b12824.
- [40] P. Wagener, A. Schwenke, B.N. Chichkov, S. Barcikowski, Pulsed Laser Ablation of Zinc in Tetrahydrofuran: Bypassing the Cavitation Bubble, *J. Phys. Chem. C.* 114 (2010) 7618–7625, doi.org/10.1021/jp911243a.
- [41] N. Löwa, J.M. Fabert, D. Gutkelch, H. Paysen, O. Kosch, F. Wiekhorst, 3D-printing of novel magnetic composites based on magnetic nanoparticles and photopolymers, *J. Magn. Magn. Mater.* 469 (2019) 456–460, doi.org/10.1016/j.jmmm.2018.08.073.
- [42] B.G. Compton, J.W. Kemp, T. V. Novikov, R.C. Pack, C.I. Nlebedim, C.E. Duty, O. Rios, M.P. Paranthaman, Direct-write 3D printing of NdFeB bonded magnets, *Mater. Manuf. Process.* 33 (2018) 109–113, doi.org/10.1080/10426914.2016.1221097.

- [43] R. Domingo-Roca, J.C. Jackson, J.F.C. Windmill, 3D-printing polymer-based permanent magnets, *Mater. Des.* 153 (2018) 120–128, doi.org/10.1016/j.matdes.2018.05.005.
- [44] M. Wehner, R.L. Truby, D.J. Fitzgerald, B. Mosadegh, G.M. Whitesides, J.A. Lewis, R.J. Wood, An integrated design and fabrication strategy for entirely soft, autonomous robots, *Nature*. 536 (2016) 451–455, doi.org/10.1038/nature19100.
- [45] Y. Kim, H. Yuk, R. Zhao, S.A. Chester, X. Zhao, Printing ferromagnetic domains for untethered fast-transforming soft materials, *Nature*. (2018) 274–279.
- [46] T. Gornet, T. Wohlers, History of additive manufacturing, in: *Wohlers Rep. 2014*, 2014: p. 34.
- [47] X. Kuang, D.J. Roach, J. Wu, C.M. Hamel, Z. Ding, T. Wang, M.L. Dunn, H.J. Qi, Advances in 4D Printing: Materials and Applications, *Adv. Funct. Mater.* 29 (2019) 1–23, doi.org/10.1002/adfm.201805290.
- [48] P. Basiliere, 3D Printing Accelerates, 4D Printing Gets Started, *Gartner*. (2019). <https://blogs.gartner.com/pete-basiliere/2019/01/03/3d-printing-accelerates-4d-printing-gets-started/> (accessed January 3, 2019).
- [49] F. Momeni, S. M.Mehdi Hassani.N, X. Liu, J. Ni, A review of 4D printing, *Mater. Des.* 122 (2017) 42–79, doi.org/10.1016/j.matdes.2017.02.068.
- [50] S. Tibbits, C. McKnelly, C. Olguin, D. Dikovskiy, S. Hirsch, 4d Printing and Universal Transformation, *ACADIA 14 Des. Agency Proc. 34th Annu. Conf. Assoc. Comput. Aided Des. Archit.* (2014) 539–548.
- [51] S. Tibbits, 4D printing: Multi-material shape change, *Archit. Des.* 84 (2014) 116–121, doi.org/10.1002/ad.1710.
- [52] 5 Trends Appear on the Gartner Hype Cycle for Emerging Technologies, 2019, *Gartner*. (2019). <https://www.gartner.com/smarterwithgartner/5-trends-appear-on-the-gartner-hype-cycle-for-emerging-technologies-2019/> (accessed September 27, 2019).
- [53] T.D. Ngo, A. Kashani, G. Imbalzano, K.T.Q. Nguyen, D. Hui, Additive manufacturing (3D printing): A review of materials, methods, applications and challenges, *Compos. Part B Eng.* 143 (2018) 172–196, doi.org/10.1016/j.compositesb.2018.02.012.
- [54] S.C. Ligon, R. Liska, J. Stampfl, M. Gurr, R. Mülhaupt, Polymers for 3D Printing and Customized Additive Manufacturing, *Chem. Rev.* 117 (2017) 10212–10290, doi.org/10.1021/acs.chemrev.7b00074.
- [55] All3DP, Leo Gregurić, How Much Does a 3D Printed House Cost in 2019?, (2019). <https://all3dp.com/2/3d-printed-house-cost/>.
- [56] B. Panda, S.C. Paul, N.A.N. Mohamed, Y.W.D. Tay, M.J. Tan, Measurement of tensile bond strength of 3D printed geopolymer mortar, *Meas. J. Int. Meas. Confed.* 113 (2018) 108–116, doi.org/10.1016/j.measurement.2017.08.051.
- [57] K. Vithani, A. Goyanes, V. Jannin, A.W. Basit, S. Gaisford, B.J. Boyd, An Overview of 3D Printing Technologies for Soft Materials and Potential Opportunities for Lipid-based Drug Delivery Systems, *Pharm. Res.* 36 (2019), doi.org/10.1007/s11095-018-2531-1.
- [58] Mehr als jedes vierte Industrieunternehmen setzt auf 3D-Druck, *Bitkom*. (2018). <https://www.bitkom.org/Presse/Presseinformation/Mehr-als-jedes-vierte-Industrieunternehmen-setzt-auf-3D-Druck.html> (accessed October 5, 2019).
- [59] S.F.S. Shirazi, S. Gharehkhani, M. Mehrali, H. Yarmand, H.S.C. Metselaar, N. Adib Kadri, N.A.A. Osman, A review on powder-based additive manufacturing for tissue engineering: Selective laser sintering and inkjet 3D printing, *Sci. Technol. Adv. Mater.* 16 (2015), doi.org/10.1088/1468-6996/16/3/033502.
- [60] S. Vock, B. Klöden, A. Kirchner, T. Weißgärber, B. Kieback, Powders for powder bed fusion: a review, *Prog. Addit. Manuf.* 4 (2019) 383–397, doi.org/10.1007/s40964-019-00078-6.
- [61] W. Associates, *Wohlers Report 2018*, 2018, doi.org/ISBN 978-0-9913332-0-2.
- [62] Frost & Sullivan’s Global 360° Research Team, *Global Additive Manufacturing Market - Forecast to 2025*, Frost & Sullivan. (2016) 61.
- [63] Autonomous Manufacturing (AMFG), *THE ADDITIVE MANUFACTURING LANDSCAPE 2019*, 2019. <https://amfg.ai/whitepaper-the-additive-manufacturing-landscape-2019/>.
- [64] AMPower, *Additive Manufacturing: Make or Buy*, (2017).
- [65] G. Flodberg, H. Pettersson, L. Yang, Pore analysis and mechanical performance of selective laser sintered objects, *Addit. Manuf.* 24 (2018) 307–315, doi.org/10.1016/j.addma.2018.10.001.
- [66] M.R. Parvaiz, S. Mohanty, S.K. Nayak, P.A. Mahanwar, Effect of surface modification of fly ash on the mechanical, thermal, electrical and morphological properties of polyetheretherketone composites, *Mater. Sci. Eng. A.* 528 (2011) 4277–4286, doi.org/10.1016/j.msea.2011.01.026.
- [67] Roland Berger, *Additive Manufacturing in Aerospace and Defense*, (2017).
- [68] AEROTEC, EOS, Daimler, NextGenAM – pilot project for automated metallic 3D printing proves a complete success, (2019). <https://www.eos.info/nextgenam> (accessed September 29, 2019).
- [69] J. Savolainen, M. Collan, How Additive Manufacturing Technology Changes Business Models? – Review of Literature, *Addit. Manuf.* 32 (2020), doi.org/10.1016/j.addma.2020.101070.
- [70] Deutsche Bahn, Drucken, damit die Züge schneller aufs Gleis kommen, *Pressrelease*. (2019). https://www.deutschebahn.com/de/presse/pressestart_zentrales_uebersicht/Drucken-damit-die-Zuege-schneller-aufs-Gleis-kommen-4256402 (accessed September 29, 2019).
- [71] Nationale Akademie der Wissenschaften Leopoldina, *Deutschen Akademie der Technikwissenschaften Acatech*,

- Additive Fertigung, Munich, 2017.
- [72] Additive Manufacturing - General principle - Terminology, DIN EN ISO-ASTM 52900, 2018.
- [73] S. Beitz, R. Uerlich, T. Bokelmann, A. Diener, T. Vietor, A. Kwade, Influence of powder deposition on powder bed and specimen properties, *Materials (Basel)*. 12 (2019), doi.org/10.3390/ma12020297.
- [74] L. Papadakis, D. Chantzis, K. Salonitis, On the energy efficiency of pre-heating methods in SLM/SLS processes, *Int. J. Adv. Manuf. Technol.* 95 (2018) 1325–1338, doi.org/10.1007/s00170-017-1287-9.
- [75] R. Mertens, B. Vrancken, N. Holmstock, Y. Kinds, J.P. Kruth, J. Van Humbeeck, Influence of powder bed preheating on microstructure and mechanical properties of H13 tool steel SLM parts, *Phys. Procedia*. 83 (2016) 882–890, doi.org/10.1016/j.phpro.2016.08.092.
- [76] M. Schmid, K. Wegener, Thermal and molecular properties of polymer powders for Selective Laser Sintering (SLS), *AIP Conf. Proc.* 1779 (2016), doi.org/10.1063/1.4965571.
- [77] F. Shen, S. Yuan, C.K. Chua, K. Zhou, Development of process efficiency maps for selective laser sintering of polymeric composite powders: Modeling and experimental testing, *J. Mater. Process. Technol.* 254 (2018) 52–59, doi.org/10.1016/j.jmatprotec.2017.11.027.
- [78] D. Drummer, S. Greiner, M. Zhao, K. Wudy, A novel approach for understanding laser sintering of polymers, *Addit. Manuf.* 27 (2019) 379–388, doi.org/10.1016/j.addma.2019.03.012.
- [79] K. Dotchev, W. Yusoff, Recycling of polyamide 12 based powders in the laser sintering process, *Rapid Prototyp. J.* 15 (2009) 192–203, doi.org/10.1108/13552540910960299.
- [80] S. Yuan, J. Bai, C.K. Chua, J. Wei, K. Zhou, Material evaluation and process optimization of CNT-coated polymer powders for selective laser sintering, *Polymers (Basel)*. 8 (2016), doi.org/10.3390/polym8100370.
- [81] M. Vasquez, B. Haworth, N. Hopkinson, Methods for quantifying the stable sintering region in laser sintered polyamide-12, *Polym. Eng. Sci.* 53 (2013) 1230–1240, doi.org/10.1002/pen.23386.
- [82] C.T. Bellehumeur, M.K. Bisaria, J. Vlachopoulos, An experimental study and model assessment of polymer sintering, *Polym. Eng. Sci.* 36 (1996) 2198–2207, doi.org/10.1002/pen.10617.
- [83] T. Laumer, T. Stichel, K. Nagulin, M. Schmidt, Optical analysis of polymer powder materials for Selective Laser Sintering, *Polym. Test.* 56 (2016) 207–213, doi.org/10.1016/j.polymertesting.2016.10.010.
- [84] EOS GmbH, EOS at the K 2019 trade fair: LaserProFusion technology for tool free injection molding, Press Release. (2019). <https://www.eos.info/presse/eos-auf-der-k-messe-2019> (accessed September 29, 2019).
- [85] M. Schmid, A. Amado, K. Wegener, Materials perspective of polymers for additive manufacturing with selective laser sintering, *J. Mater. Res.* 29 (2014) 1824–1832, doi.org/10.1557/jmr.2014.138.
- [86] M. Schmid, K. Wegener, Additive Manufacturing: Polymers applicable for laser sintering (LS), *Procedia Eng.* 149 (2016) 457–464, doi.org/10.1016/j.proeng.2016.06.692.
- [87] R.D. Goodridge, C.J. Tuck, R.J.M. Hague, Laser sintering of polyamides and other polymers, *Prog. Mater. Sci.* 57 (2012) 229–267, doi.org/10.1016/j.pmatsci.2011.04.001.
- [88] A. Wegner, New polymer materials for the laser sintering process: Polypropylene and others, 9th Int. Conf. Photonic Technol. LANE 2016. 83 (2016) 1003–1012, doi.org/10.1016/j.phpro.2016.08.105.
- [89] M. Schmid, F. Amado, G. Levy, K. Wegener, Flowability of powders for Selective Laser Sintering (SLS) investigated by Round Robin Test, *High Value Manuf. Adv. Res. Virtual Rapid Prototyp. - Proc. 6th Int. Conf. Adv. Res. Rapid Prototyping, VR@P 2013.* (2014) 95–99, doi.org/doi.org/10.3929/ethz-a-010057806.
- [90] T. Laumer, T. Stichel, M. Rath, M. Schmidt, Analysis of the influence of different flowability on part characteristics regarding the simultaneous laser beam melting of polymers, *Phys. Procedia*. 83 (2016) 937–946, doi.org/10.1016/j.phpro.2016.08.098.
- [91] G. Flodberg, H. Pettersson, L. Yang, Pore analysis and mechanical performance of selective laser sintered objects, *Addit. Manuf.* 24 (2018) 307–315, doi.org/10.1016/j.addma.2018.10.001.
- [92] D. Drummer, D. Rietzel, F. Kühnlein, Development of a characterization approach for the sintering behavior of new thermoplastics for selective laser sintering, *Phys. Procedia*. 5 (2010) 533–542, doi.org/10.1016/j.phpro.2010.08.081.
- [93] K. Wudy, D. Drummer, F. Kühnlein, M. Drexler, Influence of degradation behavior of polyamide 12 powders in laser sintering process on produced parts, *AIP Conf. Proc.* 1593 (2014) 691–695, doi.org/10.1063/1.4873873.
- [94] D. Drummer, K. Wudy, M. Drexler, Modelling of the aging behavior of polyamide 12 powder during laser melting process, *AIP Conf. Proc.* 1664 (2015), doi.org/10.1063/1.4918514.
- [95] S. Monsheimer, M. Grebe, F.E. Baumann, W. Christoph, T. Schiffer, H. Scholten, Laser-Sinter-Pulver mit verbesserten Recyclingeigenschaften, Verfahren zu dessen Herstellung und Verwendung des Laser-Sinter-Pulvers, EP1413594A2, 2004.
- [96] E. Hornbogen, *Werkstoffe*, 11. Auflage, Springer Vieweg, 2017.
- [97] G.W. Ehrenstein, *Polymer Werkstoffe Struktur-Eigenschaften-Anwendung*, (2011).
- [98] Y. Shi, Z. Li, H. Sun, S. Huang, F. Zeng, Effect of the properties of the polymer materials on the quality of selective laser sintering parts, *Proc. Inst. Mech. Eng. Part L J. Mater. Des. Appl.* 218 (2004) 247–252, doi.org/10.1177/146442070421800308.
- [99] A. Wegner, New polymer materials for the laser sintering process: Polypropylene and others, *Phys. Procedia*. 83 (2016) 1003–1012, doi.org/10.1016/j.phpro.2016.08.105.

- [100] M.A. Dechet, A. Demina, L. Römling, J.S. Gómez Bonilla, F.J. Lanyi, D.W. Schubert, A. Bück, W. Peukert, J. Schmidt, Development of poly(L-lactide) (PLLA) microspheres precipitated from triacetin for application in powder bed fusion of polymers, *Addit. Manuf.* 32 (2020), doi.org/10.1016/j.addma.2019.100966.
- [101] S. Berretta, K.E. Evans, O. Ghita, Predicting processing parameters in High Temperature Laser Sintering (HT-LS) from powder properties, *Mater. Des.* 105 (2016) 301–314, doi.org/10.1016/j.matdes.2016.04.097.
- [102] S. Kloos, M.A. Dechet, W. Peukert, J. Schmidt, Production of spherical semi-crystalline polycarbonate microparticles for Additive Manufacturing by liquid-liquid phase separation, *Powder Technol.* 335 (2018) 275–284, doi.org/10.1016/j.powtec.2018.05.005.
- [103] I.F. Ituarte, O. Wiikinkoski, A. Jansson, Additive manufacturing of polypropylene: A screening design of experiment using laser-based powder bed fusion, *Polymers (Basel)*. 10 (2018), doi.org/10.3390/polym10121293.
- [104] D.L. Bourell, T.J. Watt, D.K. Leigh, B. Fulcher, Performance limitations in polymer laser sintering, *Phys. Procedia*. 56 (2014) 147–156, doi.org/10.1016/j.phpro.2014.08.157.
- [105] S. Dadbakhsh, L. Verbelen, T. Vandeputte, D. Strobbe, P. Van Puyvelde, J.P. Kruth, Effect of powder size and shape on the SLS processability and mechanical properties of a TPU elastomer, *Phys. Procedia*. 83 (2016) 971–980, doi.org/10.1016/j.phpro.2016.08.102.
- [106] S. Yuan, F. Shen, J. Bai, C.K. Chua, J. Wei, K. Zhou, 3D soft auxetic lattice structures fabricated by selective laser sintering: TPU powder evaluation and process optimization, *Mater. Des.* 120 (2017) 317–327, doi.org/10.1016/j.matdes.2017.01.098.
- [107] S. Berretta, K.E. Evans, O. Ghita, Processability of PEEK, a new polymer for high temperature laser sintering (HT-LS), *Eur. Polym. J.* 68 (2015) 243–266, doi.org/10.1016/j.eurpolymj.2015.04.003.
- [108] S. Berretta, O. Ghita, K.E. Evans, Morphology of polymeric powders in Laser Sintering (LS): From Polyamide to new PEEK powders, *Eur. Polym. J.* 59 (2014) 218–229, doi.org/10.1016/j.eurpolymj.2014.08.004.
- [109] D. Gan, S. Lu, Z. Wang, Synthesis and characterization of poly(ether ketone ketone) (PEKK)/sodium sulfonated poly(arylene ether ketone) (S-PAEK) block copolymers, *Polym. Int.* 50 (2001) 812–816, doi.org/10.1002/pi.700.
- [110] S.L. Edwards, J.A. Werkmeister, Mechanical evaluation and cell response of woven polyetheretherketone scaffolds, *J. Biomed. Mater. Res. - Part A*. 100 A (2012) 3326–3331, doi.org/10.1002/jbm.a.34286.
- [111] A.R. McLauchlin, O.R. Ghita, L. Savage, Studies on the reprocessability of poly(ether ether ketone) (PEEK), *J. Mater. Process. Technol.* 214 (2014) 75–80, doi.org/10.1016/j.jmatprotec.2013.07.010.
- [112] S. Berretta, Y. Wang, R. Davies, O.R. Ghita, Polymer viscosity, particle coalescence and mechanical performance in high-temperature laser sintering, *J. Mater. Sci.* 51 (2016) 4778–4794, doi.org/10.1007/s10853-016-9761-6.
- [113] E. Piorkowska, G.C. Rutledge, *Handbook of Polymer Crystallization*, 2013, doi.org/10.1002/9781118541838.
- [114] I. Kolesov, D. Mileva, R. Androsch, C. Schick, Structure formation of polyamide 6 from the glassy state by fast scanning chip calorimetry, *Polymer (Guildf)*. 52 (2011) 5156–5165, doi.org/10.1016/j.polymer.2011.09.007.
- [115] S. Gogolewski, K. Czerntawska, M. Gastorek, Effect of annealing on thermal properties and crystalline structure of polyamides. Nylon 12 (polylauro lactam), *Colloid Polym. Sci. Kolloid Zeitschrift Zeitschrift Für Polym.* 258 (1980) 1130–1136, doi.org/10.1007/BF01382456.
- [116] C. Ramesh, Crystalline transitions in Nylon 12, *Macromolecules*. 32 (1999) 5704–5706, doi.org/10.1021/ma990494o.
- [117] M. Ito, K. Mizuochi, T. Kanamoto, Effects of crystalline forms on the deformation behaviour of nylon-6, *Polymer (Guildf)*. 39 (1998) 4593–4598, doi.org/10.1016/S0032-3861(97)10132-X.
- [118] M. Van Drongelen, T. Meijer-Vissers, D. Cavallo, G. Portale, G. Vanden Poel, R. Androsch, Microfocus wide-angle X-ray scattering of polymers crystallized in a fast scanning chip calorimeter, *Thermochim. Acta*. 563 (2013) 33–37, doi.org/10.1016/j.tca.2013.04.007.
- [119] J.E.K. Schawe, Analysis of non-isothermal crystallization during cooling and reorganization during heating of isotactic polypropylene by fast scanning DSC, *Thermochim. Acta*. 603 (2015) 85–93, doi.org/10.1016/j.tca.2014.11.006.
- [120] A. Jungmeier, G.W. Ehrenstein, D. Drummer, New aspects of process induced properties of microinjection moulded parts, *Plast. Rubber Compos.* 39 (2010) 308–314, doi.org/10.1179/174328910X12691245470392.
- [121] A. Jungmeier, I. Kuehnert, G.W. Ehrenstein, T.A. Osswald, Process induced properties of micro injection molded parts - New aspects, *Annu. Tech. Conf. - ANTEC, Conf. Proc.* 3 (2009) 1328–1332.
- [122] A. Toda, R. Androsch, C. Schick, Insights into polymer crystallization and melting from fast scanning chip calorimetry, *Polym. (United Kingdom)*. 91 (2016) 239–263, doi.org/10.1016/j.polymer.2016.03.038.
- [123] M. Schmidt, M. Merklein, D. Bourell, D. Dimitrov, T. Hausotte, K. Wegener, L. Overmeyer, F. Vollertsen, G.N. Levy, Laser based additive manufacturing in industry and academia, *CIRP Ann.* 66 (2017) 561–583, doi.org/10.1016/j.cirp.2017.05.011.
- [124] W. Griehl, D. Ruesteivi, Nylon-12-Preparation, Properties, and Applications, *Ind. Eng. Chem.* 62 (1970) 16–22, doi.org/10.1021/ie50723a005.
- [125] M.A. Dechet, S. Kloos, W. Peukert, J. Schmidt, Production of spherical micron-sized polymer particles for additive manufacturing by liquid phase processes, *AIP Conf. Proc.* 2055 (2019) 1–6, doi.org/10.1063/1.5084905.
- [126] M. Sachs, J. Schmidt, F. Toni, C. Blümel, B. Winzer, W. Peukert, K.E. Wirth, Rounding of irregular polymer particles in a downer reactor, *Procedia Eng.* 102 (2015) 542–549, doi.org/10.1016/j.proeng.2015.01.119.
- [127] V.E. Beal, R.A. Paggi, G. V. Salmoria, A. Lago, Statistical evaluation of laser energy density effect on mechanical

- properties of polyamide parts manufactured by selective laser sintering, *J. Appl. Polym. Sci.* 113 (2009) 2910–2919, doi.org/10.1002/app.30329.
- [128] A.W. Powell, A. Stavrinadis, I. De Miguel, G. Konstantatos, R. Quidant, White and Brightly Colored 3D Printing Based on Resonant Photothermal Sensitizers, *Nano Lett.* 18 (2018) 6660–6664, doi.org/10.1021/acs.nanolett.8b01164.
- [129] A.W. Powell, A. Stavrinadis, S. Christodoulou, R. Quidant, G. Konstantatos, On-Demand Activation of Photochromic Nanoheaters for High Color Purity 3D Printing, *Nano Lett.* 20 (2020) 3485–3491, doi.org/10.1021/acs.nanolett.0c00414.
- [130] P.K. Jain, P.M. Pandey, P.V.M. Rao, Selective laser sintering of clay-reinforced polyamide, *Polym. Compos.* 31 (2010) 732–743, doi.org/10.1002/pc.20854.
- [131] J. Kim, T.S. Creasy, Selective laser sintering characteristics of nylon 6/clay-reinforced nanocomposite, *Polym. Test.* 23 (2004) 629–636, doi.org/10.1016/j.polymertesting.2004.01.014.
- [132] C.Z. Yan, Y.S. Shi, J.S. Yang, J.H. Liu, An organically modified montmorillonite/nylon-12 composite powder for selective laser sintering, *Rapid Prototyp. J.* 17 (2011) 28–36, doi.org/10.1108/13552541111098608.
- [133] Y. Wang, Y. Shi, S. Huang, Selective laser sintering of polyamide-rectorite composite, *Proc. Inst. Mech. Eng. Part L J. Mater. Des. Appl.* 219 (2005) 11–16, doi.org/10.1243/146442005X10229.
- [134] Y. Chunze, S. Yusheng, Y. Jinsong, L. Jinhui, A nanosilica/nylon-12 composite powder for selective laser sintering, *J. Reinf. Plast. Compos.* 28 (2008) 2889–2902, doi.org/10.1177/0731684408094062.
- [135] J. Wang, P. Bai, Z. Zhang, Y. Li, Processing and characterization of core-shell PA12/silica composites produced by selective laser sintering, *Adv. Mater. Res.* 160–162 (2011) 756–761, doi.org/10.4028/www.scientific.net/AMR.160-162.756.
- [136] S.R. Athreya, K. Kalaitzidou, S. Das, Processing and characterization of a carbon black-filled electrically conductive Nylon-12 nanocomposite produced by selective laser sintering, *Mater. Sci. Eng. A.* 527 (2010) 2637–2642, doi.org/10.1016/j.msea.2009.12.028.
- [137] Zheng W. Lu X. Wong S-C., Electrical and mechanical properties of expanded graphite-reinforced high density polyethylene, *J. Appl. Polym. Sci.* 91 (2004) 2781–2788.
- [138] R.D. Goodridge, M.L. Shofner, R.J.M. Hague, M. McClelland, M.R. Schlea, R.B. Johnson, C.J. Tuck, Processing of a Polyamide-12/carbon nanofibre composite by laser sintering, *Polym. Test.* 30 (2011) 94–100, doi.org/10.1016/j.polymertesting.2010.10.011.
- [139] G. V. Salmoria, R.A. Paggi, A. Lago, V.E. Beal, Microstructural and mechanical characterization of PA12/MWCNTs nanocomposite manufactured by selective laser sintering, *Polym. Test.* 30 (2011) 611–615, doi.org/10.1016/j.polymertesting.2011.04.007.
- [140] J. Bai, R.D. Goodridge, R.J.M. Hague, M. Song, Improving the Mechanical Properties of Laser-Sintered Polyamide 12 Through Incorporation of Carbon Nanotubes, *Polym. Eng. Sci.* 53 (2013) 1937–1946, doi.org/DOI 10.1002/pen.23459.
- [141] J. Bai, R.D. Goodridge, R.J.M. Hague, M. Song, M. Okamoto, Influence of carbon nanotubes on the rheology and dynamic mechanical properties of polyamide-12 for laser sintering, *Polym. Test.* 36 (2014) 95–100, doi.org/10.1016/j.polymertesting.2014.03.012.
- [142] K. Shahzad, J. Deckers, S. Boury, B. Neirinck, J.P. Kruth, J. Vleugels, Preparation and indirect selective laser sintering of alumina/PA microspheres, *Ceram. Int.* 38 (2012) 1241–1247, doi.org/10.1016/j.ceramint.2011.08.055.
- [143] M.S. Wahab, H.W. Dalgarno, R.F. Cochrane, S. Hassan, Development of Polymer Nanocomposites for Rapid Prototyping Process, *Proc. World Congr. Eng. II* (2009) 1–6.
- [144] J. Christian Nelson, N.K. Vail, J.W. Barlow, J.J. Beaman, D.L. Bourell, H.L. Marcus, Selective Laser Sintering of Polymer-Coated Silicon Carbide Powders, *Ind. Eng. Chem. Res.* 34 (1995) 1641–1651, doi.org/10.1021/ie00044a017.
- [145] O. Ivanova, C. Williams, T. Campbell, Additive manufacturing (AM) and nanotechnology: Promises and challenges, *Rapid Prototyp. J.* 19 (2013) 353–364, doi.org/10.1108/RPJ-12-2011-0127.
- [146] J. Bai, R.D. Goodridge, R.J.M. Hague, M. Song, H. Murakami, Nanostructural characterization of carbon nanotubes in laser-sintered polyamide 12 by 3D-TEM, *J. Mater. Res.* 29 (2014) 1817–1823, doi.org/10.1557/jmr.2014.126.
- [147] F. Qi, N. Chen, Q. Wang, Preparation of PA11/BaTiO₃ nanocomposite powders with improved processability, dielectric and piezoelectric properties for use in selective laser sintering, *Mater. Des.* 131 (2017) 135–143, doi.org/10.1016/j.matdes.2017.06.012.
- [148] S. Xi, P. Zhang, Y. Huang, M. Kong, Q. Yang, G. Li, Laser sintering of cryogenically ground polymer powders into high-performance parts: The role of dry particle coating with a conductive flow agent, *Polymer (Guildf.)* 186 (2020) 122044, doi.org/10.1016/j.polymer.2019.122044.
- [149] D. Wang, C. Song, G. Gu, Z. Hu, Preparation of Fe₂O₃ microcages from the core/shell structures, *Mater. Lett.* 59 (2005) 782–785, doi.org/10.1016/j.matlet.2004.11.020.
- [150] I. Krupa, I. Chodak, Physical properties of thermoplastic/graphite composites, *Eur. Polym. J.* 37 (2001) 2159–2168, doi.org/10.1016/S0014-3057(01)00115-X.
- [151] W. Zheng, S.C. Wong, Electrical conductivity and dielectric properties of PMMA/expanded graphite composites, *Compos. Sci. Technol.* 63 (2003) 225–235, doi.org/10.1016/S0266-3538(02)00201-4.
- [152] J.W. Shen, X.M. Chen, W.Y. Huang, Structure and electrical properties of grafted polypropylene/graphite

- nanocomposites prepared by solution intercalation, *J. Appl. Polym. Sci.* 88 (2003) 1864–1869, doi.org/10.1002/app.11892.
- [153] Y.X. Pan, Z.Z. Yu, Y.C. Ou, G.H. Hu, New process of fabricating electrically conducting nylon 6/graphite nanocomposites via intercalation polymerization, *J. Polym. Sci. Part B Polym. Phys.* 38 (2000) 1626–1633, doi.org/10.1002/(SICI)1099-0488(20000615)38:12<1626::AID-POLB80>3.0.CO;2-R.
- [154] Y. Li, J. Zhu, S. Wei, J. Ryu, L. Sun, Z. Guo, Poly(propylene)/graphene nanoplatelet nanocomposites: Melt rheological behavior and thermal, electrical, and electronic properties, *Macromol. Chem. Phys.* 212 (2011) 1951–1959, doi.org/10.1002/macp.201100263.
- [155] S. Wei, R. Patil, L. Sun, N. Haldolaarachchige, X. Chen, D.P. Young, Z. Guo, Ex situ solvent-assisted preparation of magnetic poly(propylene) nanocomposites filled with Fe@FeO nanoparticles, *Macromol. Mater. Eng.* 296 (2011) 850–857, doi.org/10.1002/mame.201100010.
- [156] X. Chen, S. Wei, A. Yadav, R. Patil, J. Zhu, R. Ximenes, L. Sun, Z. Guo, Poly(propylene)/carbon nanofiber nanocomposites: Ex situ solvent-assisted preparation and analysis of electrical and electronic properties, *Macromol. Mater. Eng.* 296 (2011) 434–443, doi.org/10.1002/mame.201000341.
- [157] C. Doñate-Buendía, F. Frömel, M.B. Wilms, R. Streubel, J. Tenkamp, T. Hupfeld, M. Nachev, E. Gökce, A. Weisheit, S. Barcikowski, F. Walther, J.H. Schleifenbaum, B. Gökce, Oxide dispersion-strengthened alloys generated by laser metal deposition of laser-generated nanoparticle-metal powder composites, *Mater. Des.* 154 (2018) 360–369, doi.org/10.1016/j.matdes.2018.05.044.
- [158] K. Suttiponparnit, J. Jiang, M. Sahu, S. Suvachittanont, T. Charinpanitkul, P. Biswas, Role of Surface Area, Primary Particle Size, and Crystal Phase on Titanium Dioxide Nanoparticle Dispersion Properties, *Nanoscale Res. Lett.* 6 (2010) 1–8, doi.org/10.1007/s11671-010-9772-1.
- [159] S. Bhattacharjee, DLS and zeta potential - What they are and what they are not, *J. Control. Release.* 235 (2016) 337–351, doi.org/10.1016/j.jconrel.2016.06.017.
- [160] C. Streich, S. Koenen, M. Lelle, K. Peneva, S. Barcikowski, Influence of ligands in metal nanoparticle electrophoresis for the fabrication of biofunctional coatings, *Appl. Surf. Sci.* 348 (2015) 92–99, doi.org/10.1016/j.apsusc.2014.12.159.
- [161] G. Marzun, J. Nakamura, X. Zhang, S. Barcikowski, P. Wagener, Size control and supporting of palladium nanoparticles made by laser ablation in saline solution as a facile route to heterogeneous catalysts, *Appl. Surf. Sci.* 348 (2015) 75–84, doi.org/10.1016/j.apsusc.2015.01.108.
- [162] A. FOJTIK, A. HENGLEIN, Laser ablation of films and suspended particles in a solvent : formation of cluster and colloid solutions, *Berichte Der Bunsen-Gesellschaft.* 97 (1993) 252–254.
- [163] J. Neddersen, G. Chumanov, T.M. Cotton, Laser Ablation of Metals: A New Method for Preparing SERS Active Colloids, *Appl. Spectrosc.* 47 (1993) 1959–1964, doi.org/10.1366/0003702934066460.
- [164] V. Amendola, P. Riello, M. Meneghetti, Magnetic Nanoparticles of Iron Carbide, Iron Oxide, Iron@Iron Oxide, and Metal Iron Synthesized by Laser Ablation in Organic Solvents, *J. Phys. Chem. C.* 115 (2011) 5140–5146, doi.org/10.1021/jp109371m.
- [165] V. Amendola, M. Meneghetti, Laser ablation synthesis in solution and size manipulation of noble metal nanoparticles, *Phys. Chem. Chem. Phys.* 11 (2009) 3805–3821, doi.org/10.1039/b900654k.
- [166] G. Yang, Laser ablation in liquids: Applications in the synthesis of nanocrystals, *Prog. Mater. Sci.* 52 (2007) 648–698, doi.org/10.1016/j.pmatsci.2006.10.016.
- [167] D. Amans, W. Cai, S. Barcikowski, Status and demand of research to bring laser generation of nanoparticles in liquids to maturity, *Appl. Surf. Sci.* 488 (2019) 445–454, doi.org/10.1016/j.apsusc.2019.05.117.
- [168] R. Streubel, S. Barcikowski, B. Gökce, Continuous multigram nanoparticle synthesis by high-power, high-repetition-rate ultrafast laser ablation in liquids, *Opt. Lett.* 41 (2016) 1486–1489, doi.org/10.1364/OL.41.010486.
- [169] R. Streubel, G. Bendt, B. Gökce, Pilot-scale synthesis of metal nanoparticles by high-speed pulsed laser ablation in liquids, *Nanotechnology.* 27 (2016) 205602, doi.org/10.1088/0957-4484/27/20/205602.
- [170] S. Kohsakowski, F. Seiser, J.P. Wiederrecht, S. Reichenberger, T. Vinnay, S. Barcikowski, G. Marzun, Effective size separation of laser-generated, surfactant-free nanoparticles by continuous centrifugation, *Nanotechnology.* 31 (2020), doi.org/10.1088/1361-6528/ab55bd.
- [171] S. Jendrzej, B. Gökce, M. Epple, S. Barcikowski, How Size Determines the Value of Gold: Economic Aspects of Wet Chemical and Laser-Based Metal Colloid Synthesis, *ChemPhysChem.* 18 (2017) 1012–1019, doi.org/10.1002/cphc.201601139.
- [172] B.M. Hunter, J.D. Blakemore, M. Deimund, H.B. Gray, J.R. Winkler, A.M. Müller, Highly active mixed-metal nanosheet water oxidation catalysts made by pulsed-laser ablation in liquids, *J. Am. Chem. Soc.* 136 (2014) 13118–13121, doi.org/10.1021/ja506087h.
- [173] D. Zhang, J. Liu, P. Li, Z. Tian, C. Liang, Recent Advances in Surfactant-Free, Surface-Charged, and Defect-Rich Catalysts Developed by Laser Ablation and Processing in Liquids, *ChemNanoMat.* 3 (2017) 512–533, doi.org/10.1002/cnma.201700079.
- [174] D. Zhang, B. Gökce, Perspective of laser-prototyping nanoparticle-polymer composites, *Appl. Surf. Sci.* 392 (2017) 991–1003, doi.org/10.1016/j.apsusc.2016.09.150.
- [175] J. Xiao, P. Liu, C.X. Wang, G.W. Yang, External field-assisted laser ablation in liquid: An efficient strategy for

- nanocrystal synthesis and nanostructure assembly, *Prog. Mater. Sci.* 87 (2017) 140–220, doi.org/10.1016/j.pmatsci.2017.02.004.
- [176] S. Barcikowski, T. Baranowski, Y. Durmus, U. Wiedwald, B. Gökce, Solid solution magnetic FeNi nanostrand-polymer composites by connecting-coarsening assembly, *J. Mater. Chem. C* 3 (2015) 10699–10704, doi.org/10.1039/C5TC02160J.
- [177] S. Ibrahimkutti, P. Wagener, A. Menzel, A. Plech, S. Barcikowski, Nanoparticle formation in a cavitation bubble after pulsed laser ablation in liquid studied with high time resolution small angle x-ray scattering, *Appl. Phys. Lett.* 101 (2012) 103104, doi.org/10.1063/1.4750250.
- [178] L. Delfour, T.E. Itina, Mechanisms of ultrashort laser-induced fragmentation of metal nanoparticles in liquids: Numerical insights, *J. Phys. Chem. C* 119 (2015) 13893–13900, doi.org/10.1021/acs.jpcc.5b02084.
- [179] C.-Y. Shih, C. Wu, M. V. Shugaev, L. V. Zhigilei, Atomistic modeling of nanoparticle generation in short pulse laser ablation of thin metal films in water, *J. Colloid Interface Sci.* 489 (2016) 3–17, doi.org/10.1016/j.jcis.2016.10.029.
- [180] H. Zeng, X.-W. Du, S.C. Singh, S.A. Kulinich, S. Yang, J. He, W. Cai, Nanomaterials via Laser Ablation/Irradiation in Liquid: A Review, *Adv. Funct. Mater.* 22 (2012) 1333–1353, doi.org/10.1002/adfm.201102295.
- [181] V. Amendola, M. Meneghetti, What controls the composition and the structure of nanomaterials generated by laser ablation in liquid solution?, *Phys. Chem. Chem. Phys.* 15 (2013) 3027–3046, doi.org/10.1039/C2CP42895D.
- [182] B.N. Chichkov, C. Momma, S. Nolte, F. von Alvensleben, A. Tünnermann, Femtosecond, picosecond and nanosecond laser ablation of solids, *Appl. Phys. A Mater. Sci. Process.* 63 (1996) 109–115, doi.org/10.1007/s003390050359.
- [183] K.K. Kim, M. Roy, H. Kwon, J.K. Song, S.M. Park, Laser ablation dynamics in liquid phase: The effects of magnetic field and electrolyte, *J. Appl. Phys.* 117 (2015), doi.org/10.1063/1.4913253.
- [184] J. Lam, D. Amans, C. Dujardin, G. Ledoux, A.R. Allouche, Atomistic Mechanisms for the Nucleation of Aluminum Oxide Nanoparticles, *J. Phys. Chem. A* 119 (2015) 8944–8949, doi.org/10.1021/acs.jpca.5b05829.
- [185] M. Dell’Aglio, R. Gaudiuso, O. De Pascale, A. De Giacomo, Mechanisms and processes of pulsed laser ablation in liquids during nanoparticle production, *Appl. Surf. Sci.* 348 (2015) 4–9, doi.org/10.1016/J.APSUSC.2015.01.082.
- [186] X. Chen, R.-Q. Xu, J.-P. Chen, Z.-H. Shen, L. Jian, X.-W. Ni, Shock-wave propagation and cavitation bubble oscillation by Nd:YAG laser ablation of a metal in water., *Appl. Opt.* 43 (2004) 3251–3257, doi.org/10.1364/AO.43.003251.
- [187] D. Amans, M. Diouf, J. Lam, G. Ledoux, C. Dujardin, Origin of the nano-carbon allotropes in pulsed laser ablation in liquids synthesis, *J. Colloid Interface Sci.* 489 (2017) 114–125, doi.org/10.1016/j.jcis.2016.08.017.
- [188] R. Fabbro, P. Peyre, L. Berthe, X. Scherpereel, Physics and applications of laser-shock processing, *J. Laser Appl.* 10 (1998) 265–279, doi.org/10.2351/1.521861.
- [189] S. Reich, P. Schönfeld, A. Letzel, S. Kohsakowski, M. Olbinado, B. Gökce, S. Barcikowski, A. Plech, Fluence Threshold Behaviour on Ablation and Bubble Formation in Pulsed Laser Ablation in Liquids, *ChemPhysChem* 18 (2017) 1084–1090, doi.org/doi: 10.1002/cphc.201601198.
- [190] H. Oguchi, T. Sakka, Y.H. Ogata, Effects of pulse duration upon the plume formation by the laser ablation of Cu in water, *J. Appl. Phys.* 102 (2007), doi.org/10.1063/1.2759182.
- [191] A. Matsumoto, A. Tamura, A. Kawasaki, T. Honda, P. Gregorčič, N. Nishi, K.I. Amano, K. Fukami, T. Sakka, Comparison of the overall temporal behavior of the bubbles produced by short- and long-pulse nanosecond laser ablations in water using a laser-beam-transmission probe, *Appl. Phys. A Mater. Sci. Process.* 122 (2016), doi.org/10.1007/s00339-016-9755-x.
- [192] R. Tanabe, T.T.P. Nguyen, T. Sugiura, Y. Ito, Bubble dynamics in metal nanoparticle formation by laser ablation in liquid studied through high-speed laser stroboscopic videography, *Appl. Surf. Sci.* 351 (2015) 327–331, doi.org/10.1016/j.apsusc.2015.05.030.
- [193] T. Tsuji, D.-H. Thang, Y. Okazaki, M. Nakanishi, Y. Tsuboi, M. Tsuji, Preparation of silver nanoparticles by laser ablation in polyvinylpyrrolidone solutions, *Appl. Surf. Sci.* 254 (2008) 5224–5230, doi.org/10.1016/j.apsusc.2008.02.048.
- [194] J. Lam, J. Lombard, C. Dujardin, G. Ledoux, S. Merabia, D. Amans, Dynamical study of bubble expansion following laser ablation in liquids, *Appl. Phys. Lett.* 108 (2016) 074104, doi.org/10.1063/1.4942389.
- [195] S. Reich, P. Schönfeld, P. Wagener, A. Letzel, S. Ibrahimkutti, B. Gökce, S. Barcikowski, A. Menzel, T. dos Santos Rolo, A. Plech, Pulsed laser ablation in liquids: Impact of the bubble dynamics on particle formation, *J. Colloid Interface Sci.* 489 (2017) 106–113, doi.org/10.1016/j.jcis.2016.08.030.
- [196] N. Dabir-Moghaddam, Z. Liu, B. Wu, Modeling of the shrinking process of a bubble induced by laser metal ablation in water and experimental verification, *J. Appl. Phys.* 121 (2017) 044908, doi.org/10.1063/1.4973621.
- [197] K. Sasaki, T. Nakano, W. Soliman, N. Takada, Effect of Pressurization on the Dynamics of a Cavitation Bubble Induced by Liquid-Phase Laser Ablation, *Appl. Phys. Express* 2 (2009) 046501, doi.org/10.1143/APEX.2.046501.
- [198] A. De Giacomo, M. Dell’Aglio, A. Santagata, R. Gaudiuso, O. De Pascale, P. Wagener, G.C. Messina, G. Compagnini, S. Barcikowski, Cavitation dynamics of laser ablation of bulk and wire-shaped metals in water during nanoparticles production, *Phys. Chem. Chem. Phys.* 15 (2013) 3083–3092, doi.org/10.1039/C2CP42649H.
- [199] N. Takada, A. Fujikawa, K. Sasaki, Control of plasma and cavitation bubble in liquid-phase laser ablation using supersonic waves, *Jpn. J. Appl. Phys.* 50 (2011) 126201, doi.org/10.1143/JJAP.50.126201.

- [200] A. Tamura, A. Matsumoto, K. Fukami, N. Nishi, T. Sakka, Simultaneous observation of nascent plasma and bubble induced by laser ablation in water with various pulse durations, *J. Appl. Phys.* 117 (2015) 173304, doi.org/10.1063/1.4919729.
- [201] A. Letzel, B. Gökce, P. Wagener, S. Ibrahimkutty, A. Menzel, A. Plech, S. Barcikowski, Size Quenching during Laser Synthesis of Colloids Happens Already in the Vapor Phase of the Cavitation Bubble, *J. Phys. Chem. C* 121 (2017) 5356–5365, doi.org/10.1021/acs.jpcc.6b12554.
- [202] M. Tiberi, A. Simonelli, G. Cristoforetti, P. Marsili, F. Giammanco, E. Giorgetti, Effect of picosecond laser induced cavitation bubbles generated on Au targets in a nanoparticle production set-up, *Appl. Phys. A Mater. Sci. Process.* 110 (2013) 857–861, doi.org/10.1007/s00339-012-7165-2.
- [203] C.Y. Shih, R. Streubel, J. Heberle, A. Letzel, M. V. Shugaev, C. Wu, M. Schmidt, B. Gökce, S. Barcikowski, L. V. Zhigilei, Two mechanisms of nanoparticle generation in picosecond laser ablation in liquids: The origin of the bimodal size distribution, *Nanoscale* 10 (2018) 6900–6910, doi.org/10.1039/c7nr08614h.
- [204] J. Tomko, J.J. Naddeo, R. Jimenez, Y. Tan, M. Steiner, J.M. Fitz-Gerald, D.M. Bubb, S.M. O'Malley, Size and polydispersity trends found in gold nanoparticles synthesized by laser ablation in liquids, *Phys. Chem. Chem. Phys.* 17 (2015) 16327–16333, doi.org/10.1039/C5CP01965F.
- [205] S. Ibrahimkutty, P. Wagener, T.D.S. Rolo, D. Karpov, A. Menzel, T. Baumbach, S. Barcikowski, A. Plech, A hierarchical view on material formation during pulsed-laser synthesis of nanoparticles in liquid, *Sci. Rep.* 5 (2015) 16313, doi.org/10.1038/srep16313.
- [206] N. Lasemi, U. Pacher, L. V. Zhigilei, O. Bomati-Miguel, R. Lahoz, W. Kautek, Pulsed laser ablation and incubation of nickel, iron and tungsten in liquids and air, *Appl. Surf. Sci.* 433 (2018) 772–779, doi.org/10.1016/j.apsusc.2017.10.082.
- [207] S. Kohsakowski, B. Gökce, R. Tanabe, P. Wagener, A. Plech, Y. Ito, S. Barcikowski, Target geometry and rigidity determines laser-induced cavitation bubble transport and nanoparticle productivity – a high-speed videography study, *Phys. Chem. Chem. Phys.* 18 (2016) 16585–16593, doi.org/10.1039/C6CP01232A.
- [208] W. Soliman, T. Nakano, N. Takada, K. Sasaki, Modification of Rayleigh-Plesset theory for reproducing dynamics of cavitation bubbles in liquid-phase laser ablation, *Jpn. J. Appl. Phys.* 49 (2010), doi.org/10.1143/JJAP.49.116202.
- [209] F. Hegedus, S. Koch, W. Garen, Z. Pandula, G. Paál, L. Kullmann, U. Teubner, The effect of high viscosity on compressible and incompressible Rayleigh-Plesset-type bubble models, *Int. J. Heat Fluid Flow* 42 (2013) 200–208, doi.org/10.1016/j.ijheatfluidflow.2013.04.004.
- [210] K.L. De Graaf, I. Penesis, P.A. Brandner, Comparison of the Rayleigh-Plesset and Gilmore equations and additional aspects for the modelling of seismic airgun bubble dynamics, *Proc. 18th Australas. Fluid Mech. Conf. AFMC 2012* (2012) 3–6.
- [211] A. Letzel, M. Santoro, J. Frohleiks, A.R. Ziefuß, S. Reich, A. Plech, E. Fazio, F. Neri, S. Barcikowski, B. Gökce, How the re-irradiation of a single ablation spot affects cavitation bubble dynamics and nanoparticles properties in laser ablation in liquids, *Appl. Surf. Sci.* 473 (2019) 828–837, doi.org/10.1016/j.apsusc.2018.12.025.
- [212] S. Reich, A. Letzel, B. Gökce, A. Menzel, S. Barcikowski, A. Plech, Incubation Effect of Pre-Irradiation on Bubble Formation and Ablation in Laser Ablation in Liquids, *ChemPhysChem* 20 (2019) 1036–1043, doi.org/10.1002/cphc.201900075.
- [213] A. De Giacomo, A. De Bonis, M. Dell'Aglio, O. De Pascale, R. Gaudioso, S. Orlando, A. Santagata, G.S. Senesi, F. Taccogna, R. Teghil, Laser Ablation of Graphite in Water in a Range of Pressure from 1 to 146 atm Using Single and Double Pulse Techniques for the Production of Carbon Nanostructures, *J. Phys. Chem. C* 115 (2011) 5123–5130, doi.org/10.1021/jp109389c.
- [214] J. Tomko, S.M.O. Malley, C. Trout, J.J. Naddeo, R. Jimenez, J.C. Gripenburg, W. Soliman, D.M. Bubb, Colloids and Surfaces A: Physicochemical and Engineering Aspects Cavitation bubble dynamics and nanoparticle size distributions in laser ablation in liquids, *Colloids Surfaces A Physicochem. Eng. Asp.* 522 (2017) 368–372, doi.org/10.1016/j.colsurfa.2017.03.030.
- [215] C. Lechner, W. Lauterborn, M. Koch, R. Mettin, Fast, thin jets from bubbles expanding and collapsing in extreme vicinity to a solid boundary: A numerical study, *Phys. Rev. Fluids* 4 (2019) 021601, doi.org/10.1103/PhysRevFluids.4.021601.
- [216] M. Koch, C. Lechner, F. Reuter, K. Köhler, R. Mettin, W. Lauterborn, Numerical modeling of laser generated cavitation bubbles with the finite volume and volume of fluid method, using OpenFOAM, *Comput. Fluids* 126 (2016) 71–90, doi.org/10.1016/j.compfluid.2015.11.008.
- [217] S.R. Gonzalez Avila, C. Song, C.D. Ohl, Fast transient microjets induced by hemispherical cavitation bubbles, *J. Fluid Mech.* 767 (2015) 31–51, doi.org/10.1017/jfm.2015.33.
- [218] S. Reich, A. Letzel, A. Menzel, N. Kretschmar, B. Gökce, S. Barcikowski, A. Plech, Early appearance of crystalline nanoparticles in pulsed laser ablation in liquids dynamics, *Nanoscale* 11 (2019) 6962–6969, doi.org/10.1039/c9nr01203f.
- [219] A. Kanitz, M.R. Kalus, E.L. Gurevich, A. Ostendorf, S. Barcikowski, D. Amans, Review on experimental and theoretical investigations of the early stage, femtoseconds to microseconds processes during laser ablation in liquid-phase for the synthesis of colloidal nanoparticles, *Plasma Sources Sci. Technol.* 28 (2019) 1–21, doi.org/10.1088/1361-

- 6595/ab3dbe.
- [220] M.R. Kalus, V. Reimer, S. Barcikowski, B. Gökce, Discrimination of effects leading to gas formation during pulsed laser ablation in liquids, *Appl. Surf. Sci.* 465 (2019) 1096–1102, doi.org/10.1016/j.apsusc.2018.09.224.
- [221] M.-R. Kalus, R. Lanyumba, N. Lorenzo-Parodi, M.A. Jochmann, K. Kerpen, U. Hagemann, T.C. Schmidt, S. Barcikowski, B. Gökce, Determining the role of redox-active materials during laser-induced water decomposition, *Phys. Chem. Chem. Phys.* 21 (2019) 18636–18651, doi.org/10.1039/c9cp02663k.
- [222] M.R. Kalus, N. Bärsch, R. Streubel, E. Gökce, S. Barcikowski, B. Gökce, How persistent microbubbles shield nanoparticle productivity in laser synthesis of colloids - Quantification of their volume, dwell dynamics, and gas composition, *Phys. Chem. Chem. Phys.* 19 (2017) 7112–7123, doi.org/10.1039/c6cp07011f.
- [223] T. Schmitz, U. Wiedwald, C. Dubs, B. Gökce, Ultrasmall Yttrium Iron Garnet Nanoparticles with High Coercivity at Low Temperature Synthesized by Laser Ablation and Fragmentation of Pressed Powders, *ChemPhysChem*. 18 (2017) 1125–1132, doi.org/10.1002/cphc.201601183.
- [224] T. Sasaki, Y. Shimizu, N. Koshizaki, Preparation of metal oxide-based nanomaterials using nanosecond pulsed laser ablation in liquids, *J. Photochem. Photobiol. A Chem.* 182 (2006) 335–341, doi.org/10.1016/j.jphotochem.2006.05.031.
- [225] K. V. Anikin, N.N. Melnik, A. V. Simakin, G.A. Shafeev, V. V. Voronov, A.G. Vitukhnovsky, Formation of ZnSe and CdS quantum dots via laser ablation in liquids, *Chem. Phys. Lett.* 366 (2002) 357–360, doi.org/10.1016/S0009-2614(02)01534-8.
- [226] D. Amans, C. Malaterre, M. Diouf, C. Mancini, F. Chaput, G. Ledoux, G. Breton, Y. Guillin, C. Dujardin, K. Masenelli-Varlot, P. Perriat, Synthesis of Oxide Nanoparticles by Pulsed Laser Ablation in Liquids Containing a Complexing Molecule: Impact on Size Distributions and Prepared Phases, *J. Phys. Chem. C*. 115 (2011) 5131–5139, doi.org/10.1021/jp109387e.
- [227] H. Wang, O. Odawara, H. Wada, Facile and Chemically Pure Preparation of YVO₄: Eu³⁺ + Colloid with Novel Nanostructure via Laser Ablation in Water, *Sci. Rep.* 6 (2016), doi.org/10.1038/srep20507.
- [228] H. Kobayashi, K. Fujii, Surface modification of Y₂O₃:Er, Yb upconversion nanoparticles prepared by laser ablation in water, *Jpn. J. Appl. Phys.* 04 (2014) 05FK04. <http://iopscience.iop.org/1347-4065/53/5S1/05FK04>.
- [229] A.A. Salim, N. Bidin, S.K. Ghoshal, S. Islam, H. Bakhtiar, Synthesis of truncated tetrahedral cinnamon nanoparticles in citric acid media via PLAL technique, *Mater. Lett.* 217 (2018) 267–270, doi.org/10.1016/j.matlet.2018.01.103.
- [230] A.A. Salim, N. Bidin, A.S. Lafi, F.Z. Huyop, Antibacterial activity of PLAL synthesized nanocinnamon, *Mater. Des.* 132 (2017) 486–495, doi.org/10.1016/j.matdes.2017.07.014.
- [231] J. Zhang, D.N. Oko, S. Garbarino, R. Imbeault, M. Chaker, A.C. Tavares, D. Guay, D. Ma, Preparation of PtAu alloy colloids by laser ablation in solution and their characterization, *J. Phys. Chem. C*. 116 (2012) 13413–13420, doi.org/10.1021/jp302485g.
- [232] A. Neumeister, J. Jakobi, C. Rehbock, J. Moysig, S. Barcikowski, Monophasic ligand-free alloy nanoparticle synthesis determinants during pulsed laser ablation of bulk alloy and consolidated microparticles in water, *Phys. Chem. Chem. Phys.* 16 (2014) 23671–23678, doi.org/10.1039/C4CP03316G.
- [233] F. Waag, Y. Li, A.R. Ziefuß, E. Bertin, M. Kamp, V. Duppel, G. Marzun, L. Kienle, S. Barcikowski, B. Gökce, Kinetically-controlled laser-synthesis of colloidal high-entropy alloy nanoparticles, *RSC Adv.* 9 (2019) 18547–18558, doi.org/10.1039/c9ra03254a.
- [234] R. Nadarajah, S. Barcikowski, B. Gökce, Picosecond laser-induced surface structures on alloys in liquids and their influence on nanoparticle productivity during laser ablation, *Opt. Express.* 28 (2020) 2909, doi.org/10.1364/oe.28.002909.
- [235] V. Amendola, S. Polizzi, M. Meneghetti, Free silver nanoparticles synthesized by laser ablation in organic solvents and their easy functionalization, *Langmuir.* 23 (2007) 6766–6770, doi.org/10.1021/la0637061.
- [236] T. Iwamoto, T. Ishigaki, Fabrication of iron oxide nanoparticles using laser ablation in liquids, *J. Phys. Conf. Ser.* 441 (2013), doi.org/10.1088/1742-6596/441/1/012034.
- [237] N. V Tarasenko, A. V Butsen, A.A. Nevar, Laser ablation of gadolinium targets in liquids for nanoparticle preparation, *Appl. Phys. A*. 93 (2008) 837–841, doi.org/10.1007/s00339-008-4737-2.
- [238] A. Chemin, J. Lam, G. Laurens, F. Trichard, V. Motto-Ros, G. Ledoux, V. Jarý, V. Laguta, M. Nikl, C. Dujardin, D. Amans, Doping nanoparticles using pulsed laser ablation in a liquid containing the doping agent, *Nanoscale Adv.* (2019), doi.org/10.1039/C9NA00223E.
- [239] A. Letzel, S. Reich, T. Dos Santos Rolo, A. Kanitz, J. Hoppius, A. Rack, M.P. Olbinado, A. Ostendorf, B. Gökce, A. Plech, S. Barcikowski, Time and Mechanism of Nanoparticle Functionalization by Macromolecular Ligands during Pulsed Laser Ablation in Liquids, *Langmuir.* 35 (2019) 3038–3047, doi.org/10.1021/acs.langmuir.8b01585.
- [240] H. Usui, Y. Shimizu, T. Sasaki, N. Koshizaki, Photoluminescence of ZnO nanoparticles prepared by laser ablation in different surfactant solutions., *J. Phys. Chem. B*. 109 (2005) 120–124, doi.org/10.1021/jp046747j.
- [241] A. Essaidi, M. Chakif, B. Schöps, A. Aumman, S. Xiao, C. Esen, A. Ostendorf, Size control of gold nanoparticles during laser ablation in liquids with different functional molecules, *J. Laser Micro Nanoeng.* 8 (2013) 131–136, doi.org/10.2961/jlmn.2013.02.0003.
- [242] R.M. Tilaki, A. Irajizad, S.M. Mahdavi, Stability, size and optical properties of silver nanoparticles prepared by laser

- ablation in different carrier media, *Appl. Phys. A Mater. Sci. Process.* 84 (2006) 215–219, doi.org/10.1007/s00339-006-3604-2.
- [243] A. Baladi, R. Sarraf Mamooory, Investigation of different liquid media and ablation times on pulsed laser ablation synthesis of aluminum nanoparticles, *Appl. Surf. Sci.* 256 (2010) 7559–7564, doi.org/10.1016/j.apsusc.2010.05.103.
- [244] P. Boyer, M. Meunier, Modeling solvent influence on growth mechanism of nanoparticles (Au, Co) synthesized by surfactant free laser processes, *J. Phys. Chem. C.* 116 (2012) 8014–8019, doi.org/10.1021/jp2092994.
- [245] S. Barcikowski, A. Menéndez-Manjón, B. Chichkov, M. Brikas, G. Račiukaitis, Generation of nanoparticle colloids by picosecond and femtosecond laser ablations in liquid flow, *Appl. Phys. Lett.* 91 (2007) 083113, doi.org/10.1063/1.2773937.
- [246] C.L. Sajti, A. Barchanski, P. Wagener, S. Klein, S. Barcikowski, Delay Time and Concentration Effects During Bioconjugation of Nanosecond Laser-Generated Nanoparticles in a Liquid Flow, *J. Phys. Chem. C.* 115 (2011) 5094–5101, doi.org/10.1021/jp1093405.
- [247] A. Pyatenko, H. Wang, N. Koshizaki, T. Tsuji, Mechanism of pulse laser interaction with colloidal nanoparticles, *Laser Photonics Rev.* 7 (2013) 596–604, doi.org/10.1002/lpor.201300013.
- [248] M. Lau, S. Reichenberger, I. Haxhijaj, S. Barcikowski, A.M. Müller, Mechanism of Laser-Induced Bulk and Surface Defect Generation in ZnO and TiO₂ Nanoparticles: Effect on Photoelectrochemical Performance, *ACS Appl. Energy Mater.* 1 (2018) 5366–5385, doi.org/10.1021/acsaem.8b00977.
- [249] A.R. Ziefuß, S. Reichenberger, C. Rehbock, I. Chakraborty, M. Gharib, W.J. Parak, S. Barcikowski, Laser Fragmentation of Colloidal Gold Nanoparticles with High-Intensity Nanosecond Pulses is Driven by a Single-Step Fragmentation Mechanism with a Defined Educt Particle-Size Threshold, *J. Phys. Chem. C.* 122 (2018) 22125–22136, doi.org/10.1021/acs.jpcc.8b04374.
- [250] A. Menéndez-Manjón, S. Barcikowski, Hydrodynamic size distribution of gold nanoparticles controlled by repetition rate during pulsed laser ablation in water, *Appl. Surf. Sci.* 257 (2011) 4285–4290, doi.org/10.1016/j.apsusc.2010.12.037.
- [251] Y. Ishikawa, N. Koshizaki, A. Pyatenko, Submicrometer-Sized Spherical Iron Oxide Particles Fabricated by Pulsed Laser Melting in Liquid, *Electron. Commun. Japan.* 99 (2016) 37–42, doi.org/10.1002/ecj.11898.
- [252] T. Tsuji, Y. Higashi, M. Tsuji, H. Fujiwara, Y. Ishikawa, N. Koshizaki, Fabrication of spherical-shaped submicron particles of ZnO using laser-induced melting of submicron-sized source materials, *J. Laser Micro Nanoeng.* 8 (2013) 292–295, doi.org/10.2961/jlmn.2013.03.0017.
- [253] S.-L. Hu, K.-Y. Niu, J. Sun, J. Yang, N.-Q. Zhao, X.-W. Du, One-step synthesis of fluorescent carbon nanoparticles by laser irradiation, *J. Mater. Chem.* 19 (2009) 484–488, doi.org/10.1039/B812943F.
- [254] V. Nguyen, L. Yan, J. Si, X. Hou, Femtosecond laser-induced size reduction of carbon nanodots in solution: Effect of laser fluence, spot size, and irradiation time, *J. Appl. Phys.* 117 (2015), doi.org/10.1063/1.4909506.
- [255] C. Doñate-Buendia, R. Torres-Mendieta, A. Pyatenko, E. Falomir, M. Fernández-Alonso, G. Mínguez-Vega, Fabrication by Laser Irradiation in a Continuous Flow Jet of Carbon Quantum Dots for Fluorescence Imaging, *ACS Omega.* 3 (2018) 2735–2742, doi.org/10.1021/acsomega.7b02082.
- [256] W. Ding, J.P. Sylvestre, E. Bouvier, G. Leclair, M. Meunier, Ultrafast laser processing of drug particles in water for pharmaceutical discovery, *Appl. Phys. A Mater. Sci. Process.* 114 (2014) 267–276, doi.org/10.1007/s00339-013-8089-1.
- [257] M. Lau, S. Barcikowski, Quantification of mass-specific laser energy input converted into particle properties during picosecond pulsed laser fragmentation of zinc oxide and boron carbide in liquids, *Appl. Surf. Sci.* 348 (2015) 22–29, doi.org/10.1016/j.apsusc.2014.07.053.
- [258] F. Waag, B. Göcke, C. Kalapu, G. Bendt, S. Salamon, J. Landers, U. Hagemann, M. Heidelmann, S. Schulz, H. Wende, N. Hartmann, M. Behrens, S. Barcikowski, Adjusting the catalytic properties of cobalt ferrite nanoparticles by pulsed laser fragmentation in water with defined energy dose, *Sci. Rep.* 7 (2017) 1–13, doi.org/10.1038/s41598-017-13333-zf.
- [259] S.H. Stelzig, C. Menneking, M.S. Hoffmann, K. Eisele, S. Barcikowski, M. Klapper, K. Müllen, Compatibilization of laser generated antibacterial Ag- and Cu-nanoparticles for perfluorinated implant materials, *Eur. Polym. J.* 47 (2011) 662–667, doi.org/10.1016/j.eurpolymj.2010.10.018.
- [260] F.H. Zhang, Z.C. Zhang, C.J. Luo, I.T. Lin, Y. Liu, J. Leng, S.K. Smoukov, Remote, fast actuation of programmable multiple shape memory composites by magnetic fields, *J. Mater. Chem. C.* 3 (2015) 11290–11293, doi.org/10.1039/c5tc02464a.
- [261] L. Jonušauskas, M. Lau, P. Gruber, B. Göcke, S. Barcikowski, M. Malinauskas, A. Ovsianikov, Plasmon assisted 3D microstructuring of gold nanoparticle-doped polymers, *Nanotechnology.* 27 (2016) 154001, doi.org/10.1088/0957-4484/27/15/154001.
- [262] M. Lau, R.G. Niemann, M. Bartsch, W. O'Neill, S. Barcikowski, Near-field-enhanced, off-resonant laser sintering of semiconductor particles for additive manufacturing of dispersed Au-ZnO-micro/nano hybrid structures, *Appl. Phys. A Mater. Sci. Process.* 114 (2014) 1023–1030, doi.org/10.1007/s00339-014-8270-1.
- [263] H.W. Tan, J. An, C.K. Chua, T. Tran, Metallic Nanoparticle Inks for 3D Printing of Electronics, *Adv. Electron. Mater.* 5 (2019), doi.org/10.1002/aelm.201800831.

- [264] T. Hupfeld, G. Laurens, S. Merabia, S. Barcikowski, B. Gökce, D. Amans, Dynamics of laser-induced cavitation bubbles at a solid-liquid interface in high viscosity and high capillary number regimes, *J. Appl. Phys.* 127 (2020), doi.org/10.1063/1.5116111.
- [265] T. Hupfeld, F. Stein, S. Barcikowski, B. Gökce, U. Wiedwald, Manipulation of the size and phase composition of yttrium iron garnet nanoparticles by pulsed laser post-processing in liquid, *Molecules.* 25 (2020), doi.org/10.3390/molecules25081869.
- [266] L. Gemini, T. Schmitz, R. Kling, S. Barcikowski, B. Gökce, Upconversion Nanoparticles Synthesized by Ultrashort Pulsed Laser Ablation in Liquid: Effect of the Stabilizing Environment, *ChemPhysChem.* 18 (2017) 1210–1216, doi.org/10.1002/cphc.201601266.
- [267] R. Streubel, M.B. Wilms, C. Doñate-Buendía, A. Weisheit, S. Barcikowski, J.H. Schleifenbaum, B. Gökce, Depositing laser-generated nanoparticles on powders for additive manufacturing of oxide dispersed strengthened alloy parts via laser metal deposition, *Jpn. J. Appl. Phys.* 57 (2018), doi.org/10.7567/JJAP.57.040310.
- [268] T. Hupfeld, T. Laumer, T. Stichel, T. Schuffenhauer, J. Heberle, M. Schmidt, S. Barcikowski, B. Gökce, A new approach to coat PA12 powders with laser-generated nanoparticles for selective laser sintering, *Procedia CIRP.* 74 (2018) 244–248, doi.org/10.1016/j.procir.2018.08.103.
- [269] K.L. Kelly, E. Coronado, L.L. Zhao, G.C. Schatz, The optical properties of metal nanoparticles: The influence of size, shape, and dielectric environment, *J. Phys. Chem. B.* 107 (2003) 668–677, doi.org/10.1021/jp026731y.
- [270] T. Hupfeld, A. Sommereyns, T. Schuffenhauer, E. Zhuravlev, M. Krebs, S. Gann, O. Keßler, M. Schmidt, B. Gökce, S. Barcikowski, How colloidal surface additivation of polyamide 12 powders with well-dispersed silver nanoparticles influences the crystallization already at low 0.01 vol%, *Addit. Manuf.* 36 (2020) 101419, doi.org/10.1016/j.addma.2020.101419.
- [271] T. Hupfeld, C. Doñate-Buendía, M. Krause, A. Sommereyns, A. Wegner, T. Sinnemann, M. Schmidt, B. Gökce, S. Barcikowski, Scaling up colloidal surface additivation of polymer powders for laser powder bed fusion, *Procedia CIRP* 94, (2020) 110–115, doi.org/10.1016/j.procir.2020.09.022
- [272] T. Hupfeld, A. Wegner, M. Blanke, C. Doñate-Buendía, V. Sharov, S. Nieskens, M. Piechotta, M. Giese, S. Barcikowski, B. Gökce, Plasmonic Seasoning: Giving Color to Desktop Laser 3D Printed Polymers by Highly Dispersed Nanoparticles, *Adv. Opt. Mater.* 2000473 (2020), doi.org/10.1002/adom.202000473.
- [273] S. Fusco, M.S. Sakar, S. Kennedy, C. Peters, R. Bottani, F. Starsich, A. Mao, G.A. Sotiriou, S. Pané, S.E. Pratsinis, D. Mooney, B.J. Nelson, An integrated microrobotic platform for on-demand, targeted therapeutic interventions, *Adv. Mater.* 26 (2014) 952–957, doi.org/10.1002/adma.201304098.
- [274] C. Huber, C. Abert, F. Bruckner, M. Groenefeld, O. Muthsam, S. Schuschnigg, K. Sirak, R. Thanhoffer, I. Teliban, C. Vogler, R. Windl, D. Suess, 3D print of polymer bonded rare-earth magnets, and 3D magnetic field scanning with an end-user 3D printer, *Appl. Phys. Lett.* 109 (2016), doi.org/10.1063/1.4964856.
- [275] C. Huber, C. Abert, F. Bruckner, M. Groenefeld, S. Schuschnigg, I. Teliban, C. Vogler, G. Wautischer, R. Windl, Di. Suess, 3D Printing of Polymer-Bonded Rare-Earth Magnets with a Variable Magnetic Compound Fraction for a Predefined Stray Field, *Sci. Rep.* 7 (2017) 1–8, doi.org/10.1038/s41598-017-09864-0.
- [276] C. Abert, C. Huber, F. Bruckner, C. Vogler, G. Wautischer, D. Suess, A fast finite-difference algorithm for topology optimization of permanent magnets, *J. Appl. Phys.* 122 (2017), doi.org/10.1063/1.4998532.
- [277] I. Pastoriza-Santos, C. Kinnear, J. Pérez-Juste, P. Mulvaney, L.M. Liz-Marzán, Plasmonic polymer nanocomposites, *Nat. Rev. Mater.* 3 (2018) 375–391, doi.org/10.1038/s41578-018-0050-7.
- [278] M. Wei, Y. Gao, X. Li, M.J. Serpe, Stimuli-responsive polymers and their applications, *Polym. Chem.* 8 (2017) 127–143, doi.org/10.1039/c6py01585a.
- [279] I. Willner, Stimuli-Controlled Hydrogels and Their Applications, *Acc. Chem. Res.* 50 (2017) 657–658, doi.org/10.1021/acs.accounts.7b00142.
- [280] S.K. Ghosh, T. Pal, Interparticle coupling effect on the surface plasmon resonance of gold nanoparticles: From theory to applications, *Chem. Rev.* 107 (2007) 4797–4862, doi.org/10.1021/cr0680282.
- [281] P. Mulvaney, Surface plasmon spectroscopy of nanosized metal particles, *Langmuir.* 12 (1996) 788–800, doi.org/10.1021/la9502711.
- [282] V. Amendola, O.M. Bakr, F. Stellacci, A study of the surface plasmon resonance of silver nanoparticles by the discrete dipole approximation method: Effect of shape, size, structure, and assembly, *Plasmonics.* 5 (2010) 85–97, doi.org/10.1007/s11468-009-9120-4.
- [283] A. Blaeser, N. Million, D.F.D. Campos, L. Gamrad, M. Köpf, C. Rehbock, M. Nachev, B. Sures, S. Barcikowski, H. Fischer, Laser-based in situ embedding of metal nanoparticles into bioextruded alginate hydrogel tubes enhances human endothelial cell adhesion, *Nano Res.* 9 (2016) 3407–3427, doi.org/10.1007/s12274-016-1218-3.
- [284] S. Klein, S. Petersen, U. Taylor, D. Rath, S. Barcikowski, Quantitative visualization of colloidal and intracellular gold nanoparticles by confocal microscopy, *J. Biomed. Opt.* 15 (2010) 036015, doi.org/10.1117/1.3461170.
- [285] T. Hupfeld, A. Sommereyns, F. Riahi, C. Doñate-Buendía, M.S. S. Gann, B. Gökce, S. Barcikowski, Analysis of the nanoparticle dispersion and its effect on the crystalline microstructure in carbon-additivated PA12 feedstock material for laser powder bed fusion, *Materials (Basel).* 13 (2020) 3312, doi.org/10.3390/ma13153312
- [286] S. Link, Z.L. Wang, M.A. El-Sayed, Alloy formation of gold-silver nanoparticles and the dependence of the plasmon

- absorption on their composition, *J. Phys. Chem. B.* 103 (1999) 3529–3533, doi.org/10.1021/jp990387w.
- [287] C. Rehbock, V. Merk, L. Gamrad, R. Streubel, S. Barcikowski, Size control of laser-fabricated surfactant-free gold nanoparticles with highly diluted electrolytes and their subsequent bioconjugation., *Phys. Chem. Chem. Phys.* 15 (2013) 3057–67, doi.org/10.1039/c2cp42641b.
- [288] A. Schwenke, P. Wagener, A. Weiß, K. Klimenta, H. Wiegel, L. Sajti, S. Barcikowski, Laserbasierte Generierung matrixbinderfreier Nanopartikel-Polymerkomposite für bioactive Medizinprodukte, *Chemie-Ingenieur-Technik.* 85 (2013) 740–746, doi.org/10.1002/cite.201200035.
- [289] K.J. Woo, C.K. Hye, W.K. Ki, S. Shin, H.K. So, H.P. Yong, Antibacterial activity and mechanism of action of the silver ion in *Staphylococcus aureus* and *Escherichia coli*, *Appl. Environ. Microbiol.* 74 (2008) 2171–2178, doi.org/10.1128/AEM.02001-07.
- [290] I. Bayraktar, D. Doganay, S. Coskun, C. Kaynak, G. Akca, H.E. Unalan, 3D printed antibacterial silver nanowire/poly lactide nanocomposites, *Compos. Part B Eng.* 172 (2019) 671–678, doi.org/10.1016/j.compositesb.2019.05.059.

Appendix

A1 Supporting Information: Dynamics of laser-induced cavitation bubbles at a solid-liquid interface in high viscosity and high capillary number regimes

Reproduced from Journal of Applied Physics 127 (2020) 044306, with the permission of AIP Publishing

Available at: doi.org/10.1063/1.5116111

1. Videos

Video_Au_water.avi corresponds to the high-speed imaging of a laser-induced bubble in water and on a gold target. Video_Au_PAO6.avi and video_Au_PAO40.avi show the videos for bubbles in PAO6 and PAO40, respectively. Bubbles videos made using a YIG target are named as the same way: video_YIG_water.avi, video_YIG_PAO6.avi, video_YIG_PAO40.avi refer to bubbles produced in water, PAO6 and PAO40, respectively. All videos start shortly before the laser impact and do not only show the expansion and shrinking of the bubble but also the oscillation after the first collapse. The time between two frames is 4.75 μs , whereas the image size is 3.92x3.92 mm^2 .

2. Error bars

The error bars are deduced from the propagation of uncertainty. As an example, $We = \rho V_t^2 R / \gamma$ is identified to $We \propto \rho R^3 / \gamma t^2$ for the assaying of the propagation of uncertainty. Assuming no uncertainties on the density ρ (weak dependence over the temperature with respect to the dependence of the viscosity) and on the time, it leads to the following standard deviation on We :

$$\sigma_{We} = We \sqrt{9 \frac{\sigma_R^2}{R^2} + \frac{\sigma_Y^2}{\gamma^2}} \quad (S1)$$

The standard deviation on $Re = V_t R / \nu$ is:

$$\sigma_{Re} = Re \sqrt{4 \frac{\sigma_R^2}{R^2} + \frac{\sigma_\nu^2}{\nu^2}} \quad (S2)$$

The standard deviation on $Ca = \rho \nu V_{cl} / \gamma$ is:

$$\sigma_{Ca} = Ca \sqrt{\frac{\sigma_X^2}{X^2} + \frac{\sigma_Y^2}{\gamma^2} + \frac{\sigma_\nu^2}{\nu^2}} \quad (S3)$$

The value of σ_ν / ν is assumed to 30% (see table S1 for the temperature dependence of the kinematic viscosity). The value of σ_Y / γ is assumed to 3% (consistent with an error on the temperature of $\pm 10^\circ\text{C}$). σ_R and σ_X correspond to a half of the resolution of the imaging system previously defined, i.e. 22 μm . In that condition, the error is mainly defined by the uncertainties on the viscosity. The errors bars in figure 3a-c are defined accordingly

Following the propagation of uncertainty, we have estimated an error on the X-axis of the figure 5b, i.e. for $x = \sqrt{\nu \frac{L}{v_e}}$, the standard deviation on x is:

$$\sigma_x = x \sqrt{\frac{1}{4} \frac{\sigma_\nu^2}{\nu^2} + \frac{1}{2} \frac{\sigma_L^2}{L^2}} \quad (S4)$$

The value σ_ν / ν is assumed to 30%. σ_L corresponds to a half of the resolution of the imaging system, i.e. 22 μm .

Table S2: The table displays the kinematic viscosity of the polyalphaolefines used as a function of the temperature (Data from the manufacturer).

Sample	Viscosity Index	Kinematic Viscosity ν		
		Temperature [°C]	ν [mm^2/s]	$\log_{10}(\nu)$
PAO 6	137	100 °C	5.9	0,77
		40 °C	30.5	1,48
		20 °C	80.8	1,91
PAO40	147	100 °C	39.0	1,59
		40 °C	396	2,60
		20°C	764	2,88
		0°C	4840	3,68

3. Absorbance measurements

It is known that volume and lifetime of the cavitation bubble change with the laser fluence [1,2]. Even at the same laser fluence unequal optical properties of the liquids could influence the effective fluence on the target surface. To determine the light extinction by the liquids, a UV-Vis absorbance spectrum is measured for each liquid. The inset of Fig. S1 shows that the absorption remains low for the three solvent at 355 nm. Fig. S1 displays the transmission at 355 nm for each solvent with a liquid layer of 1 cm thickness, as well as the maximum vertical height reached. The transmission is marginally affected by the different solvents. The difference in the absorption cannot explain the maximum volume difference between liquids.

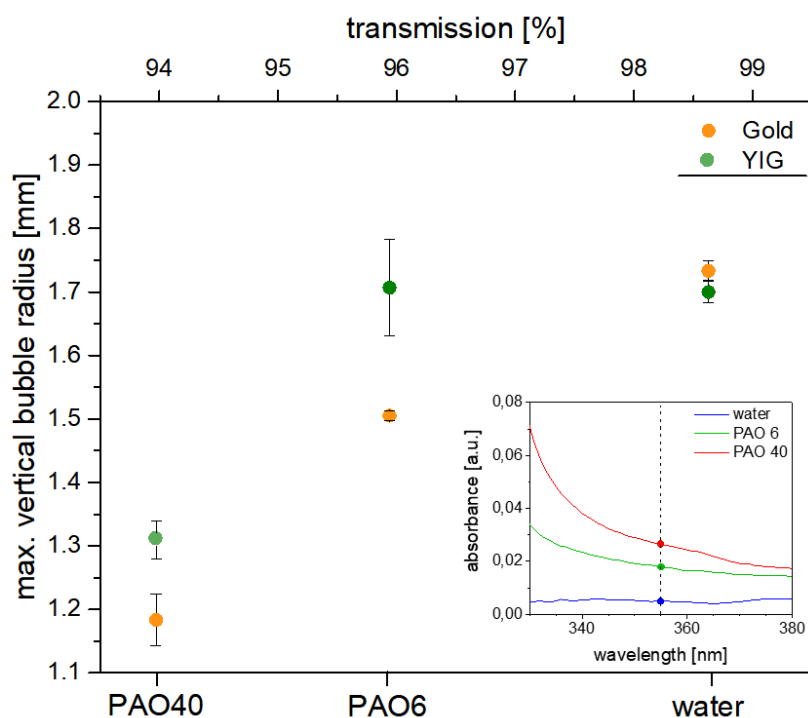


Fig. S1: Maximum vertical bubble radius for the different target-liquid combinations plotted as a function of the fluid and as a function of the absorbance of the corresponding liquid at 355 nm wavelength. The inset shows the UV-Vis spectra of the liquids, highlighting the absorbance at 355 nm wavelength.

4. Calculation of the Rayleigh collapse time

We calculated the theoretical Rayleigh collapse time T_{RCT} from two different maximum radius R_{M}

- Using the measured maximum height of a bubble ($R_{\text{M}} = R_{\text{max}}$).
- Using the equivalent radius of a sphere ($R_{\text{M}} = R_{\text{eq}}$) with the same volume as the measured maximum volume (exact volume in fig. 1d)

$$T_{\text{RCT}} = 1.83R_M \sqrt{\frac{\rho}{P_0}} \quad (\text{S5})$$

ρ is the liquid density and P_0 is the external pressure (101 kPa). Fig. S2 shows that even for shapes which strongly deviate from the hemispherical shape, the maximum bubble height leads to a theoretical Rayleigh collapse time consistent with the measured bubble lifetime (until the first collapse). The bubble height (and its derivative) appears relevant to compute Re and We . Additionally, when looking at the three-phase contact line the footprint radius (and its derivative) is more relevant to compute the capillary number Ca .

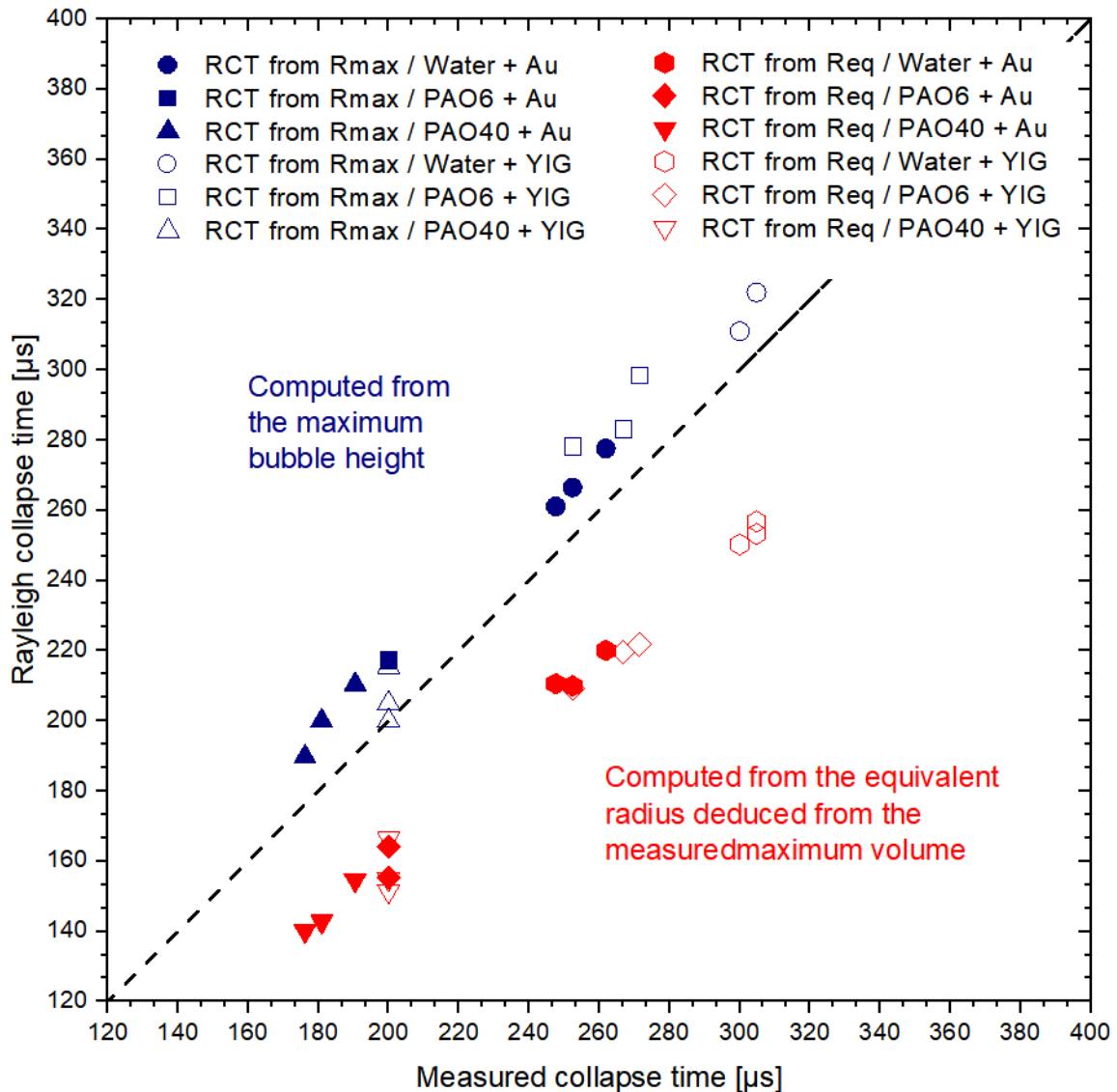


Fig. S2: Rayleigh collapse time vs. the measured collapse time. The dot line corresponds to identity. Values for the Rayleigh collapse time were calculated using the maximum radius of the bubbles (blue) or by using the equivalent radius of a sphere with the same volume (red).

5. Time dependence of the footprint radius

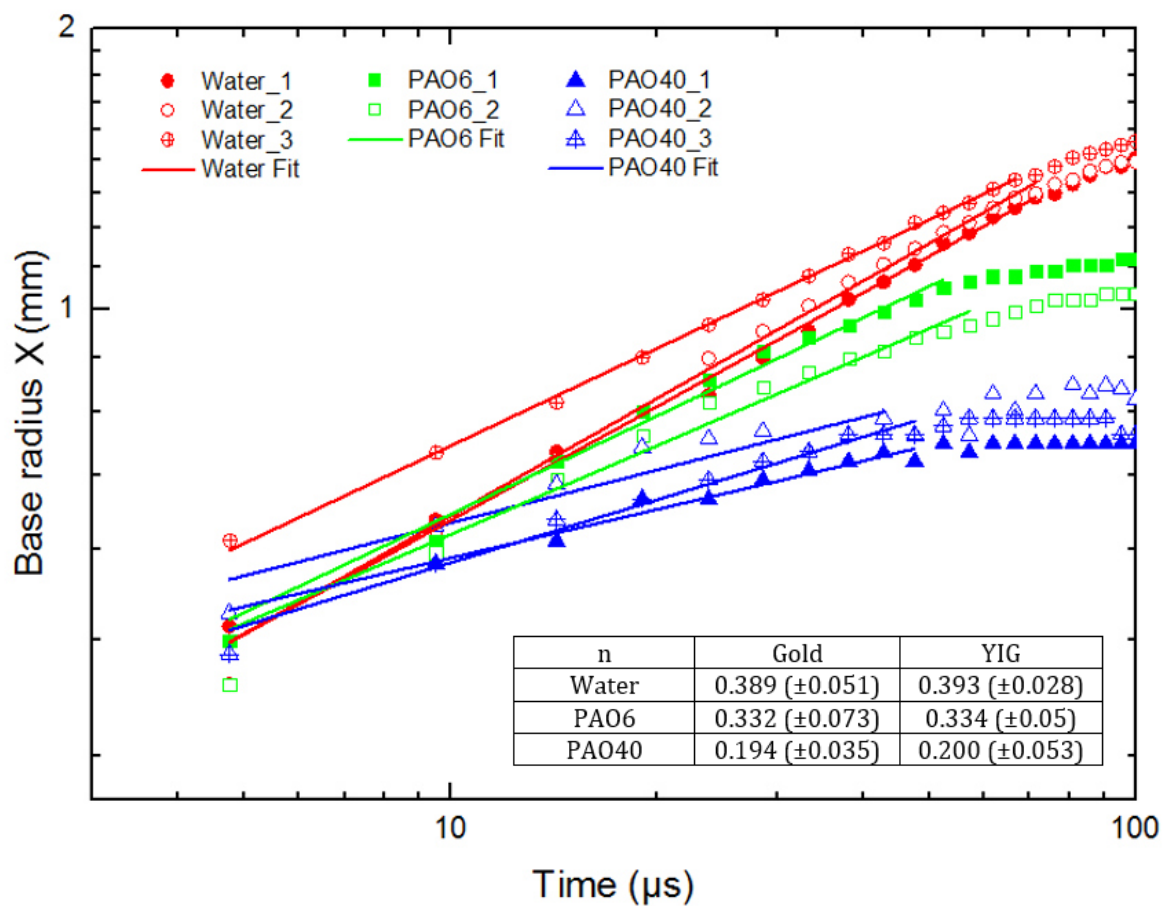


Fig. S3: Time dependence of the footprint radius of bubbles for a gold target in water, PAO6 and PAO40. A fit with a power law $\propto t^n$ of the early expansion of the bubbles (i.e. first quarter of the bubble lifetime) is displayed for a few bubbles in each liquid. The average exponents n for both gold and YIG targets are shown in the table in the inset (see Fig. S5 for YIG target). The values in brackets correspond to the 80% confidence interval according to the Student's t -distribution.

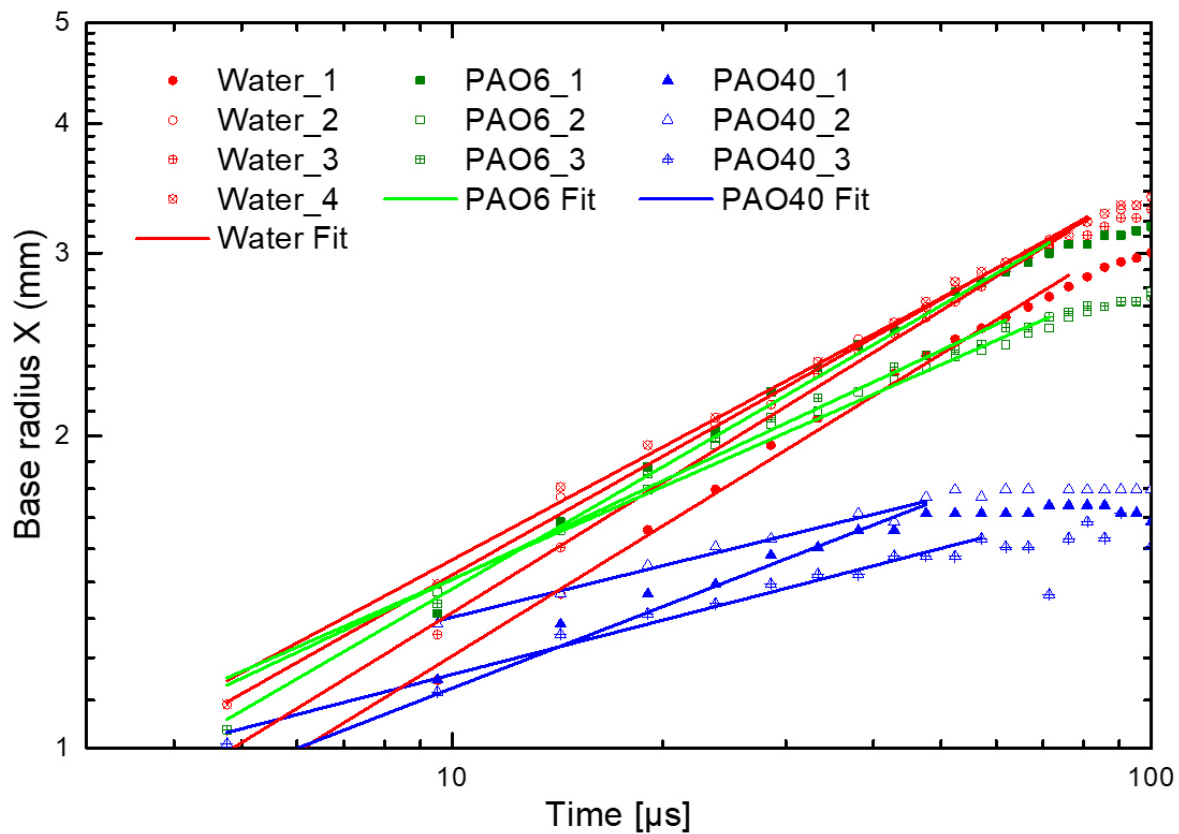


Fig. S4: Time dependence of the footprint radius of bubbles for a YIG target in water, PAO6 and PAO40. A fit with a power law $\propto t^n$ of the early expansion of the bubbles (i.e. first quarter of the bubble lifetime) is displayed for a few bubbles in each liquid.

References

- [1] S. Reich, P. Schönfeld, A. Letzel, S. Kohnsowski, M. Olbinado, B. Gökce, S. Barcikowski, A. Plech, Fluence Threshold Behaviour on Ablation and Bubble Formation in Pulsed Laser Ablation in Liquids, *ChemPhysChem*. 18 (2017) 1084–1090. doi: 10.1002/cphc.201601198.
- [2] S. Kohnsowski, B. Gökce, R. Tanabe, P. Wagener, A. Plech, Y. Ito, S. Barcikowski, Target geometry and rigidity determines laser-induced cavitation bubble transport and nanoparticle productivity – a high-speed videography study, *Phys. Chem. Chem. Phys.* 18 (2016) 16585–16593. doi:10.1039/C6CP01232A.

A2 Supporting Information: Manipulation of the size and magnetic properties of colloidal $\text{Y}_3\text{Fe}_5\text{O}_{12}$ nanoparticles by laser post-processing

Reprinted from *Molecules* 25 (2020) 1869 under CC BY

Available at: doi.org/10.3390/molecules25081869

1. Choice of laser wavelength for LPP

The energy that can be absorbed by a particle is strongly reliant on its wavelength-dependent absorption cross-section σ_{abs}^λ [1].

$$E_{abs} = \frac{E_P}{S_P} \cdot \sigma_{abs}^\lambda = J_P \cdot \sigma_{abs}^\lambda \quad (1)$$

For spherical particles, a relative absorption cross-section Q_{abs}^λ , also known as absorption efficiency, can be calculated with the geometrical cross-section $\frac{\pi \cdot d_p^2}{4}$:

$$Q_{abs}^\lambda = \frac{4 \cdot \sigma_{abs}^\lambda}{\pi \cdot d_p^2} \quad (2)$$

The size- and wavelength-dependent absorption cross-section can be determined by calculating the absorption efficiency using the classical Mie theory. It describes the interaction between a planar electromagnetic wave and a homogeneous sphere [2]. To calculate the absorption efficiency, it is necessary to know the real and imaginary part of the complex refractive index of the material at the respective laser wavelengths. Kahn et al. determined the values experimentally for the complex refractive index of YIG, which are used as a basis for the calculation in this paper [3]. Although there is no general limit for the particle size to be calculated in Mie theory, it should be noted that quantum mechanical effects can play an essential role in particles below 10 nm and must, therefore, be considered. For the sake of simplicity, the smaller particle size is thus set to 10 nm. Figure S1 shows the absorption curves for YIG at three usual laser wavelengths of 1064 nm, 533 nm, and 355 nm. Larger wavelengths can only be efficiently absorbed by large particles, whereas the absorption efficiency for particles below 1000 nm decreases rapidly for 1064 nm. By reducing the wavelength to 532 nm, it is possible that particles down to 300 nm can absorb the energy efficiently. For an efficient fragmentation process, however, it is essential that large amounts of energy can also be

absorbed by particles smaller than 100 nm, which is why a laser with a wavelength of 355 nm is best suited for our study. Using the model of Takami et al.'s "heating melting evaporation" theory, the amount of energy absorbed by a YIG particle of any size can now be calculated [4]. This work has not succeeded in determining the specific enthalpies at each temperature required for the calculations, which is why the curves in (b) provide only trends and no exact values. From the application, it can be concluded that significantly more energy is required for the evaporation and thus the fragmentation of small particles below 100 nm than for larger particles. This confirms the conclusion that the use of a 355 nm wavelength laser is the optimal choice for the fragmentation of small YIG particles.

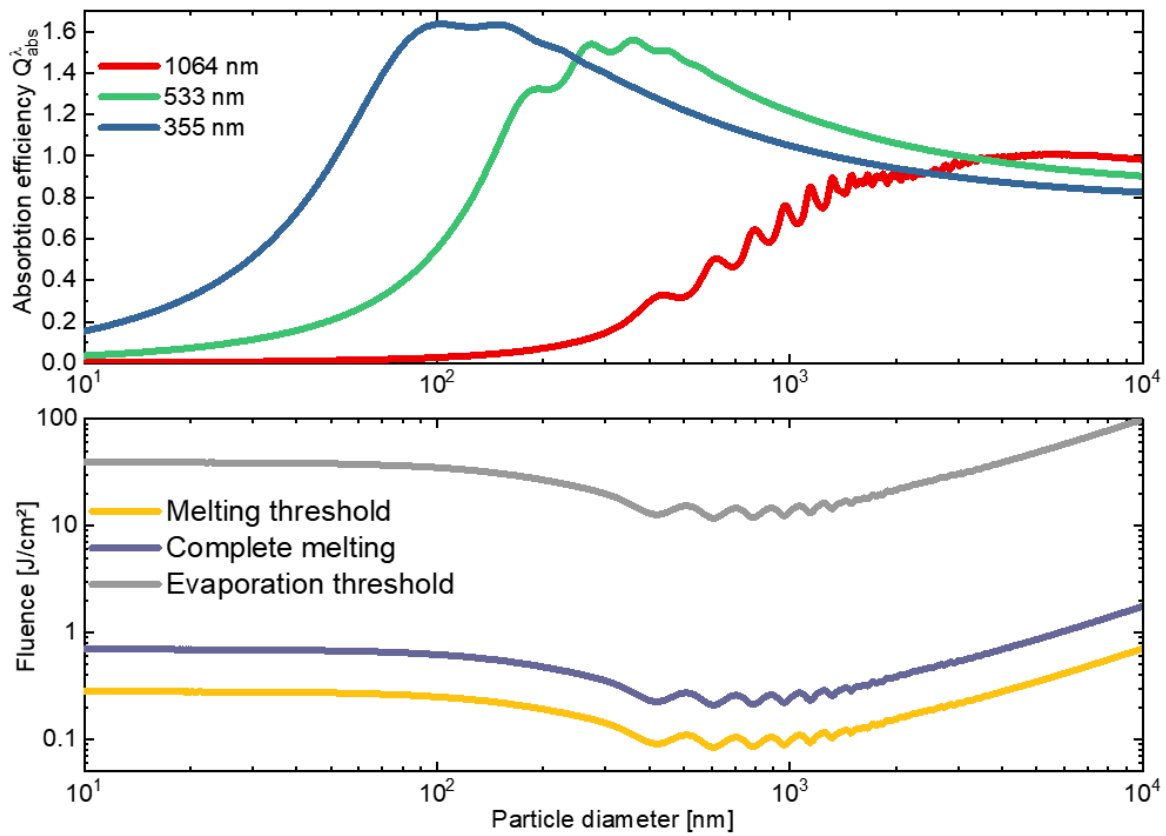


Figure S1: (a) Absorption efficiency Q_{abs}^λ as a function of the particle size, which was calculated using the Mie theory. (b) Estimation of the fluence required for melting particles (yellow line) and evaporate them (gray line), calculated using the "heating-melting-evaporation" model according to Takami et al. [4].

2. Influence of specific energy input on the UV-Vis absorbance ratio between 320 and 800 nm

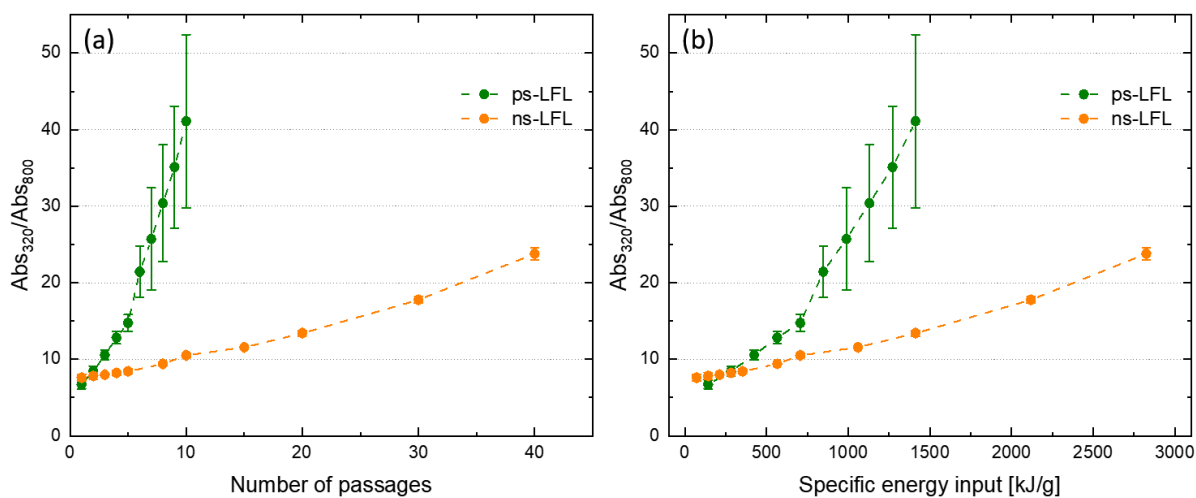


Figure S2: UV-Vis absorbance ratio between 320 and 800 nm as a function of the (a) number of passages during fragmentation and (b) specific energy input in kJ/g which considers, that the ps-laser has twice the pulse energy and total laser power compared to the ns-laser.

3. Furlong slope

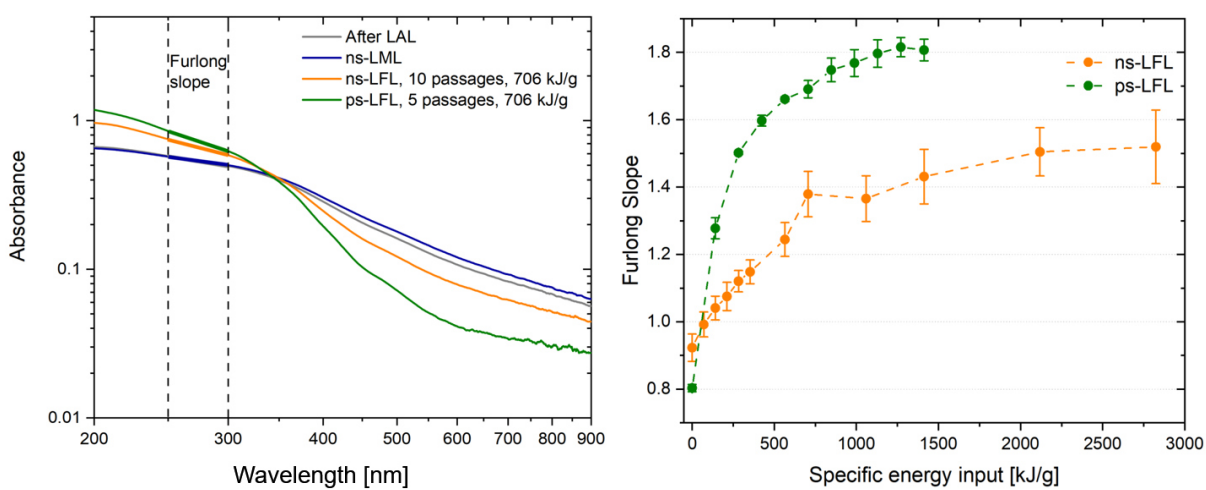


Figure S3: (a) Double logarithmic plot of the UV-Vis absorbance spectra to calculate (b) the Furlong slope from the linear slope between 250 and 300 nm.

4. XRD results after ps-LFL

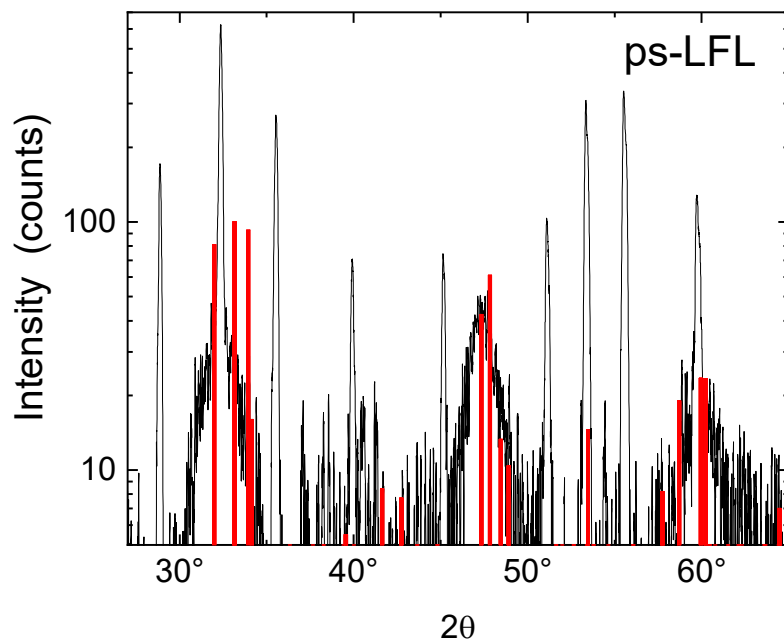


Figure S4: Experimental data of the ps-LFL sample in logarithmic scale together with the YIP reference positions and intensities (JCPDS PDF card 39-1489).

Figure S4 shows that the angular position of the broad features under discussion (32°, 47°, and 60°) are slightly shifted towards lower angles with respect to the reference data. This might be due to a distorted lattice. Note that the grain size is very small (TEM and XRD data) and such variations are possible. Nonetheless, the main features (considering the overlap of several diffraction planes to one peak observed in the experimental data) are consistent with the phase group 62 (Pnma), so presumably YIP.

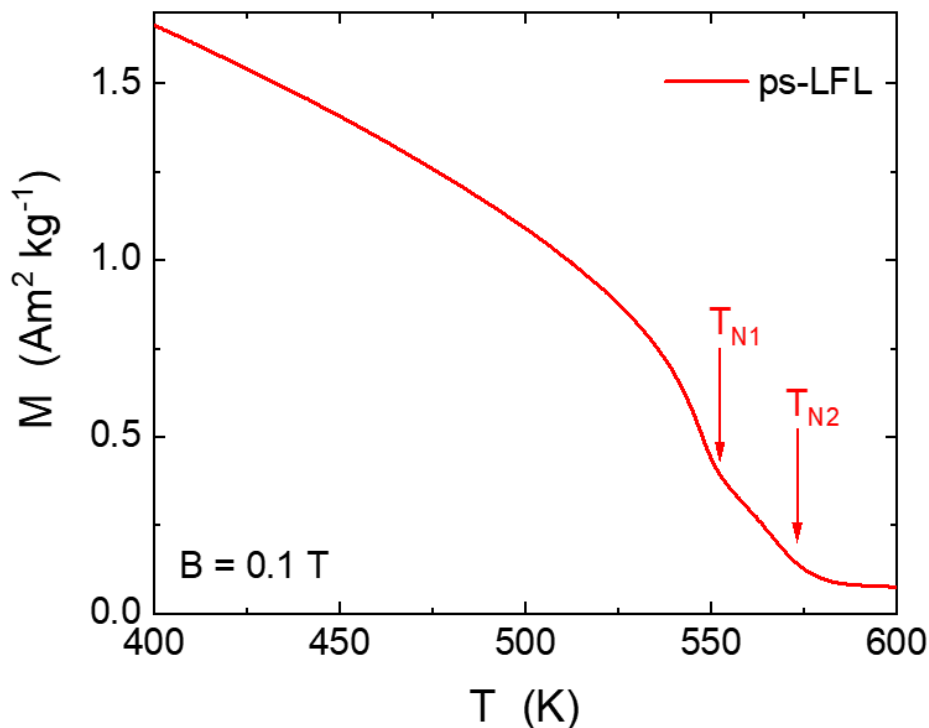
5. $M(T)$ for high temperatures

Figure S5: Magnetization as a function of temperature at $B = 0.1$ T in the high-temperature region after ps-LFL. Two ordering temperatures T_{N1} and T_{N2} are detected.

References

- [1] A. Pyatenko, M. Yamaguchi, M. Suzuki, Mechanisms of size reduction of colloidal silver and gold nanoparticles irradiated by Nd:YAG laser, *J. Phys. Chem. C.* 113 (2009) 9078–9085. doi:10.1021/jp808300q.
- [2] G. Mie, Beiträge zur Optik trüber Medien, speziell kolloidaler Metallösungen, *Ann. Phys.* 25 (1908) 377.
- [3] F.J. Kahn, P.S. Pershan, J.P. Remeika, Ultraviolet magneto-optical properties of single-crystal orthoferrites, garnets, and other ferric oxide compounds, *Phys. Rev.* 186 (1969) 891–918. doi:10.1103/PhysRev.186.891.
- [4] A. Takami, H. Kurita, S. Koda, Laser-induced size reduction of noble metal particles, *J. Phys. Chem. B.* 103 (1999) 1226–1232. doi:10.1021/jp983503o.

A3 Tools and procedure for oxide target preparation from mixed powders

During preparation of oxide targets for LAL, powders and powder mixtures are pressed and sintered as described in a previous study [223]. During this process, tilting of the press tool could be identified as one of the main causes of mechanical defects and low or inhomogeneous target densities after sintering. Especially the press plunger is deformed by the high forces and oxide nanoparticles accumulate between the plunger and the plunger guide, which hinders sliding. In addition, the oxidic nanoparticles cause surface scratches in the relatively soft tool steel. Therefore, hardened high speed steel (HSS) should be used for the plunger

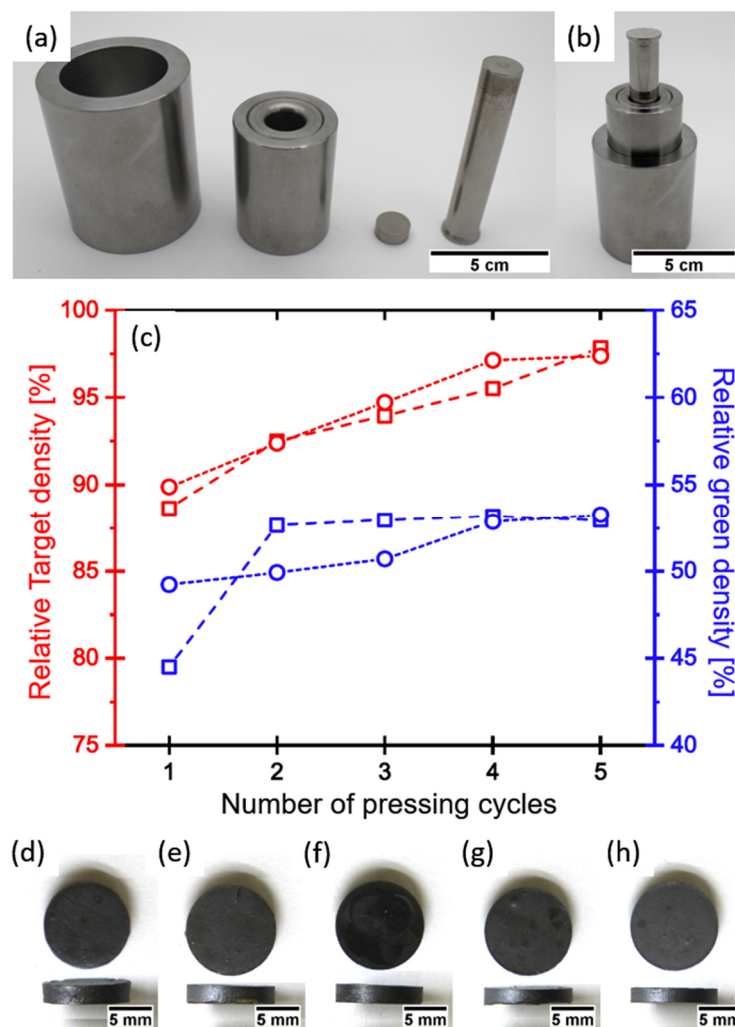


Figure 18: (a,b) Tool parts with a plunger and a plunger guide made from high speed steel (HSS) to produce oxide targets for LAL. (c) Relative target density and green part density as a function of pressing and milling cycles before final sintering of a mixture of iron oxide and yttrium oxide powder. (d-h) Corresponding targets for each cycle after sintering.

and plunger guide (Rockwell hardness of 62 HRC)(Figure 18 a,b). Due to the massive socket and the precise fit of the punch, guide and counter-pressing piece, a homogeneous force distribution is achieved. This in turn leads to a higher density of the sintered target even at lower pressure during green body manufacturing, which causes less wear of the tool. A YIG target reaches > 90 % relative density after pressing at 198 MPa instead of 300 MPa.

Another way to improve the green density and the relative density of the sintered target, is applying several pressing cycles followed by milling of the green part. The density of the green parts and sintered targets increases with each further iteration and reaches approx. 98 % of the theoretical density after five pressing cycles (Figure 18 c), whereby the number of deformations and other macroscopic defects on the surfaces and at the edges of the targets is reduced.

A4 LFL of ball milled YIG powder, ready to use as nanoadditive in AM

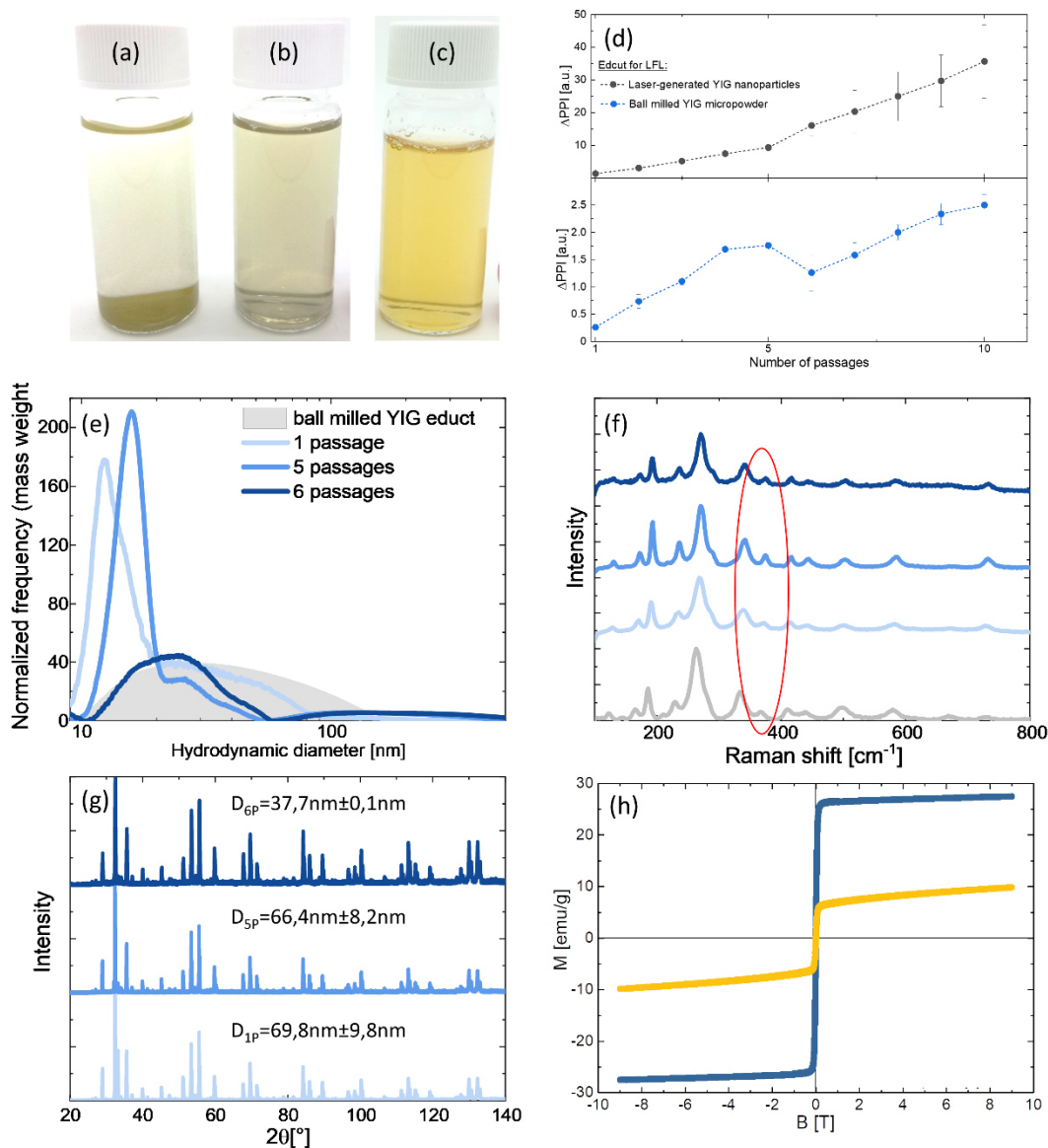


Figure 19: Results on YIG nanoparticles generated from an YIG micropowder by ball milling (Retsch PM100), subsequent ultrasonication and LPP (Edgewave ps-laser at 355 nm, same laser parameters as in [265]) in water (50 mg/l) without chemical stabilizers. (a) Image of YIG suspension after ultrasonication and (b) after LPP compared to (c) a YIG colloid generated by LAL of an YIG target, followed by LPP. (d) Difference in the $\text{Abs}_{320}/\text{Abs}_{800}$ -ratio calculated from UV-Vis absorbance spectra before and after LPP (referred to as change of PPI) for LPP of a laser-generated colloid and a colloid from ball milled powder. After five passages the hydrodynamic particle size distribution (e) as well as the Ramen spectra (f) show variations that can be attributed to decomposition of the YIG and generation of FeO_x species. In accordance with the crystallite size, calculated from XRD (g), the saturation magnetization (h) is similar to the bulk value of YIG ($26.8 \text{ Am}^2\text{kg}^{-1}$) and three times higher than after LPP of a superparamagnetic laser generated colloid (also see Chapter 4.2).

A5 Flexibel passage reactor design

For LPP of flammable solvents, a new design of the passage reactor was developed (Figure 20). The new design adds a nozzle with the purpose of generating an inert gas stream close to the liquid jet to prevent the solvent from being ignited by the laser beam. Another extension is the sleeve with the standard joint of 29/32 mm, through which further glass devices can be connected to the reactor. This enables directly adding a pump and tubing for continuous processing of a colloid, which reduces the process time and adds another degree of freedom, as it gives the opportunity for flexible adjustment of the liquid jet velocity and volume flow. However, the reactor is also suitable for batch operation.

To ensure that no solvent ignites during the irradiation of the colloids, the process was tested under extreme conditions with ps-laser irradiation (355 nm) of nitromethane, which shows strong absorption in the ultraviolet range. During several test runs no ignition could be observed. Furthermore, the directed nitrogen flow reduced the distribution of aerosols.



Figure 20: Further developed modular passage reactor for post-irradiation of colloids based on organic solvents.

A6 Supporting Information: How colloidal surface additivation of polyamide 12 powders with well-dispersed silver nanoparticles influences the crystallization already at low 0.01 vol%

Reprinted from Additive Manufacturing 36, 101419 (2020) with the permission of Elsevier

Available at: doi.org/10.1016/j.addma.2020.101419

1. Effect of PA12 on pH of the suspension

The polymer concentration has a huge effect on the pH value of the suspension (Fig. S1a). The higher the concentration, the lower the pH value until a saturation can be observed at pH 3.8 for 50 g/l. The influence of PA12 on alkaline pH adjustment was measured by titration of a PA12 suspension prepared by mixing 1 g PA12 in 75 mL ultrapure water under vigorous stirring. Fig. S1b shows the pH-shift of a PA12 suspension in water during a titration experiment with 0.1 M NaOH. The pH changes significantly even when small volumes of sodium hydroxide solution are added. After adding 10 mL of the base a difference between calculated and measured pH can be observed. This result points out that the used PA12-powder not only decreases the pH but also has a direct effect in the acid-base equilibrium acting as a buffer. Further proof to this result is given in Fig. S1c which shows the temporal evolution of the pH value directly after neutralization of the suspension.

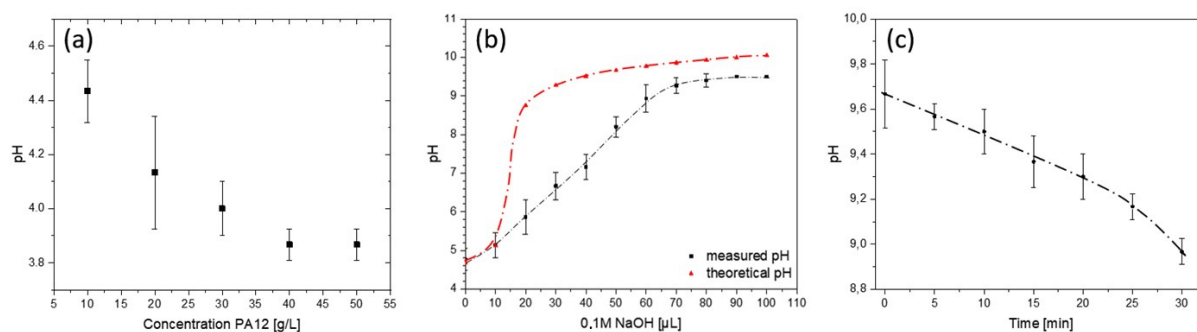


Figure S1: (a) pH of a PA12 (Vestosint 1115) suspension as a function of PA12 concentration after 15 minutes of stirring. (b, c) Influence of a 0.1M NaOH solution on the pH of an aqueous suspension of PA12 at 13.3 g/l in

deionized water. The PA12 suspensions were previously stirred for 15 minutes to ensure equilibration. (b) pH-shift depending on the volume of the NaOH solution. The red and blue dashed lines are used to illustrate the pH-change based on calculated (red) and measured (black) pH values. (c) Time-dependent change of pH after addition of 100 μL 0.1M NaOH solution, illustrated by the black dashed line.

2. Theoretical surf%

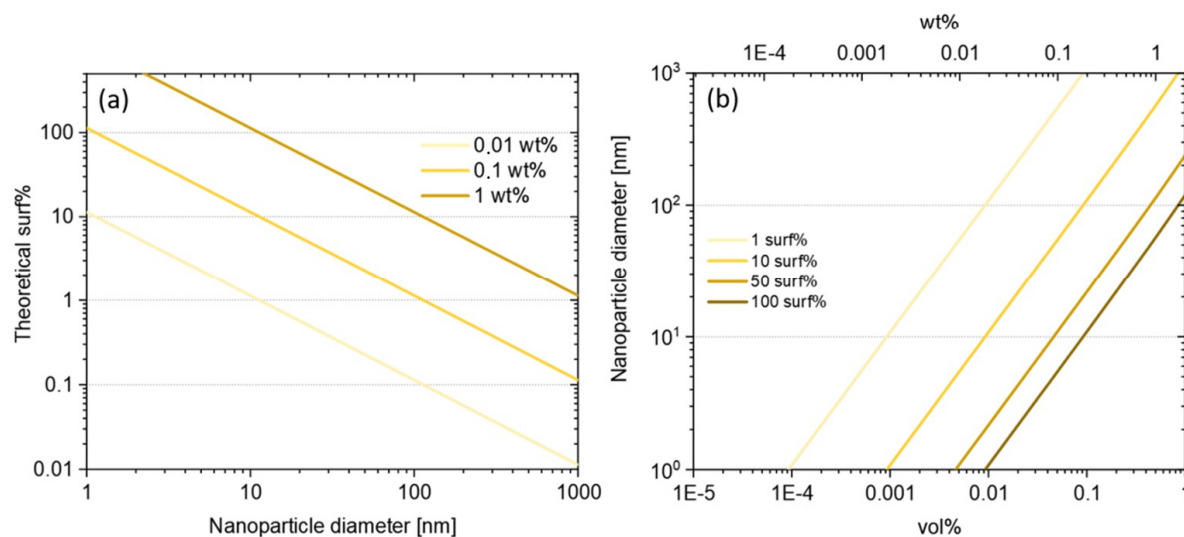


Figure S2: (a, b) Scaling graphs illustrating the connection between wt%, vol%, surface coverage (surf%) and nanoparticle size for PA12 powder with a specific surface of $0.114 \text{ m}^2/\text{g}$ which was determined based on the polymer microparticle size distribution in Fig. S3.

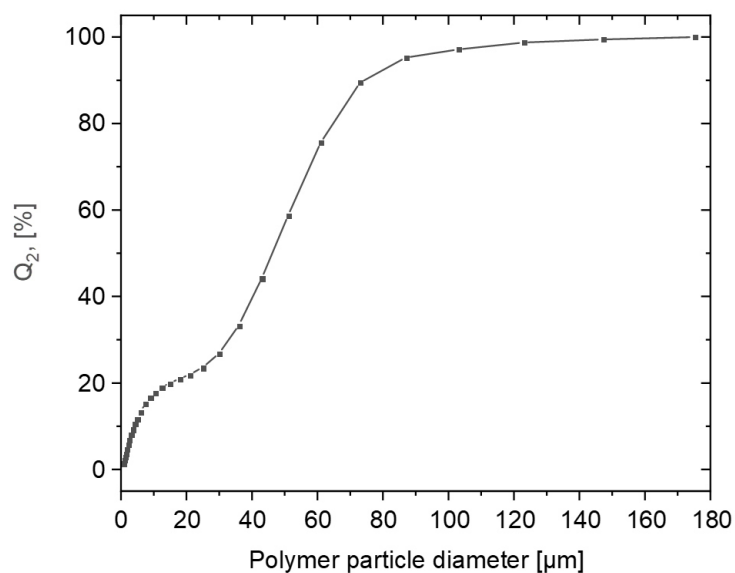


Figure S3: Surface weighed particle size distribution based on laser diffraction.

A7 Drying procedure of powders after colloidal additivition

Drying and sifting of functionalized powder after colloidal additivition are relatively easy to scale to kg/day, although these steps make up most of the overall process duration. However, if the colloidal additivition process is scaled towards kg/h, a larger drying capacities are required. In order to evaluate the necessary time for drying, experiments were conducted at 50°C with PA12 powder batches of 500 g each, which were spread in a tray (approx. 40x20 cm), resulting in a powder layer thickness of approx. 1 cm. After filtration, the powders show a typical moisture content of 20 wt%, which is drastically reduced within 24 h (Figure 21 a). It is important to note, that PA12 is a hygroscopic material and absorbs water from the surrounding air over time (up to a few wt%). The humidity of the powder does affect the powder flowability and recoating behavior through influencing the van-der-Waals forces (Hamaker constant) between polymer particles [73]. In order to illustrate the influence of the initial powder humidity, a second experiment was conducted by adding an extra portion of water to the powder after drying. Hereby, the initial humidity was increased to almost 35 wt%, which represents a failure during filtration, and the necessary time for drying almost doubled (Figure 21 b). Therefore, it is very important for scale-up of colloidal additivition to remove most of the water directly during filtration, rather than in the oven. In addition, the air humidity inside the oven also plays an important role. Moisture absorbers (silica-based, APALUS Inc.) can speed up the drying process by taking up water (Figure 21 b) which reduces the humidity inside the oven. A detailed comparison of the residual humidity in differently treated PA12 should be done in follow up experiments, especially to ensure reproducibility for large scale colloidal additivition.

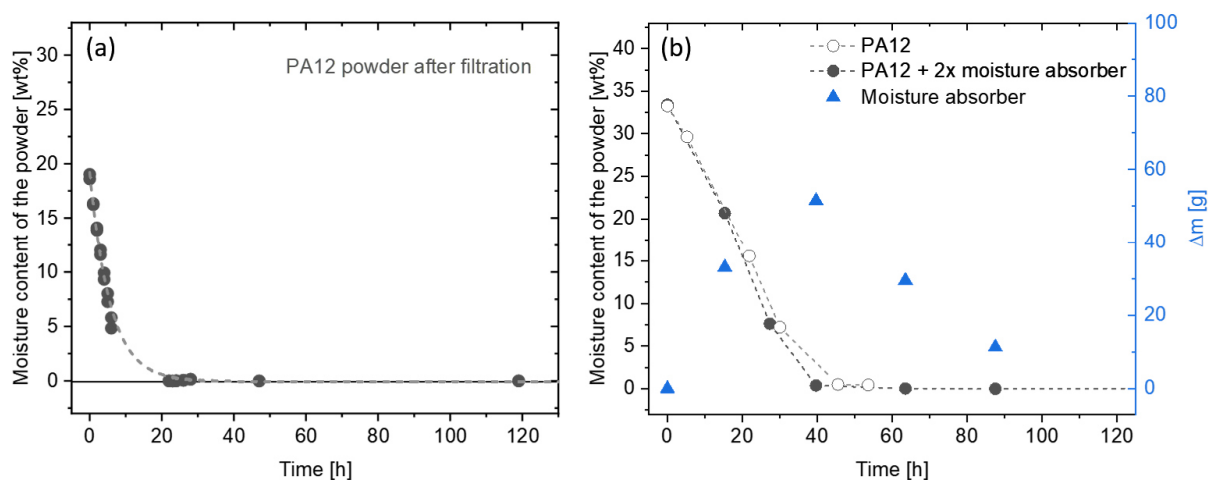


Figure 21: Moisture content of PA12 powder during drying at 50°C. Initially, the powder was immersed in deionized water followed by filtration. The moisture content is given relative to the dried powder after five days. (a) Standard evolution of moisture content and (b) evolution of moisture content with adding an extra portion of water after filtration to illustrate the impact of larger moisture content on the drying time with and without placing silica-based moisture absorbers (2x 500 g) in the oven. The right axis shows the average mass change of the moisture absorbers during drying ($500 \text{ g} \pm \Delta m$).

A8 Supporting Information

Plasmonic seasoning: Giving color to desktop laser 3D-printed polymers by highly dispersed nanoparticles

Reprinted from Advanced Optical Materials 2000473 (2020) under CC BY

Available at: doi.org/10.1002/adom.202000473

1. Particle size distribution of laser generated silver colloids and TPU micropowder

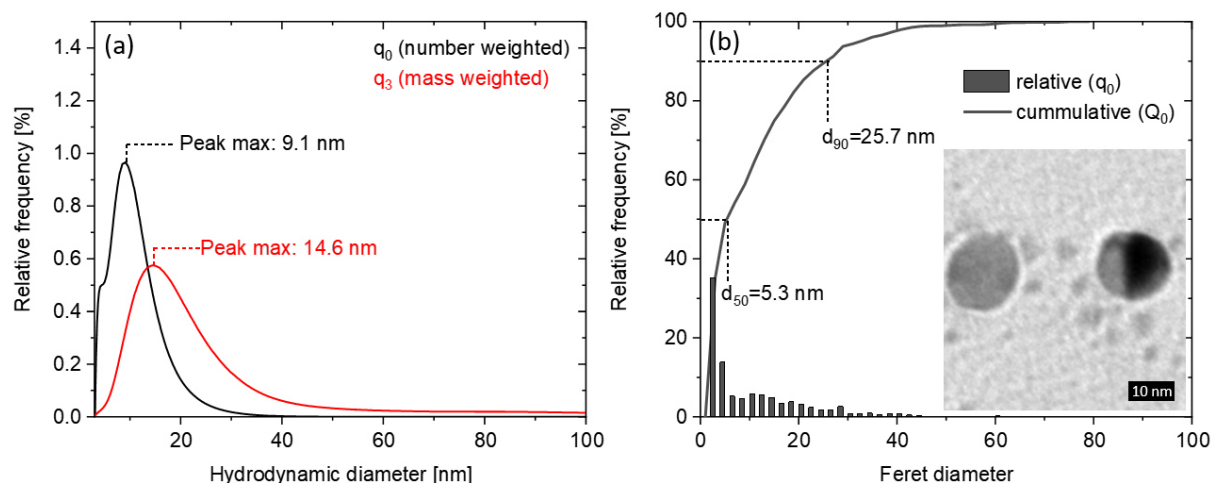


Figure S1: Particles size characterization of the laser-generated colloids stabilized with 100 $\mu\text{mol/l}$ citrate: (a) Number and volume weighted hydrodynamic size distribution and (b) Feret diameter (primary particle diameter) distribution based on TEM imaging ($n=1000$). The inset shows a representative TEM image.

Table S1: TPU particle size distribution based on microscopic images ($n > 500$ particles).

	Particle size distribution (Feret _{max} diameter) [μm]					
	X _{10,3}	X _{50,3}	X _{90,3}	X _{10,0}	X _{50,0}	X _{90,0}
TPU + 0.1 wt% Ag	42	131	153	3.7	14	47

2. Influence of colloidal stabilization on composite

It is also possible to perform the additiviation process with unstabilized silver colloids (without sodium citrate) which results in a linear correlation between powder absorption and

nanoparticle load even if pH stays at 6.0. Only above 0.5 wt% a slight yellow colouring of the permeate can be observed but after drying, the powders show clear signs of aggregation (brown, grey colour). The addition of very small amounts of additives in the range of $\mu\text{mol/l}$ is useful to increase the stability and the reproducibility of LSPC [1]. Adding sodium citrate in concentrations $> 10\mu\text{mol/l}$ results in a decrease in supporting efficiency to almost zero (see Fig. S2a), which could be attributed to electrostatically hindering similar to the results of Wagener et al., *Langmuir*, 28, 6132 (2012), which can be attributed to both pH effect of the base citrate as well as the ligand's electrosteric effects. Filtrates with $100\mu\text{mol/l}$ sodium citrate show the same absorbance as the initial colloid. Even stirring for 3 weeks does not result in any supporting. However, the process route with sodium citrate stabilization and controlled destabilization by pH adjustment comes with distinct advantages in colloidal stability, process control and reproducibility and results in a 10x higher SPR peak intensities of the composite powders compared to the route without sodium citrate.

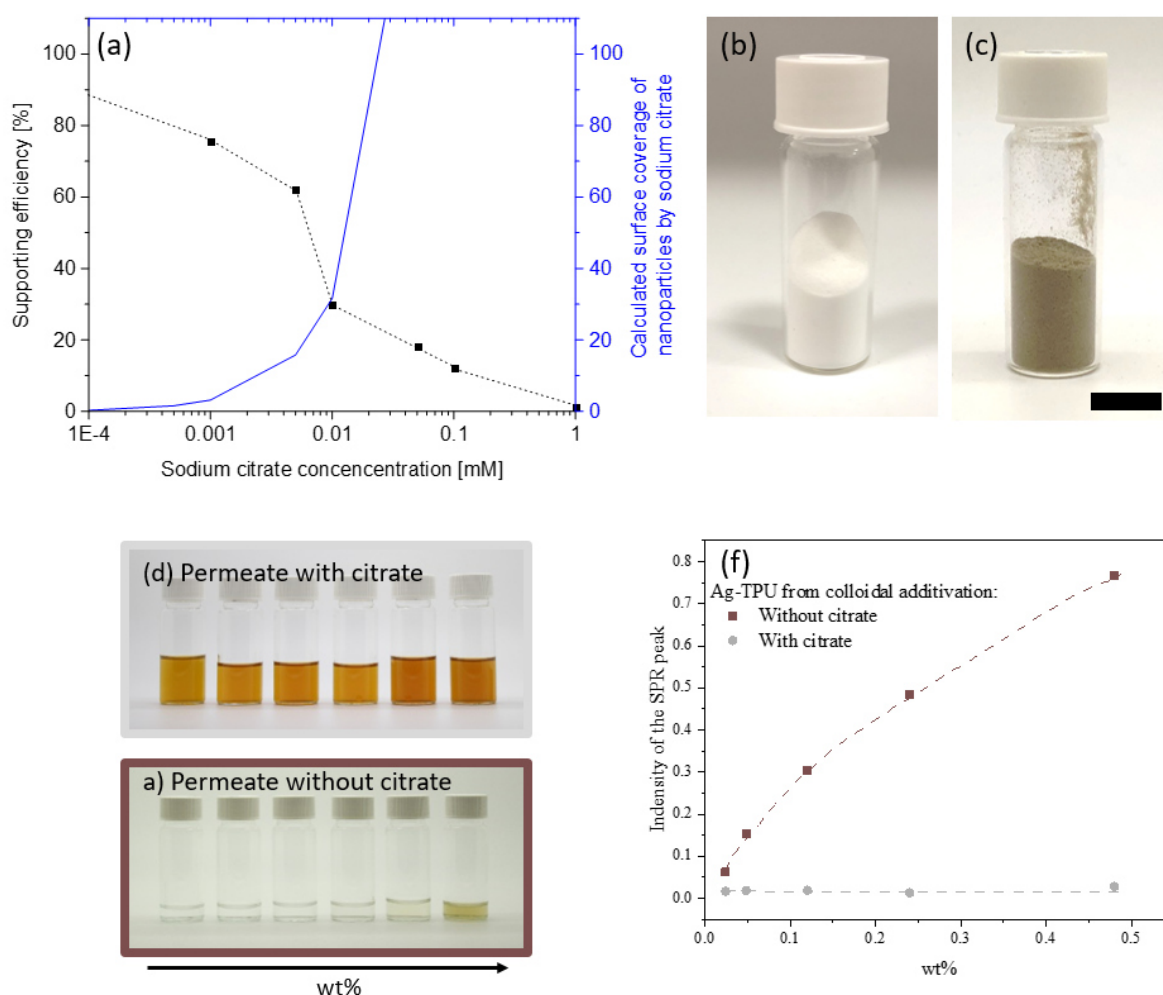


Figure S2: (a) Supporting efficiency and calculated surface coverage based on Wagener et al. as a function of citrate concentration. (b, c) Powder after additivation. The black bar measures 1 cm. (d, e) permeates after filtration for citrate stabilized and unstabilized colloidal silver nanoparticles. The absorption of the corresponding composite powders is shown in (f).

3. Zeta potential, streaming potential and supporting efficiency

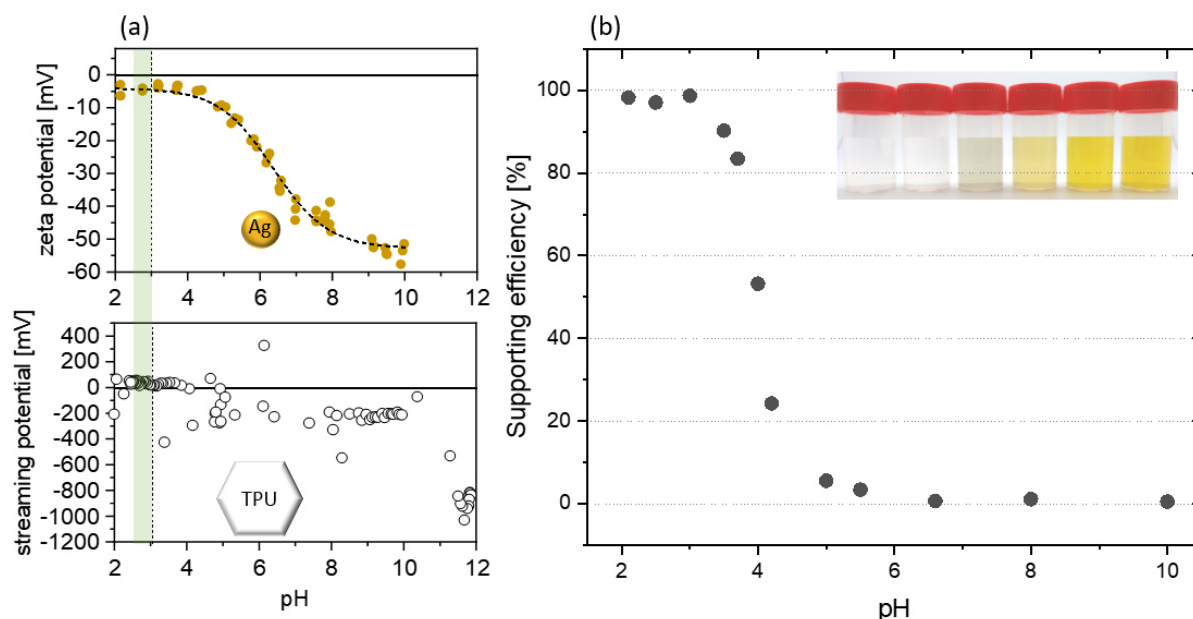


Figure S3: (a) Zeta potential of colloidal silver nanoparticles and streaming potential of the TPU microparticles as a function of pH value. (b) Supporting efficiency as a function of pH value (inset shows permeates after supporting and filtration at different pH values).

4. Aging of silver colloids and influence on composite powder properties

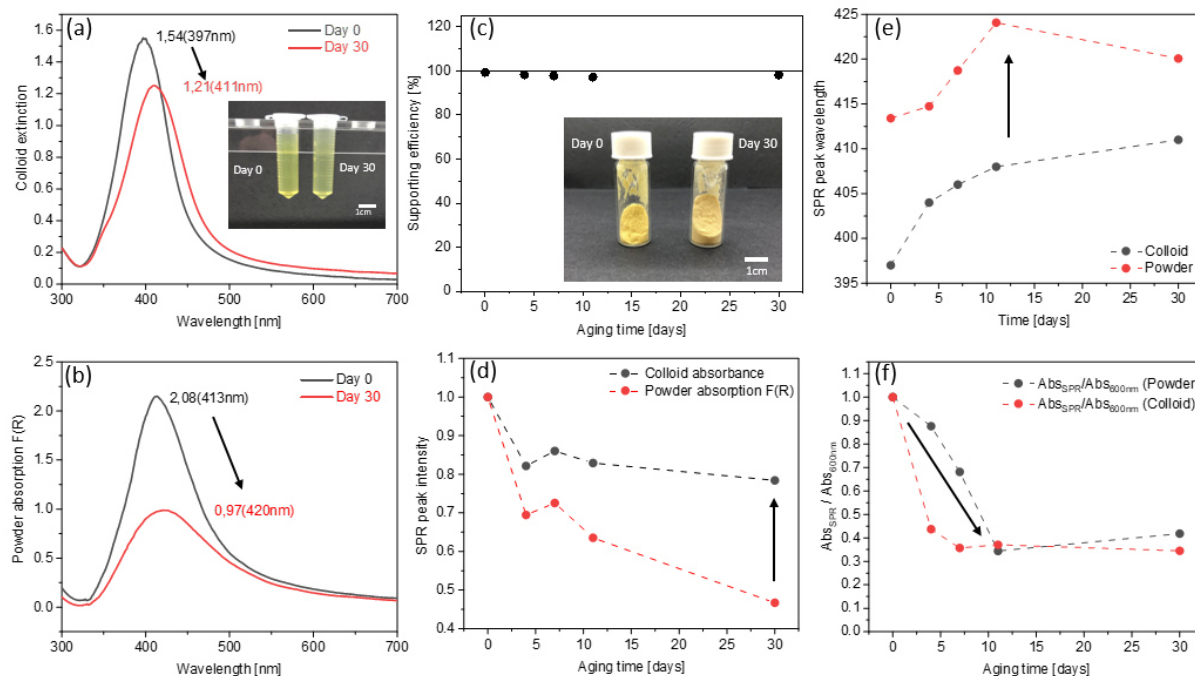


Figure S4: Influence of silver colloid aging after laser ablation (stabilized with 100µmol/l sodium citrate): (a) UV-Vis spectra directly after LAL and after 30 days and (b) corresponding powder absorption at the surface plasmon resonance peak. Influence of colloid aging on (c) supporting efficiency, (d) SPR peak position and Abs_{SPR}/Abs_{600} . The insets show the corresponding colloid and powder samples.

Storage over 30 days leads to aggregation and decrease of SPR intensity, which negatively effects the SPR intensity of composite powders (Figure S4 a,b). The aging influence can be seen clearly for the colloid as well as the powder. For both samples the yellow coloring declines with time. Over the period of 30 days the supporting efficiency stays above 97% (Figure S4c). Therefore, colloid aging has a negligible effect on supporting efficiency but strongly effects the optical properties of the composite powder.

5. Correlation between SPR wavelength and particle size

Nanoparticle size [nm]	SPR peak wavelength [nm]	Reference
10-14	395-405	[2]
35-50	420	[3]
60-80	438	[4]
22	411	[5]
13	405	
5	399	
10	400	[6]

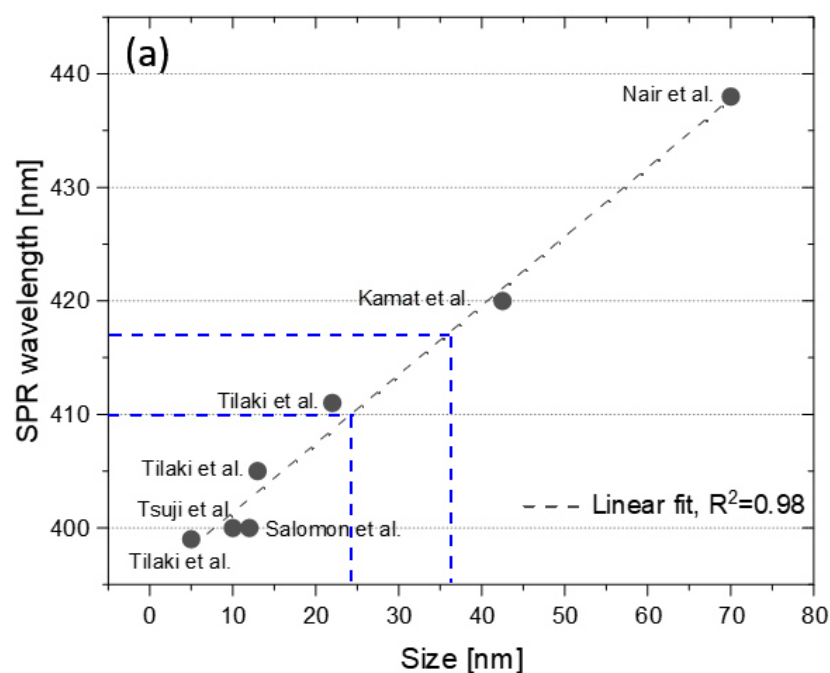


Figure S5: Correlation of SPR peak position and silver nanoparticle size (More information can be found in the given references). A theoretical approximation of the effect of aggregation on SPR peak wavelength and intensity was done according to Amendola et al. [7].

6. Additional information on influence of nanoparticle concentration and stirring time

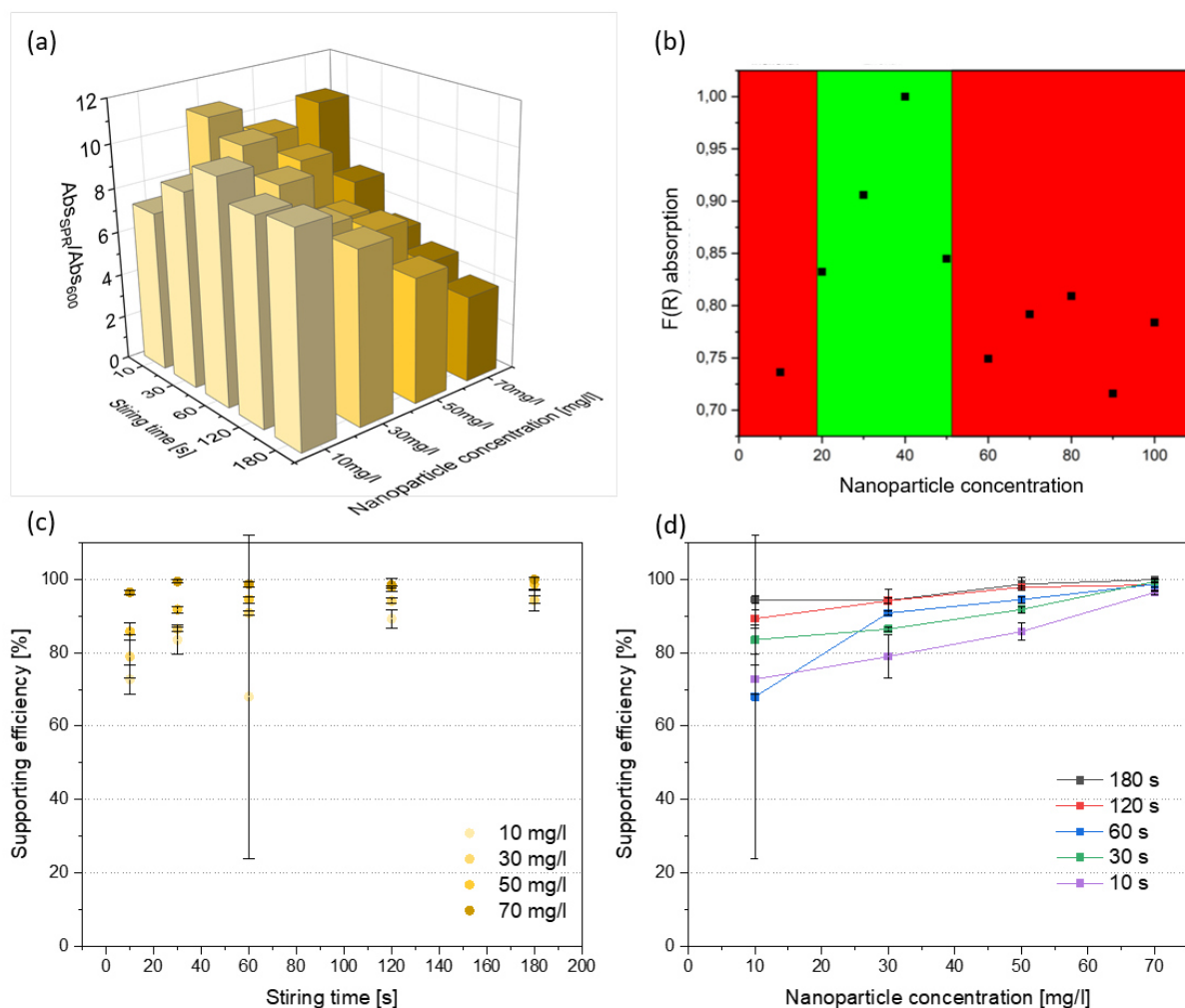


Figure S6: (a) Influence of stirring time and nanoparticle concentration on nanoparticle aggregation, quantified by the ratio of absorbance at the SPR wavelength and absorbance at 600 nm. The lower the value, the better (less aggregation). (b) Influence of concentration on F(R) powder absorption at the SPR wavelength. (c,d) Supporting efficiency as a function of stirring time for different nanoparticle concentrations and vice versa.

7. Different approaches for adjusting the nanoparticle loading

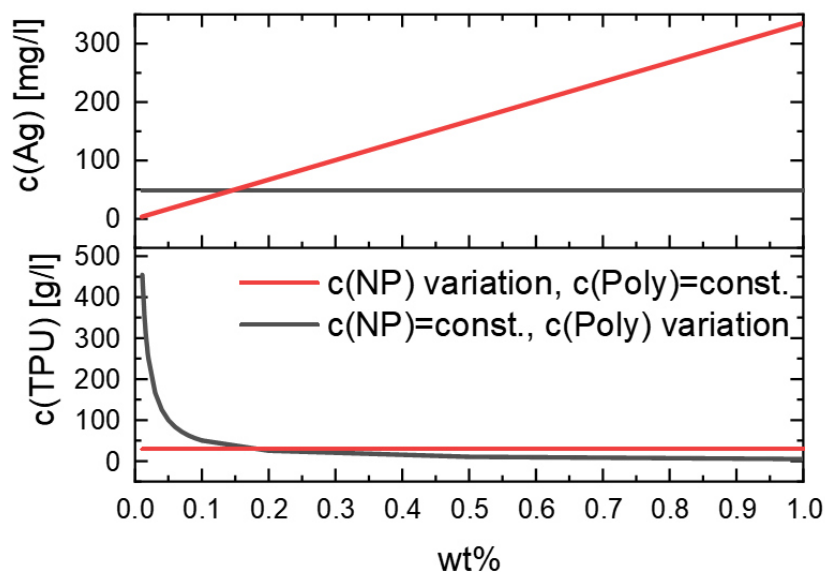


Figure S7: Ag nanoparticle concentration and TPU microparticle concentration for different nanoparticle loadings between 0.01 to 1 wt%. Variation of nanoparticle loading by variation of either $c(\text{Ag})$ or $c(\text{TPU})$.

In order to achieve different mass loadings of silver nanoparticles on the polymer microparticles, the ratio of polymer microparticle and silver nanoparticle must be varied. This can happen by either variation of nanoparticle or polymer concentration (Figure S7). Since high nanoparticle concentration negatively affects the colloidal stability and influences supporting efficiency, a variation of polymer microparticle concentration is recommended. Please note, that high polymer concentration also influences the viscosity of the suspension, which will likely influence the supporting kinetics.

8. Upscaling and reproducibility of colloidal additivation towards kg-scale

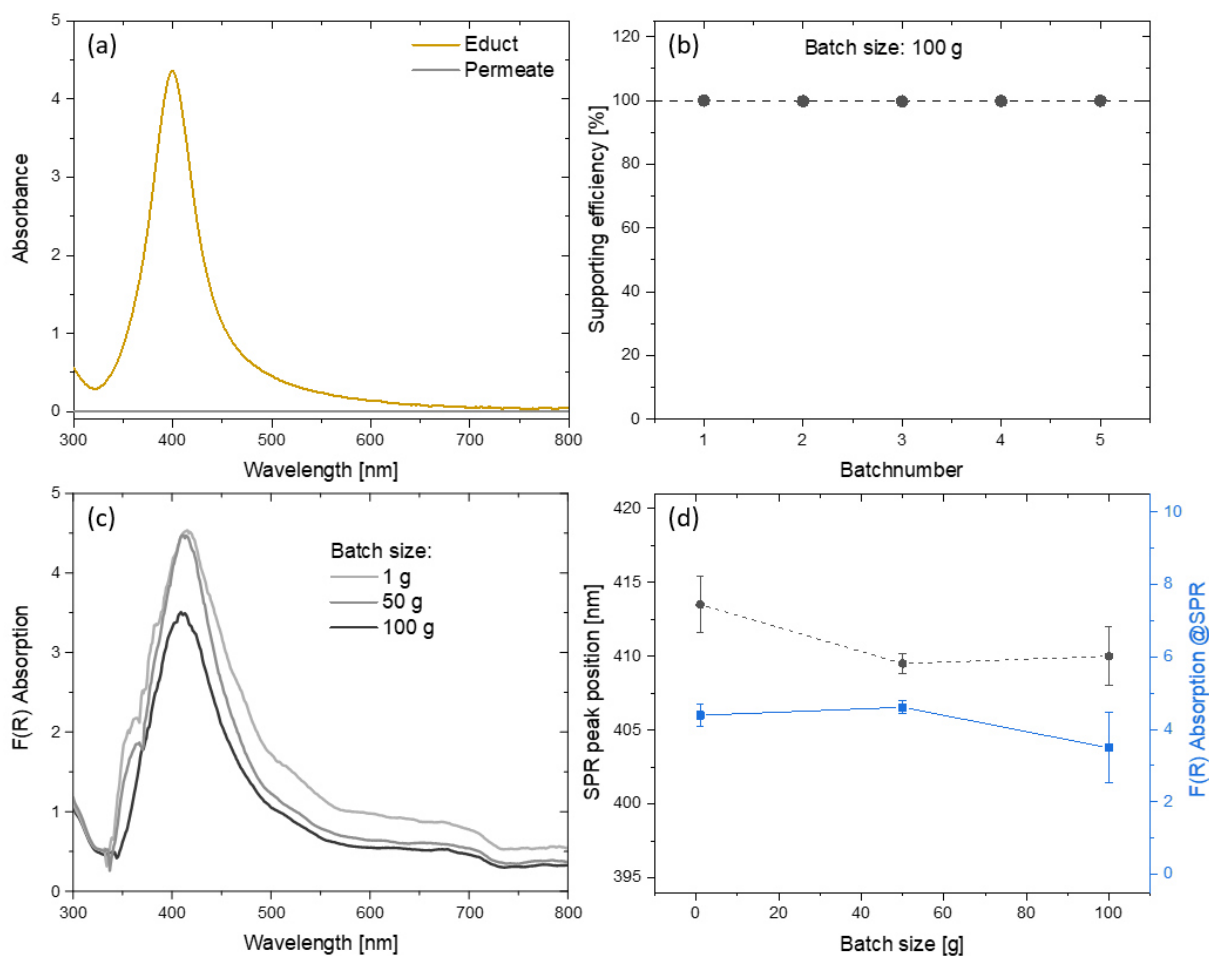


Figure S8: Upscaling towards kg-scale: (a) Absorbance spectrum of silver colloid before additivation and permeate after additivation indicating approx. 100% supporting efficiency and (b) reproducibility of the supporting efficiency for five 100 g batches. (c) F(R) powder absorption spectra and (d) SPR peak position and absorption as a function of batch size. Finally, 1 kg of nanoparticle-polymer composite powder was produced for PBF-LB tests.

Laser system parameter used for upscaling of laser ablation ^[8,9]: 3 ps, 1060 nm, 10 MHz

9. Fine-tuning of powder absorbance by AgAu-alloys

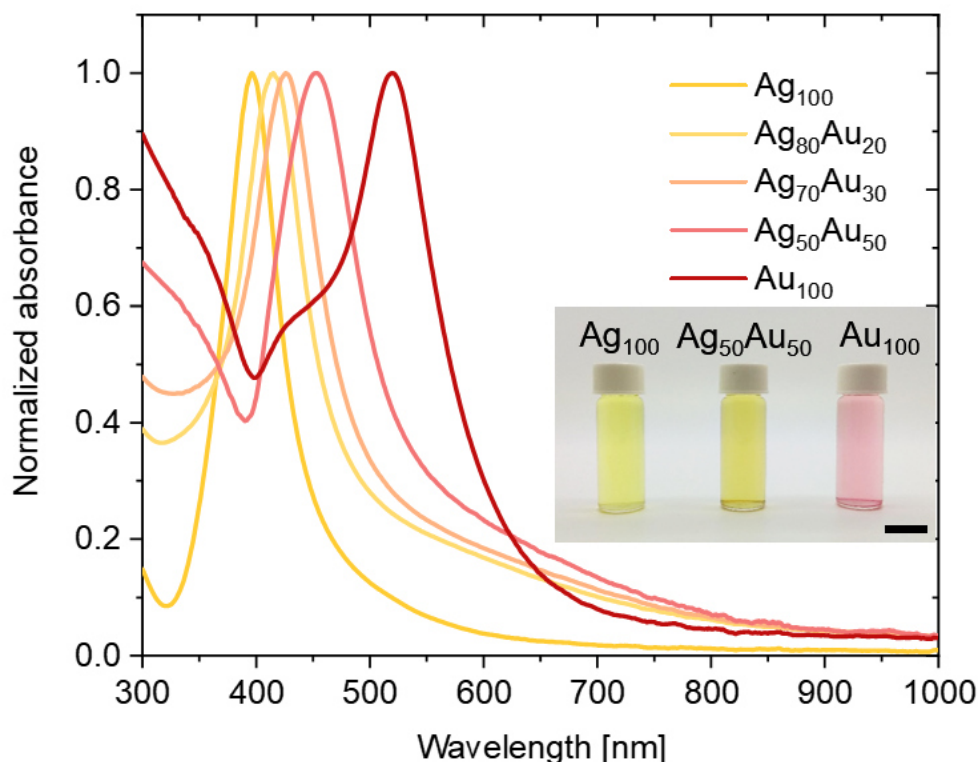


Figure S9: Normalized UV-Vis absorbance spectra of gold-silver-alloys for different molar ratio in laser-generated Ag_xAu_y alloy nanoparticle colloids. Spectra were peak-normalized to illustrate the potential for fine-tuning of SPR peak wavelength. The inset shows representative colloids (black bar measures 1 cm).

References

- [1] V. Merk, C. Rehbock, F. Becker, U. Hagemann, H. Nienhaus, S. Barcikowski, *Langmuir* **2014**, *30*, 4213.
- [2] S. D. Solomon, M. Bahadory, A. V. Jeyarajasingam, S. A. Rutkowsky, C. Boritz, L. Mulfinger, *J. Chem. Educ.* **2007**, *84*, 322.
- [3] P. V. Kamat, M. Flumiani, G. V. Hartland, *J. Phys. Chem. B* **1998**, *102*, 3123.
- [4] A. Sreekumaran Nair, T. Pradeep, *Curr. Sci.* **2003**, *84*, 1560.
- [5] R. M. Tilaki, A. Irajizad, S. M. Mahdavi, *Appl. Phys. A Mater. Sci. Process.* **2006**, *84*, 215.
- [6] T. Tsuji, D.-H. Thang, Y. Okazaki, M. Nakanishi, Y. Tsuboi, M. Tsuji, *Appl. Surf. Sci.* **2008**, *254*, 5224.

- [7] V. Amendola, O. M. Bakr, F. Stellacci, *Plasmonics* **2010**, *5*, 85.
- [8] R. Streubel, S. Barcikowski, B. Gökce, *Opt. Lett.* **2016**, *41*, 1486.
- [9] R. Streubel, G. Bendt, B. Gökce, *Nanotechnology* **2016**, *27*, 205602.

A9 Spray drying of TPU powder suspensions for nanoparticle-functionalization

Instead of colloidal additivation, surface-functionalization can also be performed by spray drying of a mixture of polymer suspension and laser-generated colloid, provided that no uncontrolled adsorption of the silver nanoparticles on the polymer surface takes place before spray drying, e.g. in the reservoir and tubing of the machine.

In order to evaluate this method, spray drying of an aqueous TPU suspension with a silver colloid was performed at Büchi Labortechnik GmbH (Büchi Sprühtrockner B-290, approx. 1 l/h). Two different TPU-nanoparticle mixtures were applied. The first mixture based on an unstabilized silver colloid, whereas the second mixture bases on a silver colloid stabilized with 5 mM of citric acid. Both experiments were conducted at a polymer concentration of 50 g/l and a silver concentration of 50 mg/l, resulting in a maximum nanoparticle loading of 0.1 wt%.

During spray drying both mixtures resulted in substantial clogging of the tubing and the nozzles of the device, which made several cleaning cycles per hour necessary. Furthermore, adsorption of the nanoparticles on the polymer particles and on the tubing of the machine could be observed for the unstabilized mixture. After spray drying, the resulting powder was rather grey than yellow. For the stabilized mixture, however, no adsorption of

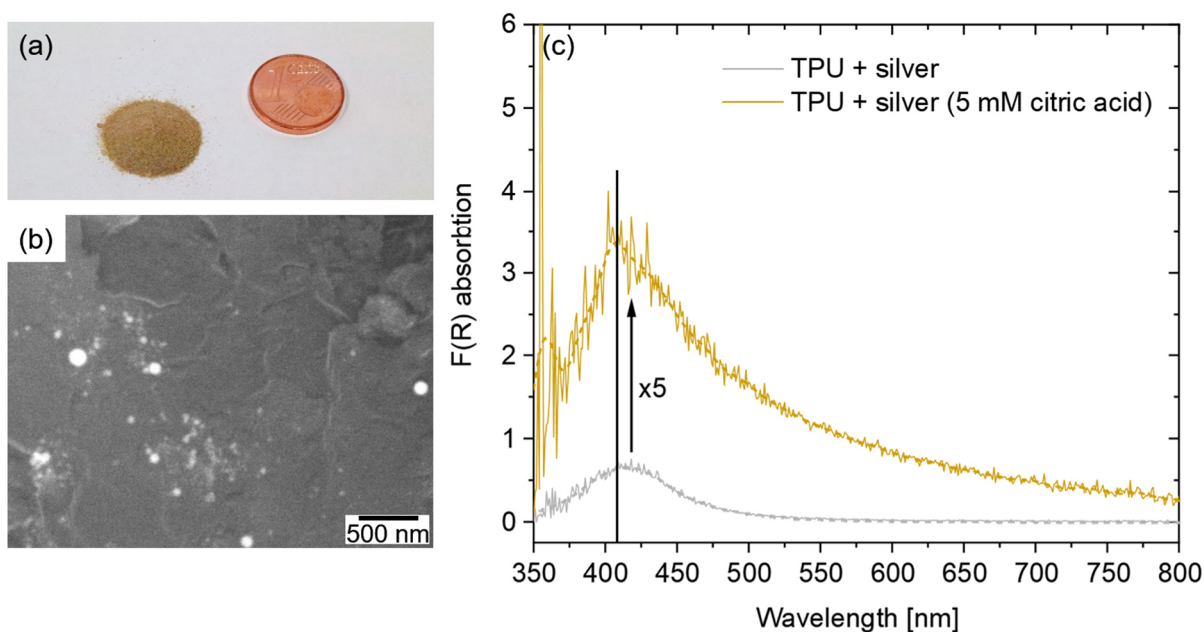


Figure 22: (a) TPU powder after spray coating of TPU immersed in a silver colloid stabilized with citric acid (5 mM). (b) Corresponding SEM image and (c) UV-Vis absorption measurement of the functionalized powder after spray drying. Comparison of stabilized and unstabilized silver colloid.

nanoparticles on the tubing could be observed and the powder had a yellow to brown color (Figure 22 a), which proves a conservation of plasmon resonance. Since the powder is almost brown, a significant degree of aggregation can also be expected. Powders were further characterized by SEM imaging (Figure 22 b) and UV-Vis absorption measurement (Figure 22 c). As expected, a pronounced SPR peak is observed, which is much broader than for colloidal additivated TPU powder in Chapter 6.1 . This is also confirmed by SEM images, which reveal aggregation and spots where nanoparticles cumulate, rather than a homogeneous decoration. Finally, the TPU particles do not change their irregular shape, do not show any morphological change, and do not melt together during spray drying (Figure 23). Please note, that a partially melting of the polymer particle surface during spray drying

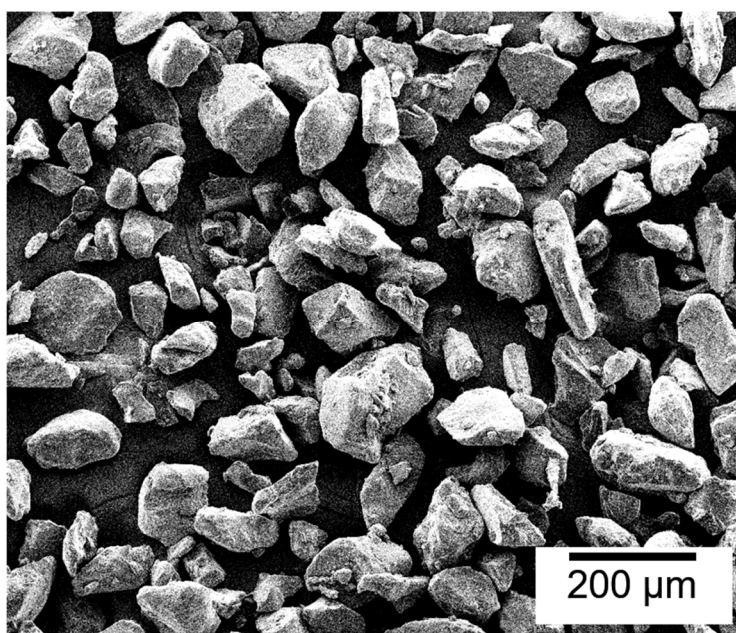


Figure 23: SEM image of a TPU powder after spray drying, showing the typical irregular shaped TPU particles.

cannot be excluded completely, since the nozzle temperature was set to 135°C, which is 10°C above the melting temperature of TPU.

A10 Adsorption efficiency as a function of polymer concentration

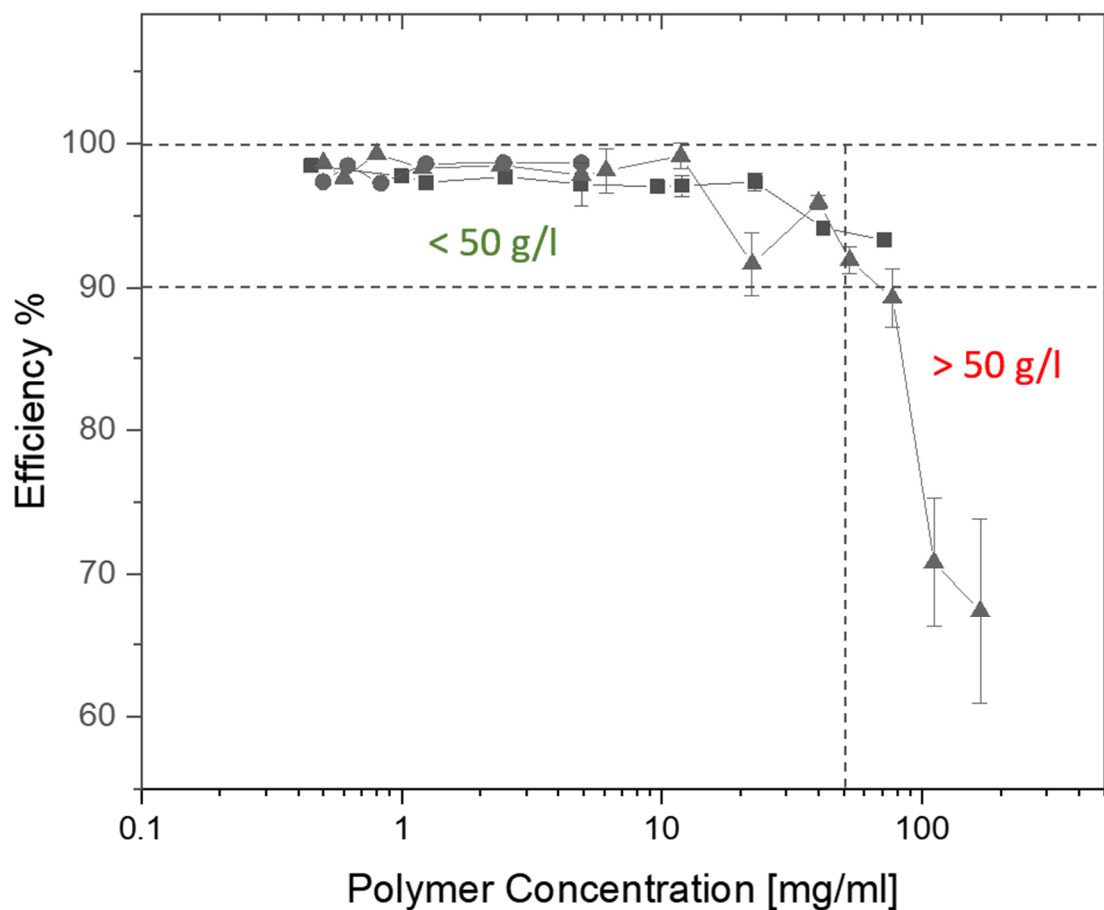


Figure 24: Pre-study on the supporting efficiency as a function of polymer concentration for carbon nanoparticle after LPP supported on PA12 (Vestosint 1115), calculated from UV-Vis spectroscopy for the laser irradiated colloid compared to the permeate after colloidal additivition. Above 10 g/l a decrease in supporting efficiency was observed. Concentrations above 50 g/l lead to a significant decreased supporting efficiency to almost 60 % for 200 g/l, which could be attributed to an increasing viscosity of the polymer suspension. Furthermore, the concentration of PA12 powder has an influence on the pH (absolute value and temporal evolution) of the suspension, which might affect supporting efficiency.

A11 Comparison of ns- and ps-LPP of iron oxide

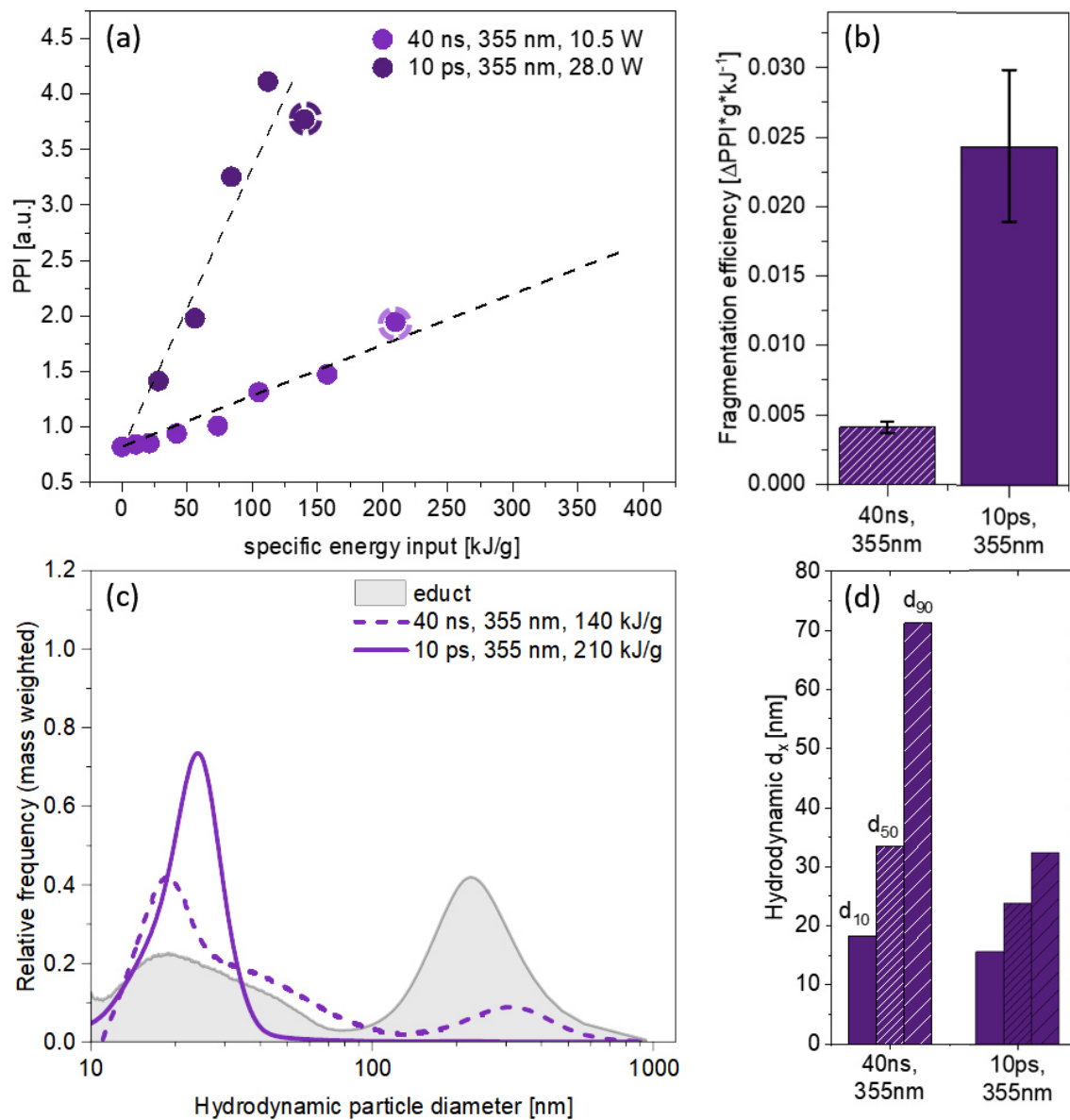


Figure 25: Influence of the pulse duration on the fragmentation efficiency during LPP of iron oxide. Significant increase of efficiency from ns-irradiation to ps-irradiation: (a) PPI as a function of the specific energy dose, (b) slope of the PPI, (c) ADC Size distribution (mass weighted) of iron oxide nanoparticles after LPP compared to the educt size distribution (grey), and (d) corresponding characteristic particle diameters.

Curriculum Vitae

Der Lebenslauf ist in der Online-Version aus Gründen des Datenschutzes nicht enthalten.

Der Lebenslauf ist in der Online-Version aus Gründen des Datenschutzes nicht enthalten.

Publications and conference contributions

Tim Hupfeld (formerly Tim Schmitz), ORCID: 0000-0001-9062-7541

Peer-reviewed journals

- [1] [T. Hupfeld](#), S. Salamon, J. Landers, A. Sommereyns, C. Doñate-Buendía, J. Schmidt, H. Wende, M. Schmidt, S. Barcikowski, B. Gökce, *3D Printing of Magnetic Parts by Laser Powder Bed Fusion of Iron Oxide Nanoparticle Functionalized Polyamide Powders*, Journal of Materials Chemistry C 8 (2020) 12204-12217
- [2] [T. Hupfeld](#), A. Sommereyns, F. Riahi, C. Doñate-Buendía, S. Gann, M. Schmidt, B. Gökce, S. Barcikowski, *Analysis of the Nanoparticle Dispersion and its Effect on the Crystalline Microstructure in Carbon-Additivated PA12 Feedstock Material for Laser Powder Bed Fusion*, Materials 13 (2020) 3312
- [3] [T. Hupfeld](#), C. Doñate-Buendía, M. Krause, A. Sommereyns, A. Wegner, T. Sinnemann, M. Schmidt, B. Gökce, S. Barcikowski, *Scaling up colloidal surface additivation of polymer powders for laser powder bed fusion*, Procedia CIRP 94 (2020) 110-115
- [4] A. Blasczyk, [T. Hupfeld](#), B. Gökce, S. Barcikowski, M. Schmidt, *Evaluation of essential powder properties through complementary particle size analysis methods for laser powder bed fusion of polymers*, Procedia CIRP 94 (2020) 116-121
- [5] [T. Hupfeld](#), A. Sommereyns, T. Schuffenhauer, E. Zhuravlev, M. Krebs, S. Gann, O. Keßler, M. Schmidt, B. Gökce, S. Barcikowski, *How colloidal surface additivation of polyamide 12 powders with well-dispersed silver nanoparticles influences the crystallization already at low 0.01 vol%*, Additive Manufacturing 36 (2020) 101419
- [6] [T. Hupfeld](#), A. Wegner, M. Blanke, C. Doñate-Buendía, V. Sharov, S. Nieskens, M. Piechotta, M. Giese, S. Barcikowski, B. Gökce, *Plasmonic Seasoning: Giving Color to Desktop Laser 3D Printed Polymers by Highly Dispersed Nanoparticles*, Advanced Optical Materials (2020) 2000473

- [7] T. Hupfeld, F. Stein, S. Barcikowski, B. Gökce, U. Wiedwald, *Manipulation of the Size and Phase Composition of Yttrium Iron Garnet Nanoparticles by Pulsed Laser Post-Processing in Liquid*, *Molecules* 25 (2020) 1869
- [8] T. Hupfeld, G. Laurens, S. Merabia, S. Barcikowski, B. Gökce, D. Amans, *Dynamics of laser-induced cavitation bubbles at a solid-liquid interface in high capillary number regimes*, *Journal of Applied Physics*, 127 (2020) 044306
- [9] T. Hupfeld, T. Laumer, T. Stichel, T. Schuffenhauer, J. Heberle, M. Schmidt, S. Barcikowski, B. Gökce, *A new approach to coat PA12 powders with laser-generated nanoparticles for selective laser sintering*, *Procedia CIRP* 74 (2018) 244
- [10] C. Doñate-Buendía, F. Frömel, M. B. Wilms, R. Streubel, J. Tenkamp, T. Hupfeld, M. Nachev, E. Gökce, A. Weisheit, S. Barcikowski, F. Walther, J. H. Schleifenbaum, B. Gökce, *Oxide dispersion-strengthened alloys generated by laser metal deposition of laser-generated nanoparticle-metal powder composites*, *Materials & Design* 154 (2018) 360
- [11] L. Gemini, T. Schmitz, R. Kling, S. Barcikowski, B. Gökce, *Upconversion nanoparticles synthesized by ultra-short pulsed laser ablation in liquid: effect of stabilizing environment*, *ChemPhysChem* 18 (2017) 1210
- [12] T. Schmitz, U. Wiedwald, C. Dubs, B. Gökce, *Ultrasmall Yttrium Iron Garnet Nanoparticles with High Coercivity at Low Temperature Synthesized by Laser Ablation and Fragmentation of Pressed Powders*, *ChemPhysChem* 18 (2017) 1125

Conference contributions

Presenting authors are marked with an asterisk.

- [1] T. Hupfeld*, T. Stichel, J. Heberle, A. Wegner, G. Witt, M. Schmidt, S. Barcikowski, B. Gökce, *Laser-processing of colloidal nanoparticles and their adsorption on polymer microparticles for Laser Additive Manufacturing*, Photonics West San Francisco, USA, February 2019
- [2] S. Barcikowski*, T. Hupfeld, R. Streubel, M. Schmidt, J. H. Schleifenbaum, B. Gökce, *Laser Synthesis of Materials for Laser Additive Manufacturing*, LAMP, Japan, May 2019
- [3] T. Hupfeld*, R. Streubel, T. Stichel, J. Heberle, M. B. Wilms, A. Weisheit, A. Wegner, J.H. Schleifenbaum, G. Witt, M. Schmidt, B. Gökce, S. Barcikowski, *Nanoparticle additivated metal and polymer powders for Laser Additive Manufacturing*, NMWP Nano Conference, Dortmund, November 2018
- [4] T. Hupfeld*, S. Gann, J. Heberle, T. Stichel, M. Schmidt, S. Barcikowski, B. Gökce, *Laser-processing of colloidal nanoparticles and their adsorption on polymer*

- microparticles for Laser Additive Manufacturing*, Material Chain International Conference, Bochum, Germany, November 2018
- [5] T. Hupfeld*, T. Laumer, T. Stickel, M. Schmidt, S. Barcikowski, B. Gökce, *A new approach to coat PA12 powders with laser-generated nanoparticles to influence the resolidification behaviour of the selective laser sintered part*, 10th Conference on Photonic Technologies, Fürth, Germany, September 2018
- [6] B. Gökce*, T. Hupfeld, R. Streubel, C. Doñate-Buendía, G. Mínguez-Vega, M. Schmidt, J.H. Schleifenbaum, S. Barcikowski, *Laser Synthesis of Nanocomposites for Additive Manufacturing*, Advanced Nanoparticle Generation and Excitation by Lasers in Liquids (ANGEL), Lyon, France, June 2018
- [7] T. Hupfeld*, G. Laurens, D. Amans, S. Barcikowski, B. Gökce, *Influence of wettability and high viscosity on the cavitation bubble dynamics during pulsed laser ablation in liquid*, Advanced Nanoparticle Generation and Excitation by Lasers in Liquids (ANGEL), Lyon, France, June 2018
- [8] S. Barcikowski*, A. Wegner, T. Hupfeld, T. Laumer, G. Witt, M. Schmidt, B. Gökce, *Nanopartikel-modifizierte Polymerpulver für die Laser-basierte additive Fertigung* DGM Fachtagung - Werkstoffe und Additive Fertigung, Potsdam, 26. April 2018
- [9] T. Schmitz*, U. Wiedwald, C. Dubs, S. Barcikowski, B. Gökce, *Synthesis of ultrasmall yttrium iron garnet nanoparticles by laserablation and fragmentation of pressed powders*, International Conference on Laser Ablation, Marseille, France, September 2017
- [10] T. Schmitz*, M.-R. Kalus, R. Streubel, S. Barcikowski, B. Gökce, *Productivity Limiting Factors in Pulsed Laser Ablation in Liquids*, International Conference on Laser Ablation (COLA), Marseille, France, September 2017

List of publications included in this thesis

- [1] T. Hupfeld, G. Laurens, S. Merabia, S. Barcikowski, B. Gökce, D. Amans, *Dynamics of laser-induced cavitation bubbles at a solid-liquid interface in high capillary number regimes*, Journal of Applied Physics 127 (2020) 044306

Conceptualization, D.A., B.G., T.H.; methodology, D.A., G.L., T.H.; formal analysis, T.H., G.L., D.A.; investigation, T.H., G.L.; data curation, T.H., G.L.; writing - original draft preparation, T.H.; writing - review and editing, T.H., D.A., G.L., B.G., S.B., S.M.; visualization, T.H., D.A.; supervision, D.A., B.G., S.B.; funding acquisition, S.B.

- [2] T. Hupfeld, F. Stein, S. Barcikowski, B. Gökce, U. Wiedwald, *Manipulation of the Size and Phase Composition of Yttrium Iron Garnet Nanoparticles by Pulsed Laser Post-Processing in Liquid*, Molecules 25 (2020) 1869

Conceptualization, T.H., U.W., B.G.; methodology, T.H., F.S.; formal analysis, T.H., F.S., U.W.; investigation, T.H., F.S.; data curation, T.H., F.S.; writing - original draft preparation, T.H., U.W.; writing - review and editing, T.H., F.S., S.B., B.G., U.W.; visualization, T.H., U.W.; supervision, B.G., U.W., S.B.; funding acquisition, B.G.

- [3] T. Hupfeld, T. Laumer, T. Stichel, T. Schuffenhauer, J. Heberle, M. Schmidt, S. Barcikowski, B. Gökce, *A new approach to coat PA12 powders with laser-generated nanoparticles for selective laser sintering*, Procedia CIRP 74 (2018) 244-248

Conceptualization, T.H., B.G.; methodology, T.H., T.L.; formal analysis, T.H., T.L., T.St.; investigation, T.H., T.L., T.St., T.Sch.; data curation, T.H.; writing - original draft preparation, T.H.; writing - review and editing, T.H., T.L., T.St., J.H.; visualization, T.H.; supervision, M.S., B.G., S.B.; funding acquisition, S.B.

- [4] T. Hupfeld, A. Sommereyns, T. Schuffenhauer, E. Zhuravlev, M. Krebs, S. Gann, O. Keßler, M. Schmidt, B. Gökce, S. Barcikowski, *How colloidal surface additivation of polyamide 12 powders with well-dispersed silver nanoparticles influences the crystallization already at low 0.01 vol%*, Additive Manufacturing 36 (2020) 101419

Conceptualization, T.H., B.G.; methodology, T.H., A.S., E.Z.; formal analysis, T.H., A.S., E.Z.; investigation, T.H., A.S., E.Z., T.S., M.K., S.G.; data curation, T.H., A.S.,

E.Z.; writing - original draft preparation, T.H., A.S., E.Z.; writing - review and editing, T.H., A.S., E.Z., T.S., M.K., B.G., M.S., S.B.; visualization, T.H.; supervision, B.G., O.K., M.S., S.B.; funding acquisition, E.Z., O.K., M.S., S.B.

- [5] T. Hupfeld, C. Doñate-Buendía, M. Krause, A. Sommereyns, A. Wegner, T. Sinnemann, M. Schmidt, B. Gökce, S. Barcikowski, *Scaling up colloidal surface additivition of polymer powders for laser powder bed fusion*, *Procedia CIRP* 94 (2020) 110-115

Conceptualization, T.H., B.G.; methodology, T.H.; formal analysis, T.H.; investigation, T.H., M.K., A.W., A.S.; data curation, T.H.; writing - original draft preparation, T.H.; writing - review and editing, T.H., C.D., A.W., A.S., M.K., T.S., B.G., M.K., M.S., S.B.; visualization, T.H.; supervision, T.S., B.G., S.B.; funding acquisition, S.B.

- [6] T. Hupfeld, A. Wegner, M. Blanke, C. Doñate-Buendía, V. Sharov, S. Nieskens, M. Piechotta, M. Giese, S. Barcikowski, B. Gökce, *Plasmonic seasoning: Giving color to desktop laser 3D-printed polymers by highly dispersed nanoparticles*, *Advanced Optical Materials* (2020) 2000473

Conceptualization, T.H., B.G., A.W.; methodology, T.H., A.W., C.D., V.S.; formal analysis, T.H., A.W., V.S., C.D.; investigation, T.H., A.W., M.B., V.S., C.D., S.N.; data curation, T.H., A.W.; writing - original draft preparation, T.H., A.W.; writing - review and editing, T.H., A.W., M.B., V.S., C.D., S.N., M.G., S.B., B.G.; visualization, T.H., A.W., V.S.; supervision, B.G., M.G., S.B.; funding acquisition, S.B.

- [7] T. Hupfeld, A. Sommereyns, F. Riahi, C. Doñate-Buendía, S. Gann, M. Schmidt, B. Gökce, S. Barcikowski, *Analysis of the Nanoparticle Dispersion and its Effect on the Crystalline Microstructure in Carbon-Additivated PA12 Feedstock Material for Laser Powder Bed Fusion*, *Materials* 13 (2020) 3312

Conceptualization, T.H., B.G., and S.B.; methodology, T.H., F.R., and A.S.; formal analysis, T.H., A.S., and F.R.; investigation, T.H., A.S., F.R., S.G., and C.D.-B; data curation, T.H. and A.S.; writing—original draft preparation, T.H. and A.S.; writing—review and editing, T.H., A.S., F.R., S.G., and B.G., M.S., S.B., and C.D.-B; visualization, T.H., F.R., A.S., and C.D.-B; supervision, B.G., S.B., and M.S.; funding acquisition, S.B., M.S.

- [8] T. Hupfeld, S. Salamon, J. Landers, A. Sommereyns, C. Doñate-Buendía, J. Schmidt, H. Wende, M. Schmidt, S. Barcikowski, B. Gökce, *3D Printing of Magnetic Parts by Laser Powder Bed Fusion of Iron Oxide Nanoparticle Functionalized Polyamide Powders*, *Journal of Materials Chemistry C* 8 (2020) 12204-12217

Conceptualization, T.H., B.G.; methodology, T.H., S.S., J.L., C.D.; formal analysis, T.H., S.S., J.L., C.D., A.S., J.S.; investigation, T.H., S.S., J.L., C.D., A.S., J.S.; data curation, T.H., S.S., J.L.; writing - original draft preparation, T.H., S.S., J.L.; writing

- review and editing, T.H., S.S., J.L., A.S., C.D., J.S., H.W., B.G., M.S., S.B.;
visualization, T.H., S.S., J.L., C.D., J.S.; supervision, H.W., B.G., M.S., S.B.; funding
acquisition, S.B., M.S., H.W.

List of student works

The student works listed below were done in the context of the present thesis at the Chair for Technical Chemistry at the University of Duisburg-Essen. The definition of the objective, the planning and conduction of experiments as well as the evaluation, interpretation and visualization of results took place under the scientific guidance of Tim Hupfeld.

- [1] Frederic Kürsten, Christian Gollner, *Einfluss des Ablationsmediums auf die Größenverteilung und Zusammensetzung von Yttrium Eisen-Granat-Nanopartikeln und deren Einbettung in eine Polymermatrix*, Master project (07.2016 - 02.2017)
- [2] Frederic Kürsten, *Größen- und Phasenselektion kolloidaler Yttrium-Eisen-Granat-Nanopartikel durch gepulste Laserbestrahlung für die Herstellung von Nanopartikel-Polymerkompositen*, Master thesis (03.2017 - 11.2017)
- [3] Karsten Knop, *Herstellung hochtransparenter Nanopartikel-Polymerkomposit-Beschichtungen auf Basis lasergenerierter magnetischer Nanopartikel*, Master thesis (02.2017 - 09.2017), Co-supervised by Elisabeth Mühlhausen
- [4] Alexander Schmitz, Alexander Schug, *Einfluss der Pulsdauer auf die Laserablation von Yttrium-Eisen-Granat-Nanopartikeln in organischen Lösungsmitteln*, Master project (03.2017 - 06.2017)
- [5] Simon Nieskens, *Herstellung von Nanopartikel-Polymerkompositen für die Additive Fertigung durch Additivierung mit kolloidalen lasergenerierten Nanopartikeln*, Bachelor thesis (05.2017 - 08.2018)
- [6] Leyla Cakir, Philipp May, Elisavet Papadopoulou, *Trägerung von lasergenerierten Silbernanopartikeln auf Polymermikropartikeln für die Additive Fertigung*, Bachelor project (10.2017 - 01.2018)
- [7] Farbod Riahi, *Additivierung von Polymerpulvern mit laserbestrahlten Kohlenstoffnanopartikeln für die laserbasierte Additive Fertigung*, Master thesis (06.2018 - 02.2019)

- [8] Vladyslav Sharov, *Herstellung von Nanopartikel-TPU-Kompositpulvern für die Additive Fertigung via Laser Sintern*, Bachelor thesis (07.2018-12.2018)
- [9] Moritz Krebs, *Untersuchung der Kompositpulverherstellung aus lasergenerierten Nanopartikel und Polymermikropartikeln für die Additive Fertigung*, Internship (10.2018 - 01.2019)

Eigenständigkeitserklärung (Declaration)

Hiermit versichere ich, dass ich die vorliegende Arbeit mit dem Titel

„Nanoparticle-Functionalized Polymers for Laser Powder Bed Fusion“

selbst verfasst und keine außer den angegebenen Hilfsmitteln und Quellen benutzt habe, und dass die Arbeit in dieser oder ähnlicher Form noch bei keiner anderen Universität eingereicht wurde.

Ort, Datum

Tim Hupfeld